Mission Design for Flyback Boosters

Towards Reusable Launch Vehicles

Irmak Çavdar

Delft University of Technology

TU Delft

Mission Design for Flyback Boosters

Towards Reusable Launch Vehicles

by

Irmak Çavdar

in partial fulfillment of the requirements for the degree of

Master of Science
in Aerospace Engineering

at Delft University of Technology
to be defended publicly on Monday August 28, 2023, at 9:30

Student number:	4782364
Supervisor:	Dr.ir. E. Mooij, TU Delft
Committee Members:	Chair: Dr. S.M. Cazaux, TU Delft
	Examiner: Dr ir E. van Kampen, TU Delft
	Supervisor: Dr.ir. E. Mooij, TU Delft
Project Duration:	December, 2022 - August, 2023
Faculty:	Faculty of Aerospace Engineering, Delft

Cover:	Flyback Booster Concept of NASA from Kerbal Space Program game (Credits: Squad and Blitworks)
Style:	TU Delft Report Style, with modifications by Daan Zwaneveld

TU Delft

Acknowledgments

I started my TU Delft journey in 2018 with a Bachelors in Aerospace Engineering. As I passed underneath the big aircraft in the faculty for the first time, I was captivated by the idea of space and had Gene Kranz's words on my mind: "Failure is not an option". Each day was more challenging than the previous one, which continued during my Masters. Nevertheless, I appreciate every second of it as I achieved my dream of becoming an aerospace engineer and have the unparalleled opportunity of contributing to the advancement of the space era.

Foremost, I am immensely grateful for my supervisor Erwin Mooij. I would like to thank you for always guiding me towards excellence. Upon completion of this thesis study, not only I learned a lot about mission design, but also what it means to be an engineer. I promise I will always keep thinking critically.

A special thank goes to my childhood friends, Ayca, Ekin, and Irmak, for always cheering for me and being my greatest supporters. Your kind words have meant the world to me. A set of thank goes to my friends from the faculty, Aytek, Gopal, Manos, Manos, Praj, and Crina. Without you guys I would not be able to survive the Bachelors and pass Mechanics of Materials (probably). Another special thank goes to Doruk for shaping my journey in the best way possible. I am grateful for the laughter we shared during these dark thesis days.

Finally, I would like to express my sincerest gratitude to my parents, Siran and Fatih, for always believing in me. Even when I told them I want to be an astronaut at the age of nine. Thank you for supporting me in the best way possible. Your sacrifices shaped me into the person I am today.

Irmak Çavdar
Delft, August 2023

Summary

In the pursuit of advancing space exploration, the development of fully reusable launch vehicles introduced a paradigm shift in the aerospace industry. Previously, the main incentive to develop a fully reusable launch vehicle was the significant development costs of such a system. As the operational benefits of the vehicles became unjustifiable against the complexity and cost of the design, various missions have been discontinued in the last two decades. Among various approaches to fully reusable launchers, a flyback booster, complemented by the emerging importance of spaceplanes, stands out as a viable solution. Nevertheless, to outweigh the drawbacks associated with the cost, a reliable mission design has to be performed for the developed flyback booster. This would increase the overall understanding of the mission characteristics and ensure that the booster is designed accordingly. Consequently, certain risks can be diminished. However, since there are various components to be focused on during a mission design, it is aimed to optimize the mission design process. As a result, the optimization can be better guided toward feasible solution spaces.

To this end, the main research question is formulated as below:

How can a mission design process be optimized for unpowered and powered flyback boosters to effectively compare the two configurations?

Upon investigating different mission heritages, the FESTIP System Study Concept 16 (FSSC-16) is selected as a reference flyback booster. The selection is mainly due to the availability of the data and the completeness of the research. From the reference vehicle, the characteristics are identified. Since the FESTIP study lacked a detailed description of certain properties, such as an aerodynamic database or mass model, they are defined from scratch using numerical methods and other available databases, for instance, the HORUS aerodynamic database. Having identified all the properties of the booster, a proper description of the mission and system requirements is generated. Considering these requirements, to simulate the fly back trajectory of the booster, a simulation environment has to be defined. This is performed by first identifying the models that are used in the simulation and then using these models to express the complete set of equations of motion.

The simulation environment propagates the booster's state using a set of guidance commands. For the unpowered flyback booster, the guidance commands consist of aerodynamic angles, and for the powered vehicle the commands are the thrust parameters. The guidance law is updated at each control node which is equidistantly separated along the trajectory. Accordingly, it is aimed to investigate the influence of these parameters on the trajectory and then obtain the optimum set of guidance commands.

Consequently, having a coherent mission design with an optimum reference trajectory is the main goal of this research. Obtaining an optimum trajectory is not a trivial task, as it requires a thorough design space exploration to identify the factors that influence the trajectory and drive the design the most. It is intended to explore the design space as efficiently as possible. Therefore, the mission design process is optimized as well as the trajectory. The first step of any optimization process is to explore the objective space and identify the influence of the decision parameters on the response, which is not only the complete trajectory but also the objectives and constraints. To obtain a structured approach, various methods are implemented for the design space exploration. The information obtained from each method is analyzed with ANOVA and is combined to improve the decision variables' range at each step. The results concluded that: the one-at-a-time simulation provided a preliminary approach to the design space. The primary level of interactions are identified between a decision variable and the trajectory. Upon confirming that the response of the booster to changing flight dynamics is reasonable, the fractional factorial design is implemented. During the first batch of fractional factorial design, inconsistent changes in the square sum of errors across different thrust magnitudes confirmed the presence of strong interactions. Accordingly, the need for a more structured method arose, such that the interaction between factors can be observed clearly and the decision variable range can be

adapted accordingly. As a result, the second batch of fractional factorial design is implemented using the Taguchi interactions and subsets of the data set.

Upon obtaining the fine-adapted decision variable range, the optimization environment is set up. Two optimization methods are compared thoroughly: NSGA-II and MOEA/D. Various performance metrics, such as hypervolume indicators, are used to compare these two optimization algorithms. Although studies have identified that MOEA/D has better performance characteristics, the comparison concluded that NSGA-II performs better than MOEA/D for the problem at hand, considering the computational limitations.

The fly back trajectory is optimized using different sets of objectives for different operational configurations. For the unpowered flyback booster, the aim is to obtain a trajectory that has the minimum final distance-to-go and does not violate the path errors. Whereas, for the powered flyback booster, it is desired to obtain a trajectory that consumes the least amount of fuel while complying with the path constraints and the final distance-to-go constraint of 0.75°. Although the unpowered trajectory optimization yielded unsuccessful results as the final distance-to-go could not be minimized below 3.48°, the powered optimization showed promising results. The vehicle successfully reached the desired final distance-to-go of 0.75° while complying with all the path constraints and consuming only 7076 kg of fuel. The optimum trajectory is then compared with the FESTIP study. The comparison suggested that the powered flyback booster consumed only 1.08% more fuel than the one evaluated by FESTIP, which verified the study. In the end, a local refinement and a second batch of global optimization are performed to investigate the vicinity of the optimum solution. By doing so, it is focused to assess whether it is possible to obtain a better solution for the powered trajectory. The findings suggest that by increasing the engine capabilities with 10% an additional 615 kg of mass can be saved.

The optimum trajectory is further evaluated to understand the flyback booster characteristics and the sensitivity of the trajectory to different parameters. This analysis concluded that the adapted decision variable range has a significant effect on the convergence speed of the optimization as well as the performance of the solution. In terms of fuel consumption, the full decision variable range tends to have a much higher solution. Another analysis is conducted around the trimmability of the vehicle. Since the presence of a thrust elevation angle introduces additional thrust moment, the relationship between the thrust elevation angle and trimmability is inspected. The results suggest that with the current propulsion system, only a weak relationship between the thrust and trim can be identified. Thus, although changing the thrust elevation angle affects the moment distribution, the booster is still trimmable with non-significant changes in the control surface deflections.

In conclusion, the optimization process of the flyback booster trajectory can be further enhanced. To do so, it is crucial to identify the trajectory in detail through literature and well-structured design space exploration methods. Especially a fractional factorial design is a key to identifying interactions and individual contributions. However, depending on the dimensionality of the problem, subsets may need to be formed, or else the computational intensity would be high. As a result, the optimization algorithm had better characteristics in terms of convergence speed and solution performance.

Contents

Nomenclature

Abbreviations

Abbreviation	Definition
3DOF	3 Degrees of Freedom
ABM	Adams-Bashforth-Moulton
AC	Aerodynamic Center
AMPI	Adaptive Multivariate Pseudo-spectral Interpolation
ANOVA	Analysis of Variance
CoM	Center of Mass
CoT	Center of Thrust
DLR	Deutschen Zentrum für Luft- und Raumfahrt (German Aerospace Center)
EA	Evolutionary Algorithm
ECEF	Earth-Centered, Earth Fixed Reference Frame
ECIF	Earth-Centered, Inertial Reference Frame
ESA	European Space Agency
FESTIP	Future European Space Transportation Programme
FFD	Fractional Factorial Design
FSSC	FESTIP System Study Concept
GA	Genetic Algorithm
GGM02	GRACE Gravity Model 02
GPS	Global Positioning System
GTO	Geostationary Transfer Orbit
HAC	Heading Alignment Cylinder
IMU	Inertial Measurement Unit
ISS	International Space Station
LFBB	Liquid Flyback Booster
MOEAD	Multi-Objective Evolutionary Algorithm Based on Decomposition
MPI	Multivariate Pseudo-spectral Interpolation
NASA	National Aeronautics and Space Administration
NED	North, East, Down
NSGA-II	Non-dominated Sorting Genetic Algorithm II
RSS	Root sum square
PaGMO	Parallel Global Multiobjective Optimizer
POST	Program to Optimize Simulated Trajectories
PSO	Particle Swarm Optimization
RCS	Reaction Control System
ReFEX	Reusability Flight Experiment
RLV	Reusable Launch Vehicle
RSS	Root Sum Square
SBX	Simulated Binary Crossover
SSTO	Single Stage to Orbit
STOL	Short Take Off and Landing
TAEM	Terminal Area Energy Management
TPS	Thermal Protection System
TSTO	Two Stage to Orbit
TUDAT	TU Delft Astrodynamic Toolbox

Abbreviation	Definition
US76	U.S. Standard Atmopshere, 1976
VTHL	Vertical Take-off and Horizontal Landing
VTVL	Vertical Take-off and Vertical Landing
WGS84	World Geodetic System 1984

Symbols

Symbol	Definition	Unit
A	Area	[m^2]
$\boldsymbol{a}$	Acceleration Vector	[m/s^2]
a	Speed of Sound	[m/s]
b_{ref}	Aerodynamic Reference Length (wingspan)	[m]
c	Speed of Light	[m/s]
$\boldsymbol{C}$	Transformation Matrix	[-]
C_D	Drag Coefficient	[-]
C_L	Lift Coefficient	[-]
C_l	Roll Moment Coefficient	[-]
C_m	Pitch Moment Coefficient	[-]
$C_{m_{ac}}$	Pitch Moment Coefficient around the AC [-]	
C_n	Yaw Moment Coefficient	[-]
c_{ref}	Aerodynamic Reference Length (cord)	[-]
D	Drag Force	[N]
dt	Time Increments	[s]
e	Ellipticity	[-]
$\boldsymbol{e(t)}$	Tracking Error	[variable]
$\boldsymbol{F}$	Force Vector	[N]
F	Reference Frame	[-]
$\boldsymbol{f}$	Dynamic System Vector	[-]
g	Gravitational Acceleration	[m/s^2]
$\boldsymbol{g}$	Gravitational Acceleration Vector	[m/s^2]
h	Altitude	[m]
I	Moment of inertia	[kgm^2]
$\boldsymbol{I}$	Inertia Tensor	[kgm^2]
I_{sp}	Specific Impulse	[-]
J	Cost Criteria	[-]
k	Number of Factors	[-]
$\boldsymbol{L}$	Design Matrix	[-]
L	Lift Force	[N]
$\mathcal{L}$	Roll Moment	[Nm]
M	Mach Number	[-]
m	Mass	[kg]
m	Number of Design Levels	[-]
m	Empirical Constant	[-]
$\dot{m}$	Mass Flow	[kg/s]
$\mathcal{M}$	Pitch Moment	[Nm]
$M_{T_{x,y,z}}$	Propulsion Moments in XYZ Axis	[Nm]
$\mathcal{N}$	Yaw Moment	[Nm]
N	Number of Experiments	[-]
n_g	G-load	[-]
n	Load Factor	[-]
n_k	Number of Factors (ANOVA)	[-]
n_l	Number of Design Levels (ANOVA)	[-]

p	Pressure	[Pa]
p_a	Atmospheric Pressure	[N/m^2]
P_i	Individual Percentage Contribution	[-]
q	Heat Flux	[kW$/$m^2]
$\bar{q}$	Dynamic Pressure	[N/m^2]
$\boldsymbol{r}$	Position Vector	[-]
r	Yaw Rate	[rad/s]
R	Radius	[m]
R	Gas Constant	[-]
R_E	Earth Radius	[m]
R_e	Equatorial Radius	[m]
R_N	Nose Radius	[m]
S	Side Force	[N]
S_E	Error Sum of Squares	[-]
S_i	Sum of Squares	[-]
S_T	Sum of Square Deviation	[-]
t	Time	[s]
T	Temperature	[K]
$\boldsymbol{T}$	Thrust Vector	[-]
$\boldsymbol{V}$	Velocity Vector	[-]
V	Velocity	[m/s]
$\boldsymbol{x}$	State Vector	[-]
y	Response/Result	[variable]
$\boldsymbol{z}$	Reference Vector	[-]

Greek Letters

Symbol	Definition	Unit
α	Angle of attack	[deg]
β	Side-slip angle	[deg]
γ	Flight-path angle	[deg]
δ	Geocentric latitude	[deg]
δ	Deflection	[deg]
η	Signal to noise ratio	[-]
ϵ	Elevation angle	[deg]
ρ	Atmospheric density	[kg/m^3]
σ	Bank angle	[deg]
τ	Longitude	[deg]
χ	Heading angle	[deg]
ψ	Azimuth angle	[deg]
ω	Angular rate	[deg/s]

1 Introduction

Ever since NASA's Space Shuttle orbiter Columbia performed its first successful landing at Edwards Air Force Base on a breezy April day in 1981, it has been desired to enhance reusable launch vehicles. Especially within the last decade, the use of launch vehicles has increased, as private companies have started taking part in space exploration. Compared to the early 1980s, the market for launch vehicles has become significantly more competitive, introducing the desire to have fully reusable launch vehicles.

Previously, the major disincentive to develop a reusable launch vehicle was the significant development costs. This caused various missions, such as the Space Shuttle by NASA or the Liquid Flyback Booster concept by German Aerospace Center (DLR), to be terminated before being improved or even developed at all since the economic benefits became unjustifiable due to the increased complexity of the design (Tetlow et al., 2001). Nevertheless, the operational cost of current launch vehicles, such as Ariane and Delta, are non-negligible due to the refurbishment and expandability costs. It is believed that successful development of a reusable launch vehicle can decrease the time associated with vehicle design and launch costs in the long run (Hanson, 2000).

It is aimed to reduce the refurbishment costs and develop a fully reusable launch vehicle through flyback boosters. Among various approaches to flyback boosters, winged boosters that utilize vertical take-off and horizontal landing (VTHL) are a feasible option. Such flyback boosters complement the importance of spaceplanes as both concepts offer unparalleled operational flexibility that cannot be matched by traditional first-stage boosters. The designs of flyback boosters differ in terms of operational configuration. The first design utilizes aerodynamic capabilities to perform an unpowered fly back trajectory. In literature, it is also identified as a glideback booster. Meanwhile, the second design uses air-breathing engines to perform a return flight. Naftel and Powell (1993) have identified that having an unpowered return is more efficient for winged boosters. This is due to two main reasons. First, the need for an airbreathing engine is eliminated along with the cost and effort required to maintain the engines. Second, powered flyback would require the vehicle to carry extra fuel that would be used once the staging maneuver is performed. Hence, increasing the mass that needs to be launched. Nevertheless, Tetlow et al. (2001) also have identified that it is possible to overcome the drawbacks associated with the powered flyback since it allows for increased payload-carrying capabilities. To ensure that a given fully reusable launch vehicle outweighs the current expandable vehicles, a reliable flyback booster system with low-cost operational functionalities has to be developed.

Often the reliability of a system is linked to its safety since a safe system is achieved by the use of reliable structures, models, simulations, and components. Through a comprehensive analysis of a mission, it is possible to obtain reliable models and simulations from the early stages of a mission design. Therefore, by revisiting the mission profiles of vehicles, the risks associated with unforeseen circumstances can be reduced. Accordingly, this leads to an increase in flight safety (Hanson, 2000). While performing a mission design, there are various parameters to take into account that affect the performance and reliability of the vehicle. It is crucial to identify the most significant parameters to focus the design around and enhance reliability. One way of achieving this is through optimizing the mission design process to increase the understanding of the overall mission.

The trajectory of re-entry vehicles has been discussed by various studies throughout the years

(Tramonti and Brusch, 1972, Sushnigdha and Joshi, 2018). However, in the pursuit of advancing space exploration, studies on flyback boosters have only emerged in the last two decades (Schlotterer, 2008). Although the winged re-entry vehicles, such as the Space Shuttle, show similarities to the structure of the flyback boosters, the mission profiles differ. The most significant difference is the performance of the two vehicles. A re-entry vehicle performs a high-speed descent in which it undergoes high aerodynamic loads, whereas, a flyback booster performs a much more controlled descent with various phases, such as the ballistic phase, return phase, and glide back phase. Therefore, understanding the principles of the booster stage would not only allow the development of a fully reusable vehicle but also allow a better understanding of sub-orbital return flights.

It is evident that whether the vehicle is powered or unpowered will have a significant effect on the trajectory architecture, as well as the guidance and control of the vehicle. The goal is to understand the mission profiles and engineering differences in the trajectories of different flyback boosters while utilizing an optimal mission design process. Through the knowledge attained from this thesis, it is possible to improve the performance, cost, and safety of the flyback boosters to make space more accessible and attainable for various endeavors.

1.1. Problem Statement

As it has been pointed out in the aforementioned discussion, the costs of current expandable launch vehicles are still significant. Yet, the cost estimation for fully reusable launch vehicles is an unknown terrain due to missing data on operational cost and reference missions (Wilken et al., 2021). Nevertheless, use of the TRANSCOT-Model allowed to perform a preliminary cost estimation of 7 to 23 billion US $. Note that the large range exists due to availability of various different concept vehicles (Koelle, 2002). To justify the cost of development, operation, and recovery of a reusable launch vehicle, a reliable system has to be obtained (Wertz, 2000). Therefore, as it was identified previously, constructing a detailed mission is one of the methods for achieving such reliability.

Nevertheless, it is crucial to carefully identify the important aspects of a trajectory. By employing an optimal mission design, it is possible to explore a vast design space in a disciplined manner. As a result, a more coherent understanding of the mission can be obtained, indicating that the engineers can increase the efficiency and reliability of the mission. Therefore, the objective of this research is to optimize the mission design process for a flyback booster, while comparing the optimal trajectory of the different operational configurations. Therefore it is aimed to answer the following research question:

RQ: *How can a mission design process be optimized for unpowered and powered flyback boosters to effectively compare the two configurations?*

It is possible to break down the above research question into sub-questions. By doing so it is aimed to conduct a comprehensive literature study that can answer the research question in a structured manner while having a more manageable research area. Note that to be able to track sub-questions a unique identification, **SQ-x**, is given to each sub-question:

- **SQ-1:** What are the characteristics of a flyback booster trajectory?
- **SQ-2:** What is the most suitable design space exploration technique for the fly back trajectory optimization problem?
- **SQ-3:** How sensitive is the flyback booster trajectory to aerodynamic and thrust parameter commands?
- **SQ-4:** How do the flight dynamics of the vehicle affect the development of the optimal trajectory?
- **SQ-5:** How does the optimal trajectory of a powered flyback booster differ from a trajectory of an unpowered flyback booster?
- **SQ-6:** How does the result of the design space exploration affect the optimization process?
- **SQ-7:** How does the optimal trajectory of the powered flyback booster perform under varying operational conditions?

1.2. Report Overview

To begin with, Chapter 2 provides a historical overview of powered and unpowered flyback boosters Later in the chapter, a reference mission is identified and the characteristics of the vehicle, including

the mass, propulsion, and aerodynamic model, are studied. Finally, the mission and system requirements are presented for a coherent understanding of the thesis assignment. In Chapter 3 the relevant environment model for setting up the simulation is presented. The effect of chosen models and the overall flight dynamics are expressed mathematically in Chapter 4. Relevant reference frames, frame transformations, and state variables are also discussed here. Chapter 5 is an introduction to the flyback booster's trajectory. The trajectory problem is set up in this chapter by defining the objectives, constraints, and decision variables. Knowing the characteristics of the trajectory and problem, a simulation is built using the software blocks that are presented in Chapter 6. The mission design begins in Chapter 7 with a comprehensive design space exploration. The results of the design space exploration are utilized in Chapter 8 for optimizing the trajectory. Meanwhile, in Chapter 9 the optimal trajectory for the powered flyback booster is investigated in more detail to identify the sensitive parameters of the design. To conclude this thesis, in Chapter 10 the objective of the study is re-stated with the main conclusions. Finally, a set of recommendations are performed for future research.

2

Mission & System Description

To unlock new possibilities and enhance the future of space exploration, new concepts have been regarded in the industry. One of these is the flyback boosters, which adopt the key features of the spaceplane and have increased operational flexibility, compared to the current boosters. The goal of this chapter is to identify the characteristics of a flyback booster by studying past and recent missions. Later on, the information obtained is used during the mission design of the flyback booster. In Section 2.1 a historical overview on the topic is presented. The mission heritage shows that there are not so many publicly available data on flyback boosters and the studies are often in preliminary design phases. Thus, the relevant re-entry missions are also studied and the need for a detailed mission design for flyback boosters is stressed. The reference vehicle is selected and the characteristics are presented in Section 2.2. In Section 2.3 the vehicle and mission requirements are identified. These requirements are the driving factors for the rest of the thesis study as they define the characteristics of the developed system.

2.1. Mission Heritage

The most famous reusable launch vehicle mission is the Space Shuttle Program by NASA. However, as technology has improved since the last flight in June 2011, the capabilities of the vehicles have also increased. As various private companies, such as SpaceX and Blue Origin, have emerged in the research, the demand for investigating mission design for reusable launch vehicles has increased. Since there are no conventional methods for recovering the first stages, various concepts such as vertical take-off and vertical landing (VTVL) or vertical take-off and horizontal landing (VTHL) are under active investigation. At this point, it should be noted that currently there are no operational flyback boosters, except for SpaceX Falcon 9 and Falcon Heavy which have very limited public data about the technical aspects of the missions. Therefore, the historical overview is more focused on different re-entry vehicles and spaceplane concept studies. By investigating the characteristics of various missions, it is aimed to comprehend the mission profile of any vehicle that performs a return flight. Consequently, the information obtain from the study of mission heritage is utilized to identify the possible flight profiles and desired objectives, which is important while setting up the trajectory problem for the design space exploration and optimization.

2.1.1. NASA Space Shuttle

The Space Shuttle by NASA is the first-ever reusable launch system that was developed. The vehicle has been used for 30 years to build one of the most significant architectures in space, the International Space Station (ISS). Although the Space Shuttle is the pioneer of reusable spacecraft, it was only partially reusable. Only the orbiter could land on a runway horizontally, whereas, the solid rocket boosters had to be extracted from the ocean. Before the next flight, the boosters had to go through an extensive maintenance process to drain the ocean water. The goal is to study the Space Shuttle to obtain an overview of mission design concepts, the re-entry corridor, and the aerodynamic guidance principle. Accordingly, it becomes a necessary first step to understand the flyback boosters and the corresponding mission.

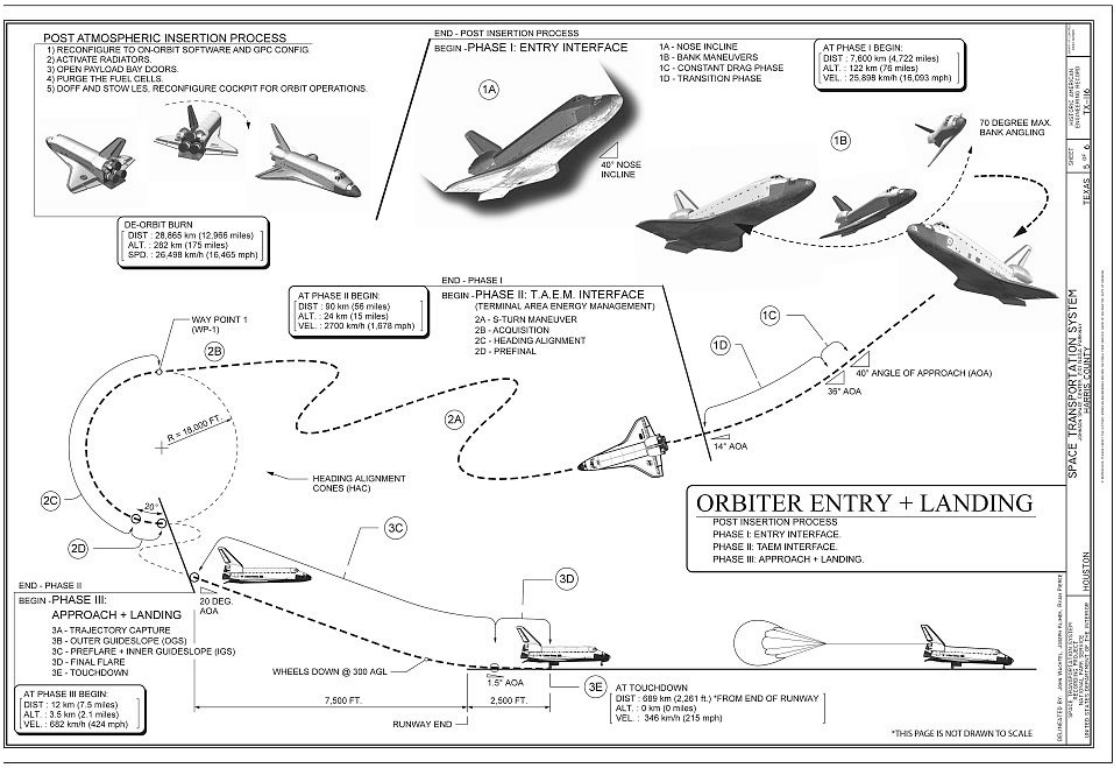

Figure 2.1: Orbiter re-entry trajectory and landing sequence (Historic American Engineering Record and National Aeronautics And Space Administration, 1968)

For the Space Shuttle, the re-entry flight began after the de-orbiting operations followed by the main engine of the booster. The overall re-entry mission profile is visualized in Figure 2.1. Upon re-entering the atmosphere at an altitude of 122 km, the orbiter had to alter its orientation. At this point, the vehicle was guided through the atmosphere by only aerodynamic capabilities. The orientation change was performed via a 70° bank angle maneuver. Note that due to the structural limitations on the vehicle, this was the maximum bank angle that was endured by the vehicle. At the end of the turn maneuver, the vehicle orientation fulfilled the Terminal Area Energy Management (TAEM) interface requirements. The primary goal of the horizontal guidance system was to manage the energy state of the orbiter to successfully meet with the TAEM phase (Mooij, 2016).

The TAEM phase started at Mach 2.5 about 25 km altitude when the orbiter reached the TAEM interface. The TAEM interface is a circular area with the center located at the targeting point and is visualized in Figure 2.2. Upon entering the TAEM phase, the orbiter was guided toward the Heading Alignment Cylinder (HAC), which is a virtual cylindrical path. Depending on the intersection conditions, either a right (HAC-R) or left (HAC-L) turn can be followed. During the HAC, the orbiter's bank angle was modulated to sustain a constant radius turn. When the orbiter achieved the desired landing direction at a distance-to-go of 0.75°, the landing operations began in a straight descending flight (Moore, 1991). Therefore, the main objective of the TAEM phase is to dissipate the energy in a desired manner while aligning the vehicle with the runway.

The vehicle was designed such that it is suitable for ascent, atmospheric re-entry, and landing. This drove the design to a great complexity as for ascent and re-entry blunt objects were preferred but the wings were necessary to allow the vehicle to land on a runway in an aircraft-like manner. The vehicle reentered the Earth's atmosphere at around 7000 m/s. Meanwhile, the re-entry angles of the vehicle were dependent on the calculated entry corridor. Certain de-orbit maneuvers were performed to avoid steep flight-path angles. As the vehicle dives deeper into the atmosphere, such angles result in excessive drag and overheating. On the other hand, shallow flight-path angles result in inadequate drag and limited aerodynamic control. Hence the vehicle could not be captured by the atmosphere (Mooij, 2016). Nevertheless, the GNC system of the Space Shuttle was successful at bringing the crew

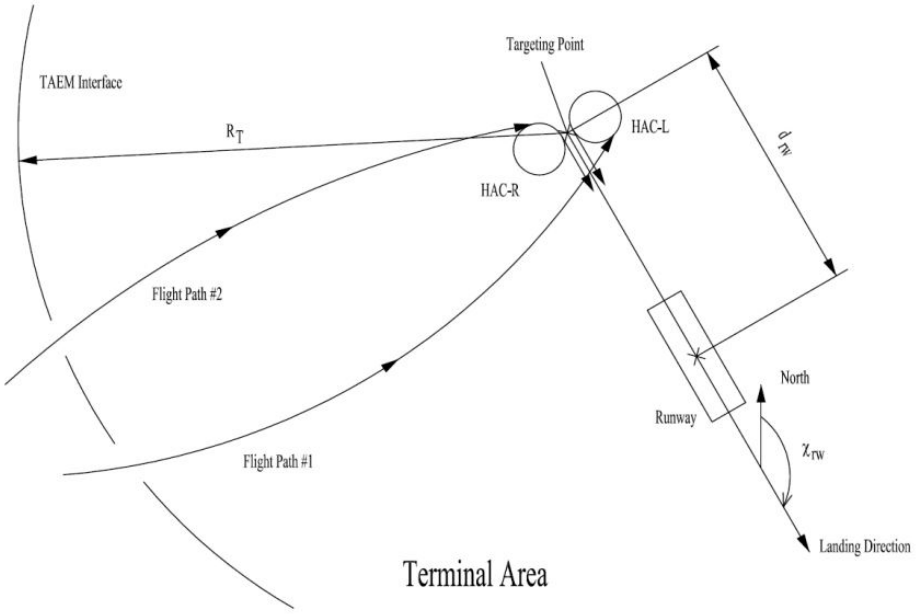

Figure 2.2: Intersection with TAEM phase and the guidance in TAEM (Mooij, 2016)

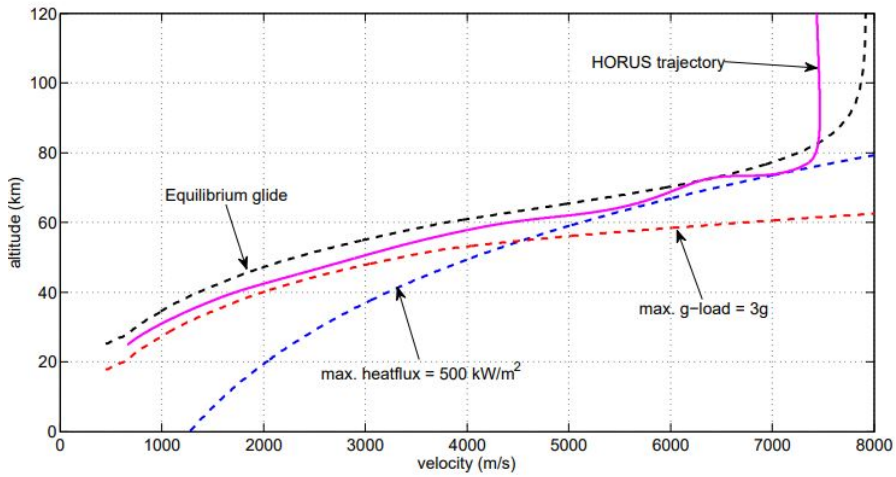

Figure 2.3: Re-entry trajectory of HORUS in three-dimensional space (Mooij, 2016)

safely to the ground by decelerating from a tremendous speed to approximately a landing speed of 101 m/s.

2.1.2. Sänger HORUS

Similar to the Space Shuttle, HORUS is a winged re-entry vehicle that is designed by Sänger. However, the vehicle differs from the Space Shuttle in terms of dimensions and performance. In this thesis, it is also desired to study HORUS to observe the differences in the two trajectories. Additionally, the HORUS is studied due to the availability of vehicle databases and mission design reports, which allowed a more comprehensive research.

During a re-entry or a descent flight, the vehicle is under certain loads. A spatial corridor is defined, as so-called re-entry corridor, to ensure that the trajectory is within the constrained region. The HORUS' trajectory and the corresponding re-entry corridor are shown in Figure 2.3. During a preliminary trajectory design, often three path constraints are regarded: the equilibrium glide, maximum heat flux, and maximum g-load. The equilibrium glide constraint is a theoretical limit that avoids the vehicle from ex-

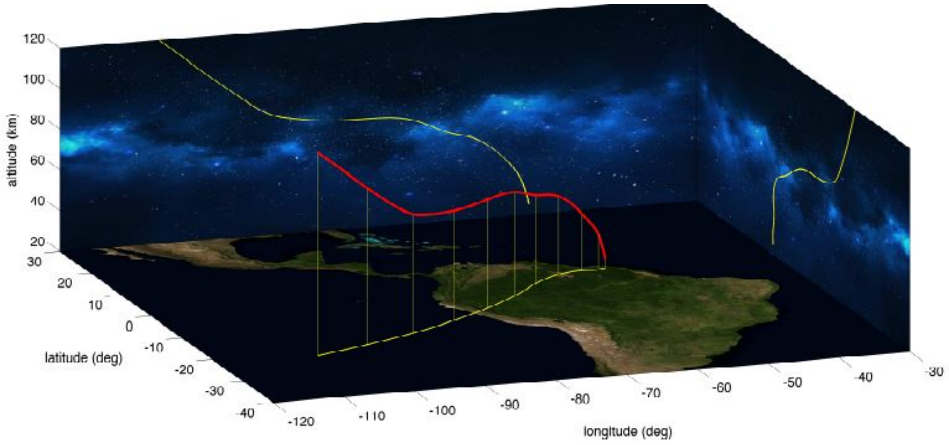

Figure 2.4: Re-entry trajectory of HORUS in three-dimensional space (Mooij, 2016)

periencing a skipping flight. The maximum allowable heat flux and maximum g-load represent the two structural limitations of the vehicle. To guide the trajectory toward a desired design space, it is possible to expose it to other constraints as well. As long as a constraint can be expressed in altitude-velocity space, it can also be used to form the re-entry corridor. An additional re-entry corridor constraint could be hinge moment control limits, which can be used for air-breathing spaceplanes (McRuer, 1991).

By regulating the angle of attack and bank angle, HORUS flies within the re-entry corridor. The initial angle of attack is set to deliver the maximum lift, which is $\alpha = 40°$. The objective of the maximum lift configuration is to obtain a smaller rate of descent for the vehicle to reduce the heat flux. However, around 6500 m/s, as also observed in Figure 2.3, the peak heat flux value is reached. To avoid a possible skipping flight, the bank angle modulation is initiated. This caused HORUS to fly further away from the maximum heat flux constraint. Through bank angle modulation, the vehicle is kept inside the entry corridor, whereas, through angle of attack modulation L/D ratio is adapted to change the cross and down-range capabilities of the vehicle. Therefore, by commanding the desired aerodynamic angles, the longitudinal guidance controls the vehicle's speed and pitch to keep the vehicle within the re-entry corridor.

Looking at the three-dimensional re-entry figure in Figure 2.4, it is observed that the re-entry trajectory is different from the Space Shuttle's trajectory. Due to the initial conditions at the point of re-entry, HORUS' heading angle is already towards the desired landing direction. This eliminates the need for an initial turn maneuver to align the heading angle with the runway. Nevertheless, at the end of the flight in Figure 2.4 the vehicle also meets with the TAEM interface to glide along the HAC. It is worthwhile to mention that the initial turn maneuver and the HAC serve different purposes. The initial turn maneuver aligns the vehicle toward the runway. A further adjustment is required to land at the desired location with precise accuracy, which is carried out by the HAC.

2.1.3. DLR ReFEx

With the emerging private companies, the design of reusable first-stage vehicles has been a popular research area. A significant number of these private companies are US-based, hence the importance of designing and building reusable launch vehicles has recently increased in Europe. Currently, the DLR is working on the Reusability Flight Experiment (ReFEx). The test vehicle is being developed to be launched in 2024 (Schwarz et al., 2019).

Similar to the Space Shuttle, ReFEx represents a VTHL approach. However, it has a unique re-entry trajectory. The booster separation is planned to occur at a velocity of 2 km/s and at an altitude of 50 km. After the separation point, the first stage follows a ballistic trajectory. However, during this phase, the vehicle is in an inverted configuration to ensure stability at high re-entry angles of attack. This indicates that the vehicle performs the re-entry while the vertical tail is pointing towards the surface of the Earth. The aforementioned high angles of attack values are between 40 ° to 50 °. Due to the high separation altitude, during the ballistic flight the aerodynamic forces are almost ineffective. As the vehicle penetrates deeper into the atmosphere the aerodynamic forces increase significantly,

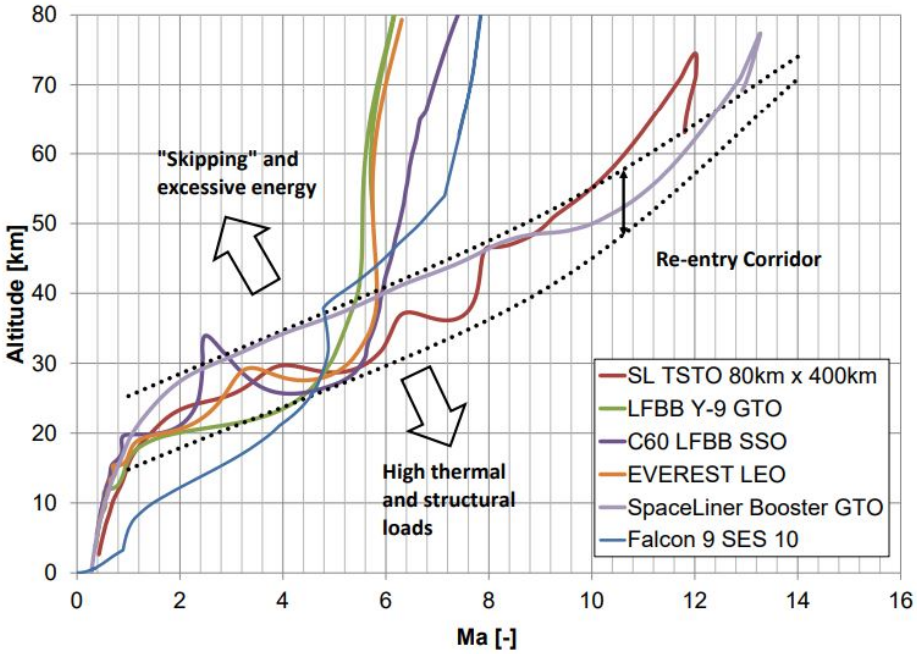

Figure 2.5: Re-entry corridor of various reusable launch vehicle stages (Stappert et al., 2019)

meanwhile, the angle of attack is reduced rapidly. Through the aerodynamic angles, thermal loads on the vehicle and cross-range is controlled. At this point, the vehicle is still in an inverted configuration. A roll maneuver is induced to return into an upright configuration around Mach 1.5 (Schwarz et al., 2019). After this, the re-entry vehicle transitions to subsonic velocities and continues the mission as a subsonic glider, until the end of the mission.

It is crucial to modulate the heat flux and integrated heat load for a sub-orbital re-entry flight since high thermal loads jeopardize the thermal protection system. Consequently, an enhanced thermal protection system could increase the overall vehicle mass and reduce the payload capabilities (Stappert et al., 2019). In Figure 2.5 a re-entry corridor for different reusable launch vehicle stages is visualized. The thermal load constraint corresponds to the lower bound in Figure 2.5. In the meantime, the upper bound corresponds to the excessive energy. If the vehicle performs the entry with a steep flight-path angle or with an excessive lift, the vehicle may experience a skipping flight. As a result, the vehicle's energy cannot be dissipated in a desired manner. A trajectory control is required to maintain such a re-entry corridor, which is achieved by providing guidance commands in aerodynamic angles, similar to the HORUS and the Space Shuttle.

It is identified that the flight profile of ReFEx is different from that of the Space Shuttle. Nevertheless, the guidance and control strategies of the vehicle are more comparable. Since the separation occurs at high altitudes at this point the aerodynamic forces are negligible. Hence, up until separation control of the vehicle is achieved through the reaction control system (RCS). As the vehicle begins to fall into the atmosphere and gains velocity, more aerodynamic forces build up on the vehicle. Hence, the aerodynamic control surfaces are activated to control the vehicle.

In the meantime, the guidance algorithm steers the vehicle through a desired trajectory by use of nominal trajectories that were computed prior to the flight, hence on the ground. Unlike the Space Shuttle, to allow autonomy on-board, the trajectories are fused with an Adaptive Multivariate Pseudospectral Interpolation (AMPI) technique. Such a technique allows calculations during the flight so that the final dispersion at the end of experiment is minimized while taking the disturbance forces into account. It is significant to note that the multivariate interpolation process on-board is applied over a limited number of nodes. Although this indicates that the technique provides a sub-optimal guidance solution, it has a greater chance of dealing with the disturbances that alter the aerodynamic forces, such as wind or changes in the atmosphere (Bauer et al., 2020). Nevertheless, the guidance logic is comparable with the Space Shuttle Orbiter. Thus, the longitudinal dynamics of the vehicle are controlled with a drag acceleration profile by adjusting the vertical lift component through a set of control actions, defined by

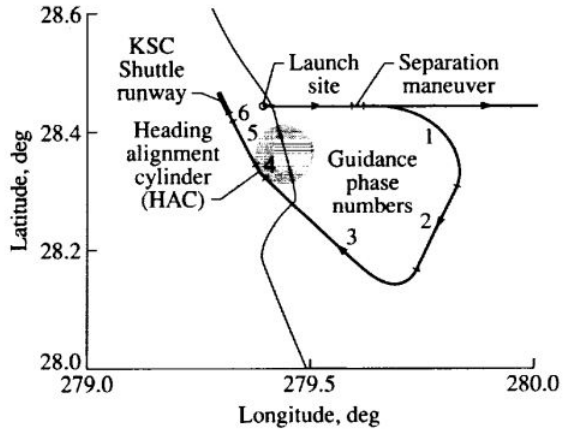

Figure 2.6: Guidance phases for the glideback booster (Naftel and Powell, 1993)

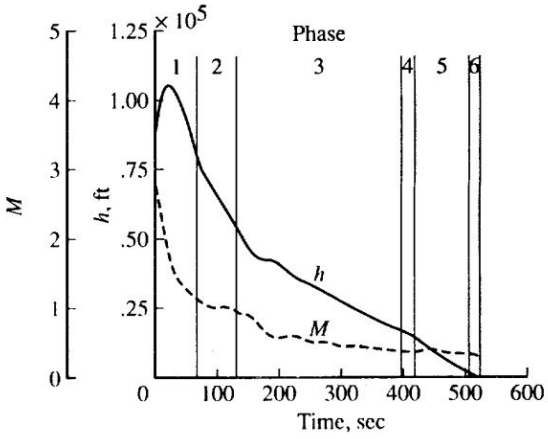

Figure 2.7: Trajectory histories for the glideback booster (Naftel and Powell, 1993)

the guidance algorithm. Meanwhile, the lateral guidance logic was the so-called bank reversal strategy as it was implemented for the Space Shuttle (Schwarz et al., 2019).

2.1.4. NASA Winged Fully Reusable Launch Vehicle

Despite the fact that flyback boosters address the reusability problem of launch vehicles, there are limited real-life examples of flyback boosters. Due to the restricted data, in the previous sections mainly re-entry vehicles, the Space Shuttle and HORUS, are taken under consideration. Although studying re-entry vehicles for understanding a general return flight through the atmosphere is a viable option, the trajectories are fundamentally different than the fly back trajectories. Naftel and Powell (1993) performed an analysis on booster glide back guidance for winged full reusable launch vehicles, which provides a starting point for the detailed mission design of flyback boosters.

Although the initial conditions may differ depending on the mission requirements, the reference trajectory identified in this study is much more comparable to the nominal mission of a flyback booster than the trajectory of a re-entry vehicle. Looking at the latitude and longitude history of the complete trajectory in Figure 2.6, it is concluded that there are six phases. These are: turning back toward the launch site, disseminating the excess energy, intersecting with the heading alignment cylinder (HAC), gliding on the HAC, approaching the runway, and the flare maneuver for landing. In this thesis, the trajectory is analyzed up until the TAEM phase, therefore, especially the first 3 phases identified carry crucial information. The first phase identifies that after the separation maneuver the vehicle is not at the desired orientation, as was also identified by Schwarz et al. (2019) for ReFEx. This indicates that some sort of a turn, or a roll, maneuver has to be performed to alter the heading angle of the vehicle and align with the landing site. The turn maneuver is optimized for the appropriate final heading angle using the maximum normal acceleration of 2.3g as a constraint. For the guidance algorithm, the optimum turning maneuver is translated into steering commands, in which the angle of attack is defined as a function of the Mach number and the bank angle is defined as a function of the heading angle until the turn is completed (Naftel and Powell, 1993).

Phase 2 aimed to dissipate the excess energy of the booster. The duration of this phase is regulated by a series of continuous range calculations, which is similar to the principle adopted by the Space Shuttle to distinguish each phase. The guidance algorithm calculates the range between the booster and the target point on the runway, when this value converges to the actual range the third phase is initiated. During Phase 3 the heading angle of the vehicle is controlled to align with the HAC in the correct orientation. Meanwhile, the angle of attack profile is set to a nominal value of 6.5° to maintain the equality of the ranges. In Figure 2.7, the altitude and Mach number history of the vehicle is provided. The altitude and velocity at the beginning of Phase 3 are used to define the TAEM conditions for flyback boosters since the energy constraint of the TAEM condition for Space Shuttle is unrealistically high for a flyback booster. Accordingly, the TAEM phase begins around Mach 0.8-1.1 at an altitude of 7-10 km.

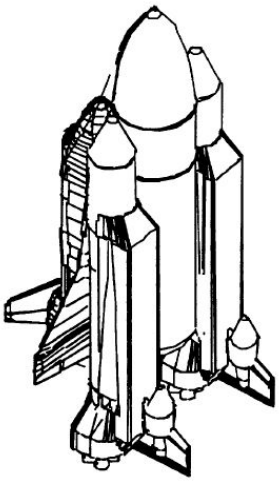

Figure 2.8: LFBB integrated with the Space Shuttle (Peterson et al., 1994)

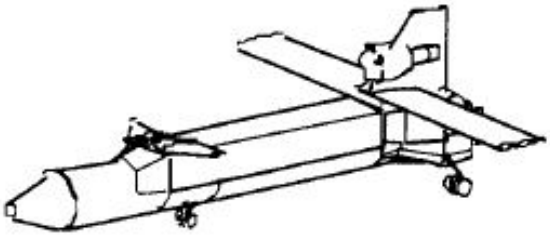

Figure 2.9: LFBB landing configuration (Peterson et al., 1994)

2.1.5. FESTIP Booster Concept Studies

During the Space Shuttle era, various flyback boosters that can be integrated with the system to obtain a fully reusable launch vehicle have been assessed by different parties. Peterson et al. (1994) performed an extensive Pre-Phase A Study on liquid flyback boosters (LFBB). The conceptually developed booster can return back to the desired landing site while complying with the performance limits to maximize the mission flexibility. The selected design for the system is shown in Figure 2.8, in which the two LFBBs are integrated with the Space Shuttle's orbiter. Since booster required operability in both subsonic and supersonic conditions, the aerodynamic surfaces are essential for the design. A distinct characteristic of the LFBB design is the deployable wings for control of the booster's landing speed, illustrated in Figure 2.9. Later on, this concept was also explored by a similar study conducted by DLR. The nominal trajectory suggested that the wings are deployed under low dynamic pressure and loading (Sippel et al., 2006).

Peterson et al. (1994), identified a more unique concept, such as an LFBB with fixed wings and a deployable canard. Initially, the LFBB concept was designed to be integrated with the Space Shuttle, visualized in Figure 2.8. Hence, a deployable wing system was preferred to minimize the effect on the Space Shuttle during the ascent phase of the mission.The commands for the deployment of wings are provided by the GNC system. The system is developed such that the booster can autonomously return to the landing location while tolerating inconsistencies in the GNC system using a fault detection isolation configuration (FDIR) scheme. However, due to unjustifiable complexity, the system was not selected for a detailed development.

As NASA and private initiatives have emerged in the study of fully reusable launch vehicles, Europe also focused on the topic to keep its market share (Caporicci, 2000). During the Space Shuttle era, significant studies were performed under the Future European Space Transportation Investigation Programme (FESTIP), which was a program for studying launcher concepts to identify which launcher was feasible for Europe in early 2000s. The study was focused on system development of technology in the areas of structures, materials, rocket and airbreathing propulsion, thermodynamics, and heat management. A wide set of single-stage to orbit (SSTO) and two-stage-to-orbit (TSTO) concepts were developed. Each concept design had a different propulsive mode, such as pure rocket or airbreathing.

The preliminary study concluded that since the technological readiness of Europe was not sufficient in the 2000s, it was not feasible to develop a single SSTO with a reasonable budget (Dujarric, 1999). Therefore, regarding the conclusion and the scope of this thesis, only the winged TSTO concepts that passed the preliminary phase and are found to be feasible by FESTIP are discussed in more detail. In Figure 2.10 all concepts that were developed by FESTIP are visualized.

The evolution of the VTHL-TSTO concept began with the FSSC-9, as depicted in Figure 2.10 at the second row. The FSSC-9 is a rocket-propelled VTHL-TSTO vehicle that was adapted from the German EARL II concept. After the EARL II was adapted to comply with the FESTIP requirements and the technology level, certain drawbacks of the system were identified. For instance, the aerodynamic

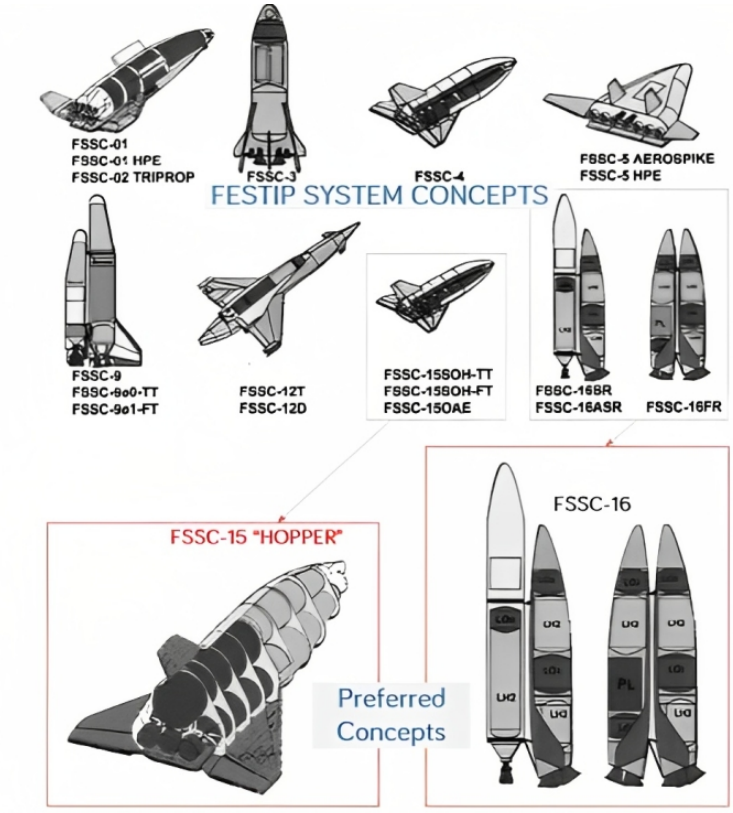

Figure 2.10: Overall FESTIP concept studies and the final selections (Rana, 2017)

assessment concluded that the booster suffers from high drag. To overcome the aerodynamic loads, a large amount of propellant is required for the fly back. Meanwhile, to sustain the powered fly back trajectory, the booster had to use the two available airbreathing engines. This restrained the engine out capabilities of the booster. Moreover, the booster size was over-dimensioned, causing an aerodynamic interference between the wing and the core stage. These drawbacks concluded that the FSSC-9 does not comply with the FESTIP requirements and design standards. Despite the disadvantages, the general idea of a fully reusable TSTO was still regarded as a viable solution with certain alterations. In the end, FESTIP stated that the design of FSSC-9 has moderate design confidence (Dujarric, 1999). Therefore, the lessons learned from the analysis of FSSC-9 were utilized to obtain a more feasible TSTO design, which was FSSC-16 (Bayer, n.d.).

Due to the limited time, certain strong points of other design concepts were combined to obtain the FSSC-16 vehicle (Bayer, n.d.). For instance, the design of FSSC-16 stages, booster and core, were derived from that of the FSSC-12's orbiter. Note that originally the orbiter of FSSC-12 was based on the HORUS that was developed by Sänger. In the final concept selection workshop, Daimler-Benz Aerospace (1998) concluded that two vehicles were recommended for further development, these are FSSC-15, which is a trans-Atlantic hopper concept, and FSSC-16.

2.2. Vehicle Description

The research that is conducted in this thesis evolves around a reference mission. Hence, regarding the aforementioned discussion, a reference vehicle selection is performed. Although the missions presented in Section 2.1 had a significant contribution to the understanding of the development of the return trajectories and algorithms, not all of them comply with the purpose of this research in terms of vehicle dynamics. The re-entry vehicles show familiarity with the flyback boosters, due to their spaceplane-based designs, but their performance is different. In Section 2.1.3 and Section 2.1.4 two possible flyback boosters are identified. Nevertheless, these two vehicles lack sufficient information or identification of the vehicles to simulate a reference mission. Meanwhile, as it is discussed in Sec-

tion 2.1.5, FESTIP has conducted detailed phase A studies for the developed vehicles. Therefore, it is decided to select the reference vehicle from the FESTIP study. In the upcoming sections, a detailed explanation of the chosen reference vehicle is provided.

2.2.1. Reference Vehicle

As FESTIP has concluded that FSSC-16 shows promising features and complies with the FESTIP requirements, it was chosen as one of the two concepts to be developed further. Accordingly, FSSC-16 is chosen as a reference vehicle in this research. The vehicle consists of two stages which have a VTHL configuration. One of the stages is the winged booster and the second stage is the orbiter that is either a winged structure, similar to the booster, or an Ariane 5 core stage. These characteristics of FSSC-16 allow the development of fully reusable launch systems to be evolutionary, as the integration of the Ariane 5 core stage is a middle step since it is a semi-reusable structure (Daimler-Benz Aerospace, 1998).

Essentially, the design of the booster and the orbiter separately resembles the design of an FSSC-1 which is an SSTO vehicle that incorporates the spaceplane concept. FSSC-16 has near-circular fuselage structure accompanied by double delta wings and winglets for directional stability. For horizontal landing capabilities, the vehicle is equipped with a tricycle landing gear, in which a single landing gear is present at the nose cone and twin wheels behind the body. There are seven engines present on-board. Two of these engines are identified as the main engines and are located on the orbiter. Meanwhile, five are placed on the booster. The arrangement allows the design to be single-point failure-free. This indicates that if a single-engine is out in either stage, the vehicle can operate without any issues (Daimler-Benz Aerospace, 1998). Meanwhile, hydrogen fuel is preferred to be used for orbiter and the booster. Hence the propellant mass that is required for the flyback phase is reduced. Considering all the components, such as payload, propellant mass, and subsystems, the launch mass of the orbiter is 225,453 kg while the launch mass of the booster is identified to be 515,984 kg (Daimler-Benz Aerospace, 1998).

As it was identified in Section 2.1.5, FSSC-16 is an improved version of FSSC-9. There were few important problems related to the engines of FSSC-9 which posed an issue for both the upper stage and the booster. The initial decision of using only two air-breathing engines for the flyback booster limited the design as if an engine fails the vehicle capabilities drop significantly (Daimler-Benz Aerospace, 1998). The location of these engines complicated the landing gear design for the booster. In the end, the feedback obtained from FSSC-9 is implemented in the design of FSSC-16. Meanwhile, FSSC-12 is taken as a basis for the redesign of both stages, since this concept was developed from the Sänger configuration and relevant data was available. Hence, FSSC-16 is developed in a way such that feasible characteristics of various concepts are combined together. The design is illustrated in Figure 2.11.

Furthermore, although the fully reusable configuration of FSSC-16 is feasible, Dujarric (1999) expresses that the limits of the siamese configuration are not fully discovered. Hence, for the sake of the research, it is assumed that the configuration is feasible and a successful launch can be performed. The overall mass properties of the reference vehicle is presented in Table 2.1. The FESTIP explicitly mentions that the vehicle is symmetric in the XZ-plane hence $I_{zx} = 0$. However, no information is provided about the remaining two products of inertia. Therefore, it is assumed that the vehicle is rotational symmetric in terms of mass. This indicates that $I_{zx} = I_{zy} = I_{xy} = 0$. This can be identified as a valid assumption since also looking at other concepts of FESTIP, that FSSC-16 was based on, it can be seen that the products of inertia are comparably lower than moments of inertia, hence can be discarded (Viavattene, 2018). On the other hand, note that during powered flyback, fuel consumption will alter the values that are presented in Table 2.1. It is expected to see a backward shift in the center of mass (CoM) and decrease in mass and moments of inertia. Mass modeling required for such a system is discussed elaborately in the upcoming section.

It is significant to note that the vehicle mass indicated in Table 2.1 is for the powered flyback booster. Therefore, the mass properties are calculated regarding the fuel that is required for the fly back. Daimler-Benz Aerospace (1998) calculated the fuel that is required for the fly back as 5,000 kg and had 2,000 kg of residual fuel. Since the unpowered flyback booster does not require this fuel, during the simulations, mass of the unpowered vehicle is taken as 50,000 kg.

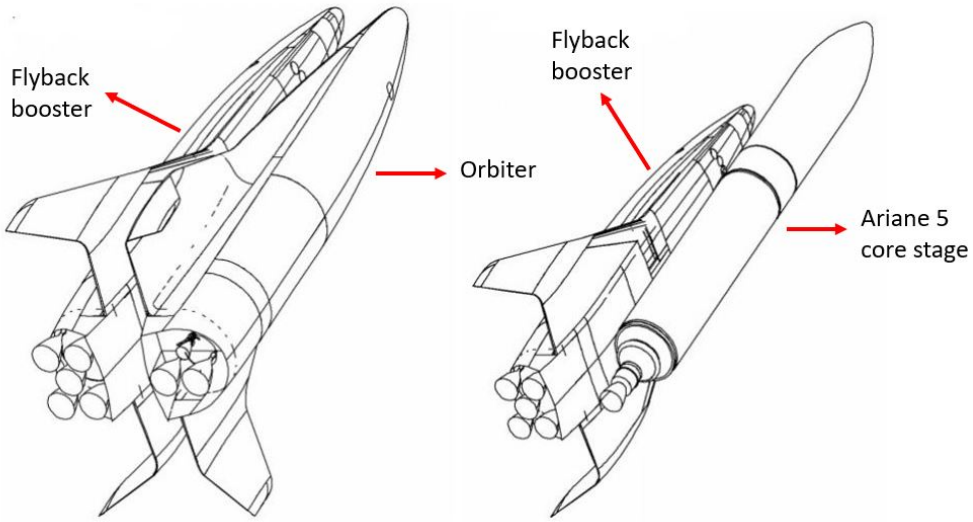

Figure 2.11: FSSC-16 the fully reusable concept (left) and FSSC-16 semi-reusable with Ariane 5 core stage (right) (Dujarric, 1999)

Table 2.1: Mass properties of FSSC-16 booster stage (Daimler-Benz Aerospace, 1998)

Event	Mass [kg]	CoM from nose [m]		Moments of inertia [kgm^2]		
		x	y	I_{xx}	I_{yy}	I_{zz}
Separation	$57 \cdot 10^3$	24.1	1.2	$536.49 \cdot 10^3$	$6414.158 \cdot 10^3$	$6771.044 \cdot 10^3$

2.2.2. Mass Model

As was identified in the previous section, the empty mass of the vehicle is 50,000 kg and the fuel mass is 7,000 kg. For the unpowered flyback booster the total mass is equal to 50,000 kg, whereas, for the powered flyback booster the total weight is equal to 57,000 kg, in which the total mass is calculated as:

$$M(t_0) = m_{empty} + m_{fuel} \tag{2.1}$$

Note that since a certain amount of fuel is consumed up until the separation point, which is identified as t_0, the above equation is not equal to the take-off mass. The mass distribution within the vehicle has a significant effect on the motion of the vehicle. For the unpowered flyback booster, this distribution can be defined as homogeneous, as the vehicle is a rigid body with a constant mass. This indicates that the center of mass of the vehicle would be constant throughout the flight. Consequently, the moments of inertia and products of inertia of the vehicle will be constant throughout the mission. Therefore, there will be only one inertia tensor. Regarding the characteristics of the unpowered flyback booster, this matrix was previously identified as:

$$\boldsymbol{I} = \begin{bmatrix} 536.49 \cdot 10^3 & 0 & 0 \\ 0 & 6414.158 \cdot 10^3 & 0 \\ 0 & 0 & 6771.044 \cdot 10^3 \end{bmatrix} \text{ kgm}^2 \tag{2.2}$$

Nevertheless, when the powered flyback booster is the subject, it is not possible to expect a homogeneous mass distribution for the entire flight. The mass distribution at the beginning of the flight is depicted in Figure 2.12. Although the vehicle preserves a rotational symmetry, the mass distribution would become less homogeneous over time as fuel is consumed, which is seen in Figure 2.13. Consequently, this would cause a shift in the center of mass and moments of inertia.

It is the control systems responsibility to account for the inequalities due to mass distribution to balance the forces and have a controllable vehicle. Yet, since a control system design is left out in this research, it is not important to account for shifts in the center of mass in all directions. As the vehicle

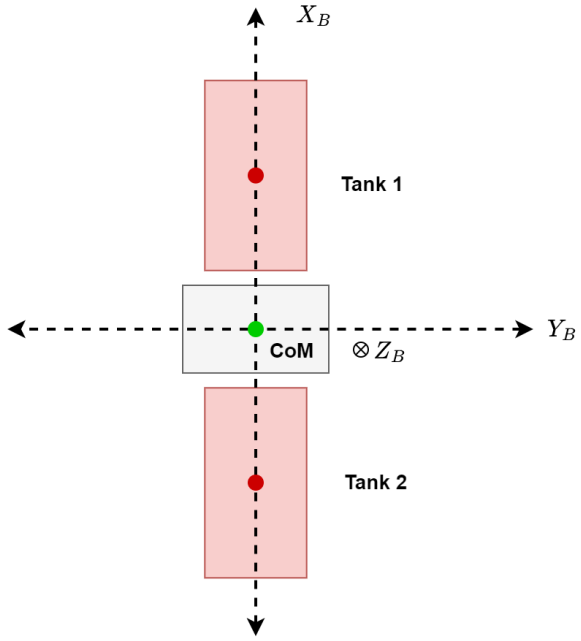

Figure 2.12: Mass model during $t = t_0$ when inclination is $90°$ or $90°$

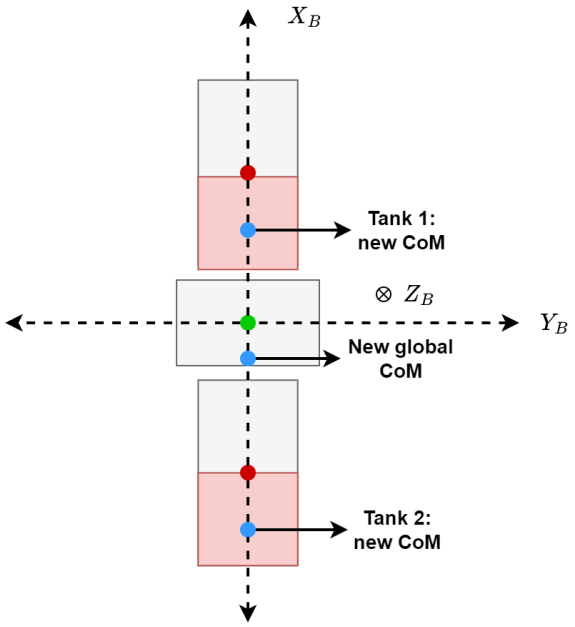

Figure 2.13: Mass model during the flight at $t = t_i$ when inclination is $90°$

will be designed to be trimmable, the pitch moment will be actively analyzed throughout a trajectory. Thus, it is assumed that the center of mass only moves along the x-axis, to account for changes in the longitudinal stability while calculating the trim condition. At each time step, the center of mass is calculated using the expression:

$$x_{com} = \frac{\sum_{i=1}^{N} m_i x_i}{M} \tag{2.3}$$

in which M is the total mass at the current instant, m_i is the mass of the independent components, such as the tank 1 and tank 2, and x_i is the distance from the mid-point of each independent component to the nose of the vehicle. In Figure 2.13 this case is explained with a figure. As half of the fuel is consumed and both tanks are only half full, a new local center of mass is obtained for each tank. These are at the aft of the original center of mass due to the $90°$ inclination. Accordingly, the global center of mass has shifted aft of the original global center of mass, which is indicated with a green dot on the figure. Since center of mass is dependent on the shape of the tanks, it is assumed to be a simple rectangle. Note that the rectangles are adapted such that it same in volume as the actual fuel tank.

2.2.3. Propulsion Model

The FSSC-16 flyback booster is equipped with four airbreathing engines. The airbreathing engines operate with cryogenic propellants, such as LO_2 and LH_2, and liquid oxygen as an oxidizer (Amar and Gowtham Manikanta, 2012). The oxygen that is used as an oxidizer is supplied from the air. As the atmospheric oxygen is utilized, the amount of oxidizer that is stored on-board is reduced compared to the rocket engines. This leads to a decrease in the weight and cost that are associated with the propulsion system of the flyback booster while introducing a better thermal cooling capability. As a result, using airbreathing engines for the first stage enhances the operational flexibility of the booster (Daimler-Benz Aerospace, 1998). It was previously mentioned that FSSC-16 is the improved version of FSSC-9. Therefore, for FSSC-16 four engines were used, unlike FSSC-9 which had only two engines. This decision allowed the vehicle to operate when a single-engine is out, indicating that four engines have lower installed excess thrust and associated engine mass when a single-engine is out. Daimler-Benz Aerospace (1998) concluded that the typical candidates for such a mission are EJ200, F414, and M88-3. These three turbofan engines are developed by various companies: Rolls-Royce, General Electric, and Safran Aircraft Engines, respectively. All three have comparable characteristics with a

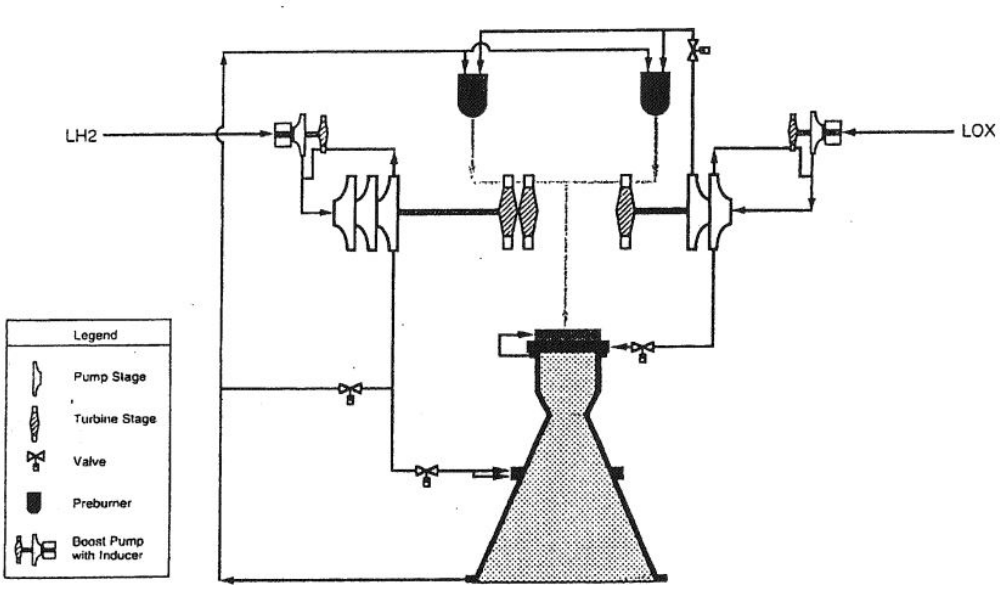

Figure 2.14: Schematic model of the airbreathing engine of FSSC-16 (Daimler-Benz Aerospace, 1998)

maximum thrust of 100 kN, an average length of 2.7-3.0 m, and a mass of 750 kg. The schematic model of a reference engine is shown in Figure 2.14.

The propulsion system is especially significant for the powered flyback mode when the thrust vectoring can be used to control the vehicle. Therefore, by changing the thrust magnitude and thrust angles, the vehicle's attitude can be controlled. Often, airbreathing engines are throttleable by the use of valves. These valves are used to control the amount of fuel and oxidizer that is delivered to the internal combustion engine. As a result of the combustion, high pressured hot gas is expelled from the expansion nozzle of the vehicle as a high velocity exhaust. This high velocity is achieved by the hot gas, as the hot gas flows through the expansion tunnel. The amount of thrust that is generated by the engine is dependent on the mass flow $\dot{m}$ through the engine with an exit area A_e with a velocity of $\boldsymbol{V_T}$.

The propulsion system has a center of thrust (CoT) that is located at a distance $\boldsymbol{r_T}$ from the center of mass of the vehicle. Therefore, by varying the thrust angles, which are thrust azimuth ψ_T and thrust elevation ϵ_T, thrust moments are generated around the center of mass. Note that, as it is depicted in Figure 2.15, thrust azimuth ψ_T is the angle between the projection of the thrust on the X_BY_B plane and the X_B-axis. Whereas, thrust elevation ϵ_T is the angle between the thrust vector and X_BY_B plane. From Figure 2.15, the components of the thrust vector can also be identified. It is possible to write that:

$$\begin{aligned} T_x &= T \cos\epsilon_T \cos\psi_T \\ T_y &= T \cos\epsilon_T \sin\psi_T \\ T_z &= -T \sin\epsilon_T \end{aligned} \tag{2.4}$$

in which T is the thrust magnitude and $\boldsymbol{r_T} = (x_T, y_T, z_T)^T$. Thus it is possible to express the moment around CoM due to the thrust can be expressed as:

$$\boldsymbol{M_T} = \begin{pmatrix} M_{T,x} \\ M_{T,y} \\ M_{T,z} \end{pmatrix} = \begin{pmatrix} T_z y_T - T_y z_T \\ T_x z_T - T_z x_T \\ T_y x_T - T_x y_T \end{pmatrix} \tag{2.5}$$

By substituting the expressions in Equation 2.4 in the above expression, one gets:

$$M_{T_x} = T_z y_T \sin\epsilon_T - T_y z_T \cos\epsilon_T \sin\psi_T \tag{2.6}$$

$$M_{T_y} = T_x z_T \cos\epsilon_T \cos\psi_T - T_z x_T \sin\epsilon_T \tag{2.7}$$

$$M_{T_z} = T_y x_T \cos\epsilon_T \sin\psi_T - T_x y_T \cos\epsilon_T \cos\psi_T \tag{2.8}$$

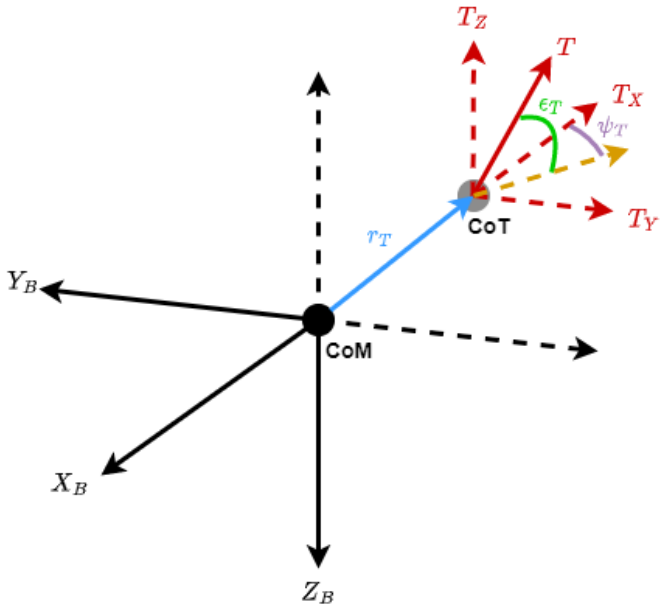

Figure 2.15: Thrust vector decomposed into components in the body reference frame when the CoM is located on the origin of the reference frame

Finally, note that the elevation angle ϵ_T is positive when a positive deflection results in a positive change in the flight path angle. Meanwhile, the azimuth angle ψ_T is positive when it contributes to a positive change in the heading angle.

2.2.4. Aerodynamic Database

Since the vehicle will perform an atmospheric flight, it is necessary to regard the atmospheric forces on the vehicle. To ensure that these forces are modelled correctly, a comprehensive aerodynamic database is required. A database for FSSC-16 is made available by Daimler-Benz Aerospace. However, the information that is provided cannot be extracted accurately as it is provided in graphs that are not easily readable due to the poor quality. It has been reported that the FSSC-16 configuration was derived from the orbiter phase of FSSC-12, which was the scaled version of HORUS (Daimler-Benz Aerospace, 1998).

The technical report of HORUS provides a complete aerodynamic database, including the aerodynamic control surfaces (Mooij, 1995). Therefore, using the HORUS database and adjusting it according to the changes in the FSSC-16 is a convenient and a more accurate method for obtaining aerodynamic database of FSSC-16 than only using the graphs provided by the FESTIP study. The geometric properties of the vehicles are compared in Table 2.2. Since FSSC-16 is a scaled version of HORUS, it is possible to use the same lift coefficient database, as well as the same drag coefficient database for the both vehicles. While calculating the aerodynamic forces, due to the scaled aerodynamic reference area, the lift and drag will be scaled accordingly.

The HORUS aerodynamic database is obtained regarding the assumption that the vehicle is a rigid body that does not get affected by the interference due to flaps. The aerodynamic coefficients are provided as a function of Mach number M, angle of attack α, altitude h, sideslip angle β, and deflection angles δ of the aerodynamic control surfaces, as it is listed in Table 2.3. The aerodynamic coefficients are defined as below (Mooij, 1995):

$$C_D = C_{D_0} + \Delta C_{D_{r,l}} + \Delta C_{D_{e,l}} + \Delta C_{D_b} + \Delta C_{D_{e,r}} + \Delta C_{D_{e,r}} - \Delta C_{D_h} \tag{2.9}$$

$$C_S = \Delta C_{l_{r,l}} + \Delta C_{S_{e,l}} + \Delta C_{l_{e,r}} + \Delta C_{l_{r,r}} + \left[\left(\frac{\partial C_S}{\partial \beta} \right)_0 + \Delta \left(\frac{\partial C_S}{\partial \beta} \right)_{e,l} + \Delta \left(\frac{\partial C_S}{\partial \beta} \right)_{e,r} \right] \beta \tag{2.10}$$

Table 2.2: Geometric data of the FSSC-16 booster and HORUS

Dimensions	FSSC-16 booster	HORUS	Units
Fuselage length	40.0	25.0	m
Fuselage width	6.4	5.4	m
Fuselage height	6.6	4.5	m
Wingspan (b_{ref})	21.8	13.0	m
Wing cord (c_{ref})	18.63	23	m
Aerodynamic ref. area (S_{ref})	405.6	110	m^2

$$C_L = C_{L_0} + \Delta C_{L_{e,l}} + \Delta C_{L_b} + \Delta C_{L_{e,r}} \tag{2.11}$$

$$C_l = \Delta C_{l_{e,l}} + \Delta C_{l_{e,r}} + \left(\frac{\partial C_l}{\partial \beta}\right)_0 \beta \tag{2.12}$$

$$C_m = C_{m_0} + \Delta C_{m_{e,l}} + \Delta C_{m_{e,r}} + \Delta C_{m_b} \tag{2.13}$$

$$\begin{aligned} C_n = {} & \Delta C_{n_{r,l}} + \Delta C_{n_{e,l}} + \Delta C_{n_{r,r}} + \Delta C_{n_{e,r}} + \\ & \left[\Delta\left(\frac{\partial C_n}{\partial \beta}\right)_0 + \Delta\left(\frac{\partial C_n}{\partial \beta}\right)_{r,l} + \Delta\left(\frac{\partial C_n}{\partial \beta}\right)_{e,l} + \Delta\left(\frac{\partial C_n}{\partial \beta}\right)_{e,r} + \Delta\left(\frac{\partial C_n}{\partial \beta}\right)_{r,r}\right]\beta \end{aligned} \tag{2.14}$$

In the above equations, the subscript 0 refers to an aerodynamic coefficient for a clean configuration with zero deflection of the control surfaces. For the subscripts with two letters divided by a comma the first letter e and r refer to elevon and rudder, respectively. Meanwhile, the second letter, r and l refer to right and left, respectively. Finally, subscript b indicates the influence of the aerodynamic coefficient due to the presence of a body flap. Furthermore, the aerodynamic coefficients are the drag coefficient C_D, lift coefficient C_L, side force coefficient C_S, roll moment coefficient C_l, pitch moment coefficient C_m, and yaw moment coefficient C_n.

The aerodynamic equations above can be simplified by regarding that there is a plane of symmetry. The vehicle has two rudders and two elevons that are identical and symmetric with respect to the XZ-plane in the body reference frame. For symmetry conditions to hold during the flight, the control surfaces should deflect equally. Thus, the surfaces induce the same moment but opposite in direction, as represented in Table 2.4.

While the HORUS database was adapted to create the FSSC-16 database an aerodynamic analysis was conducted. It was identified that up-scaling an aerodynamic database, especially a pitch moment database, is not trivial. Previously, FESTIP stated that FSSC-16 is adapted from the HORUS configuration and the aerodynamic database is also the adapted version of HORUS' database. Although this is true for the high hypersonic Mach numbers, for supersonic and transonic Mach numbers, differences in behavior can be observed. Looking at Figure 2.18 it can be observed that at Mach 3, and below, the two databases have differences in the behavior. At these supersonic Mach numbers, the HORUS database has a $C_{m_\alpha} < 0$, indicating that the vehicle is inherently statically stable. Meanwhile, for FSSC-16, in this supersonic region for $\alpha \approx 15°$ a change in the pitching moment can be observed. Suddenly, the FSSC-16 has a positive C_{m_α}, which indicates that the vehicle is unstable. This distinctive behavior can also be observed for other orbiter types, such as the Space Shuttle Orbiter and the PHOENIX (Weiland, 2014). Meanwhile for hypersonic Mach numbers the static stability is achieved at low angles of attack but is challenged for $\alpha > 20°$.

This unstable behavior has to be diminished during the simulation to have a controllable vehicle. The stability of a vehicle can be manipulated in two different manners. First, shifting the center of gravity forwards would induce a pitch-down moment, diminishing the pitch moment. The second option is trimming the vehicle by positively deflecting the flaps and elevons to induce a pitch-down moment (Weiland, 2014). Since the simulated vehicle has an active trim logic, as explained further in the upcoming

Table 2.3: Aerodynamic coefficients (Mooij, 1995)

Drag coefficients	Side-force coefficients	Lift coefficients
$C_{D_0} = f(M, \alpha)$	$\Delta C_{S_{r,l}} = f(M, \alpha, \delta_{r,l})$	$C_{L_0} = f(M, \alpha)$
$\Delta C_{D_{r,l}} = f(M, \alpha, \delta_{r,l})$	$\Delta C_{S_{w,l}} = f(M, \alpha, \delta_{w,l})$	$\Delta C_{L_{w,l}} = f(M, \alpha, \delta_{w,l})$
$\Delta C_{D_{w,l}} = f(M, \alpha, \delta_{w,l})$	$\Delta C_{S_{w,r}} = f(M, \alpha, \delta_{w,r})$	$\Delta C_{L_b} = f(M, \alpha, \delta_b)$
$\Delta C_{D_b} = f(M, \alpha, \delta_b)$	$\Delta C_{S_{r,r}} = f(M, \alpha, \delta_{r,r})$	$\Delta C_{L_{w,r}} = f(M, \alpha, \delta_{w,r})$
$\Delta C_{D_{w,r}} = f(M, \alpha, \delta_{w,r})$	$\left(\frac{\partial C_S}{\partial \beta}\right)_0 = f(M, \alpha)$	
$\Delta C_{D_{r,r}} = f(M, \alpha, \delta_{r,r})$	$\Delta\left(\frac{\partial C_S}{\partial \beta}\right)_{w,l} = f(M, \alpha, \delta_{w,l})$	
$C_{D_h} = f(M, h)$	$\Delta\left(\frac{\partial C_S}{\partial \beta}\right)_{w,r} = f(M, \alpha, \delta_{w,r})$	

Roll coefficients	Pitch coefficients	Yaw coefficients
$\Delta C_{l_{w,l}} = f(M, \alpha, \delta_{w,l})$	$C_{m_0} = f(M, \alpha)$	$\Delta C_{n_{r,l}} = f(M, \alpha, \delta_{r,l})$
$\Delta C_{l_{w,r}} = f(M, \alpha, \delta_{w,r})$	$\Delta C_{m_{w,l}} = f(M, \alpha, \delta_{w,l})$	$\Delta C_{n_{w,l}} = f(M, \alpha, \delta_{w,l})$
$\left(\frac{\partial C_l}{\partial \beta}\right)_0 = f(M, \alpha)$	$\Delta C_{m_b} = f(M, \alpha, \delta_b)$	$\Delta C_{n_{w,r}} = f(M, \alpha, \delta_{w,r})$
	$\Delta C_{m_{w,r}} = f(M, \alpha, \delta_{w,r})$	$\Delta C_{n_{r,r}} = f(M, \alpha, \delta_{r,r})$
		$\left(\frac{\partial C_n}{\partial \beta}\right)_0 = f(M, \alpha)$
		$\Delta\left(\frac{\partial C_n}{\partial \beta}\right)_{r,l} = f(M, \alpha, \delta_{r,l})$
		$\Delta\left(\frac{\partial C_n}{\partial \beta}\right)_{r,r} = f(M, \alpha, \delta_{r,r})$

Table 2.4: Symmetry conditions for the right and left rudder and elevator (Mooij, 1995)

Zero derivatives right elevon	First derivative right elevon	Zero derivatives right rudder	First derivative right rudder
$C_{D_{w,r}} = C_{D_{w,l}}$	$\left(\frac{\partial C_S}{\partial \beta}\right)_{w,r} = \left(\frac{\partial C_S}{\partial \beta}\right)_{w,l}$	$C_{D_{r,r}} = C_{D_{r,l}}$	$\left(\frac{\partial C_n}{\partial \beta}\right)_{r,r} = \left(\frac{\partial C_n}{\partial \beta}\right)_{r,l}$
$C_{S_{w,r}} = -C_{S_{w,l}}$		$C_{S_{r,r}} = -C_{S_{r,l}}$	
$C_{L_{w,r}} = C_{L_{w,l}}$		$C_{n_{r,r}} = -C_{n_{r,l}}$	
$C_{l_{w,r}} = -C_{l_{w,l}}$			
$C_{m_{w,r}} = C_{m_{w,l}}$			
$C_{n_{w,r}} = -C_{n_{w,l}}$			

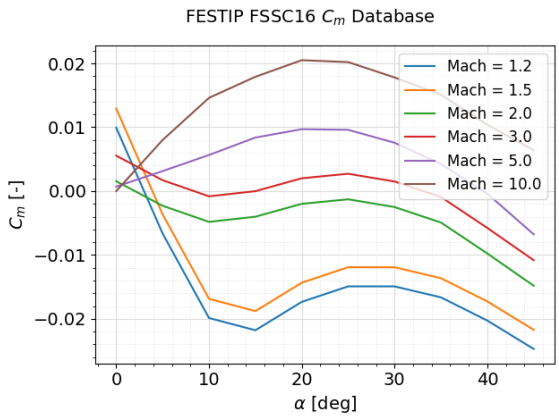

Figure 2.16: Trimmed C_m vs. α that is adapted from the HORUS database

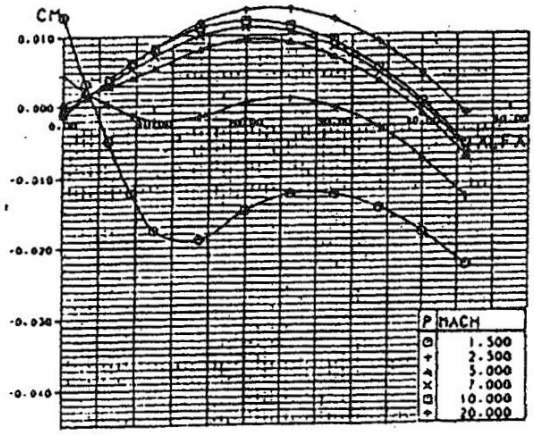

Figure 2.17: Trimmed C_m vs. α graph of FSSC-16 (Daimler-Benz Aerospace, 1998)

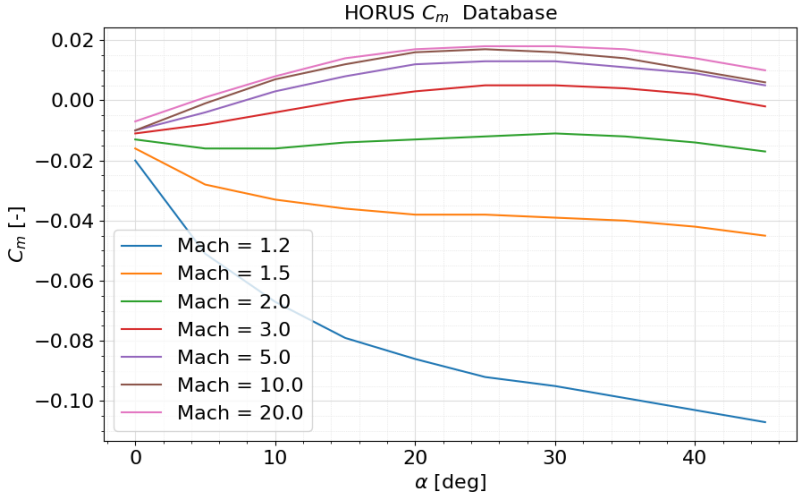

Figure 2.18: Untrimmed pitch coefficient for a reference trajectory of FSSSC16

section, the second option is adopted in this study. Furthermore, as it can be seen in Figure 2.19, the untrimmed pitch moment for a reference trajectory is mainly positive. This indicates that trimming the vehicle by positively deflecting the control surfaces and inducing a pitch-down moment, hence negative ΔC_m, is sufficient to solve the issue of stability.

However, since only a limited number of graphs were provided by the FESTIP study, the side force coefficient, roll moment coefficient, and yaw moment coefficient could have been obtained by considering the effects of the changes in the configuration on these coefficients and manually adjusting the HORUS database. Nevertheless, since the FESTIP documentation lacks the details on the re-sizing of the wings and reshaping of the elevons, the yaw and roll moment coefficient are left as it is. This did not have a major consequence on the problem at hand, since the rotational motion is not analyzed during this study. Only the pitch moment is analyzed along the trajectory for trimmability. This suggests that the lift, drag, and pitch moment coefficients of the control surfaces are also adapted. For the sake of the analysis, only the ΔC_D, ΔC_L, and ΔC_m of the body flap and rudder is adjusted. It is worthwhile to mention that, instead of the force coefficients, the increments of the force coefficients are provided in the HORUS database. The relationship between a force coefficient and an increment of a force coefficient is adopted to obtain the increments of the control surfaces of FSSC-16. The relationship is explained using the equation below:

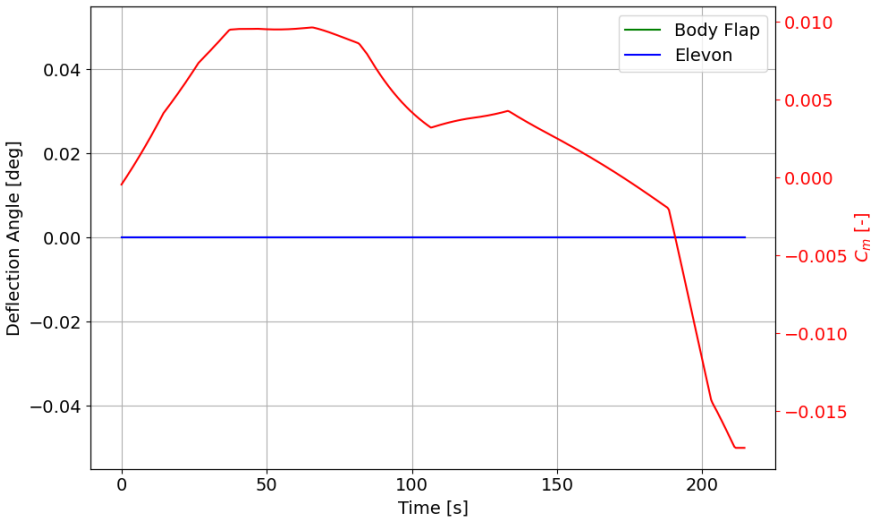

Figure 2.19: Untrimmed pitch coefficient for a reference trajectory of FSSSC16

$$L = L_0 + L_b \tag{2.15}$$

in which L_0 refers to the lift provided by the main body and the L_b refers to the lift force obtained from the body flap. The above equation can be extended as:

$$L = C_{L_0}\bar{q}S + C_{L_b}\bar{q}S_b \tag{2.16}$$

in which S refers to the surface area of the main wings and S_b refers to the surface area of the body flap. To obtain ΔC_{L_b} this can be written as:

$$L = \left(C_{L_0} + C_{L_b}\frac{S_b}{S}\right)\bar{q}S \tag{2.17}$$

$$\Delta C_{L_b} = C_{L_b}\frac{S_b}{S} \tag{2.18}$$

Knowing that Equation 2.18 provides the relationship between a force coefficient and the increment of a force coefficient, Equation 2.17 can be written for HORUS and FSSC-16, consecutively, as below:

$$L_H = \left(C_{L_{0_H}} + C_{L_{b_H}}\frac{S_{b_H}}{S_H}\right)\bar{q}S_H \tag{2.19}$$

$$L_F = \left(C_{L_{0_F}} + C_{L_{b_F}}\frac{S_{b_F}}{S_F}\right)\bar{q}S_F \tag{2.20}$$

in which the subscript H refers to HORUS and the subscript F refers to FSSC-16. Using the expression in Equation 2.18 for both vehicles, the equations below are obtained:

$$\Delta C_{L_{b_H}} = C_{L_b}\frac{S_{b_H}}{S_H} \tag{2.21}$$

$$\Delta C_{L_{b_F}} = C_{L_b}\frac{S_{b_F}}{S_F} \tag{2.22}$$

Using Equation 2.21, a general expression for C_{L_b} can be obtained:

$$C_{L_b} = \Delta C_{L_{b_H}}\frac{S_H}{S_{b_H}} \tag{2.23}$$

The above expression is then substituted in Equation 2.22 to obtain the lift force increment of the body flap of FSSC-16, such that:

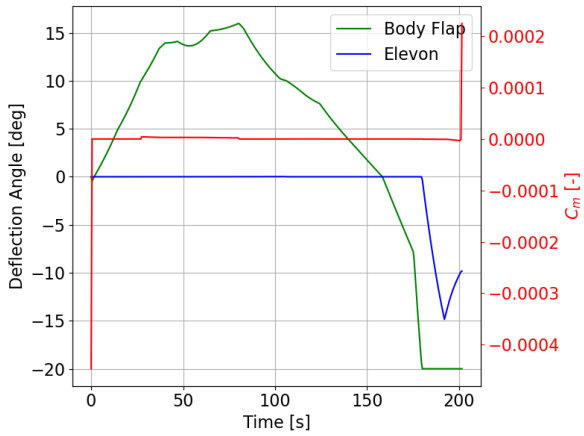

Figure 2.20: Deflection angles of the FSSC-16 control surfaces during the trim

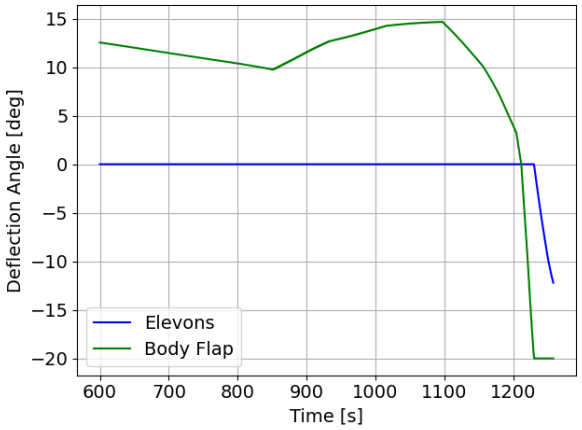

Figure 2.21: Deflection angles of the HORUS control surfaces during the trim

$$\Delta C_{L_{b_F}} = \Delta C_{L_{b_H}} \frac{S_H}{S_{b_H}} \frac{S_{b_F}}{S_F} \tag{2.24}$$

The above expression allows the force coefficient increments of FSSC-16 to be expressed in known values, which are the force coefficient increment of HORUS and the geometric values of both vehicles. The above method is adopted for the ΔC_D and ΔC_m for both the body flap and elevons to obtain a coherent aerodynamic database for the control surfaces of FSSC-16, using the HORUS database.

Trim Analysis

To complete the vehicle set-up, a trim analysis is performed for the booster. To have a vehicle that is stable and controllable, it is essential that the vehicle is trimmable. The FESTIP study did not define a concrete trim law for the FSSC-16 vehicle, neither the orbiter nor the booster stage. Therefore, the trim law that is used by HORUS is adapted for the FSSC-16 vehicle. The trim logic follows such that first the body flap of the vehicle is deflected in an attempt to trim the vehicle. Once the body flap is saturated, the elevons are deflected as well to trim the vehicle. The equation for the trim follows as below:

$$C_m = C_{m_0} + \Delta C_{m_b} + 2 \cdot \Delta C_{m_e} \tag{2.25}$$

In a real-life example, for a vehicle to be trimmable, the C_m calculated in Equation 2.25 has to be equal to 0 at all times. Note that due to the lack of aerodynamic database, the trim algorithm developed in this study is not operable below Mach 1.2. A brief step-by-step description of the trim is presented below:

1. Retrieve current C_{m_0}, α, and M.
2. If $M > 5$:
   (a) For each deflection angle of the body flap, which are $[-20°, -10°, 0°, 10°, 20°]$, obtain the ΔC_{m_b} using the current α and M.
   (b) Store each ΔC_{m_b} in a list L1.
   (c) For all the inputs in L1, check: $-0.001 < \Delta C_{m_b} \cdot C_{m_0} < 0$ and $-0.05 < \Delta C_{m_b} + C_{m_0} < 0.05$
   (d) If both conditions are fulfilled, append the ΔC_{m_b} and corresponding δ_b in list L2.
   (e) Use the values in L2 to calculate: $\Delta C_m = \Delta C_{m_b} + C_{m_0}$
   (f) Append the ΔC_m and corresponding δ_b values to a new list L3.
   (g) Using L3, create a dictionary in which the keys of the dictionary are the δ_b and the values are the ΔC_m values.
   (h) Using linear interpolation, obtain the δ_b value that corresponds to $\Delta C_m = Cm_0 + \Delta C_{m_b} = 0$.
   (i) Use the obtained δ_b to interpolate the original ΔC_{m_b} database and obtain the corresponding C_{m_b}.

3. If $1.2 \leq M \leq 1.2$:
   (a) Set $\delta_b = -20°$.
   (b) Calculate C_m using Equation 2.25.
   (c) Follow step (a)-(i) using the aerodynamic database and deflection values of elevons, instead of C_{m_0} use C_m calculated in the previous step.
4. If $M < 1.2$:
   (a) Use the deflection angles of the previous time step, for both the body flap and elevons.

It is worthwhile to mention that since the two elevons are working at the same time, when the check in step (c) is performed, the equations are adopted as:

$$-0.001 < 2\Delta C_{m_e} \cdot C_m < 0 \text{ and } -0.05 < 2\Delta C_{m_e} + C_m < 0.05 \tag{2.26}$$

The trim law is developed and tested using a reference trajectory with the nominal steering parameters that were obtained from the FESTIP study. As a result, for a reference trajectory, the corresponding deflection angles as well as the pitch moment coefficient is plotted in Figure 2.20. Once the body flap is saturated and the Mach number is below 5, the elevons are activated. It is allowed for the body flap to be saturated since it is only used for trimming the vehicle. On the other hand, although the elevons have the capability of deflecting between $[-40°, 40°]$, they are only deflected between $[-20°, 20°]$ for trimming the vehicle. Since the elevons are also used to control the vehicle, it is not desired to saturate the elevons and have maximum deflection only with trimming.

The developed trim law is verified using the HORUS trajectory and the HORUS aerodynamic database. In Figure 2.21 it can be observed that using the developed algorithm, the HORUS trim law can be replicated exactly. Hence, it is verified that the developed algorithm is applicable not only for the FSSC-16 vehicle but also for other vehicles, given a reference mission and vehicle properties.

Aerodynamic Database Verification

As it is presented above, the booster is trimmable along the trajectory. Thus, the trim analysis verified that the aerodynamic database of the vehicle is adapted successfully. Indicating that the modifications made to the HORUS aerodynamic database, to obtain the FSSC-16 aerodynamic data, is sufficient to a first approximation and enough for analysis of the trajectory.

The aerodynamic database is only provided for supersonic and hypersonic Mach numbers. Therefore, the database lacks the information for Mach numbers below 1.2. As it will be seen in Chapter 5 this poses a problem for the third phase of the trajectory, while the vehicle is flying back to the landing site at low Mach numbers. As a result, the aerodynamic forces for the third phase cannot be modelled correctly. Consequently, the vehicle cannot be trimmed for this phase of the trajectory.

It has been identified that altering the aerodynamic database of other vehicles to adapt it to the vehicle at hand is not a trivial task. Especially at transonic to subsonic Mach numbers the numerical methods are inadequate, thus experimental means are required for coherent aerodynamic databases (Weiland, 2014). Since obtaining a complete aerodynamic database is not in the scope of this thesis, it is assumed that given the correct aerodynamic database, the vehicle is also trimmable during this phase. An explanation of the problem and a method for mitigating this issue is presented in Section 10.2.

2.3. Requirements

NASA (2007) defines system engineering as a multi-disciplinary approach to operational and technical management of a system, in which system is defined as components that function together to fulfill the identified need. To identify the need, the problem has to be defined in an appropriate manner so that it is known what functionalities are expected from the system. Therefore two different requirements will be discussed in this section, mission and system requirements.

2.3.1. Mission Requirements

A mission can be identified as the actions that are taken to fulfill the interest of the system as a whole. In this study, the mission is identified as the return of the flyback booster. Hence, the mission requirements are the set of requirements that define the operational or top-level functional architecture

so that the mission can be performed successfully. To identify between requirements, mission requirements use the unique identification tag of **MIS-x**. Note that ”vehicle” refers to the combination of the orbiter and the booster, while to identify individual stages ”booster” or ”orbiter” is used.

- **MIS-01:** The vehicle shall launch from a 5.2°N latitude and 52.2°W longitude, that corresponds to Guiana Space Center in Kourou.
- **MIS-02:** The mission shall terminate the flight at a distance-to-go of 0.75°.
- **MIS-03:** The booster shall be able to withstand maximum g-load of 3.0g.
- **MIS-04:** The booster shall be able to withstand maximum head flux of 93.0 kW/m^2.
- **MIS-05:** The booster shall have a final heading angle of -70° at the end of the turn maneuver.
- **MIS-06:** The booster shall remain sub-orbital, at altitudes below 120 km.
- **MIS-07:** The booster shall have a final flight-path angle equal to 0° to sustain the cruise conditions after the turn maneuver.

2.3.2. System Requirements

System requirements are the set of requirements describing the characteristics and constraints of a system. The top level system requirements imposed by the mission are presented with an identification tag of **SYS-x-x**. The requirements on the booster system is identified with the unique identification **BST-x**. Meanwhile, the requirements on the environment in which the whole simulation operates is identified with **ENV-x**.

Booster:

- **SYS-BST-01:** The booster shall be equipped with a body-flap, two elevons and two rudders on each wing.
- **SYS-BST-02:** The booster shall be equipped with EJ200 air-breathing engines.
- **SYS-BST-03:** The booster shall be guided along the trajectory via a simple open-loop guidance system.
- **SYS-BST-04:** An ideal control and navigation shall be assumed.
- **SYS-BST-05:** The booster shall be trimmable along the trajectory with means of body-flap and elevon deflections.
- **SYS-BST-06:** The booster shall be controlled through aerodynamic control surfaces or thrust vector controlling.
- **SYS-BST-07:** The booster size shall be comparable to ones used by Daimler-Benz Aerospace (1998).

Environment:

- **SYS-ENV-01:** The environment model shall capture the gravitational effect of the oblateness of the Earth.
- **SYS-ENV-02:** The environment model shall represent the atmospheric changes without the complexity of the wind.

3

Environment Model

The environment is the main contributor to the forces that are acting on the vehicle. Thus, the environment in which a flyback booster flies affects its trajectory, alongside the parameters that guide the booster. Depending on the requirements and the desired level of accuracy of the simulation, the environment model has to be set up. Three main characteristics of a central body play a role in the forces on the entry vehicle: the shape of the body, the gravity field, and the atmospheric model. In this section, all these characteristics are discussed in detail.

3.1. Planetary Shape

The shape of a planetary body is defined by various elements such as gravitational tides due to the presence of the Moon, plate motions, size of the body or the rotational velocity of the body. An approximation that can be performed is assuming that the planetary shape of the central body is an ellipsoid of revolution. The ellipsoid is defined by the parameter that is called as ellipticity e and mathematically represented as (Vallado and McClain, 2007):

$$e = \frac{R_e - R_p}{R_e} = 1 - \frac{R_p}{R_e} \tag{3.1}$$

Note that R_p refers to the mean radius at the pole in meters and R_e refers to the mean radius at the equator in meters. When these two parameters are equal to one another, the ellipticity becomes zero, which referes to a spheroid. The ellipticity defined in Equation 3.1 can be used to derive an expression for the radius at an arbitrary point along the surface. For a first-order analysis it is sufficient to represent it as:

$$R_s = R_e(1 - e \sin \delta^2) \tag{3.2}$$

Knowing radius at an arbitrary point along the surface, it is possible to obtain the height of a re-entry vehicle from the surface of the central body. The height is given by:

$$h = R - R_s = R - R_e(1 - e \sin \delta^2) \tag{3.3}$$

Note that in the above equation, R refers to distance between the center of the vehicle and the center of the central body. When all the above equations are being derived, the central body assumed to have a constant angular rate. This indicates that the rotation of the body is constant along the Z-axis of the planetocentric frame.

During this study, it is assumed that the shape of the central body is a spheroid, as visualized in Figure 3.2. The spherical Earth model is a simplified representation of the Earth's shape. The main advantage of such simplification is that it reduces the complexity of derivations of the analytical equations of motion. In return, this reduced complexity requires less computational power compared to the ellipsoid model. This is especially beneficial for this study, since during the design space exploration and optimization, the trajectory is simulated countless times. Furthermore, the difference between the spheroid and ellipsoid Earth model is more prominent at the poles than at the Equator. Since the

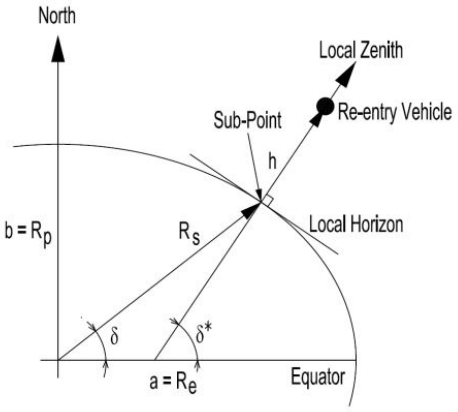

Figure 3.1: The re-entry vehicle above the surface in which the body is represented as an ellipsoid.(Mooij, 2016)

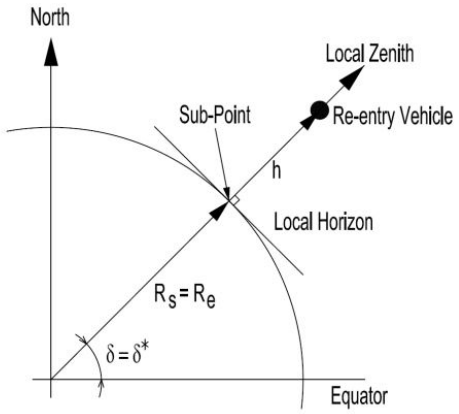

Figure 3.2: The re-entry vehicle above the surface in which the body is represented as a spheroid. (Mooij, 2016)

return trajectory is analyzed at a location that is relatively close to the Equator, at 5.2°N and below, the difference between a spheroid and ellipsoid Earth will not significantly impact the result of the trajectory analysis.

3.2. Gravitational Field

The gravitational force is one of the external forces that is acting on the re-entry vehicle. The simplest form of representation is assuming that both bodies are point masses. Therefore, by Newton's law of attraction it is possible to express the force between two point masses, M and m, with a distance R as:

$$\boldsymbol{F_G} = \frac{GMm}{R^2}\hat{\boldsymbol{r}} \tag{3.4}$$

Note that the hat above the vector, $\hat{r}$, indicates that it is normalized. Meanwhile, G is the universal gravity constant, M is the mass of the central body and m is the mass of the vehicle. At this point, it is convenient to define the gravitational constant $\mu = GM$. Therefore, the gravitational force can be written as a gradient of gravitational potential U:

$$\boldsymbol{F_G} = -m\frac{\mu}{R^2}\hat{\boldsymbol{r}} = -m\nabla U \tag{3.5}$$

For a point mass approximation the gravitational potential U can be expressed as:

$$U = -\frac{\mu}{R} \tag{3.6}$$

Although often the gravity field is modelled as a regular variable, in real life it is far from being regular. The gravity field mainly depends on the internal mass distribution of the central body. Looking at Earth, it can be identified that the planet has a rich topography with countless oceans and mountains that affect the gravity field of the planet. It is important to model the gravity field accurately for vehicles that are in close distance to the surface as the stability of the vehicle will be affected by the gravity field.

Thus, often the point mass acceleration is used as an approximation when the gravitational pull of a planetary body is considered as a third body perturbations for the vehicle. At a close proximity of a body, the irregularities on the central body has to be accounted by treating it as a body with finite dimensions and inhomogenous mass distribution. Therefore, for spheroids, it is possible to express U as a summation of a central field term, which represents a mass-symmetric body, and a correction term for the Earth's non-symmetric mass distribution:

$$U = -\frac{\mu}{R} + U_c(R, \tau, \theta) \tag{3.7}$$

where τ is the geocentric longitude, ω is the co-latitude and R is the radial distance. As it is identified in Equation 3.7, U_c is a correction term that is used to account for the deviations from a perfect sphere. Note that, the above expression is identified as a spherical harmonic expansion.

For a vehicle that perform a return flight, the atmospheric forces become dominant as the vehicle penetrates deeper into the atmosphere (Mooij, 2016). Therefore, in the upper layers of the atmosphere, the gravitational forces are dominating hence a more accurate gravity model is required. In the upper layers, the central body is considered to be an ellipsoid with mass symmetry about the polar axis. For the remaining mass inhomogeneity in the lateral direction is considered. This indicates that only zonal terms $(m = 0)$ contribute to the definition of the gravity model.

The coefficient J_2 accounts for the flattening effect on the Earth due to the equatorial bulge. Since the Earth has a rotational speed, more mass is located around the equator and less around the poles. Therefore the oblateness of the Earth affect the gravitational field that is experienced by the vehicles. Table 3.1, presents the spherical harmonic coefficients according to the GRACE Gravity Model 02 (GGM02) for the Earth, in which $R = R_e$. Looking at the Table 3.1, it can be identified that the first perturbing term, hence J_2, produces the largest force as it is three orders of magnitude higher than other J-coefficients. Hence in this study, only constants up to n=2 and m=0 are regarded, since the J2 effect is enough to capture the gravitational effect due to oblateness of the Earth, thus complying the requirements on the environment. The effect of any higher-term is neglected as their contribution to the non-orbital trajectories are small (Jordan-Culler, 2016).

Table 3.1: Spherical harmonic coefficients according to the GRACE GGM02C Earth gravity field model (Tapley et al., 2005). Note that $R = 6378.1363$ km and $\mu = 398600.4415$ km^3/s^2.

n	m	$J_{n,m}(10^6)$	$\Lambda_{n,m}(^\circ)$
Zonal harmonics			
2	0	1082.6357	-
3	0	-2.5324737	-
4	0	-1.6199743	-
5	0	-0.2279051	-
Tesseral and sectorial harmonics			
2	1	0.0018225	98.3325
2	2	1.8155628	-14.9287
3	1	2.2094849	6.9684
4	1	0.6786576	-138.5480

Now that the extend of the spherical harmonic model is known, the gravitational acceleration that will be used to model the environment can be identified more accurately.

$$\boldsymbol{g} = \begin{pmatrix} g_N & 0 & g_D \end{pmatrix}^T \tag{3.8}$$

in which the individual components are computed as (Mooij, 2016):

$$g_N = -3\frac{\mu}{R^2}\left(\frac{R_e}{R}\right)^2 J_2 \cos\delta \sin\delta \tag{3.9}$$

$$g_D = \frac{\mu}{R^2}\left[1 - \frac{3}{2}J_2\left(\frac{R_e}{R}\right)^2 (3\sin\delta)^2 - 1\right] \tag{3.10}$$

Finally, it should also be noted that the gravitational force is computed in the NED reference frame. However propagation of the vehicle is performed in ECI, hence an inertial reference frame. Therefore, it is significant to perform the frame transformation before using the gravitational acceleration in the simulation. This is discussed in more detail in Section 4.3.

3.3. Atmospheric Model

As it was indicated in the earlier discussion, atmosphere contributes to the development of the two most dominant forces: lift and drag. When a vehicle is flying in the atmosphere, it encounters friction

due to air particles, also known as atmospheric drag. Due to the friction and the fact that air particles are compressed due to the presence of a vehicle within the atmosphere, the vehicle experiences aerodynamic heating. This could have severe effects on the vehicle such as ablation or excessive mechanical stress. However, the presence of the atmosphere can be used to the advantage of the vehicle. If the vehicle that is descending in the atmosphere has a high kinetic energy, such as a re-entry vehicle, this kinetic energy can be dissipated in the atmosphere before steering the vehicle to the landing site.

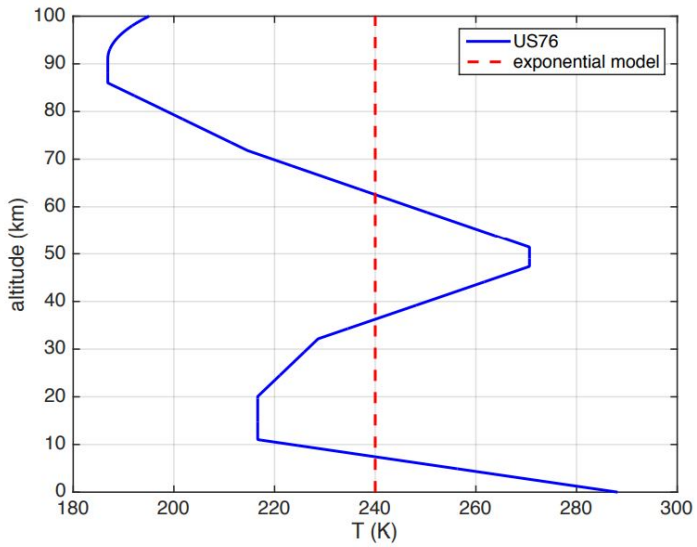

Figure 3.3: Comparison of temperature profiles of the exponential atmosphere and US76 atmosphere model (Mooij, 2016)

There are various atmosphere models for Earth. A widely preferred atmospheric model for different aerospace studies is the U.S. Standard Atmosphere, 1976 (US76) due to its sufficiently accurate representation of the atmosphere regarding the simplicity of the model (Vaughan, 2010). The model can closely approximate the actual behavior of the atmosphere at various altitudes, using a layered structure. This is highly advantageous for missions that cover a wide range of altitudes, such as a re-entry or a return flight. In Figure 3.3 the temperature profile as a function of altitude for two atmosphere models, US76 and exponential atmosphere, is presented. While the temperature is constant across different altitudes for the exponential model, US76 captures the atmospheric behavior and allows the aerodynamic forces to be calculated more accurately.

Note that since the trajectory of the flyback booster starts from 56 km altitude, the modelling approached of US76 for high altitudes are not relevant. Below 86 km altitude, the US76 assumes that the temperature is equal to the molecular scale temperature T_M. Mathematically this is expressed as:

$$T_M = T_{Mi} + L_{zi}(z - z_i) \tag{3.11}$$

in which i is used to indicate the i^{th} layer, z is the geopotential altitude, and L is the scale height, which is equal to:

$$L = \frac{RT}{g_0} \tag{3.12}$$

in which R is the air gas constant and is equal to 287 J/kg K. The US76 data is often employed as a look-up table that is based on known atmospheric values within the different layers. In this study, the US76 model is preferred, since precisely representing the aerodynamic forces will have a great influence on the trajectory of the flyback booster. Furthermore, it is important to have a model that is comparable with the industry, so that, if desired, a sensitivity analysis can be performed and the results can be compared. Note that the US76 model represents the Earth's atmosphere in a steady state. Therefore, the wind that is present in the atmosphere is not taken into account. This indicates that the airspeed is equal to the groundspeed and the ideal behavior of a descent vehicle is studied.

4

Flight Dynamics

Flight dynamics is the study that identifies how the vehicle moves through a medium. This is achieved by assessing the state of the vehicle along with the external forces that are acting on the vehicle. Therefore, operational state of the vehicle can be identified. As a result, this section begins with the identification of various reference frames. Section 4.2 a general overview of the state variables and the ones that are relevant for the problem at hand are presented. Afterwards, the models that are chosen to set up the environment are identified. Finally, the equations of motion associated with the vehicle are presented along with the external forces experienced by the vehicle.

4.1. Reference Frames

To represent the dynamics of the vehicle correctly, it is significant to define the forces in correct magnitudes and directions. This indicates that forces are vectors. Hence, by definition, a vector has to be defined within a coordinate system. It should be noted that forces that are used in the same equations should be defined with respect to the same reference frame. Hence, if needed, certain frame transformations have to be performed. It should be noted that different coordinate systems allow observations from different reference points. For instance, Earth-centered reference frames allow vehicle dynamics to be defined from an observer's point of view. On the other hand, reference frames in which the origin is fixed on the center of mass of the vehicle allow observations from the vehicle's perspective. In this section reference frames that are frequently used for defining the re-entry vehicles are presented (Mooij, 2016).

Earth-Centered Inertial (ECI) Reference Frame - F_I

The origin of the reference frame is located on the center of mass of the Earth. Z_I coincides with the rotational axis of Earth, which is pointing north. Meanwhile, X_I points towards the prime meridian at zero time. Finally, Y_I is oriented such that the reference frame is right-handed. Note that the $0_I X_I Y_I$ plane coincides with the equatorial plane of the Earth. It is worthwhile to mention that the ECI reference frame is a type of inertial planetocentric reference frame in which the central body is the Earth. Hence, the reference frame does not rotate with Earth.

Earth-Centered, Earth Fixed (ECEF) Reference Frame - F_e

Unlike the ECI reference frame, in the ECEF reference frame, X_e points towards the Greenwich meridian. Meanwhile, Z_e passes from the Earth's spin axis and Y_e is orthogonal to X_e and Z_e. As a result of this orientation, the reference frame rotates with respect to the inertial reference frame to keep a fixed position on the surface of the Earth. Consequently, there is an angular difference between the ECI and ECEF, as represented in Figure 4.1 (Holmes, 2012). Since the ECEF reference system is fixed with respect to the surface of the Earth and is not affected by the rotation of the body, it is convenient to use this reference system to point to locations on Earth. Therefore, the ECEF is preferred as a primary reference frame by positioning systems such as the global positioning system (GPS).

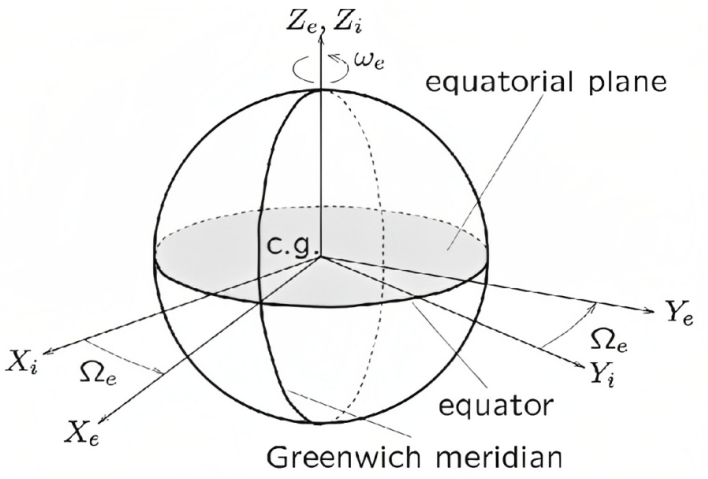

Figure 4.1: The relationship between the ECI and ECEF reference frames (Borst, 2012)

Body-fixed Reference Frame - F_B

The reference frame is fixed with respect to the vehicle. The origin locates in the center of mass. X_B lies on the plane of symmetry and is defined positive in the forward direction. Note that the positive definition of X_B is convenient for defining the motion of a re-entry vehicle since the nose of the vehicle encounters the atmosphere first. Meanwhile, positive Z_B points downwards and Y_B is oriented such that it completes the right-handed system. It is essential to introduce this reference frame since the way body-fixed reference frame is oriented defines the attitude of the vehicle.

Vertical Reference Frame - F_V

The vertical reference frame is oriented such that north and east axes form a plane tangent to the surface of the Earth at the given position. Meanwhile, the y-axis points down towards Earth's center, according to World Geodetic System 1984 (WGS84) ellipsoid, and completes the right-handed system.

Propulsion Reference Frame - F_P

The propulsion reference frame is often used to express the thrust force, either due to main engines or thrust-controllers. The reference frame is oriented such that X_P is collinear with the thrust vector. Meanwhile, Y_P and Z_P follow the transformation from the body-fixed reference frame. Since essentially X_P is related to the body frame but rotated due to elevation angle ϵ_T and azimuth angle $\psi_T e$ of the thruster.

Trajectory Reference Frame - F_T

The origin of the reference frame is located on the center of mass of the vehicle. It is significant to note that the trajectory reference frame is often identified with index TA or TG. The first defines that it is airspeed based, and the latter defines that it is groundspeed based. Since the thesis study will not consider the wind, more extensively discussed in Section 3.3, index TG is used. The X_{TG}-axis is defined positive in the direction of the velocity vector relative to the ECEF frame. The Z_{TG}-axis lies in the vertical plane. Meanwhile, the Y_{TG}-axis completes the right-handed coordinate system.

Aerodynamic Reference Frame - F_A

The origin of the reference frame is located on the center of mass of the vehicle. The aerodynamic reference frame is also often identified with index AA or AG, in which index AG is more relevant for this thesis. The X_{AG}-axis is defined positive along the velocity vector relative to the ECEF frame, hence the groundspeed. Therefore, the X_{AG} is collinear with the X_{TG}. Meanwhile, the Z_{AG} is collinear with the aerodynamic lift force but in an opposite direction. Finally, the Y_AG-axis completes the right-handed reference frame. It can be interpreted that in case the vehicle is not banking, the F_A and F_T are coinciding.

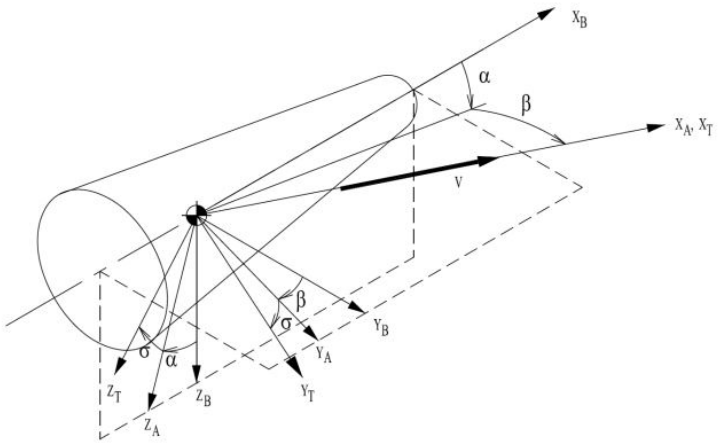

Figure 4.2: The relationship between the F_B, F_A, and F_T (Mooij, 2016)

North, east, down (NED) Reference Frame

The origin of the reference frame is located on the center of mass of the vehicle. The Z-axis is defined positive towards the center of mass of the Earth, along the direction of the radial component of the gravitational acceleration. The X-axis points towards the northern hemisphere and lies on a meridian plane. Finally, the Y-axis completes the right-handed reference system.

4.2. Translational State Variables

State variables are a set of variables that are used to define the state of a dynamical system. It is significant to identify the state variables correctly for the described problem, to ensure that the equations of motion are defined correctly. Since there are various state variables, choosing an appropriate set of variables depends on the applications of the vehicle. The state variables that are widely used to identify re-entry vehicles are presented in this section. Since the translational motion is the focus of this study, the state variables that define the translational motion are regarded.

The motion of a body is identified as a translational motion when all points on a body move uniformly in the same direction or line. This indicates that, all points on the body experience the velocity and acceleration with the same direction and magnitude at any given time. To represent this motion, position and velocity are used. It is possible to express the state variables for position and velocity in Cartesian elements, spherical elements, orbital elements, spherical elements, dual quaternions, and more.

Motion of a spacecraft is preferred to be defined in terms of orbital elements when the body is orbiting a celestial body. Since the study focuses on suborbital entry and does not include orbital motion, orbital elements are not presented in detail. Cylindrical elements are often used for motions that resemble the shape of a cylinder. Therefore, it is often preferred to describe geostationary orbits without singularities (Chen, 2021). Finally, dual quaternion state representation combine the rotational and translational motion in one. This is beneficial since singularities associated with Euler angles are reduced as well as the non-linearity of the dynamics (Wan et al., 2021). However, compared to others, it is a complex representation and require coding effort for appropriate implementation with guidance and control (Kenwright, 2012). Meanwhile, for re-entry and return vehicles, the state variables that are used to define the position and velocity of the vehicle are the Cartesian elements and spherical elements. Therefore, below, these two are explained in more detail. Finally, a trade-off between the two is presented.

Cartesian Elements

Cartesian elements define the position of a vehicle in three orthogonal position vectors that are indicated as x, y, z. It is the simplest form of representation as it can express the position of the vehicle with respect to any desired reference frame. Meanwhile, velocity components of corresponding position vector are indicated as $\dot{x}, \dot{y}, \dot{z}$. Note that in case the Cartesian elements are represented in the ECEF reference frame, for velocity variables u, v, w are used.

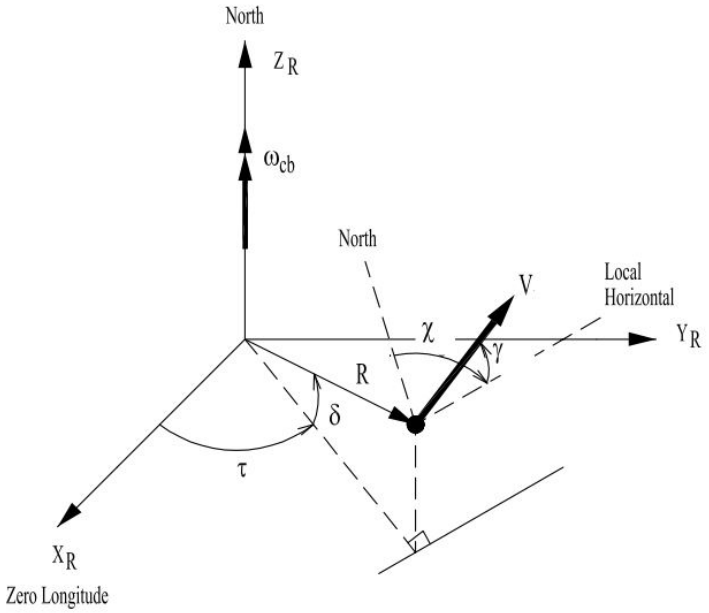

Figure 4.3: Visual representation of six spherical state variables, the position (R, τ, δ) and velocity (V, γ, χ). Note that here τ, δ, γ, and χ are defined positive. (Mooij, 1998)

Spherical Elements

Spherical elements are often used to define the position and velocity of a vehicle in the ECEF reference frame. The six state variables that describe the translational motion of a body are visualized in Figure 3.2 and presented as below:

- **Position:** distance R, longitude τ, geocentric latitude δ
- **Velocity:** groundspeed V, flight-path angle γ, heading angle χ

R is identified as the distance from the origin, hence center of mass of the body, to the center of mass of the vehicle. Longitude is identified as zero at the Greenwich meridian and measured positive towards the east $(-180° \leq \tau < 180°)$. Latitude is measured for the equatorial plane and zero at the equator $(-90° \leq \delta \leq 90°)$. It is identified as positive in the north direction. Meanwhile, angle between the local horizontal plane and the relative velocity V is identified as the flight-path angle γ. The angle is identified as negative if the velocity vector is below the local horizontal. Hence for a vehicle that is performing an atmospheric re-entry, the flight path angle is defined negatively. Finally, χ defines the direction of the projection of V on the horizontal plane with respect to the local north $(-180° \leq \chi < 180°)$.

It is worthwhile to note that when $\gamma = \pm 90°$ a singularity is present in the spherical elements. Therefore, no solution exists for the equations of motion when this equality is reached. However, it is possible to avoid this singularity while designing the trajectory of the vehicle.

Trade-off

Cartesian elements are often used to describe a body that has a ”linear” motion. Meanwhile, spherical elements are used to define a circular motion. From a flight simulation point of view, it is favorable to use the Cartesian elements in the F_I or F_e reference frames, since the Cartesian elements can be integrated numerically in these frames without any trouble. The representation of equations of motion is dependent on the chosen state variables. It should be noted that the Cartesian representation is much more compact and readable compared to spherical representation. On the contrary, spherical elements represented in the F_e reference frame is a widely used representation while designing a control system. The F_e reference frame is preferred over the F_I reference frame, since it accounts for the rotation of the Earth. Therefore, a fixed point on the Earth will always have the same position vector with the vehicle, which is an advantage in case of a precise landing. Thus, it is concluded to use the Cartesian elements in the F_I reference frame when motion of the vehicle is simulated.

Table 4.1: Symmetry conditions for the right and left rudder and elevator (Mooij, 1994)

Standard Frame Transformation		
From → To	Transformation Matrix	Specifications
$\mathscr{F}_R \rightarrow \mathscr{F}_I$	$\mathbf{C_{I,R}} = \mathbf{C_z}(-\omega_{cb}t)$	ω_{cb}: Earth rotational rate [rad/s] t: time from epoch [s]
$\mathscr{F}_V \rightarrow \mathscr{F}_R$	$\mathbf{C_{R,V}} = \mathbf{C_z}(-\tau)\mathbf{C_y}(\frac{\pi}{2}+\delta)$	τ: Earth-centred longitude [rad] δ: Earth-centred latitude [rad]
$\mathscr{F}_W \rightarrow \mathscr{F}_V$	$\mathbf{C_{V,W}} = \mathbf{C_z}(-\chi_w)\mathbf{C_y}(-\gamma_w)$	χ_w: flight-path angle for wind vector [rad] γ_w: heading angle for wind vector [rad]
$\mathscr{F}_{TG} \rightarrow \mathscr{F}_V$	$\mathbf{C_{V,TG}} = \mathbf{C_z}(-\chi_g)\mathbf{C_y}(-\gamma_g)$	χ_g: flight-path angle for groundspeed [rad] γ_g: heading angle for groundspeed [rad]
$\mathscr{F}_{TA} \rightarrow \mathscr{F}_V$	$\mathbf{C_{V,TA}} = \mathbf{C_z}(-\chi_a)\mathbf{C_y}(-\gamma_a)$	χ_a: flight-path angle for airspeed [rad] γ_a: heading angle for airspeed [rad]
$\mathscr{F}_{AA} \rightarrow \mathscr{F}_{TA}$	$\mathbf{C_{TA,AA}} = \mathbf{C_x}(\sigma_a)$	σ_a: bank angle based on airspeed [rad]
$\mathscr{F}_B \rightarrow \mathscr{F}_{AA}$	$\mathbf{C_{AA,B}} = \mathbf{C_z}(\beta_a)\mathbf{C_y}(-\alpha_a)$	β_a: sideslip angle for airspeed [rad] α_a: angle of attack for airspeed [rad]
$\mathscr{F}_B \rightarrow \mathscr{F}_{AG}$	$\mathbf{C_{AG,B}} = \mathbf{C_z}(\beta_g)\mathbf{C_y}(-\alpha_g)$	β_g: sideslip angle for groundspeed [rad] α_g: angle of attack for groundspeed [rad]
$\mathscr{F}_B \rightarrow \mathscr{F}_P$	$\mathbf{C_{P,B}} = \mathbf{C_y}(\epsilon_T)\mathbf{C_z}(\psi_T)$	ϵ_T: thrust elevation angle [rad] ψ_T: thrust azimuth angle [rad]

4.3. Frame Transformations

In section 4.1 it was discussed that often each force is defined in their corresponding reference frame. For instance, the thrust force is applied in the propulsion reference frame. Yet, using the thrust elevation and azimuth angles, it is possible to convert the thrust force in the propulsion reference frame to a thrust force in the body-fixed reference frame. The equations of motion combine all the forces and moments on the vehicle. For these equations to be coherent and solvable, all forces must be represented in the same reference frame. A set of standard frame transformations are defined by Mooij (1994) as in Table 4.1.

Consider a vector $\boldsymbol{v_A}$ in a reference frame A, F_A. Using the frame transformation matrix C, the same vector can be expressed in a reference frame B,F_B. The corresponding relation is expressed as below:

$$\boldsymbol{v_B} = \boldsymbol{C_{B,A}}\boldsymbol{v_A} \tag{4.1}$$

in which $\boldsymbol{C_{B,A}}$ is the transformation matrix from F_A to F_B. Transformation from F_A to F_B, or from and to any right-handed Cartesian frame, can be expressed through unit-axis rotations. Unit-axis rotations are positive rotations about the X,Y, and Z axes. The unit rotation matrix about the X axis is expressed as:

$$\boldsymbol{C}_X(\alpha) = \begin{bmatrix} 1 & 0 & 0 \\ 0 & \cos\alpha & \sin\alpha \\ 0 & -\sin\alpha & \cos\alpha \end{bmatrix} \tag{4.2}$$

Accordingly, the unit rotation matrices about the Y and Z-axes is expressed as:

$$\boldsymbol{C}_Y(\alpha) = \begin{bmatrix} \cos\alpha & 0 & -\sin\alpha \\ 0 & 1 & 0 \\ \sin\alpha & 0 & \cos\alpha \end{bmatrix} \tag{4.3}$$

$$\boldsymbol{C}_Z(\alpha) = \begin{bmatrix} \cos\alpha & \sin\alpha & 0 \\ -\sin\alpha & \cos\alpha & 0 \\ 0 & 0 & 1 \end{bmatrix} \tag{4.4}$$

in which α is an arbitrary angle used for the rotation. These matrices are and their products are orthonormal. Thus, the inverse of the matrix is equal to its transpose. This suggests that the transformation matrix from F_A to F_B can be used to determine the transformation matrix from F_B to F_A. Mathematically, this is expressed as:

$$\boldsymbol{C_{A,B}} = \boldsymbol{C_{B,A}^{-1}} = \boldsymbol{C_{B,A}^{T}} \tag{4.5}$$

Often, the body-fixed reference frame is preferred to visualize and understand the forces that are acting on the vehicle. In this thesis, the equations of motion are solved using a numerical propagator. Within the chosen library, the propagators support state propagation only in the inertial reference frame. Thus, the external forces are first computed in their respective reference frame and then transformed to the inertial reference frame to be propagated. For a more comprehensive explanation of the propagation set-up and the simulation model refer to Chapter 6. The main transformation matrices can be used to deduce all the other transformation matrices. An example of a transformation from the propulsion reference frame F_P to the inertial reference frame F_I is expressed as:

$$\boldsymbol{C_{I,P}} = \boldsymbol{C_{I,R}C_{R,V}C_{V,TG}C_{TG,AG}C_{AG,B}C_{B,P}} \tag{4.6}$$

4.4. Equations of Motion

The equations of motion are set of equations that represent the behavior of a system as a function of time. Compared to the speed of light the vehicle has a relatively low speed, therefore it is suitable to discard the general relativity and use Newtonian mechanics. Motion of the non-elastic velocity with a variable mass m is divided into two sets of equations. The first is the translational equation of motion that describes the velocity and position of the vehicle in three directions, x,y, and z. After introducing the forces that contribute to this motion, translational motion is presented in Section 4.4.2.

4.4.1. External Forces

Before describing the translational motion, the forces that act on the vehicle and contribute to the motion has to be identified. The vehicle that is entering atmosphere encounters three main external forces: aerodynamic force, gravitational force, and thrust force. These forces and equations related to them are identified extensively in the upcoming section.

Aerodynamic Force

The aerodynamic forces are defined in aerodynamic reference frame, index A, and consists of drag D, side force S, and lift L:

$$\boldsymbol{F_{A,A}} = -\begin{pmatrix} D \\ S \\ L \end{pmatrix} = -\begin{pmatrix} C_D \bar{q} S_{ref} \\ C_S \bar{q} S_{ref} \\ C_L \bar{q} S_{ref} \end{pmatrix} \tag{4.7}$$

in which S_{ref} indicates the aerodynamic reference area in m^2. Furthermore, the forces are dependent on respective force coefficients C_D, C_S, and C_L. These aerodynamic coefficients are unique for each vehicle and can be obtained through aerodynamic tests, such as the wind-tunnel test. Usually, C_D and C_L, are a function of Mach number M and angle of attack α. C_S is a function of Mach number M and side-slip angle β. Meanwhile, Mach number is the relation between the speed of a vehicle V, in m/s, to the speed of sound a in the surrounding medium. Therefore, the Mach number is expressed as:

$$M = \frac{V}{a} = \frac{V}{\sqrt{\gamma R T}} \tag{4.8}$$

in which the speed of sound a can be written in terms of the ratio of specific heat γ, the gas constant R, and the temperature of the surrounding medium T. Furthermore, $\bar{q}$ is the dynamic pressure that is

dependent on the atmospheric density ρ, in kg/m^3, and the groundspeed of the vehicle V, expressed by:

$$\bar{q} = \frac{1}{2}\rho V^2 \tag{4.9}$$

Gravitational Force

As it was identified in Section 3.2, the gravitational acceleration is conventionally defined in the NED reference frame as indicated below:

$$\boldsymbol{F}_g = m \begin{pmatrix} g_N \\ 0 \\ g_D \end{pmatrix} \tag{4.10}$$

Thrust force

The thrust force is represented in the propulsion reference frame, in which thrust T, in N, is co-linear with the X-axis of the reference frame. Thus thrust force is written as:

$$\boldsymbol{F_{T,P}} = \begin{pmatrix} T \\ 0 \\ 0 \end{pmatrix} \tag{4.11}$$

in which T is expressed as

$$T = I_{sp} g_0 \dot{m} \tag{4.12}$$

4.4.2. Translational Equations of Motion

Once the forces that contribution to the motion of the body are identified, it is possible to write the translational equation of motion as (Mooij, 2016):

$$\tilde{\boldsymbol{F}}_{\boldsymbol{I}} = \boldsymbol{F_I} + \boldsymbol{F_C} + \boldsymbol{F_{rel}} = m\frac{d^2\boldsymbol{r_{cm}}}{dt^2} \tag{4.13}$$

in which

- $\tilde{\boldsymbol{F}}_{\boldsymbol{I}}$: pseudo external force vector [N]
- $\boldsymbol{F_I}$: sum of all the external forces acting on the vehicle in the inertial reference frame [N]
- m: uniform mass of the vehicle (point mass) [kg]
- $\frac{d^2\boldsymbol{r_{cm}}}{dt^2}$: acceleration of the center of mass of the vehicle with respect to the inertial frame [m/s^2]
- $\boldsymbol{r_{cm}}$: position vector of the vehicle with respect to the center of the Earth, hence the center of the inertial reference frame [m]
- $\boldsymbol{F_C}$: the Coriolis force due to variations in the mass distribution [N]
- $\boldsymbol{F_{rel}}$: the relative force due to variations in the mass distribution [N]

The equation above can vary for powered and unpowered flight. To begin with, for unpowered flight, the vehicle can be assumed to be a rigid body. Therefore, Newton's second law of motion for uniform masses can be applicable, such that the Coriolis force and relative force are neglected. Thus the equation becomes:

$$\tilde{\boldsymbol{F}}_{\boldsymbol{I}} = \boldsymbol{F_I} = m\frac{d^2\boldsymbol{r_{cm}}}{dt^2} \tag{4.14}$$

During a powered flight, due to fuel usage, the mass varies during the return flight, hence, affecting the motion of the vehicle. Regarding the *principle of solidification*, it is possible to express the equations of motion for a variable mass at time t as equations of motion for a rigid body with mass m equal to the mass of the vehicle at time t, while regarding the two apparent forces and moments that are applied, hence the Coriolis and relative forces and moments (Mooij, 1998). The first term is the Coriolis force which acts on the body since the body is in a rotating frame with respect to the inertial reference frame, ECI. However, it is worthwhile to mention that these rotations are insignificantly small, making $\boldsymbol{F_C}$

smaller than $\boldsymbol{F_{rel}}$ (Mooij, 1998). Therefore, the Coriolis force $\boldsymbol{F_C}$ is neglected even if the center of mass flow is not along the X_B axis and causes rotation about the Y_B and Z_B axis. The relative force is due to the relative acceleration of the body in the moving reference frame. Thus, due to the powered flight, mass is being expelled with a velocity $\boldsymbol{V_T}$. Knowing that $\dot{m}$ is the rate of mass flow, it is possible to express the relative force as:

$$\boldsymbol{F_{rel}} = \dot{m}\boldsymbol{V_T} \tag{4.15}$$

Furthermore, the kinematic equation that is needed to solve the equations of motion can be written as:

$$\frac{d\boldsymbol{r_{cm}}}{dt} = \boldsymbol{V_I} \tag{4.16}$$

in which $\boldsymbol{V_I}$ indicates a velocity of the vehicle in the inertial reference frame in m/s. It is significant to note that the above equations are expressed using the F_I reference frame. As it was discussed in section 4.2, the F_I reference frame is selected for propagating and optimizing the trajectory. Meanwhile the F_e reference frame with spherical components are preferred for the design of the guidance and control systems. The dynamic equations of motion for the translational motion of an unpowered vehicle in spherical elements are expressed as (Mooij, 2017):

$$\dot{V} = -\frac{D}{m} - g\sin\gamma + \omega_{cb}^2 R\sin\delta(\sin\gamma\sin\delta - \cos\gamma\sin\delta\cos\chi) \tag{4.17}$$

$$\dot{\gamma} = \frac{L\cos\sigma}{mV} - \frac{g}{V}\cos\gamma + 2\omega_{cb}\cos\delta\sin\chi + \frac{V}{R}\cos\gamma + \omega_{cb}^2\frac{R}{V}(\cos\gamma\cos\delta + \sin\gamma\sin\delta\cos\chi) \tag{4.18}$$

$$\dot{\chi} = \frac{L\cos\sigma}{mV\cos\gamma} + 2\omega_{cb}(\sin\delta - \cos\delta\tan\gamma\cos\chi)\frac{V}{R}\cos\gamma\tan\delta\sin\chi + \omega_{cb}^2\frac{R}{V\cos\gamma}\cos\delta\sin\delta\sin\chi \tag{4.19}$$

in which ω_{cb} is the rotational rate of the Earth, in rad/s. Meanwhile, the kinematic equations of motion for the translational motion are expressed as:

$$\dot{R} = \dot{h} = V\sin\gamma \tag{4.20}$$

$$\dot{\tau} = \frac{V\sin\chi\cos\gamma}{R\cos\delta} \tag{4.21}$$

$$\dot{\delta} = \frac{V\cos\chi\cos\gamma}{R} \tag{4.22}$$

$$\dot{m} = \frac{T}{I_{sp}g_0} \tag{4.23}$$

in which $\dot{m}$ is the mass flow rate and is relevant when the booster performs a powered flight.

4.4.3. External Moments

A vehicle that is entering the atmosphere of Earth encounters external moments, along with external forces. Therefore, these moments are generated due to external forces and categorized in the same manner: aerodynamic, gravitational, and thrust. When a vehicle is modelled as a spherical rigid body, the center of mass and the center of gravity of the body are coinciding. Therefore, the gravitational force does not generate any moments around the center of mass. However, since the vehicle is not modelled as a spherical rigid body, the moment due to the gravitational force is also regarded. Meanwhile, neither the aerodynamic force nor the thrust force act on the center of mass, therefore they induce moments around this center. Aerodynamic moment and moment due to thrust force is expressed, respectively, in the body reference frame as:

$$\boldsymbol{M_{g,B}} = \begin{pmatrix} M_{g,x} \\ M_{g,y} \\ M_{g,z} \end{pmatrix} \tag{4.24}$$

$$\boldsymbol{M_{A,B}} = \begin{pmatrix} \mathcal{L} \\ \mathcal{M} \\ \mathcal{N} \end{pmatrix} = \begin{pmatrix} C_l \bar{q} S_{ref} b_{ref} \\ C_m \bar{q} S_{ref} c_{ref} \\ C_n \bar{q} S_{ref} b_{ref} \end{pmatrix} \tag{4.25}$$

$$\boldsymbol{M_{T,B}} = \begin{pmatrix} M_{P,x} \\ M_{P,y} \\ M_{P,z} \end{pmatrix} \tag{4.26}$$

In the above equation $\mathcal{L}$ refers to the rolling moment, $\mathcal{M}$ is the pitching moment, and $\mathcal{N}$ is the yawing moment, all are in Nm. Similar to external forces, external moments also have moment coefficients C_l, C_m, and C_n respectively. Meanwhile, b_{ref} is the reference length, which is the wingspan, for roll and yaw. c_{ref} is the mean aerodynamic cord that is taken as the reference length for the pitching moment. It is worthwhile to mention that all these moments are dependent on aerodynamic surfaces, again just like external forces. For instance, the pitch moment coefficient can be divided into sub-components, such as pitch moment around the aerodynamic center $C_{m_{ac}}$ or pitch moment due to horizontal surfaces C_{m_h}:

$$C_m = C_{m_{ac}} + C_{m_h} \tag{4.27}$$

These surfaces are often the control surfaces, ailerons, elevators, and body flap, and the deflection of such surfaces and change in angle of attack induce the moment around the center of mass. Therefore, in case the pitch moment is a function of elevator deflection δ_e and angle of attack α (Stengel, 2019):

$$C_{m_h} = C_{m_h}(\alpha, \delta_e) \tag{4.28}$$

Furthermore, for conventional winged structures, such as aircraft, often at small angles pitch moment varies linearly with these variables. Nevertheless, although the design of the FSSC-16 resembles the design of an aircraft, when it comes to stability certain differences has to be regarded due to the lack of vertical surfaces. For instance, the main contributor of the side force is not present anymore, since there is no vertical tail present. The aerodynamic surfaces and forces are discussed more extensively in Chapter 4.

5

Trajectory Design

The first step for a complete mission design is assessing and understanding the reference trajectory. In Chapter 2 the trajectory of different re-entry and flyback missions are discussed. In the scope of this research, the characteristics of the fly back trajectory for FSSC-16 is identified in Section 5.1. Next, in Section 5.2 the trajectory problem is explained mathematically. This includes defining the objectives, constraints, and decision variables. The information obtained in the previous two sections is utilized during the design space exploration to identify the reasonable interactions between the parameters and the trajectory. Thus in Section 5.3, different design space exploration methodologies are introduced.

5.1. FESTIP Trajectory Review

FESTIP also provided a preliminary mission profile for the booster of FSSC-16. However, certain details, such as a complete aerodynamic database, are not reported in the FESTIP documents. Although, the study had missing information, it has provided the information required for the preliminary analysis of the mission profile. The return flight of the booster was broken down to three main phases. Below each of these phase and their characteristics are identified individually. In the end, a general overview of the complete trajectory is presented.

Phase 1 Ballistic Trajectory

Phase 1 initiates with a stage separation at an altitude of 56 km and at Mach 6.5 and ends when the vehicle reaches a flight path angle of 0°. Immediately after the separation the flyback booster remains at its high velocity from the separation. Due to the inertia of the vehicle and high speed, the flyback booster enters a ballistic trajectory, as it is depicted in Figure 5.1 with an altitude increase between 0 and 70 seconds. Phase 1 is the ascent of this ballistic trajectory. As the flyback booster ascends, it enters the atmosphere with lower density. This causes the vehicle to have lower dynamic pressure, as seen in Figure 5.2, consequently lower lift and drag. This is significant to note as it limits the aerodynamic capabilities of the vehicle. This indicates that the vehicle is less responsive to steering commands, such as angle of attack α or bank angle σ from the guidance system. Note that right after the separation the vehicle is in the inverted configuration, in which the tail is pointing towards the Earth. Before initiating the return to launch site, the vehicle has to correct its orientation. Therefore, it is expected to observe rapid changes in the bank angle during this phase. Since the vehicle does not have sufficient lift, any steering command is ineffective.

Phase 2 Turn Maneuver

The second phase begins upon the completion of the first phase, after the peak altitude point is reached. During the first instants of Phase 2, the vehicle gains lift as it descent towards the denser part of the atmosphere. During Phase 1 the vehicle sustains the initial heading angle of 110°. This value causes vehicle to fly away from the launch site. Therefore, for vehicle to initiate the return to the launch site, first the vehicle has to be pointed towards the landing site. Therefore, a turn maneuver should be induced to change the heading angle from 110° to -70°. Looking at the latitude and longitude history of the booster, in Figure 5.3, it can be seen that the turn is terminated at the point that is identified with a red cross.

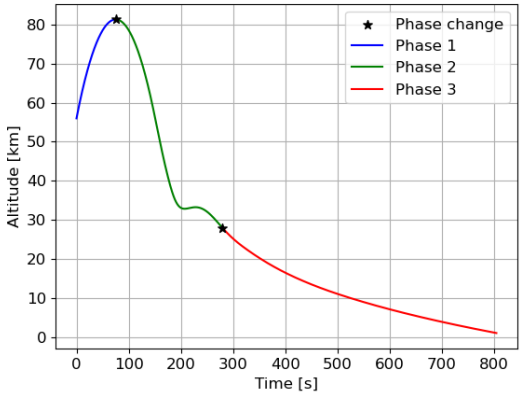

Figure 5.1: Altitude profile of a reference return flight of the FSSC-16 flyback booster

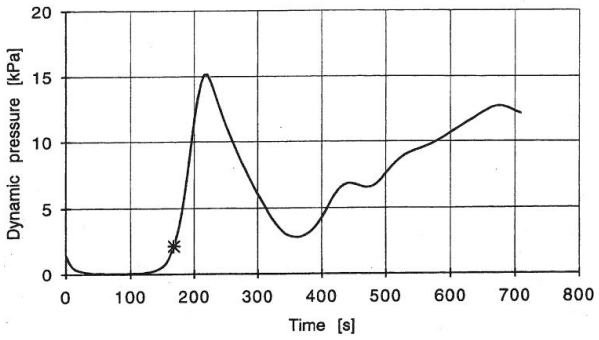

Figure 5.2: Dynamic pressure of the booster flyback trajectory optimized by ALTOS (Daimler-Benz Aerospace, 1998)

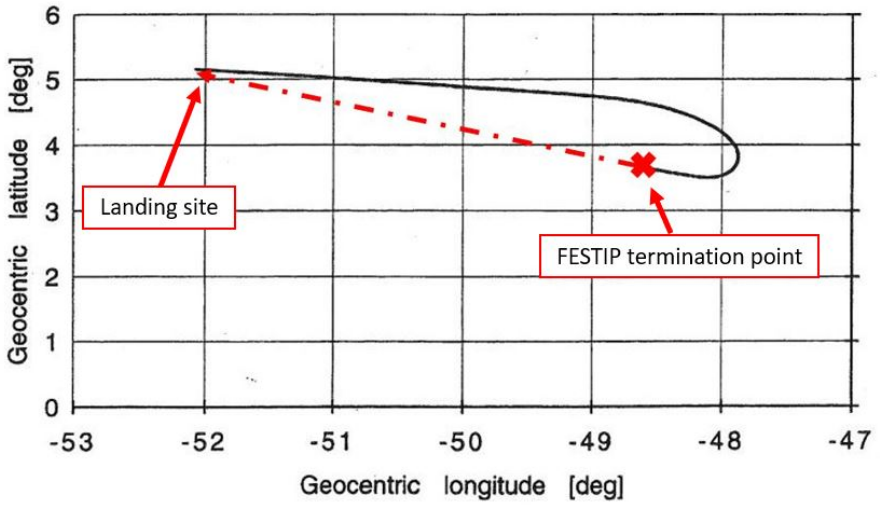

Figure 5.3: Latitude and longitude of the booster flyback trajectory optimized by ALTOS (Daimler-Benz Aerospace, 1998)

Phase 3 Fly Back to Launch

Phase 3 begins right after the desired heading angle is obtained by the booster. Looking at the latitude and longitude graph in Figure 5.3, it can be seen that the vehicle has to cover a downrange of 500 km during the third phase, which is identified with the red dashed arrows in the figure. The booster first covers this distance with aerodynamic capabilities. When an 6 km altitude is reached, the vehicle activates the boosters to complete the return flight in leveled flight, just like an aircraft. Phase 3 is terminated upon meeting the TAEM conditions, which is a 0.75° of distance-to-go. Throughout this phase, the vehicle must sustain its final heading angle and have sufficient energy to have a successful TAEM entry.

General Overview

Further investigation of the first phase yielded that due to the ballistic flight, the vehicle flies further away from the landing site by 2°, which is approximately 200 km. Since the mission aims to turn the vehicle around and fly back to the landing site, it would be desired to perform this with a smaller range, which reduces the distance-to-go to Kourou. Consequently, this ensures that the TAEM conditions can be met with sufficient energy. Therefore, as will be explained in more detail in Chapter 8, the vehicle's turn maneuver is optimized. This optimization is performed in two separate ways; first only the aerodynamic capabilities of the vehicle are used, and secondly, the engines are activated from

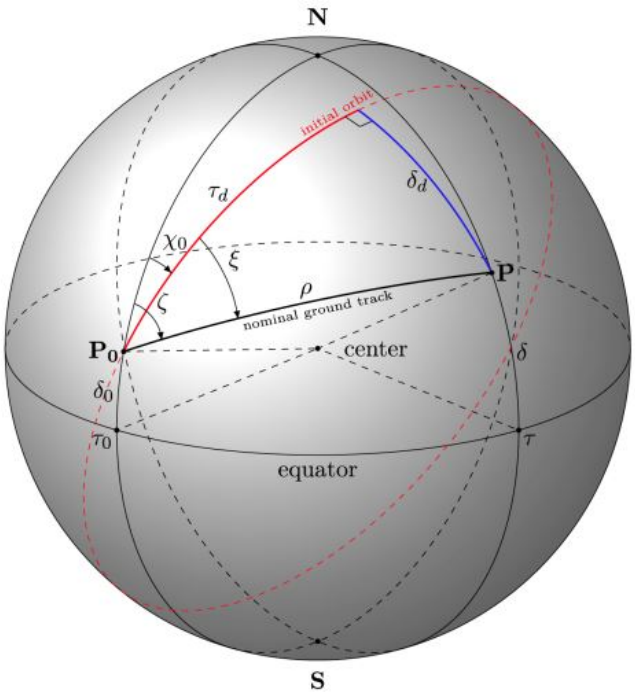

Figure 5.4: Spherical geometry of the crossrange, downrange and distance-to-go (Mooij, 2016)

separation onward to counteract the gravitational force and drag force, so that the vehicle responds to the steering commands. The focus is to observe to what extent the use of aerodynamic forces in combination with a propulsion system reduces the force required by the propellant, while complying the trajectory and boundary constraints of the problem.

5.2. Problem Description

Mathematical expressions allow physical phenomena to be expressed in a quantitative environment. To analyze the fly back trajectory, it is essential to express the problem in terms of mathematical equations. In this section, the objectives, constraints, guidance principle via the decision variables, and the node control method are discussed in detail and expressed in mathematical terms.

5.2.1. Objectives

The definition of the objective function is significant for the optimization problem and the design space exploration. During the optimization problem, the objective function is a mathematical expression that is actively optimized. Meanwhile, during the design space exploration, the objective function is used to guide the exploration process. The value of the objective function determines the performance of the design options. Therefore, by evaluating the value of the objective function, different design options can be compared. Note that, in this context, a design option refers to a different set of decision variables, as it will be explained in more detail in Section 5.2.3. Below the objective functions and the reasoning behind choosing these functions are presented.

Minimum Final Distance-to-go

The final distance-to-go refers to the remaining distance that needs to be covered by the booster at the end of the simulation. For the unpowered vehicle, this is the main objective that needs to be minimized. As the unpowered optimization follows a decoupled optimization, Phase 2 and Phase 3 are optimized individually. If the optimizer can find a solution such that the turn maneuver is initiated earlier and with a smaller radius at Phase 2, the distance-to-go at the end of Phase 2 would be much smaller than a turn maneuver that is initiated later in the trajectory with a large turn radius. Consequently, the range that needs to be covered in Phase 3 would be much smaller.

Since the Earth is assumed to be a spherical object, the distance-to-go can be calculated as an arc length. In Figure 5.4 the crossrange and downrange of a trajectory are visualized on a sphere. The point P_0 is the target point and the point P is the location of the vehicle at the given instant in time. The arcs that are represented on the sphere, also the one connecting these two points, can be expressed in radians or degrees. To calculate the distance represented by an arc, the arc length in radians is multiplied by the radius of the sphere. From Figure 5.4 it can be seen that the circular arc ρ is connecting point P_0 and P. The length of this circular arc is equal to the distance between the two points. To derive the equation of the ρ, the point P_0 and P can be imagined as the end points of two vectors. Thus, the spherical coordinates of the points $\boldsymbol{p_0}$ and $\boldsymbol{p}$ can be expressed as (Mooij, 2016):

$$\boldsymbol{p_0} = \begin{pmatrix} \cos\delta_0 \cos\tau_0 \\ \cos\delta_0 \sin\tau_0 \\ \sin\delta_0 \end{pmatrix} \tag{5.1}$$

$$\boldsymbol{p} = \begin{pmatrix} \cos\delta \cos\tau \\ \cos\delta \sin\tau \\ \sin\delta \end{pmatrix} \tag{5.2}$$

Note that to ease the calculations the sphere in question is assumed to be a unit sphere, which has a radius 1. The distance-to-go ρ, or θ_d as it is referred to in this study, is mathematically expressed as:

$$\cos\theta_d = \boldsymbol{p} \cdot \boldsymbol{p_0} = \cos\delta_0 \cos\delta \cos(\tau - \tau_0) + \sin\delta_0 \sin\delta \tag{5.3}$$

Accordingly, the associated cost function is formulated as:

$$J_D = \min(\theta_d) = \min(\arccos(\cos\delta_0 \cos\delta \cos(\tau - \tau_0) + \sin\delta_0 \sin\delta)) \tag{5.4}$$

Minimum Fuel Consumption

For the powered vehicle, it is desired to have a minimum fuel consumption. To begin with, a minimum fuel consumption for the return flight would allow more fuel to be consumed for the launch phase, potentially increasing the efficiency of the launcher. Moreover, by minimizing the fuel consumption, more payload can be carried either on the orbiter or the booster. Finally, since any additional mass increases the cost of a space mission, decreasing the consumed fuel would drop the launch costs. The fuel that is consumed at any given point in the trajectory can be calculated by subtracting the initial mass of the vehicle $M(t_0)$ from the mass at that point $M(t)$. The associated cost function is formulated as:

$$J_{FC} = \min(M_{FC}) = \min\left(M(t_0) - M(t_f)\right) \tag{5.5}$$

in which M_{FC} refers to the mass of the consumed fuel.

Minimum RSS of Path Constraint Violations

The root sum square (RSS) is a method that is used to calculate the overall path constraint violations by individually accounting for each violation. Both powered and unpowered configurations actively minimize the path constraint violation since surpassing the limit values of path constraints pose a structural and operational challenge for the booster. The RSS of the path constraints are calculated as below:

$$RSS_{constraints} = \sqrt{\sum_{i=1}^{n} \left(\frac{x_i - C_i}{C_i}\right)^2} \tag{5.6}$$

in which x_i refers to the current value of the constraint and C_i is the limit value for the constraint. The associated objective function is formulated as below:

$$J_{RSS} = \min(RSS_{constraints}) \tag{5.7}$$

The constraints that are accounted for in this objective function are the g-load constraint, heat flux constraint, and trim violation constraint. The complete list of constraints and more detailed explanation is provided in Section 5.2.2.

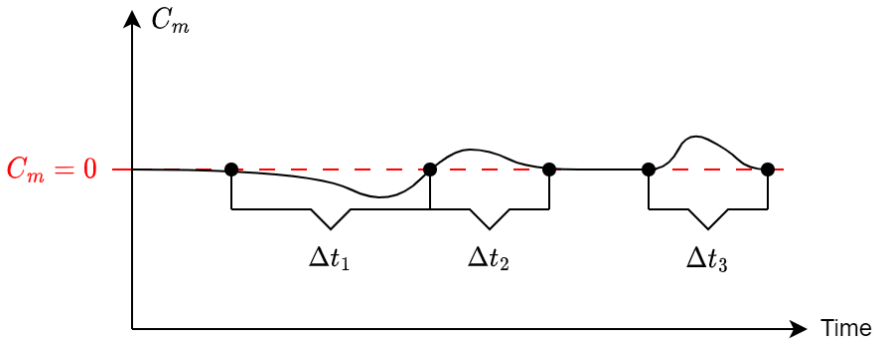

Figure 5.5: Total pitch moment coefficient vs. time graph to visualize the trim violation condition

5.2.2. Constraints

Constraints are the driving factors of the optimization. Often the solution space contains more than one feasible solution. However, when there are constraints incorporated, it is ensured that the obtained solution is guided towards the specific areas of the search space. So that the certain limitations of the problem are regarded and the solution does not conflict with these limitations.

Path Constraints

The physical constraints on the trajectory are identified as the path constraints. These are the values that cannot be surpassed, since they pose operational and structural limits on the vehicle. The path constraints are defined as below:

- Maximum heat flux: $q_c = 93$ kW/m^2
- Maximum g-load: $n_g = 3$g
- Maximum trim violation: $t_T = 0$ s

in which the maximum g-load is calculated by retrieving the acceleration history from the simulation, dividing by gravitational acceleration g, and calculating the maximum value. Mathematically, the g-load is calculated as:

$$n_g = \frac{a_a + a_T + a_g}{g} \tag{5.8}$$

in which a_a refers to aerodynamic acceleration, a_T refers to thrust acceleration, and a_g is the acceleration due to gravitational force. In the meantime, the heat flux is calculated using the Chapman's Equation, expressed as below, and calculating the maximum value:

$$q_c = c_1 \frac{1}{R_N^n} \rho^{1-n} V^m \tag{5.9}$$

in which $n = 0.5$ for laminar boundary layer, R_N is the nose radius of the vehicle, m is an empirical constant which is often taken as $m = 3$. On the other hand, the maximum trim violation is calculated differently. As long as the vehicle is above Mach 1.2, it is desired to have a trimmable trajectory. Therefore, for 20 > M > 1.2, the trim violation is calculated such that for the duration in which the total pitch moment coefficient C_m is not zero is added up. For instance, looking in Figure 5.5 it can be seen that in different instances along the trajectory the vehicle is not trimmable for Δt_1, Δt_2 and Δt_3. To obtain the trim violation duration these two values are added up. In the end, the trim violation is expressed as:

$$t_T = \Delta t_1 + \Delta t_2 + \Delta t_3 \tag{5.10}$$

Table 5.1: Values of the initial and termination state for the return flight of the flyback booster

State Variable	Initial Value	Final Value	Units
Altitude	56,000	7,000	m
Velocity	2000	100	m/s
Latitude	5.2	*Depends on final* θ_d	deg
Longitude	-52.8	*Depends on final* θ_d	deg
Flight-path Angle	20	*Free*	deg
Heading Angle	110	-70	deg

Control Constraints

Although a control system design is not carried out in this study, by regarding certain control constraints, it is aimed to obtain a more realistic trajectory. After all, the control system of the vehicle is a physical system and it is not possible for these components to move instantly. In real life, when the guidance system commands to the control system, it is expected to have certain limitations in the deflection of the control systems. A delay in the control system is an example of these limitations. By regarding the control constraints, it is aimed to obtain a more realistic trajectory. The control constraints are defined as below:

- Maximum angle of attack rate: $\dot{\alpha} = 10$ deg/s
- Maximum bank angle rate: $\dot{\sigma} = 10$ deg/s

Boundary Constraints

Mathematically, a trajectory is defined by solving the equations of motion at each time step. The boundary constraints determine the behavior of the solution at the defined domain. Therefore, solution of the optimization is guided towards the areas that satisfy both the initial and final conditions. In Table 5.1, the boundary constraints for the flyback booster is defined.

Note that the initial values are provided as an initial condition for the ordinary differential equations. This allows the simulation to always start at the mission-specific initial state. Meanwhile, the final values are handled differently. Some of these final values are implemented as a termination condition, while others are implemented as terminal constraints on the objective. Although an altitude of 7 km is desired, it is not a hard constraint. Yet, it is only implemented as a termination condition. On the other hand, the equations of motion approach singularity when the velocity is zero since it is not possible to divide a value with zero. To avoid the trajectories that are prone to singularity, the final velocity of 100 m/s is incorporated as a termination condition. Therefore, trajectories that have a lower velocity are terminated and not regarded in the fitness evaluation during the optimization process. Consequently, this guides the design space towards trajectories that have a better, which is higher, final velocity. Finally, the heading angle defines the direction in which the vehicle is pointing at. To have a successful landing operation and meet the TAEM condition, the vehicle has to point towards the landing site. Therefore, the heading angle is evaluated as a hard constraint with a penalty function, as explained further in the next section.

Constraint Handling

For each run, a vector of different constraint values are obtained. As was identified in Section 5.2.1, the path constraint violations are handled by introducing the RSS of the violations as an objective. Meanwhile, another method for handling the constraints is to introduce each violation as a penalty function. A penalty is formulated as below:

$$Penalty = \sum_{i=1}^{n} \left(\frac{x_i - C_i}{C_i} \right) \cdot k_1 \tag{5.11}$$

where k_1 is a constant. Depending on the original value of the objective, the original value of the constraint and the severity of the constraint, k_1 is chosen through trial and observation. The penalty function essentially identifies the degree of the constraint violation. Therefore, by introducing a constant the degree of the violation can be increased, which in return would allow to adjust the severity of the penalty function. The remaining constraints, such as the final heading angle or distance-to-go, are

introduced as penalty functions, which is later on added to the first objective, which is the minimum final distance-to-go for the unpowered booster and minimum fuel consumption for the powered booster. For instance, since final distance-to-go of 0.75° is a hard constraint for the powered booster, the severity of this constraint is high. It is expected to observe fuel consumption around few tons, 2,000-5,000 kg, for early terminated trajectories, thus the ones that cannot reach the desired final distance-to-go. The k_1 of the final distance-to-go penalty is then chosen to be around 6,000. Usually these early terminated trajectories have the final distance-to-go of $2.0° - 2.7°$, which roughly corresponds to 200-270 km. Even at the low range of of both values, the penalty function would rise the value of the fuel consumption from 2,000 kg to 14,000 kg, which will be eliminated via the optimization algorithm due to its large value. The same logic is followed for the other constraints, final heading angle, as well. Note that after a familiarity is gained with the value of the objectives during the first few optimization batches, the weight values are re-adjusted to ensure that the severity is implemented accurately.

Overall, two different constraint handling methods are identified throughout this section. The first one is introducing the constraints as an objective and the second one is using the penalty function. The different methods used to handle the constraints affect the way the optimization problem is formulated. It was discussed that when a penalty function is implemented, the constraint violation is added to an objective. To scale the penalty a constant k_1 is used. If the value of k_1 is too large, the penalty could introduce a bias, which may cause some feasible trajectories to be discarded by the optimizer. On the other hand, if the value of k_1 is too small, then infeasible trajectories will not be killed off by the optimizer. For instance, if the g-load constraint were to be implemented as a penalty function, it has to be known how much of a g-load violation corresponds to how much of a fuel consumption, so that the k_1 value can be estimated correctly. Since the relationship between the path constraint violation and fuel consumption is not trivial, it is decided to adopt the path constraints as a separate objective.

5.2.3. Guidance and Decision Variables

When the fly back trajectory is optimized, the guidance logic is an output of the optimization process. Each individual within the optimization is defined by a set of decision variables, also known as the decision vector. At a number of points along the trajectory, the guidance parameters are defined by this decision vector. The optimization algorithm obtains the values of these variables for the required objective and the constraints. Consequently, the vehicle is steered towards the optimum trajectory with a set of optimum guidance parameters. Depending on the vehicle type, powered or unpowered, the guidance parameters differ. Therefore, for the unpowered and powered flyback booster, the decision variable is identified as below, respectively:

$$\mathbf{x}_{unpowered} = \begin{bmatrix} \alpha & \sigma \end{bmatrix}^T \tag{5.12}$$

$$\mathbf{x}_{powered} = \begin{bmatrix} T & \epsilon_T & \psi_T \end{bmatrix}^T \tag{5.13}$$

in which α is the angle of attack, σ is the bank angle, T is the thrust magnitude, ϵ_T is the thrust elevation angle, and ψ_T is the thrust azimuth angle. It can be seen that for the powered vehicle, α and σ are left out as a guidance parameter. The vehicle follows a pre-defined α profile. The α value guides the longitudinal motion. Thus, the α profile influence the trimmability of the vehicle, as well as the distance covered. The goal is to choose an α profile in which the vehicle is always trimmable. Thus, not only it would be ensured that the trim constraint is fulfilled but also the dimensionality of the problem is reduced. As will be discussed in Section 5.2.4 and Chapter 7, this will be highly important when the simulation is run multiple times to discover and optimize the design space. Whereas, the covered distance can be controlled with the thrust parameters since the thrust elevation angle also influences the longitudinal motion.

In the meantime, the reference bank angle profile is obtained through literature on the flyback boosters (Tetlow, 2003, Naftel and Powell, 1993). During Phase 1, the bank angle profile is adapted such that the vehicle is performing a maneuver to roll around its x_B axis to orient itself correctly. Therefore, it is out of the inverted configuration and in the conventional re-entry configuration, such that the bottom of the booster is pointing towards the Earth. At Phase 2, the bank angle profile is adapted such that a turning flight is performed, within the limits of the g-load constraint. Finally, as Daimler-Benz Aerospace (1998) stated for FSSC-16, it is expected to have a cruise flight after Phase 2, around 15 km altitude.

At this point, the cruise condition has to be maintained to sustain a leveled flight and the desired heading angle. Due to couplings in the flight dynamics, especially the yaw and roll coupling, to control the heading angle the bank angle has to be controlled (Tetlow, 2003). Although a control system design is not carried out in this research, the bank angle history is commanded to the powered vehicle in the simulation. Thus, the system in the simulation assumes an ideal controller such that the commanded states are directly achieved by the vehicle. The required bank angle to maintain the desired heading angle is expressed as (Tetlow, 2003):

$$\sigma = k_{heading}\left[\left(-\arctan\left(\frac{\delta-\delta_t}{\tau-\tau_t}\right)-\frac{\pi}{2}\right)-\chi\right] \tag{5.14}$$

in which δ and τ are the latitude and longitude, respectively and the subscript t refers to the target point, which is the landing site, χ is the current heading angle and $k_{heading}$ is the controller gain. Usually, a precise tuning using eigenvalues which are defined through analyzing the free response of the vehicle. However, it is also possible to obtain a placeholder value through trial and error tuning method. Trial and error yields that $k_{heading} = 0.15$. Below each thrust parameter and their effect on the trajectory is explained thoroughly.

Note that, the flyback booster is equipped with four air-breathing engines that are planned to be used during the return flight. The thrust settings identified above represent the combination of all four engines. This simplification is performed to decrease the dimensionality of the design space, as well as the computational load. However, if controllability were to be covered in this research, it would be important to model each engine. Modelling each engine independently may allow for specific control strategies in which certain engines are inoperable while others are operable to assist the maneuver that is being carried out. Therefore, in case a control design has to be carried out for the flyback booster, each engine has to be accounted for separately.

5.2.4. Node Control Definition

Due to the complex flight dynamics of a flyback booster, it is not realistic to expect the steering parameters to be constant along the trajectory. In Section 5.2.3, it was discussed that the decision variables are defined at number of points. Thus, the aerodynamic angles and thrust parameters have to be re-defined along the trajectory to obtain a realistic simulation. This is achieved by a node control method. Each node contains a decision variable vector and is located at a certain point that is identified with an independent variable. For the unpowered booster, the independent variable is chosen to be the Mach number. However, for the powered flyback booster, the variables are lacking to show a monotonically increasing or decreasing trend for the entire flight, as it is depicted in Figure 5.6.

The flight time is one variable that is always increasing irregardless of the flight dynamics. However, flight time is not a suitable variable for the problem at hand, since the response characteristics of the simulation is unknown. This indicates that the final flight time is unknown and is dependent on the aerodynamic angles and thrust settings that are provided. To cope with this limitation other candidates are considered, such as Mach number, velocity, specific energy or flight-path angle. As a result, up until the end of Phase 1, the independent variable is identified as the flight-path angle γ, since it is constantly reducing until the peak altitude point. For Phase 2 and Phase 3, the independent variable is set to be the altitude. For instance, looking back at the reference trajectory in Figure 5.6, the independent variable change occurs around 80 seconds after the separation. Note that, in the simulation, the instant in which the independent variable change occurs is dependent on the value of the flight-path angle, not the flight time. Once within the limits of Phase 1, a zero flight-path angle is obtained, the independent variable is switched from flight-path angle to altitude, since a zero flight-path angle at this point is the peak point of the ballistic flight and from there onward the vehicle continues its descending return flight. By doing so, it is aimed to simulate the trajectory without any discontinuities in the thrust parameters.

For the powered vehicle, eight nodes are placed along the trajectory. The distance between each node is defined as the node height. The number of control nodes introduces a sensitivity to the optimization. Limited number of nodes are troublesome at identifying the nature of the dynamic solution, meanwhile, excessive number of nodes increase the dimensionality of the problem (Dijkstra et al., 2013). Consequently, this poses a problem for the performance of the optimization, as well as the convergence speed. Bilgen (2017) looked into combination of different number of control nodes and decision variables in a spaceplane re-entry optimization problem. The study concluded that 18 optimization variables are optimum. Since there are three thrust parameters at each node, this corresponds

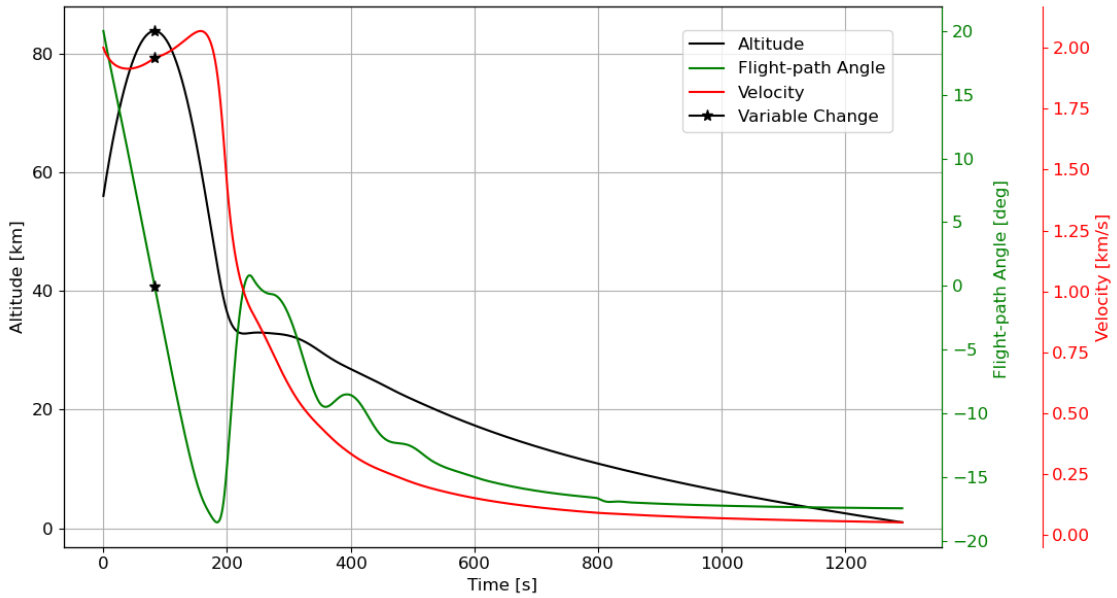

Figure 5.6: Powered trajectory history of possible independent variables for the node control method

to 6 nodes. Moreover, Bislip-Morales (2020) concluded that when there are phases included in an optimization, it is feasible to use 5 to 6 nodes to control each phase. Since Phase 1 is a relatively quick phase, due to the forces on the booster, it is decided to control this phase with 3 nodes. The remaining 5 nodes are placed along Phase 2 and Phase 3. Note that the third node of Phase 1 is placed at the peak point of the ballistic flight, to ease the transition between the independent variables. This approximately corresponds to 80 km, although note that the exact value is dependent on the thrust parameters at Phase 1. Rest of the nodes are placed depending on the altitude value of the final node. Literature suggests that around 10 km altitude the vehicle begins to control its altitude and bank angle to sustain the cruise conditions (Daimler-Benz Aerospace, 1998, Tetlow, 2003). According to Naftel and Powell (1993), small winged vehicles reach the TAEM phase around 7 km altitude. Therefore, the final node is placed on 10 km altitude to sustain the values up until the TAEM phase. Once the value of the third node and the final node is known, the remaining nodes are equidistantly placed along Phase 2 and Phase 3. This yields a node height of 14 km approximately.

Therefore, at each node the decision variables are updated by the values set in the full decision vector. To control the vehicle and make sure that a smooth reference flight profile is adapted, the nodes are connected with a Hermite spline interpolation. The range of the decision variables is identified in Table 5.2. Note that this range is a preliminary range as during the design space exploration, especially with one-at-a-time simulation, the range of each decision variable at each node is tuned more specifically. This will be discussed in more detail in Section 5.3.

Meanwhile, the preliminary aerodynamic angle ranges in Table 5.2 are obtained from reference missions and the thrust settings are obtained from the operational limits of the vehicle. Note that the bank angle range is significantly high. That is due to the fact that the bank angle convention is not mentioned. Often the bank angle convention could be mixed, indicating that a negative bank angle could induce a turn a right turn while a positive angle could induce a left turn, which opposes to the common convention. Therefore, an initial approach is made with a full range to identify the bank angle's sign convention during the one-at-a-time simulation of the unpowered vehicle.

Table 5.2: Preliminary decision variable ranges

Decision Variable	Minimum Value	Maximum Value	Units
Angle of Attack α	-10	40	deg
Bank Angle σ	-70	70	deg
Thrust Magnitude T	0	400	kN
Thrust Elevation Angle ϵ_T	0	50	deg
Thrust Azimuth Angle ψ_T	0	50	deg

5.3. Design Space Exploration Methods

Upon describing the problem, a process for analyzing the problem is introduced. A design space exploration is a significant pre-optimization process that is used to properly identify the design space. It focuses on observing the relationship and dependencies between different decision variables. A design space exploration is an essential process to understand the full capabilities of the vehicle and how these capabilities influence the trajectory. Through a structured analysis of the decision variables, it is possible to conclude that certain decision variables are ineffective. Consequently, the dimensionality of the problem would be decreased, easing the optimization process. In this section, the first Analysis of Variance (ANOVA) method is explained, which is a method for systematically analyzing the results of the design space exploration. Then, different design space exploration methods are explained in detail.

5.3.1. ANOVA

Design space exploration is an experimental process in which the design space is explored through variations in the decision variables. Numerous variations are performed to obtain a diverse set of results, or responses. To find the relationship between the decision variables and the response in a structured manner, ANOVA is used. This statistical approach is adopted to compare variances across the average of different groups to identify which factor group influences the response the most. Therefore, the results obtained from the design space exploration is meaningful through ANOVA.

The ANOVA is initiated by calculating the sum of square deviation from the mean $\bar{y}$ as below (Mooij and Dirkx, 2022):

$$S_T = \sum_{i=1}^{N} y_i^2 - \frac{T^2}{N} \tag{5.15}$$

in which y is a response, N is the number of experiments, $\frac{T^2}{N}$ is a correction factor, CF, in the magnitude of the sum of squares of individual responses. Whereas, the sum of squares is calculated as:

$$S_i = \frac{1}{n_L} \frac{\left(\sum^N y(x_i^+) - \sum^N y(x_i^-)\right)}{n_k} \tag{5.16}$$

in which n_L is the number of levels and n_k is the number of experiments at each of the levels. The sum of squares and the sum of square deviation from the mean are two important parameters that are used to calculate the individual contribution of a factor, such that:

$$P_i = \frac{S_i}{S_T} 100\% \tag{5.17}$$

in which P_i is the percentage contribution of a factor and is used to explain the contribution of that factor to the variability of the response. The error sum of squares is identified as:

$$S_E = S_T - \sum S_i \tag{5.18}$$

The error sum of squares is a value that is used to quantify the variability in the model that cannot be explained through the individual contribution of the current factors. If the error sum of squares has a high value, this indicates that there are lots of variations in the response that cannot be attributed to the factors that are accounted in the current model. Although the interactions between the factors

are not directly calculated by the ANOVA analysis, the error sum of squares represents the influence they have on the response. Therefore, ANOVA divides the total variability within the response to two main parameters: the individual contribution of a factor, which is also the explained variability, and the error sum of squares, which is the unexplained variance. Since the total variability has to be equal to 100%, the sum of these values should be equal to 100%. This is a simple, yet important, check that is performed to assess whether ANOVA is implemented correctly.

ANOVA is a statistical method for distributing the total variance into individual percentage contribution for each factor. Accordingly, it is possible to calculate the total variance, which is a square of the standard deviation, in the data set. The standard deviation is a quantity that is used to measure how much the values in a data set differ from the mean value of that data set. It is an indication, on average, how far the values lie from the mean value. The total variance and standard deviation provide additional information on the possible outliers. They are used to assess the quality and compare different data sets. The standard deviation is calculated as below:

$$\sigma = \sqrt{\frac{1}{N-1}\sum_{i=1}^{N}(y_i - \bar{y})^2} \tag{5.19}$$

5.3.2. One-at-a-time Simulation and Monte Carlo Analysis

Two design space exploration methods are used to identify the preliminary design space. These are: one-at-a-time simulation and a Monte Carlo analysis. One-at-a-time simulation is a simple analysis that is performed by observing the effect of varying only one decision variable on the trajectory. This is achieved by varying the decision variable in fixed discrete steps from minimum to maximum value while keeping the other decision variables at their nominal values to avoid extreme design cases. Identifying the effect of a single decision variable on the entire trajectory is the first step in understanding the decision variables and the trajectory. Since most likely there is a complex relationship between the decision variables and the trajectory, it is important to identify the basics.

Monte Carlo analysis serves the same purpose as one-at-a-time simulation. However, the decision variables are not varied in a structured manner. A Monte Carlo analysis randomly generates a decision variable set using a probability distribution, such as a random uniform distribution. Note that to ensure that the experiment is reproducible and the same decision variable can be obtained again, seeds are used to initialize the randomizer. Unlike a one-at-a-time simulation, during a Monte Carlo analysis, a few decision variables are varied at once. By doing so, it is focused to observe the impact of varying multiple inputs on a model's response. However, if there are large number of decision variables it is more likely to have interactions between different variables. Without any prior information on the model dynamics, only using Monte Carlo to identify the interactions could be time consuming. Since it is not a structured approach, to observe a proper relationship often many runs are required. This complicates the problem at hand since it is not trivial to know how many runs are enough. Furthermore, as the number of runs increased the amount of data to analyze also increases. Due to excessive data, the post-processing could be time consuming and difficult to analyze to derive coherent conclusions (Mooij and Dirkx, 2022).

For instance, for the powered flyback booster, there are 8 nodes and 3 thrust parameters for each node. This suggests that there are 24 factors. If a Monte Carlo simulation is run to analyze the whole decision space of 24 variables, it could be difficult to identify certain relationships. Since the sample space is significantly large and as more variables are introduced the interaction between the variables is also increased. Although a Monte Carlo analysis is a simple approach for providing an insight into the range of possible solutions, it is not the most suitable method for every design space.

5.3.3. Full and Fractional Factorial Design

Upon outlining the preliminary decision variable range through a one-at-a-time simulation, a need for a more structured design space exploration arises. In a full factorial design, all the decision variables, or the factors, are varied at the same time to study the interactions between factors. Given k number of factors, investigating all combinations at m levels is called a factorial design (Mooij and Dirkx, 2022). The minimum value m can get is two, indicating a minimum and a maximum value. A design with two levels would model the main effects and linear interactions via ANOVA. For instance, if there are 2 number of factors and 2 levels, then the possible combinations are: $(x_{1,min}, x_{2,min})$, $(x_{1,min}, x_{2,max})$,

$(x_{1,max}, x_{2,min})$, $(x_{1,max}, x_{2,max})$. Therefore 2^2, or in more general m^k, expresses the number of simulations to execute. Meanwhile, such a design is also expressed with a design matrix. In case there are 2 levels, minimum and maximum, with 2 factors, the design matrix is expressed as below:

$$L_4 = \begin{bmatrix} -1 & -1 \\ 1 & -1 \\ -1 & 1 \\ 1 & 1 \end{bmatrix} \tag{5.20}$$

in which -1 refers to the minimum and 1 refers to the maximum value of the factor. During the ANOVA analysis, each column has a percentage contribution. Since, columns are attributed to a factor, through ANOVA each factor's percentage contribution is calculated.

If quadratic effects are desired to be analyzed, the factors have to be varied over three levels, $m = 3$: minimum, nominal, and maximum. In that case, with k factors, the number of simulations to execute is 3^k. This suggests that, in a full factorial design all possible combinations of factor levels are tested. As the number of levels are increased, a wider range of potential conditions are captured. Consequently, with the captured conditions, there is a higher chance of observing the full variability of the response. However, if there are large number of factors, decision variables, there would be an immense number of combinations. For instance, regard the 24 factors of the powered flyback booster problem. Even only with 2 levels this takes $2^{24} = 16,777,216$ combinations. Even if each simulation takes one second, running all these combinations takes 195 days. Given the computational resources that would be spent while running all the combinations and the limited time allocated for this thesis, it is not possible to conduct a full factorial design for this research.

Nevertheless, it is possible to assess a subset of all possible combinations. Such a method is called the fractional factorial design. A fractional factorial design copes with the problem by selecting a subset of the factorial design space. However, the method combines certain factors and interactions into a single effect to be able to reduce the number of simulations. This introduces a confounding, which refers to the situation when certain effects cannot be distinguished from one another. The severity of the confounding effect is determined by the chosen design matrix.

During a fractional factorial design, orthogonal arrays are used as a design matrix. In an orthogonal array, all combinations of factor levels occur an equal number of times. For instance, if an L_{32} orthogonal array is used, then for each column there are 16 maximum values and 16 minimum values. Accordingly, the balancing property of the orthogonal arrays introduces a deliberate confounding to the factors. By doing so, all combinations of factor levels are not included which allows the run time to be smaller and results to be analyzed efficiently. In the meantime, orthogonal arrays assume that there are no interactions between the factors. Therefore, a factor is assigned to each column. If it is suspected that interactions are significant then the associated column within the orthogonal array has to be kept empty for a more coherent analysis. If prominent interactions are ignored, this could cause the result to be a poor representation of the response.

5.3.4. Fractional Factorial Design with Taguchi Interactions

In Section 5.3.3 it was discussed that the fractional factorial design does not account for interactions directly. Instead, through confounding analysis and comparing the error sum of squares, it is identified that there are interactions. Due to confounding, the interaction variances are confounded with certain factor variances. Thus, it is not possible to identify which factors are contributing to the interactions or which factors have high individual contributions. To cope with this problem, no factor should be assigned to columns that indicate interactions in the design matrix, as was mentioned in Section 5.3.3.

It is not an arbitrary decision to choose which columns to leave empty. The decision is related to the interactions and the level of confounding. This can often be assessed by an interactions table, which shows the confounded columns. The information obtained from the table is utilized to assign the factors to array columns in a structured manner.

Table 5.3: Interaction table for the L_8 array

	1	**2**	**3**	**4**	**5**	**6**	**7**
1		3	2	5	4	7	6
2			1	6	7	4	5
3				7	6	5	4
4					1	2	3
5						3	2
6							1

The interaction table for an L_8 array is presented in Table 5.3. Looking at the table it can be seen that the interaction between column 1 and column 2 can be found in cell (1, 2). The value in cell (1, 2) suggest that column 1 and column 2 are confounded with column 3. If decision variables A_1, A_2, and A_3 are assigned to columns 1,2, and 3, respectively, the interaction between A_1 and A_2 cannot be studied independent of A_3. If it is believed or suspected that the interaction between A_1 and A_2 is significant then the dependence should be broken by not assigning any factor to column 3. This decreases the confounding and allows the main effects to be analyzed more efficiently.

The amount of confounding in a design matrix is identified with a resolution value. When the matrix is constructed such that it is free from all confounding between the two-way interactions and the main interactions, this array is referred to as a Resolution V array. Meanwhile, a Resolution IV array has some two way-interactions confounded with other two-way interactions and a Resolution III array has two way-interactions confounded with main effects (Fowlkes and Creveling, 1995). By assigning a resolution value to design matrices, it is possible to have a general overview of the amount of confounding, without a detailed analysis.

The type of design matrix that is used for the analysis is dependent on the number of factors that are analyzed. For the problem at hand, 24 decision variables are used to alter the trajectory. Although the fractional factorial design reduced the dimensionality, compared to a full factorial design, assigning 24 parameters to analyze them with minimal confounding would require a significantly large array. Not only this would again increase the computational time but also would introduce complexity in the code as the interaction tables are constructed manually in the simulation since there are no publicly available libraries that provide these tables. In terms of computational and coding intensity, an L_{32} matrix with Resolution IV is chosen as a feasible option.

In this array, as depicted in detail in Appendix A, seven factors are introduced with certain two-way interactions confounded. This indicates that the 24 decision variables have to be analyzed in subsets of 7, the results will be discussed in detail in Section 7.4. The factors are assigned to columns 1, 2, 4, 7, 8, 16, and 29. While the percentage contribution of these columns represents the main effects, the rest of the columns represent the interactions. Note that within the rest, columns 3, 5, and 6 are the columns that have confounded interactions. Knowing the exact distribution of the interactions, an analysis can be performed in a more structured manner. However, if interactions with high impact are represented in columns 3, 5, and 6, then there could be a confounding effect that has to be regarded. This can be assessed by swapping the column location of factors within a subset. Therefore, if factor A is assigned to column 1, in the next round factor A is assigned to column 16 while keeping the same factors but also changing their column location. If the original subset and the column-swapped subset yield similar amount of percentage contributions, then it can be concluded that the subset is not suffering from any confounding effects.

6

Simulation Environment

In Chapter 5, it was identified that a trajectory design is carried out. To achieve this objective, a simulator is required. In this chapter, the simulation environment that is developed and used in this study is identified. First in Section 6.1, the preferred software language is presented. In Section 6.2, the fundamental simulation structure is presented.

6.1. Software Language

Creating a trajectory simulation is the first step of a detailed mission design. NASA and ESA use accurate trajectory simulation tools, such as Program to Optimize Simulated Trajectories (POST) to achieve this first step. POST is an optimization software that has the capability of optimizing ascent, on-orbit, and re-entry trajectories for multiple objectives while accounting both equality and inequality constraints. However, these fully developed simulation tools are often not commercial. Meanwhile, the commercially available trajectory simulation software are limited by the vehicle models and capabilities, since they are developed for aircrafts. Therefore, it is essential to develop the trajectory simulation manually, using the desired vehicle and atmospheric properties.

This can be achieved by using various languages such as C++, Python, and MATLAB. However, the trade-off between the most appropriate language is made regarding the performance of the each programming language, availability of packages, and familiarity with the language.

C++ often has a rapid execution, since it is a compiled language, meaning that it is comparably faster than Python. Generally, this characteristic makes a significant difference when 3D simulations are programmed. Since the trajectory simulation is prior to the flight and is not real-time, the computational speed is not a critical factor.

Not only the computational performance and familiarity, but the availability of libraries and toolboxes are also an important point to regard. Both C++ and Python are compatible with TU Delft Astrodynamics Toolbox (Tudat). The library is often used to simulate astrodynamic problems using a wide variety of environment and propagation set-ups. A few example use cases for Tudat are: creating a state estimator, analyzing a preliminary mission, or designing a guidance model. Tudat has been developing frequently with new updates. Upon release of the new updates, it is ensured that all the components within the library are verified and passed the unit and system tests (Tudat Space, 2022).

Tudat is compatible with Parallel Global Multiobjective Optimizer (PaGMO) by ESA. The library is also known as PyGMO in Python and it provides access to various local and global optimization algorithms. Additionally, Python has various toolboxes that are available for trajectory optimization and mission analysis, such as Orekit or Astropy. This is advantageous, since in certain cases, other toolboxes can be used for verification of certain code blocks, to ensure that the libraries are not inconsistent.

Finally, familiarity with the language is an important aspect. Although C++ could be beneficial in terms of computational effort and time, the duration of this study is not sufficient to learn a high-level new programming language from scratch. Therefore, during this study, the main programming language is identified as Python, while using Tudat as the main astrodynamics toolbox, and PyGMO as the optimization library. It is important to note that there are certain limitations associated with Tudat, especially regarding the available environment model and guidance models. However, the library has

the flexibility of creating custom models, allowing the environment or propagation to be manipulated in the desired manner. An additional advantage of Tudat is that the library has an active online community. This indicates that in case of encountering unexpected errors in the library, one can seek guidance through this community.

6.2. Software Architecture

The complete software is a combination of three simulations. These are: the trajectory simulation, design space exploration and optimization. For the purpose of this study, the trajectory simulation is always run together either with the design space exploration or optimization. The output of the trajectory simulation, which is the objectives and constrains, are used within the design space exploration or optimization to guide the design towards regions that are desired. In the meantime, certain inputs are provided through the design space exploration and optimization to initiate the trajectory simulation. Note that, since using the design space exploration and optimization does not alter the working principle of the algorithm significantly, in the top level architecture the optimization is selected to explain in detail. Meanwhile, the design space exploration is explained in detail separately.

The goal of this section is to explain the interaction between each model to understand the overall software. To achieve that, first the top level architecture of the software is presented. Then both the Tudat models and the newly developed models are explain in more detail.

Top Level Architecture

The top level architecture is first presented to provide an overview of the complete software, which includes various models to simulate a fly back trajectory. In Figure 6.1 the top level architecture is depicted. At the beginning of the software, certain parameters are input to the trajectory simulation. These parameters are:

- Initial state
- Vehicle type: Powered or unpowered vehicle
- Decision vector
- Node height
- Integration time-step
- Trim activity
- Termination time
- Termination velocity
- Termination altitude

All the above inputs are a user-defined parameters and can be altered manually. For the decision vector an exception can be made, such that the value of the decision vector is not user-defined but defined through the design space exploration or optimization algorithm. As visualized in Figure 6.1, upon initiating the software, a random initial decision variable list is generated through the optimization algorithm. This is the very first set of aerodynamic angles or thrust parameters for the first population.

For each trajectory, the software runs a guidance algorithm that inputs the decision vector and integrates the commanded parameters to the vehicle. Therefore, the guidance model acts as a bridge between the trajectory simulation and optimization, or design space exploration.

Upon obtaining the aerodynamic angles or the thrust parameters for the current instant in time, the information is sent to the vehicle model. The model updates the vehicle properties such as the deflection angles of the control surfaces or the engine to deliver the values that are requested by the guidance system. It is significant to note that, in this study, it is assumed that the booster has an ideal control system. Since no delay in control surface deflection is simulated within the software, the actual attitude of the vehicle is equal to the commanded attitude. Once the vehicle model is created, the information is sent to compute the external forces. Within this block, not only the aerodynamic forces but also the gravitational force from the environment and, if applicable, the thrust force is calculated. This information is then fed into the propagation block to propagate the current state to the next time step. The propagation block iterates until a termination condition is reached. This concludes the explanation of the trajectory simulation block in Figure 6.1.

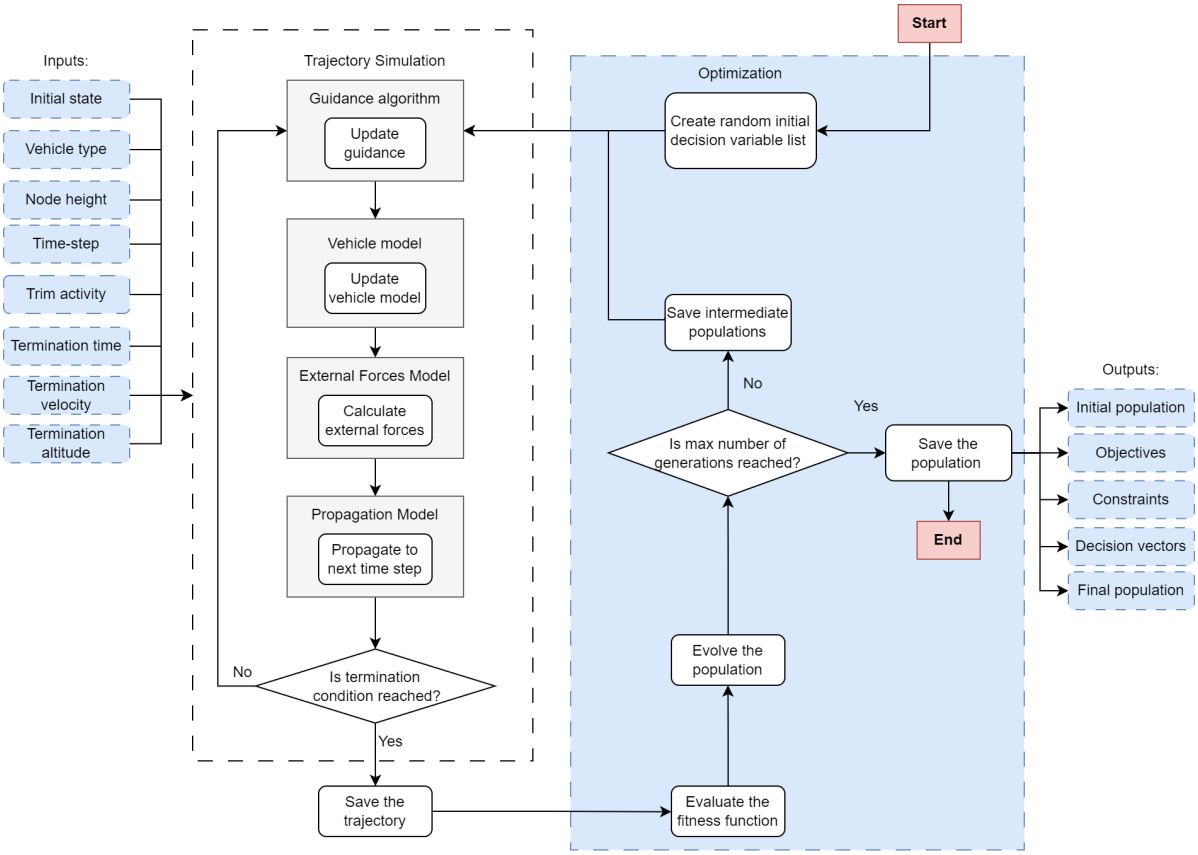

Figure 6.1: Top level software architecture of the trajectory simulation and the optimization

However, once a trajectory simulation is ran for every individual in a population, the values obtained from the simulation are fed into the optimization to evaluate the fitness function. Depending on the value of the fitness function and the selected optimization algorithm, the population is evolved to the next generation. For this new population the trajectory simulation is re-initiated. This suggests that the initial conditions, the control surface deflections, and the attitude of the booster is set to their original values. The cycle is terminated once the maximum number of generations are obtained. To avoid data clustering, only the complete trajectory history of the first and the last population's individuals are saved. For the rest of the individuals, only the objective values, constraints, and decision variables are saved.

Note that the top level architecture is presented with an optimization simulation. When the fractional factorial design analysis is conducted, instead of the optimization simulation block in Figure 6.1, the design space exploration model is implemented. The design space exploration model and the trajectory simulation components, which are the external force model, propagation model, and guidance model, are explained in detail below.

Environment Model

The environment model simulates the properties that were discussed in Chapter 3. The model includes an atmosphere model, Earth's shape, rotation and gravity model. There are variety of options for the shape, rotation and gravity models. Among the existing models, the right ones are implemented. However, the US76 atmosphere model is not available in Tudat. Yet, the library had a custom function to implement any atmosphere model that is in a look-up table format.

External Forces Model

The external forces are the driving parameters that influence the trajectory of the booster. The following forces are considered in the simulation:

- Thrust force in the propulsive reference frame
- Drag and lift force in the aerodynamic reference frame

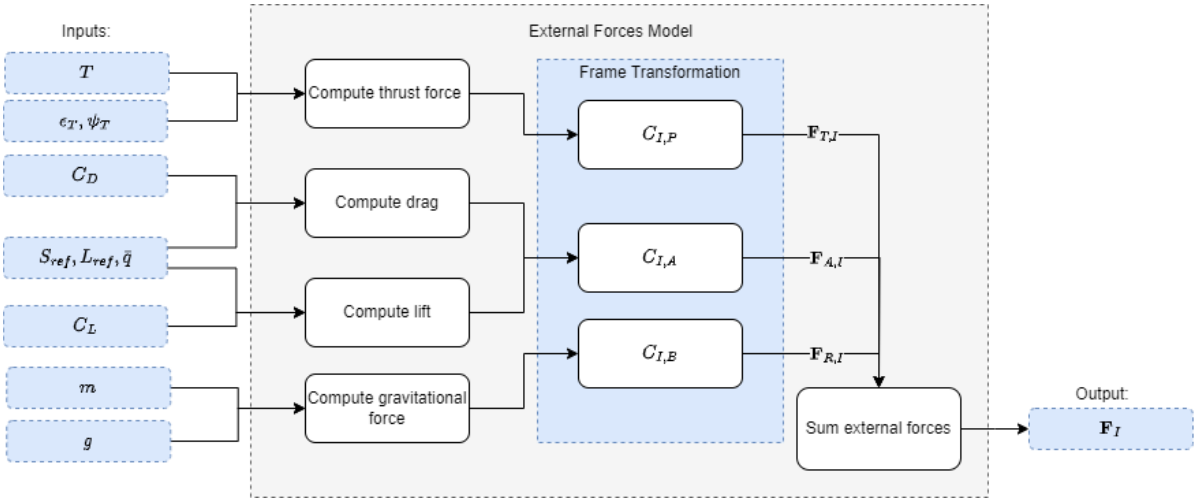

Figure 6.2: External forces model architecture

- Gravitational force in the rotating reference frame

It is of utmost importance to regard that each force is calculated in its reference frame. However, since the propagation is performed in the inertial reference frame, J2000, a frame transformation is performed before the external forces are calculated, which is also in the inertial reference frame and hence the subscript I. The gravitational force acting on the vehicle is a function of the current mass of the booster and the gravitational acceleration, which is dependent on the chosen gravity model. For the powered vehicle, the thrust force is calculated depending on the thrust parameters, which are provided through the decision variable vector and interpolated inside the guidance algorithm. On the other hand, for the unpowered vehicle, the thrust parameters are equal to zero. Consequently, the thrust force is equal to zero. In that case, the aerodynamic angles are defined through the decision variable vector. Using the current independent variable, Mach number for the unpowered vehicle, the decision variables are interpolated and updated inside the guidance algorithm.

The aerodynamic coefficient database for the booster's main body is provided as a function of the angle of attack and the Mach number, whereas, the aerodynamic database for the control surfaces is provided as a function of the angle of attack, Mach number, and deflection angles. At each instant in time, the current angle of attack and Mach number are determined by the simulation which are fed into the aerodynamic database to obtain the current aerodynamic coefficients by a linear interpolation. Once the coefficients are obtained, they are fed into the external force model to calculate the aerodynamic forces, using the reference length L_{ref} and the reference area S_{ref}, and the dynamic pressure $\bar{q}$.

Propagation Model

The forces obtained in the external forces model are input to the propagation model as well as the user defined fixed time-step, and current state. Note that for the powered vehicle the mass rate is also input to the model since the mass of the vehicle is also propagated as fuel is consumed. The forces acting on the vehicle and the corresponding equations of motion were identified in Chapter 4. Although it is possible to solve the equation of motion with analytical means, the numerical approaches are preferred. In case of a complex behavior and non-linearities, it is not possible to obtain an analytical solution without approximations, which simplifies the model and the complex behavior. Meanwhile, a numerical propagation provides high-fidelity solutions that accurately represent the physical forces on the vehicle. Consequently, the solution to the equations of motion is approximated using discrete time steps, as depicted in Figure 6.3. At each time step, the Runge-Kutta 4 integrator is used to calculate the equations of motion and the current state. The general form of the numerical propagation is expressed as below:

$$\dot{\boldsymbol{x}}(t) = \boldsymbol{f}(\boldsymbol{x}, t) \tag{6.1}$$

in which $\boldsymbol{f}(\boldsymbol{x}, t)$ represents the dynamics of the system, $\boldsymbol{x}$ is the state vector, $\dot{\boldsymbol{x}}$ is the state vector derivative, and t is the time. The initial condition of the above equation is expressed as:

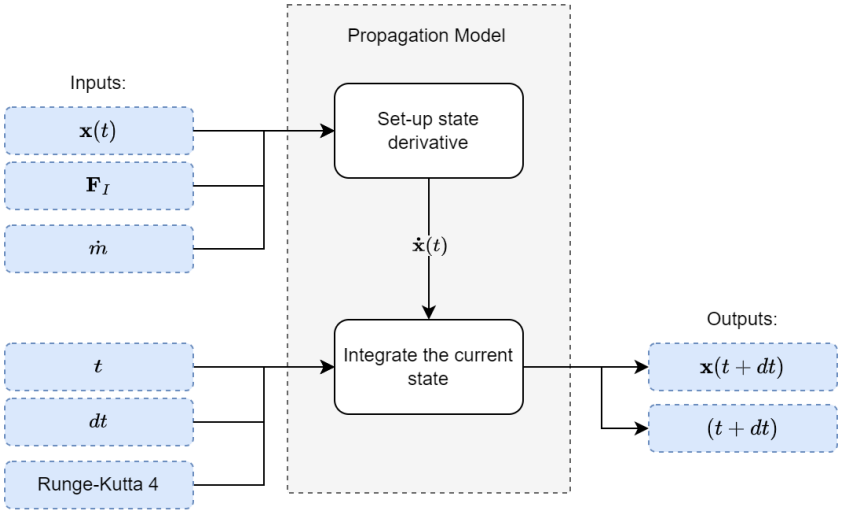

Figure 6.3: Propagation model architecture

$$\boldsymbol{x}(t_0) = \boldsymbol{x}_0 \tag{6.2}$$

Note that for the problem at hand, the $\boldsymbol{x}$ contains the mass, the position and velocity in the inertial reference frame. Whereas, the state derivative $\dot{\boldsymbol{x}}$ contains the mass rate, the velocity and acceleration in the inertial reference frame and the mass rate.

Guidance Algorithm

For a more coherent understanding of the guidance block, the architecture of the algorithm is presented in Figure 6.4. Within the guidance algorithm, the update guidance function is highlighted. This function runs at each time step. On the other hand, the blocks outside of this function are executed only once, when the guidance algorithm is called for the first time in the simulation.

When the guidance algorithm is called inside the simulation, the decision variables vector, which is a set of guidance parameters at each node, is provided in the simulation. Using this decision variables vector and the initial independent variable, the algorithm first decides on the type of vehicle that is currently flying. The algorithm needs to distinguish the two vehicles from one another, as there are two sets of dictionaries for the powered vehicle due to the presence of two independent variables. This was identified in detail in Section 5.2.4. For the algorithm shown in Figure 6.4, powered flyback booster characteristics are adapted. Nevertheless, for the unpowered flyback booster the algorithm operates in the same manner, except instead of thrust parameters, the aerodynamic angles are interpolated.

Once the decision variables vector is provided, the dictionaries and corresponding Hermite spline interpolation functions are created. The entries of the dictionary contain the corresponding parameter from the decision vector, whereas, the keys of the dictionary represent the independent variable. In between each node, the values are interpolated using a Hermite spline interpolation. These two parameters are then provided as input, indicated with the dashed-blue arrows, to the update guidance function to interpolate the thrust parameter dictionaries. The interpolated values are the thrust parameters for that instant and are used to update the vehicle.

In the meantime, there is an active trim algorithm inside the update guidance function. This algorithm inputs the aerodynamic database and the current angle of attack α and Mach number M to calculate the deflection angles δ required to fulfill the trim condition. The calculation is performed at each time step. In between the time steps, the deflection angles are interpolated linearly. The obtained angles are fed to the vehicle model to update the values from the previous time step.

Design Space Exploration Model

The design space exploration is an integral part of this research. It is significant to note that the design space exploration is performed as an independent simulation. However, the components and the way each component interact with each other in the optimization simulation and the design space exploration simulation are identical. Since the optimization model is briefly discussed in the top-level

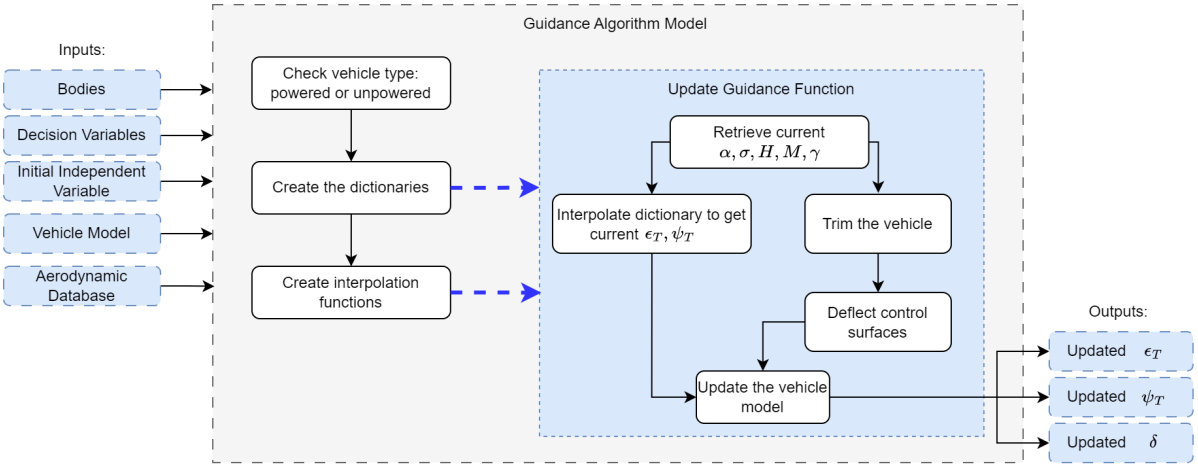

Figure 6.4: Guidance algorithm architecture

architecture, as visualized in Figure 6.1, the design space exploration model is discussed here in detail. The model has certain user defined inputs, depending on the type of design space exploration that wants to be conducted. In a more general sense it is possible to choose either a Monte Carlo analysis or a fractional factorial design analysis. In Figure 6.5, the design space exploration model for the fractional factorial design study is depicted. First, the user defines the number of levels and number of factors that are assessed in the fractional factorial design. These inputs are used to create the design matrix. Afterwards, the main columns are defined by the user. The defined main columns identify the resolution of the array. As was discussed in Section 5.3.4, looking at the Figure A.1, when a resolution IV is required in an L_{32} array, the main columns are column 1, 2, 4, 7, 8, 16, and 29. Therefore, a subset method is adopted and seven different decision variables are assigned to this design matrix. The decision variables that are not assigned to a column are fixed to their nominal values. Once a column is assigned to each decision variable, the decision vector is fed into the trajectory simulation. Within this trajectory simulation, the guidance algorithm interpolates the decision variables and updates the vehicle properties accordingly. Finally, the complete trajectory history is obtained through the propagation model.

The trajectory history contains all the information regarding the trajectory. This includes the altitude, velocity, and bank angle profiles as well as the objective and constraint values for that trajectory. All this information is then used in the ANOVA analysis, which is a crucial post-processing method for identifying the influence of the chosen decision variables on different objectives and constraints. Upon choosing the response that is being analyzed, the percentage contribution of the individual factors and interactions, standard deviation, variance, and error sum of squares are calculated. Later on, a visual inspection is performed to assess the influence of the variables, as it will be discussed extensively in Section 7.4.

Developed Functionalities

A few of the components that are used in this simulation are developed and integrated from scratch. In Table 6.1 an overview of all the models is presented. The newly developed algorithms are verified with the methods that are presented in Section 6.3.

First of all, the chosen atmospheric environment was not readily available in the library. However, Tudat had the functionality of implementing a user-defined custom atmosphere model. The US76 atmosphere model is provided as a look-up table, which is later on interpolated by the environment module as a function of altitude. Therefore, using the current altitude of the booster the density and temperature at that point are calculated continuously. Secondly, the trim algorithm was also written from scratch. At every time step, the trim algorithm inside the update guidance function checks whether the vehicle has the aerodynamic capabilities to trim at that Mach number M and angle of attack α. If a vehicle is not trimmable for a certain amount of time, this duration raised the path error RSS. Finally, the fractional factorial design code for the design space exploration is developed without any reliance on publicly available libraries or templates. This was performed to make sure that the design matrices

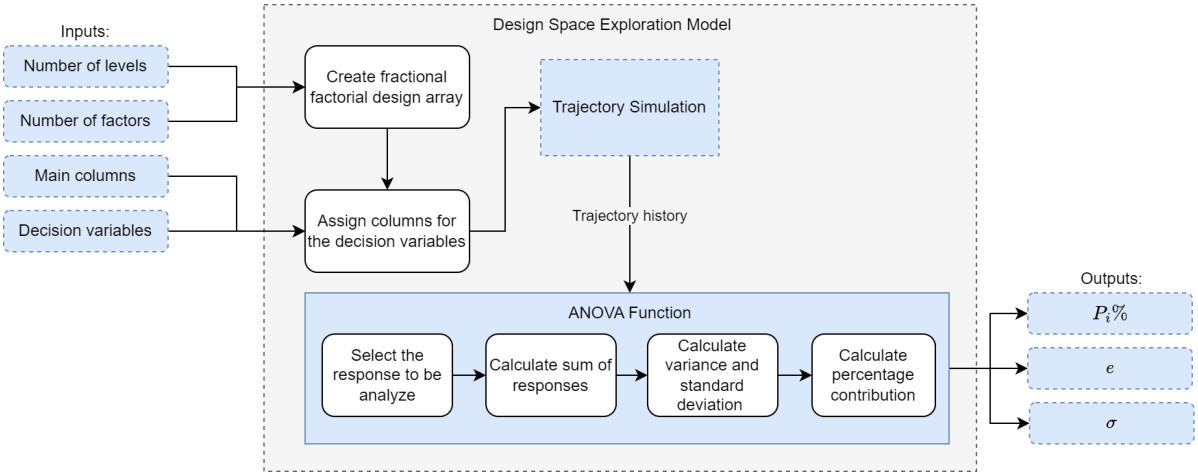

Figure 6.5: Design space exploration model architecture

Table 6.1: Overview of the developed functionalities

Tudat	New
Environment model	Atmospheric database
External force model	Trim algorithm
Propagation model	Guidance model
	Design space exploration model

are correctly implemented. Since there are no verified libraries that are publicly available, it is decided to write this code from scratch using the tables provided by Fowlkes and Creveling (1995).

6.3. Software Verification

The simulation model is prone to certain limitations, primarily due to the fact that a real life scenario can be simulated with certain approximations. Nevertheless, often software bugs cause the simulation to have additional limitations. To ensure that these limitations are minimized, and a trajectory is simulated as accurately as possible, a software verification process is followed. The simulation blocks are systematically examined and executed to identify any unexpected behaviors. This is performed across different levels, such as the unit tests, integration tests, and system tests.

6.3.1. Unit and Integration Tests

A unit test is a software test that aims to assess the smallest building blocks of the code, such as functions and classes. It is essential for any software development as it identifies the bugs at early stages and allows the code to be structured properly. In Section 6.1, it was briefly mentioned that Tudat is a verified library. Therefore, independent from the verification performed in this thesis, the developers of the library verified Tudat through unit tests and system tests. Furthermore, Tudat has also been used in various research projects (Dirkx et al., 2016, Kumar et al., 2015, Dirkx et al., 2019). For the rest of the development process, the functions of Tudat are assumed to be correct and not verified in this study, unless the analysis of other components indicates that there is a conflict. In that case, the Tudat function is reviewed in more detail and if needed the developers are contacted through the online community. The components of the simulation that are tested and the corresponding unit tests are explained below.

Aerodynamic Coefficients

The aerodynamic coefficients are provided as an aerodynamic database for the simulation. The aerodynamic interface model is then defined by the user-defined aerodynamic coefficients file. Since an aerodynamic database is usually a function of two variables, Mach number M and angle of attack α, the file is tabulated with respect to these independent variables. Meanwhile, the coefficients of the

aerodynamic control surfaces are defined as a function of three independent variables, Mach number M, angle of attack α, and deflection angle δ. This complicated the matter as the coefficients file had to be structured in a proper manner so that at the desired M, α, and δ, linear interpolation is used to correctly interpolate the table. To ensure that, throughout the development process of the aerodynamic interface, a unit test is implemented by terminating the simulation after a few seconds of propagation and checking the aerodynamic coefficients from the table manually using the current independent variables. This is performed for different instants along the trajectory to ensure that at all instants the coefficients are identified correctly.

Initial Conditions and Attitude

During the design space exploration and optimization, multiple individual simulations are run continuously. To ensure that each simulation is independent from one another, the vehicle and trajectory settings has to be re-set to their original initial value after the each simulation. A unit test is implemented to compare the initial conditions of each simulation, independent from the correctness of the rest of the simulation.

Thrust Parameters and Engine Model

A similar issue to the one above is identified for the engine parameters. After the booster with aerodynamic capabilities is developed, the engine model is integrated to the simulation. To ensure that the engine can deliver the input parameters, such as thrust force, a unit test is performed. First a fixed thrust magnitude, with fixed thrust angles are provided. Afterwards, thrust force in the body-fixed reference frame is plotted. Finally, the same test is run by changing the thrust parameters to time dependent functions. This also provided the integration with the guidance algorithm since the update guidance functionality provided the thrust parameters at each instant. The resulting thrust force is again plotted in the body-fixed reference frame. This ensured that the thrust parameters that are defined in the simulation provide coherent results with the body-fixed reference frame, in terms of direction of the thrust vector and the magnitude. An example case it set by providing a fixed thrust of 400 kN with $\epsilon_T = 60°$ and $\psi_T = 35°$. Using the equations in Equation 2.4, the expected values of thrust, in kN, is calculated as below:

$$\begin{aligned} T_x &= 400 \cos 60° \cos 35° = 163.83 \text{ kN} \\ T_y &= T \cos 60° \sin 35° = 114.72 \text{ kN} \\ T_z &= -T \sin 60° = -346.41 \text{ kN} \end{aligned} \tag{6.3}$$

The output concluded that the values obtained from the equation are same as the values obtained from the simulation. Note that since the propagation is performed in the inertial reference frame, the acceleration values obtained are also in the inertial reference frame. To obtain the thrust parameters in the body reference frame a frame transformation is performed. Once, the inertial to body transformation matrix is saved as an independent variable in the simulation, for each time step, the frame transformation below is performed:

$$\boldsymbol{T}_B = \boldsymbol{C}_{B,I} \boldsymbol{T}_I \tag{6.4}$$

in which $\boldsymbol{C}_{B,I}$ is the transformation matrix from inertial to body reference frame, $\boldsymbol{T}_B$ is the thrust vector in the body reference frame and $\boldsymbol{T}_I$ is the thrust vector in the inertial reference frame. $\boldsymbol{T}_I$ is calculated using the thrust acceleration and the current mass as below:

$$\boldsymbol{T}_I = m \boldsymbol{a}_{T_I} \tag{6.5}$$

Note that Tudat has a custom function for saving the transformation matrices, such as $\boldsymbol{C}_{B,I}$. Since the matrix is obtained through Tudat, the calculations used to obtain $\boldsymbol{C}_{B,I}$ have already been verified. Nevertheless, the above test showed that the value calculated in Equation 6.3 was equal to the $\boldsymbol{T}_B$ value that was calculated using Equation 6.4. Upon this observation, it is confirmed that the transformation matrix is adopted correctly.

Trim Condition

In Section 2.2.4 it was discussed that an algorithm is developed to trim the vehicle throughout the trajectory. As long as there is a database present, the trim algorithm operates. Since this algorithm is developed from scratch, it is important to verify it.

A unit test is performed to verify that when the trim is active, the total pitch moment coefficient C_m of the vehicle is indeed equal to zero. The test is implemented by providing a different angle of attack α profile to the vehicle. For each of the α profiles, first the deflection angles are analyzed. It is investigated whether the body-flap δ_b and elevon δ_e are deflected within their limits. It is also observed whether elevon deflection is initiated once the Mach number M is below 5. Once it is confirmed that the control surfaces are deflected in a desired manner, C_m of the vehicle is checked. Observing that the value is equal to 0 for various α profiles, it is concluded that the trim algorithm can fulfill the trim condition. The algorithm is also tested by adapting the vehicle and aerodynamic database to match with the HORUS' values, as it was discussed in Section 2.2.4. The results indicate that the trim algorithm is applicable for the other M and α profiles as well.

As it was observed from the guidance logic in Figure 6.4, the trim algorithm runs inside the guidance algorithm. The current flight conditions M and α, are determined by the guidance algorithm. Once these values are updated, the trim algorithm calls the updated values to calculate the trim condition for the current instant. An integration test is performed to assess the relationship between the two algorithms. The test is performed by outputting the updated M and α different instants in time. Next, the C_{m_0} that is used inside the trim logic is printed. Finally, it is checked whether the C_{m_0} that is used inside the trim logic corresponds to C_{m_0} that is obtained by using the look-up tables. By doing so, it is aimed to check whether the trim algorithm correctly extracts and uses the updated M and α. Consequently, it is verified that the trim algorithm is integrated correctly with the guidance algorithm.

Interaction Tables in Taguchi Designs

Taguchi design is a method that is often adapted in design space exploration. The idea behind the method is based on selecting the most likely interactions. As it was explained in more detail in Section 5.3.4, the interaction tables based on the Taguchi design is adapted to study the main effects and interactions in a controlled manner. To implement the method, an orthogonal array is constructed. Factors are assigned to certain columns of the array. However, if a factor is randomly assigned to a column, there is a high probability it is confounded with another factor. This cases the interactions or the main effects to be impossible to observe or interpret.

A Resolution IV array had to be constructed to observe the two-way interactions that are confounded with some other two-way interactions but not the main effects (Fowlkes and Creveling, 1995). Note that the complete overview on the Resolution IV array that is implemented in this study can be found in Appendix A. It was not a trivial task to automate the array generation and column assignment. Therefore, both of these tasks are performed manually. Once, the L_{32} Resolution IV array is constructed, unit tests are implemented to ensure that the correct decision vector is assigned to the correct column. This is performed by randomly selecting a set of columns and inspecting whether the column value (-1 or 1) match with the decision vector that is assigned to that column. Once it is ensured that the table is implemented correctly, the post processing results are more coherent as the main effects and interactions are much more observable.

6.3.2. System Test

Once it is identified that different code blocks have been developed correctly, the overall output and performance of the simulation is assessed. This is performed via a system test. The test is conducted by running a complete trajectory simulation with the HORUS vehicle. It is aimed to verify that once the correct input is provided, the simulation can be used to simulate different vehicles and trajectories accurately. In order to assess this it was crucial to use a trajectory with a complete test or simulation data, hence HORUS is a suitable candidate for the task. The unpowered vehicle simulation is then fed with the aerodynamic coefficients and vehicle properties, such as size and mass, of the HORUS vehicle. The initial state that is input to the simulation and the final state that is obtained as the output is presented in Table 6.2.

The graphical comparison with the results in the literature suggested that the two trajectories are comparable, as depicted in Figure 6.6 and Figure 6.7. A small level of disturbance can be identified in the altitude-velocity plot between velocity of 6-7 km/s. As it is visualized in Figure 6.8, at this point,

Table 6.2: HORUS reference trajectory verification

Property	Symbol	Initial Value	Final Value	Units
Altitude	h	122	25	km
Velocity	V	7435.5	645.9	m/s
Latitude	δ	-22.3	4.73	deg
Longitude	τ	-106.58	-54.54	deg
Flight-path Angle	γ	-1.43	-8.95	deg
Heading Angle	χ	70.75	79.5	deg

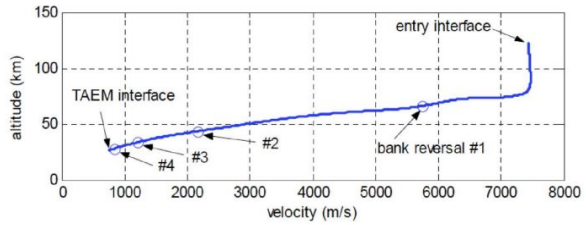

Figure 6.6: Horus reference trajectory from literature (Mooij, 2016)

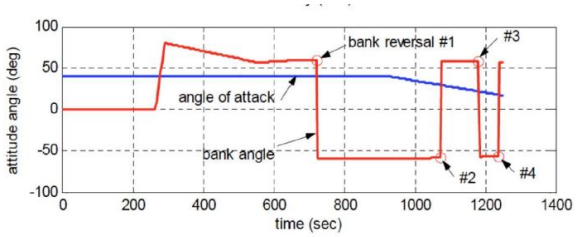

Figure 6.7: HORUS nominal control history from literature (Mooij, 2016)

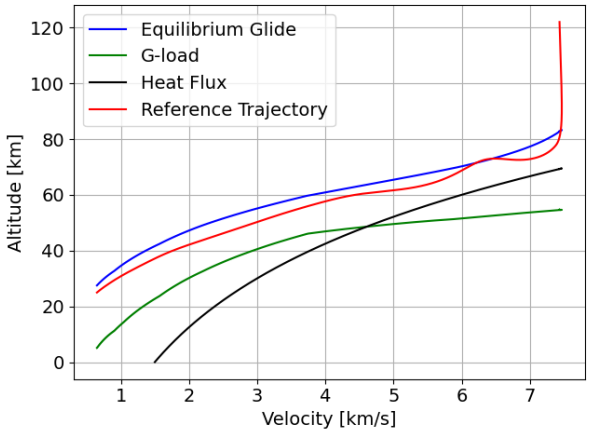

Figure 6.8: Horus reference trajectory with the entry corridor

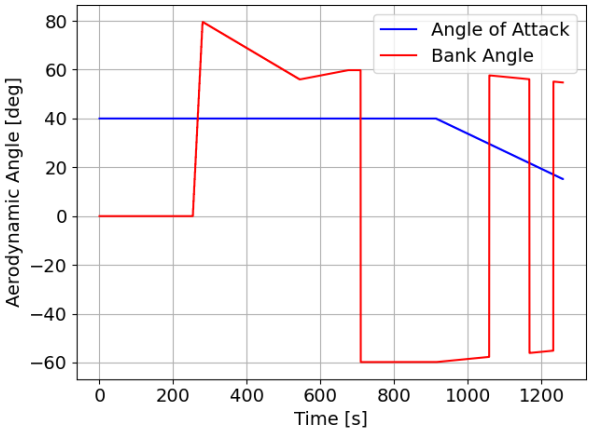

Figure 6.9: HORUS nominal control history from the simulation

the trajectory coincides with the equilibrium glide constraint. It is concluded that this could be due to the difference in the control methodology. Meanwhile, in Figure 6.9 the nominal control history that is fed to the simulation is presented. To calculate the re-entry corridor, the maximum heat-flux is set as 500 kW/m^2 and the maximum g-load is set as 3g. Finally, note that another system level test was conducted in Section 2.2.4, in which the trim algorithm was tested using the HORUS aerodynamic database.

7

Design Space Exploration

A design space exploration aims to provide insights into the relationship between the design variables and how this relationship affects the overall result. Therefore, to have a coherent understanding of the optimization results, it is essential to conduct a design space exploration. Although there are various design space exploration methods, as was identified in Section 5.3, the choice of method is problem dependent. This chapter focuses on different experiments and methods that are implemented to identify the most applicable design space exploration method. Since several different results are discussed throughout the chapter, in Section 7.5 a summary and the overview of the main findings are presented.

7.1. Unpowered: One-at-a-time Simulation

As was identified before, a limited insight is provided on the trajectory of the booster. To obtain a better understanding of the vehicle capabilities and the booster trajectory, a one-at-a-time simulation is performed. During this simulation, bank angle σ is varied only once, from its initial value that follows from the first phase, and kept constant for the entire trajectory. To observe the effect of changing the angle of attack α, the angle of attack profile is first set to be equal to deliver the maximum L/D ratio. And then a sensitivity analysis is performed by varying the angle of attack around its neighboring values to see how it affects the trajectory.

To begin with, looking at Figure 7.1, when the angle of attack is set to deliver values for the $(L/D)_{max}$ the varying bank angles have different effects on the trajectory. Too low bank angles cause the vehicle to skip while increasing the flight time. The skipping flight is induced by the vertical component of the lift force. Therefore, to control the skipping flight, the lift has to be tilted away from the vertical plane. In other words, a bank angle has to be introduced. From the graph below, it can be interpreted that the bank angle within the range $[-40°, 0°]$ are not sufficient to control the lift force and tilt it sufficiently away from the vertical plane. Note that the reason why the trajectories with these σ values have a flight duration much higher than the others is that they fail to comply with the main termination condition, which was the desired heading angle of $-70°$. As can be seen from Figure 7.2, these first five trajectories struggle to provide the turn maneuver. Therefore, the trajectory is terminated by the Mach number condition, which was a Mach number below 1, before the desired heading angle is achieved.

In Figure 7.3, the value of the first objective across different σ values is depicted. Considering the latitude and longitude histories of the first five trajectories, it is reasonable to observe high final distance-to-go values, which are around 14°. These trajectories fail to execute a turn maneuver, especially the first two trajectories with $\sigma = -10°$ and $\sigma = 0°$. Consequently, the vehicle flies away from the target point and the distance to the landing site keeps increasing. Furthermore, due to the high turn radius that yields from the low σ values, the desired heading angle cannot be achieved. On top of a natural increase in the final distance-to-go, the distance-to-go objective is also penalized as the desired heading angle is not achieved.

Meanwhile, in Figure 7.4, value of the second objective across different σ values is visualized. At this point, it is significant to note that the path constraint error is a hard constraint. Thus, the value of this objective has to be equal to zero, else the vehicle would not be in the re-entry corridor, which is not

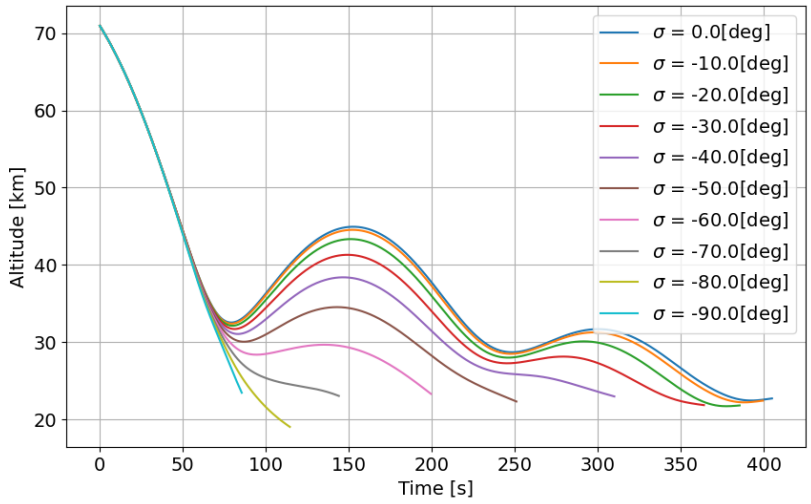

Figure 7.1: Altitude history for various bank angle magnitudes

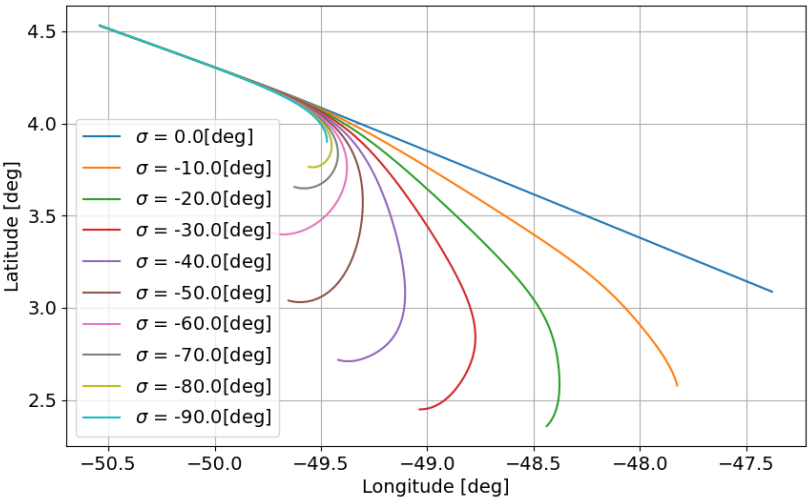

Figure 7.2: Latitude and longitude history for various bank angle magnitudes

desired as it would pose structural and operational challenges for the vehicle. Therefore, when the first half of the bank angle values are observed, it can be seen that the value of the objective varies between 10 to 20. When the path error RSS is segmented, it is identified that the raise in this objective is primarily due to trim constraint violation. As was stated previously, the first five trajectory was terminated once Mach 1.0 is reached. Since in the range of $1.0 < M < 1.2$ the aerodynamic properties of the control surfaces are not defined, the trim algorithm is not working actively. Instead, the trim algorithm keeps the deflection angle of the previous time step. This continues until for the current values an aerodynamic database is available.

During the optimization process, if trim is violated while $M < 1.2$,the trajectory is not penalized. Since no aerodynamic database is present at that instant, it is evident that the trim condition cannot be fulfilled effectively. Yet, during this analysis, it is regarded as a penalty. By doing so, it is aimed to observe how quickly the trim violation arises with fixed deflection values when $M < 1.2$. The results yield that the vehicle becomes untrimmable instantly, once $M < 1.2$. As a result, the longer the flight time in this Mach number range, the larger the path error RSS is. As observed in Figure 7.4 with

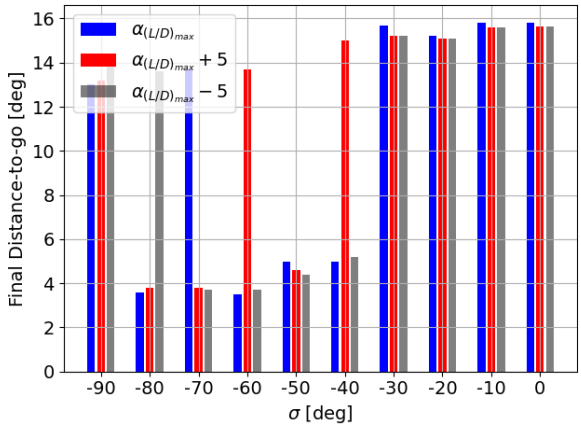

Figure 7.3: Distribution of Objective 1 against different bank angles

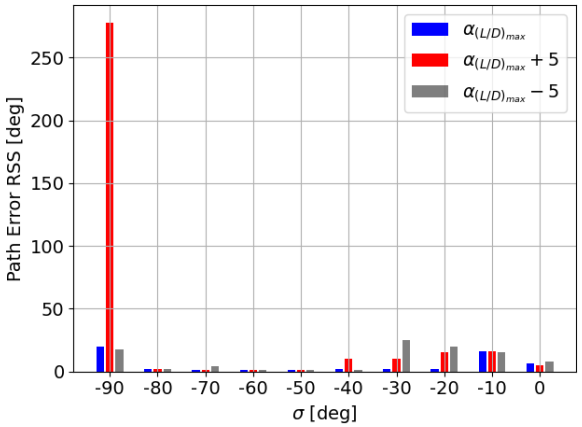

Figure 7.4: Distribution of Objective 2 against different bank angles

changing angle of attack, there is minimal change with this value. Often it is observed that when angle of attack profile is increased by 5° the path error RSS is also increased, compared to the other two α profiles. This is because when α is increased the required C_m that needs to be trimmed with the control surfaces is also increased. Note that ΔC_{m_e} would also increase with increasing α, indicating that to deliver the same ΔC_{m_e} it would need to be deflected less. Nevertheless, it is possible that due to increasing α, C_m that needs to be trimmed increases more than the ΔC_{m_e}, indicating it is not possible to trim the vehicle correctly.

Looking at the objective space in Figure 7.4, it is noticeable that certain bank angles challenge the path constraint significantly more than the others, such as the $\sigma = -90°$. It is seen that the path error RSS is much larger in magnitude than the other values, mainly because of the g-load. Except the immense raise in path error RSS in $\alpha_{(L/D)_{max}} + 5$ profile, which is due to the violated trim condition. Since it gives a significantly high rise to the second objective, $-90°$ is directly identified as an unsuitable candidate for this flight. Therefore, it will not be included in the decision variable range.

Meanwhile, the values at the lower end of the σ range, such as $-50°$ to $-80°$, behave in a desired manner for the path constraints, as seen in Figure 7.4. Mainly again the g-load and the load factor are violated around these values. However, that could be further limited with the optimization. A final observation is made when the graphs in Figure 7.3 and Figure 7.4 are compared. The results suggest that Objective 1 is more sensitive to changing α and σ couples than Objective 2. A greater range of variability can be observed for a σ value with different α profiles. For instance, for $\sigma = -70°$, α profile that delivers the maximum L/D has a final distance-to-go of $13°$, whereas, when α profile is deviated by $\pm 5°$, the final distance-to-go has dropped to $4°$. For the same bank angle value, the path constraint error is insignificantly small for all three angle of attack profiles. As a result, changing the angle of attack could be necessary to obtain the desired final distance-to-go.

7.2. Powered: One-at-a-time Simulation

The equations of motion can be utilized to derive the effect of a thrust force on the trajectory. However, this result would be more local since the equations of motion would have been solved analytically. To obtain a coherent understanding and analyze the interaction between the thrust parameters and the trajectory, a simulation is necessary. For this task, a One-at-a-time simulation is adapted. As a secondary mean, the One-at-a-time simulation is also used to verify that the thrust model is implemented correctly in the simulation. This is performed by providing a trivial decision vector to the simulation and checking the resulting trajectory. For instance, when the thrust magnitude is equal to 0 kN across the trajectory, the simulation should yield a zero fuel consumption.

The design space exploration primarily aims to answer the following sub-research question: How sensitive is the flyback booster trajectory to aerodynamic and thrust parameter commands? To answer the question, a systematic design space exploration is performed. The first simulation is a one-at-a-time simulation, which is performed by changing one thrust parameters, such as the thrust magnitude, while

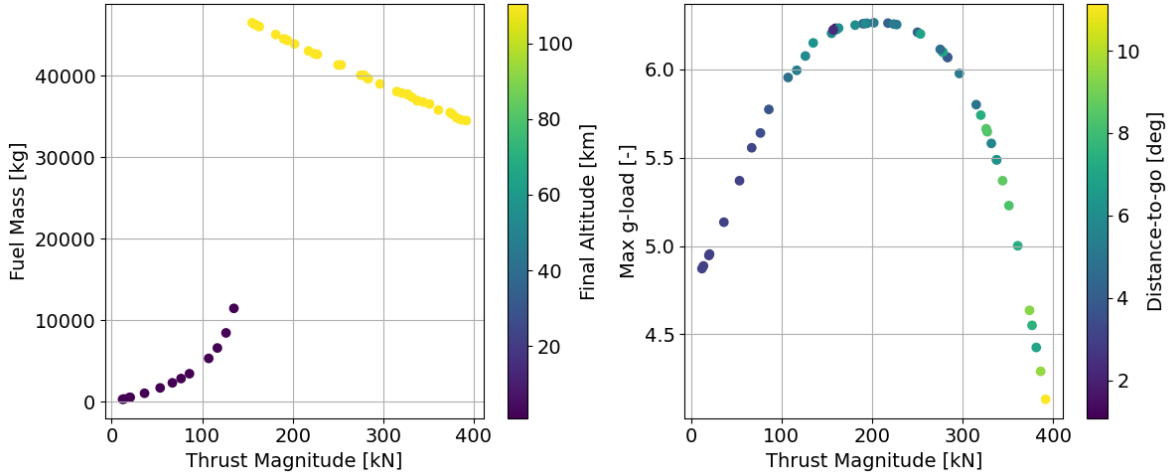

Figure 7.5: Powered booster's objective and constraint space when only the thrust magnitude is changed

keeping the other two parameters fixed. The simulation focuses on identifying the linear relationship between each variable and the trajectory. The nominal decision variable vector is identified as below:

$$\mathbf{x}_{nominal} = \begin{bmatrix} 200,000 & 45 & 45 \end{bmatrix}^T \tag{7.1}$$

in which the first entry refers to the thrust magnitude in Newtons, the second entry refers to the thrust elevation angle in degrees, and the final entry refers to the thrust azimuth angle in degrees.

Thrust Magnitude

The thrust magnitude is changed between 0-400 kN. Since higher thrust requires higher engine performance, hence increases the fuel that is expelled from the booster. Thus, as it can be observed from Figure 7.5 as thrust magnitude is increased, the fuel consumption is increased. Especially between 0-150 kN the booster behaves in a desired manner, in which the fuel consumption increases with increasing thrust magnitude, while the final altitude is around 20-25 km range. After 150 kN the mid-range thrust magnitudes consume more fuel than the high-end thrust magnitudes. All these trajectories are terminated due to upper altitude limit of 120 km, as the vehicle leaves the atmosphere. However, the trajectories with mid-range values experience a skipping flight after completing Phase 1. At that point, the lift component is so high that it can counteract the gravitational pull. The vertical lift component has to be reduced to avoid skipping flight. Note that it is possible to control the vertical component of the lift by implementing an active bank angle control. However, often certain bank angles pose structural limitations, therefore it could be that the maximum allowable bank angle is not sufficient to control the vertical lift component. Hence, requiring active control of the thrust magnitude.

Meanwhile, the high-end thrust magnitudes increases the acceleration of the booster to a point where the thrust force exceeds the gravitational and aerodynamic forces. Therefore, instead of performing a ballistic flight, the booster continues to ascent. Consequently, the booster directly leaves the atmosphere. This can also be seen from the right graph of Figure 7.5, as the distance-to-go is increased significantly for high-end thrust magnitudes. Meanwhile, for the mid-range thrust magnitudes, as the vehicle skips from the atmosphere, an increase in the final distance-to-go value can already be observed.

The thrust magnitude control ensured that the vehicle can be accelerated and decelerated at certain points in the trajectory. This allows the energy to be controlled and providing the benefit of having the potential to manage the energy more efficiently to ensure that the vehicle has sufficient energy to meet the TAEM conditions. However, it is also concluded that certain magnitudes could cause vehicle to either continue to ascent, without the ballistic phase, or perform a skipping flight after the ballistic phase, due to increased vertical lift component. Therefore, controlling only the thrust magnitude has limitations and precise control over the thrust vector could potentially allow the vehicle to follow the desired maneuvers more efficiently.

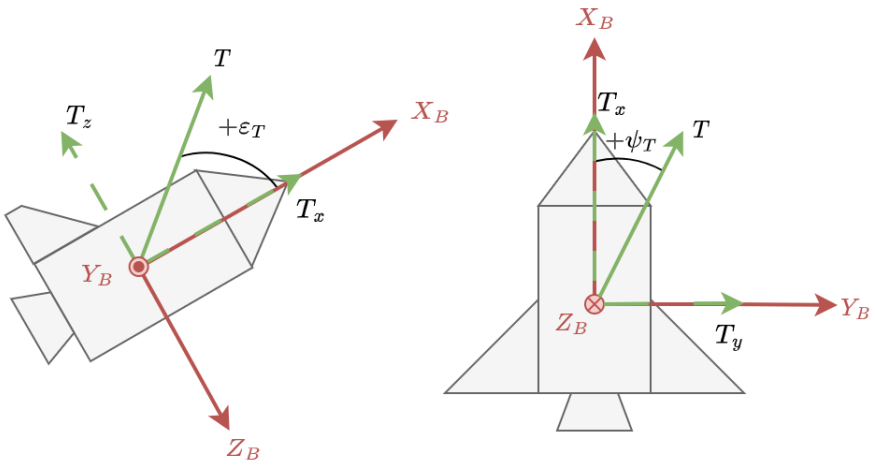

Figure 7.6: Thrust vector decomposed into components in the body reference frame in which CoM is the origin of the reference frame

Furthermore, the importance of node control can also be interpreted from the thrust magnitude variation results. Controlling the thrust along the trajectory at different nodes would allow the vehicle to accelerate and decelerate at desired locations along the trajectory. This could potentially increase the efficiency of the vehicle, as it would provide high thrust only at points that is necessary. Consequently, by adjusting the thrust magnitude at key locations along the trajectory, the booster could maintain a proper attitude and ensure flight safety.

Moreover, a high acceleration potentially effect the maneuverability of the booster as it induces more rapid changes in the velocity. Therefore, a highly responsive control system has to be developed to accurately follow the desired trajectory.

Thrust Elevation

As the previous section identified the importance of thrust magnitude controlling, it comes down to analyzing the effect of the thrust angles on the flyback booster. When only the thrust elevation angle is increased, it is expected to observe an increase in the vertical component of the thrust force in the body-frame, hence in the T_{z_B}, as depicted in Figure 7.6. When the forces on the vehicle are considered, this T_{z_B} force will be counteracting the gravitational force exerted by the Earth. If the interactions were to be linear, it could have been concluded that larger the elevation angle higher the T_{z_B}, resulting a steeper ascent during Phase 1. This would have indicated that for high elevation angles, the maximum altitude reached at the top of the ballistic phase would have been higher. However, looking at Figure 7.7, it can be observed that this is not the case.

The maximum altitude peaks for the elevation angle of 20°. This indicates that there is a non-linearity in the problem which can be explained by the equations of the motion that are expressed below:

$$\frac{dV}{dt} = \frac{T_x}{m}\cos\gamma - \frac{D}{m} - \frac{g}{m}\sin\gamma \tag{7.2}$$

$$V\frac{d\gamma}{dt} = \frac{T_z}{m}\cos\gamma + \frac{L}{m}\cos\sigma - \frac{g}{m}\cos\gamma\left[1 - \left(\frac{V}{V_c}\right)^2\right] \tag{7.3}$$

in which Equation 7.2 represent the acceleration that is parallel along the velocity vector and Equation 7.3 represent the acceleration that is perpendicular to the velocity vector. Looking at Equation 7.3, c that a change in the flight-path angle γ also affects change of rate of the flight-path angle, $\frac{d\gamma}{dt}$. Meanwhile, as T_{x_B} is acting along the nose of the vehicle and affecting the velocity vector, the aerodynamic acceleration is also not constant. Finally, the mass of the vehicle is also not constant as the booster actively consumes fuel. Since the components within the equations of motion are not constant and there are interplay between various components, the trajectory portraits complex behaviors that cannot be

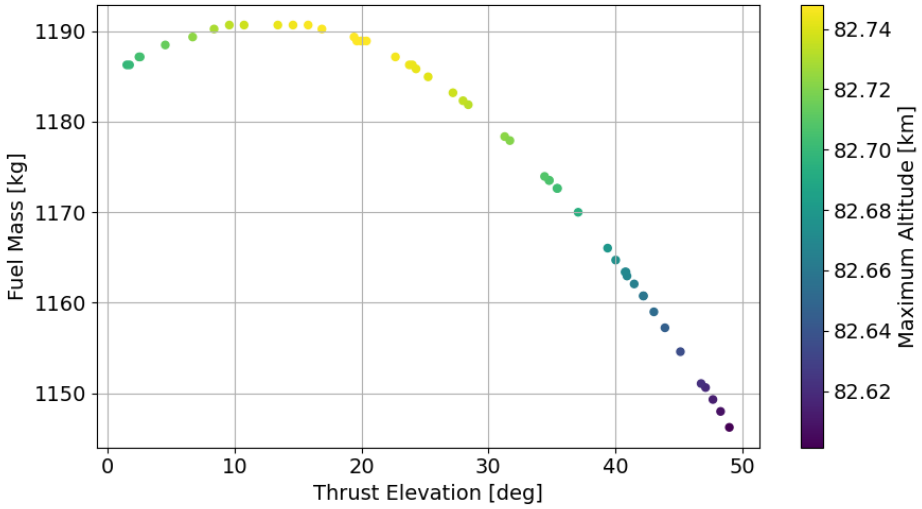

Figure 7.7: Powered booster's objective space when only the thrust elevation is changed

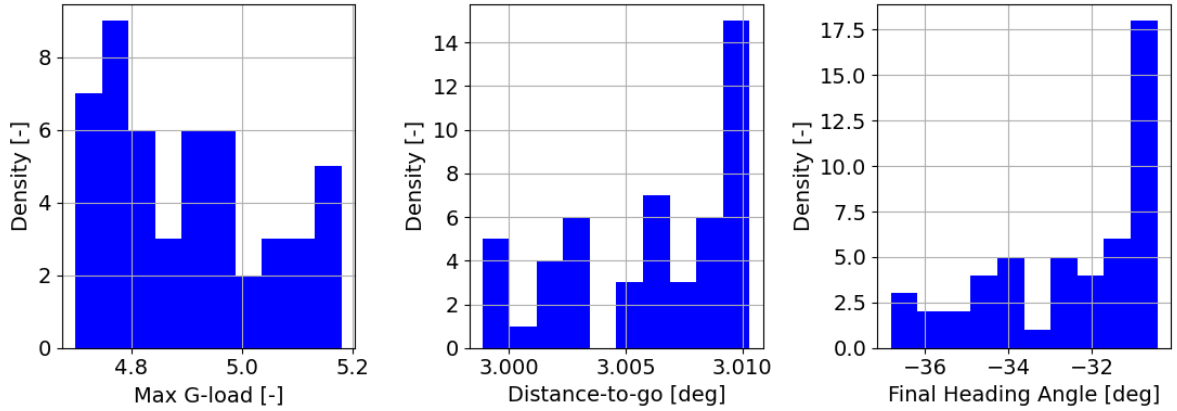

Figure 7.8: Powered booster's objective space when only the thrust elevation is changed

explained by linear relationships. Therefore, analytical results, such as depicted in Figure 7.7, have to be used to fully understand the relations.

Meanwhile looking at the constraints,

Thrust Azimuth

The thrust azimuth is the final thrust parameter that is altered. Providing a positive thrust azimuth, while the thrust elevation is kept at 0°, causes the vehicle to have a thrust force in the positive X_B and the positive Y_B direction, as depicted in Figure 7.6. When the thrust vector is decomposed into components, the force in the Y_B direction, points to right of the vehicle's center of mass. This thrust force induces a moment around the Z_B axis, thus causing the vehicle to rotate around the Z_B axis. Consequently, the rotation of the vehicle induces a change in the heading angle. Since the thrust force is pointed to right, it induces a counterclockwise turn, leading to a change in the heading angle to the left.

The results in Figure 7.9 visualize the turn maneuver by providing the heading angle change with respect to time and latitude-longitude change of the flyback booster. In Figure 7.9 the graph on the left visualizes the heading angle change. The point in time at which the heading angle rapidly drops from a positive value to a negative value refers to the mid-point of the turn maneuver. It can be observed that this instant is smaller for large azimuth angles, indicating that the turn is performed earlier. The latitude-longitude graph of these cases confirms that when the thrust azimuth angle is high, the turn is performed slightly earlier, with a smaller turn radius. During Phase 2, the booster is changing its

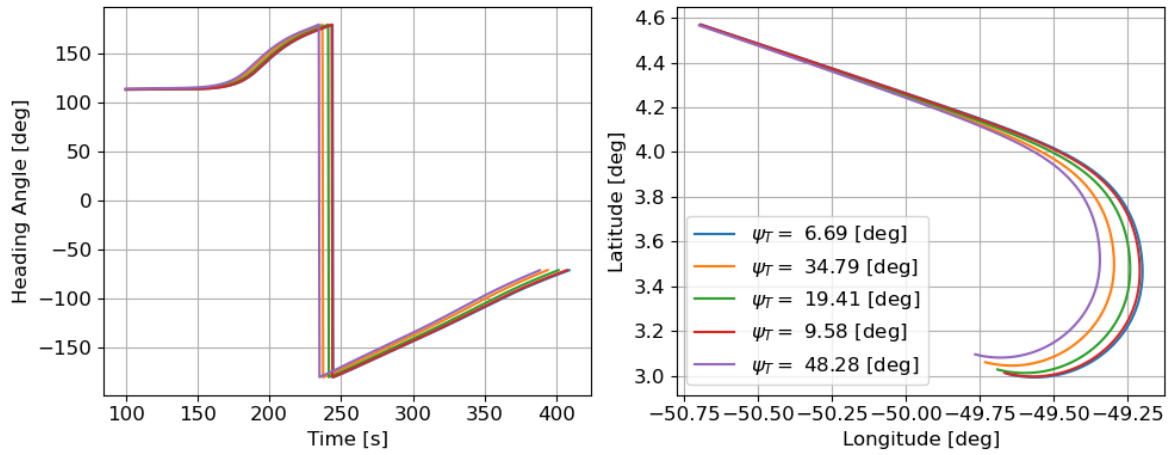

Figure 7.9: Heading angle vs. time graph (left) and latitude vs. longitude graph (right) of different individuals from the design-space exploration

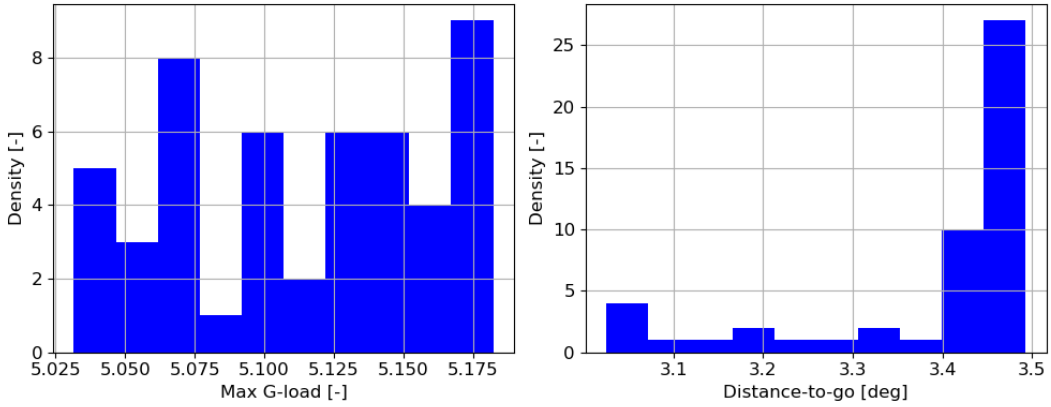

Figure 7.10: Powered booster's constraint space when only the thrust azimuth is variable

heading angle from 110° to −70°. The presence of a positive thrust force in the Y_B axis assists the turn maneuver in Phase 2 by providing an additional force to induce a counterclockwise moment around the Z_B axis. Thus, the larger the additional force is, the quicker the turn is induced.

Note that the first 100 seconds of both graphs are discarded and the simulations are terminated once the desired final heading angle of −70° is achieved. The first 100 seconds approximately corresponds to the ascent part of the ballistic phase and do not carry a significance to observe the relationship between changing azimuth angle and the heading angle.

As an additional force in the Y_b axis continues to exist, due to presence of thrust azimuth, the turn maneuver will continue. It is significant to note that, if the force is strong enough, the booster could even be stuck into a spiral motion. In fact, looking at the first histogram in Figure 7.11, it can be observed that trajectories could not comply the desired final heading angle constraint of −70°. Meanwhile, trajectories could not successfully meet with the TAEM interface since 0.75° of final distance-to-go is not reached, as it is interpreted from the second histogram in Figure 7.10.

To avoid the spiral motion and allow the vehicle to continue a straight flight, the thrust force in the Y_b axis has to be controlled. One method for achieving this control over the thrust force would be increasing the amount of nodes at which the thrust azimuth angles are re-defined. For instance, when a second thrust node is implemented around 20 km altitude, an improvement in the final heading angles can be observed from the second graph in Figure 7.11. Note that another method for controlling the turn maneuver would be terminating the simulation once the desired heading angle is achieved. However this would generate a decoupled trajectory, since in that case Phase 3 has to be simulated independently. Decoupling the trajectory has potential consequences such as discontinuous trajectory

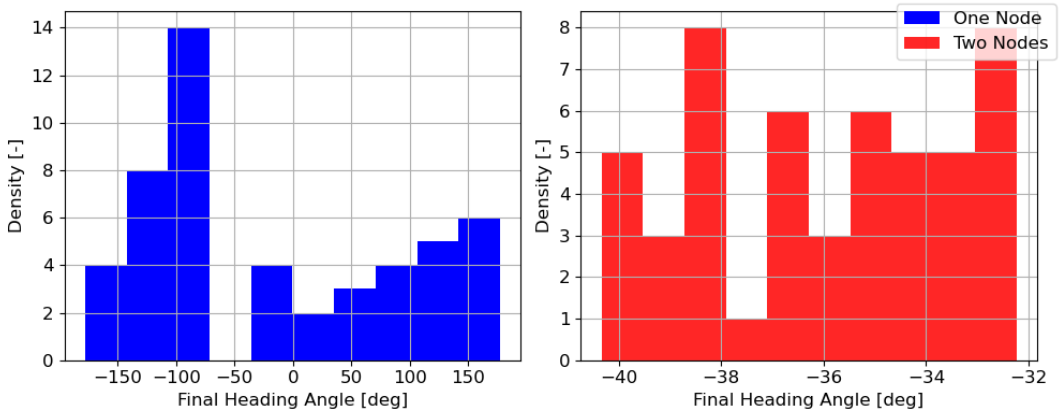

Figure 7.11: Powered booster's constraint space when only the thrust azimuth is variable

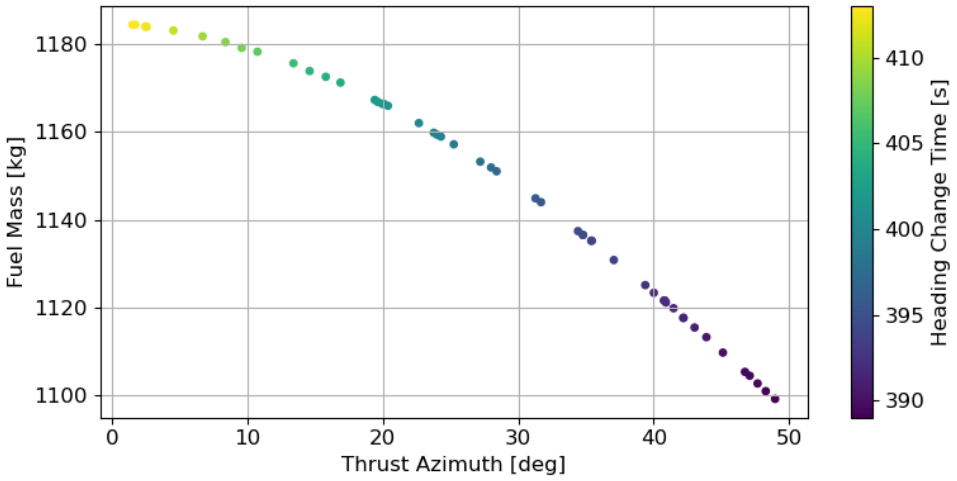

Figure 7.12: Powered booster's objective space when only the thrust azimuth is changed

or that the optimum of each phase not summing up to be the global optimum for the whole trajectory.

Finally, the fuel consumption with respect to different thrust azimuth angles is observed in Figure 7.12. The amount of consumed fuel is increased with small thrust azimuth angles. As the vehicle has a small azimuth angle, the time that it takes to execute the heading change is also longer. Since a fixed magnitude of fuel is consumed during this simulation, this directly yields a higher fuel consumption. Therefore, to find the most suitable thrust azimuth angle that could potentially minimize the heading angle change and yield a better objective, while accounting for other variables, an optimization has to be performed.

7.3. Powered: Fractional Factorial Design

As was elaborated upon in Section 5.3.3, the choice of the design matrix is dependent on the number of factors that are used to set-up the experiment. The first fractional factorial design is performed in a simple manner, using all 24 decision variables. This indicates that an L_{32} matrix is chosen in which a factor is assigned to each column, consecutively. Since fractional factorial design introduce confounding in expense of reduced number of executions, when such a column distribution is used, all the factors suffer from confounding. Nevertheless, by using such a method it is aimed to clarify two main points. First of all, the goal is to observe whether or not there are interactions between different thrust parameters. It is suspected that for certain responses, such as the final distance-to-go, there are strong interactions between the thrust parameters. Consequently, it is expected to observe a change in one thrust parameter at one node affects the value of the parameter at another node. The fractional

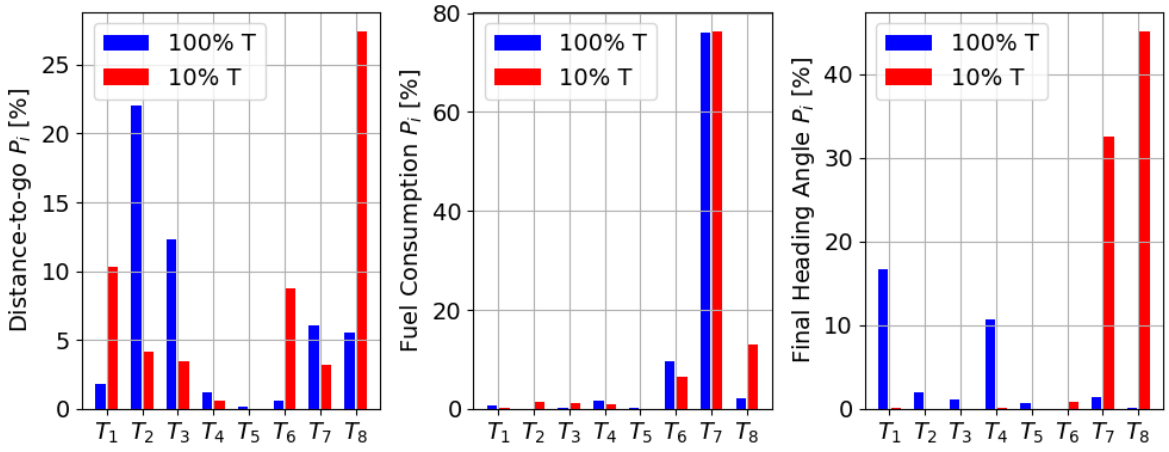

Figure 7.13: The individual percentage contribution of thrust magnitude parameters across different thrust levels

factorial design is first used to confirm these suspicions. Secondly, the fractional factorial design is utilized to re-assess the design variables range and obtain a smaller range.

To identify whether or not there are strong interactions, the fractional factorial design is performed across different thrust magnitude levels. If the model at hand is a good representation, irregardless of the factor magnitude, the percentage contribution of the individual factors should be the same. In Figure 7.13 the percentage contribution of the thrust magnitudes are presented, which is a subset of the all individual contributions since the thrust angles are discarded. It is observed that the percentage contribution of the thrust magnitude at each node changes significantly as the thrust magnitude is changed from 10% to 100% of the maximum available thrust. For each response the variation across different thrust magnitudes are not the same. For instance, as it can be seen from the first graph in Figure 7.13 the final distance-to-go value has significant variations in the percentage contribution of thrust magnitudes at each node. Whereas, for fuel consumption, there are almost minimal differences across thrust levels. This initial observation suggests that each response has a different sensitivity to changes in the thrust magnitude level. As a result, there are different levels of interaction for each response.

The error sum of squares for various thrust magnitudes is depicted in Figure 7.14. In a factorial design, due to the initial confounding, the interactions are not accounted for directly. During the analysis of variance (ANOVA) of the fractional factorial design the higher-order interactions are accounted for indirectly while calculating the sum of square errors. As it was discussed in Section 5.3.1, the error sum of squares is an indication of the effect of the unaccounted interactions and random variations on the model. If the error sum of squares has a high value, this indicates that there are lots of variations in the response that cannot be attributed to the factors that are accounted for in the current model. Although ANOVA analysis does not calculate the interactions directly, the error sum of squares presents the influence they have on the response. Be aware that, for the data represented in Figure 7.13 and Figure 7.14, it is confirmed that the condition $S_E + \sum P_i = 100\%$ is fulfilled for each one of the response. If the condition were not fulfilled, it would have suggested that ANOVA is performed mistakenly.

Thus, as it is noticeable in Figure 7.14, for both the final distance-to-go and heading angle there are inconsistent percentage contributions for thrust parameters across different thrust levels. Meanwhile, for the final heading angle, not only the error sum of squares are relatively high, it is also varying significantly with different thrust levels. This indicates that when the thrust magnitude is increased, the current model has a significantly lower accuracy at explaining the variations in the final heading angle with the current model. This could be attributed to the presence of confounding between the factors and the interactions. Therefore, for both these responses the current model is very limited at explaining the variations in the responses. Meanwhile, for the fuel consumption, a lower error and change in error can be observed. This could potentially indicate that the confounding interactions are less driving for this response, than the other two responses. The discrepancy between how the square sum of errors and the percentage contribution values respond to changes in the thrust magnitude confirm that the effect of the factors and interactions are not constant. Therefore, not only there are interactions present, but

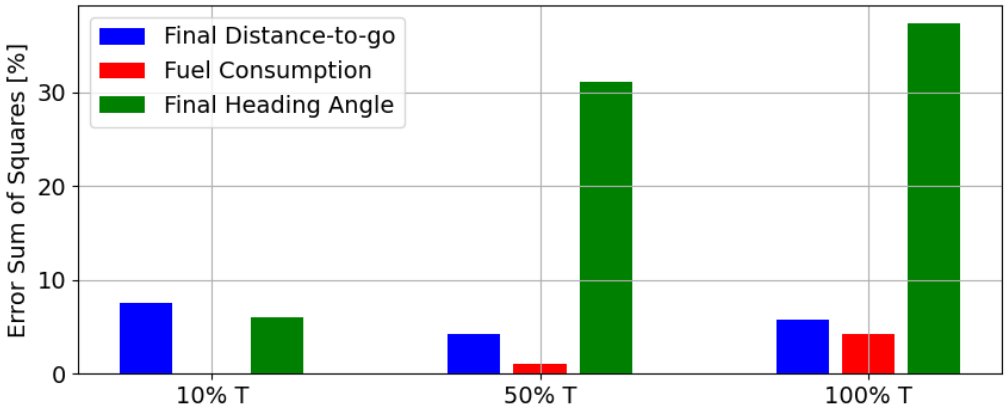

Figure 7.14: The error sum of squares of various responses for different factor levels

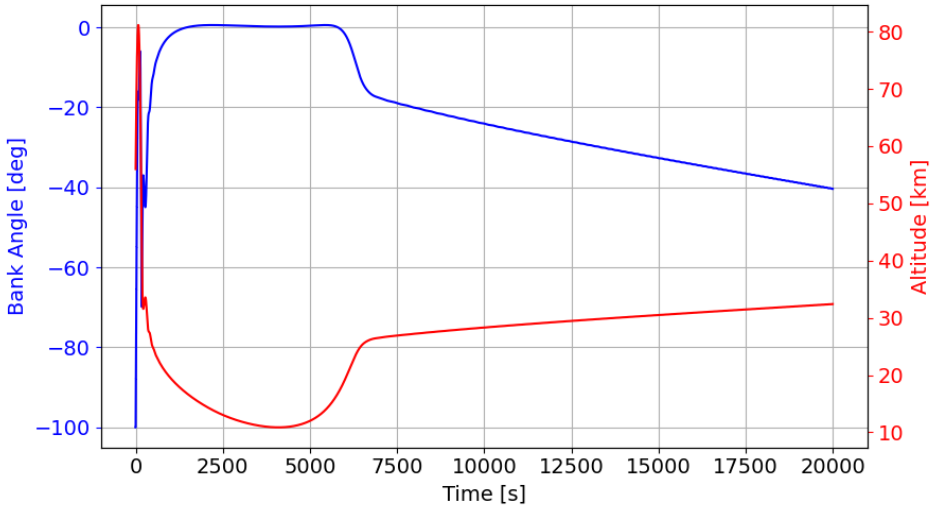

Figure 7.15: Trajectory history of the problematic flight

the sensitivity of the response to each factor and interaction is varying depending on the response.

It is noteworthy to mention that the analysis of each response is conducted after the responses are normalized. Originally, each response has a different measurement unit, such as kilograms for fuel consumption and degrees for the final heading angle and distance-to-go. Through normalization, a common scale is obtained, which allowed percentage contributions to be attributed in a more fair manner. Once it is confirmed that there are interactions, further analysis is performed using the interaction tables and adapting the Taguchi design, as will be introduced in Section 7.4.

While the fractional factorial design mainly aimed to confirm the presence of the interactions, it also identified a new range for the decision variables. The fractional factorial design is first begun by giving the full range to each decision variable. Therefore, at each node, the thrust magnitude varied between 0-400 kN, while each thrust angle varied between 0°-50°. However, since the fractional factorial design aims to explore the edges of the design space, there are various combinations of maximum and minimum decision variables. Combining the maximum value of certain parameters, especially at the final node, results in unexpected trajectories. It is realized that few runs had a flight time of around 30,000 seconds, which roughly corresponds to 8 hours of a flight. Although the time of flight of the vehicle is an independent variable, 8 hours of flight is not expected. Therefore, the few trajectories with a long time of flight are further analyzed.

Looking at Figure 7.15 it is observed that the vehicle is performing a descending flight after the turn maneuver at Phase 2. In a nominal trajectory, the vehicle is expected to perform a level flight

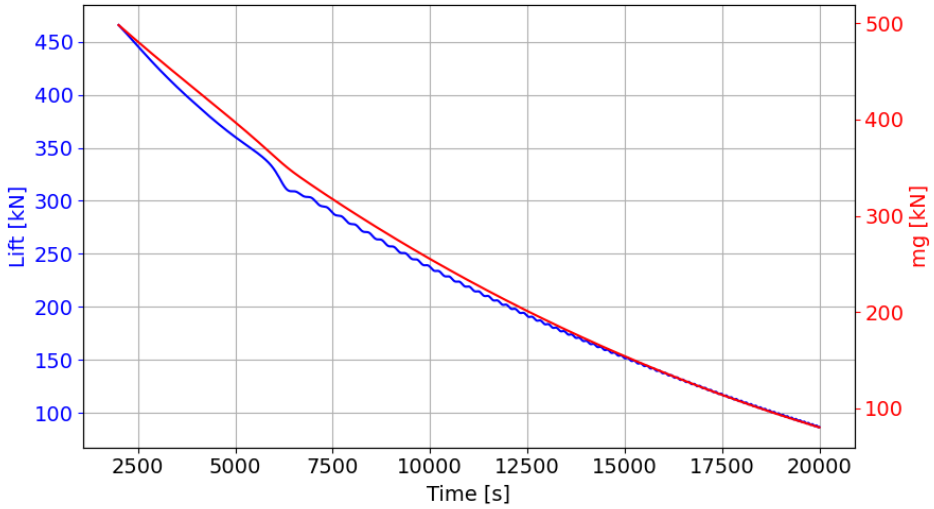

Figure 7.16: Lift and gravitational force comparison of the problematic flight

until the final distance-to-go of 0.75° is reached. In the current trajectory, instead of pulling the nose up, the vehicle is descending with a very slow rate. When the thrust parameters are analyzed, it is concluded that this is due to the fact that the high thrust magnitude requires a high elevation angle to overcome the gravitational force and the drag that is experienced to pull up the nose of the vehicle. If this elevation angle cannot be provided by the engine, due to the negative flight-path angle and the parallel component of the thrust, T_x, the vehicle is slowly descending. Not only the slow rate of descent increases the time but also after a certain amount of time, the thrust force in the normal plane has a higher impact on the vehicle than the gravitational force, since the mass of the vehicle is decreasing due to consumed fuel. Consequently, this phenomena causes the vehicle to accelerate horizontally and begin ascending, as depicted in Figure 7.16. This increases the flight time causing the booster to fly until the trajectory meets with the upper altitude termination condition of 110 km.

To avoid the ascending flight and increased flight duration, the decision variable range can be adjusted in two ways. Either the thrust magnitude can be decreased, so that the fuel flow hence the mass consumption, would be decreased or higher thrust elevation values can be allowed. However, both have consequences. To begin with, if the thrust magnitude is lowered too much, regardless of the elevation angle, the thrust force could never compensate for the drag and gravitational force. As it is depicted in Figure 7.17 when the thrust force at the final node is decreased to 100 kN the acceleration provided by the thrust is significantly lower than the acceleration provided by the drag and gravity. As a result, the nose of the vehicle cannot be pulled up, hence the vehicle continues to descend until the lower termination condition is reached. Looking at the nominal acceleration graph in Figure 7.17, even if 400 kN is provided, just like at the beginning of the trajectory, the thrust acceleration in the nominal component is not sufficient to compensate for the gravitational acceleration. This already yields that the second solution could be more appealing.

The second option is to allow for higher elevation angles. Note that this is dependent on the type of engine and the engine placement on-board. If there are structural obstacles that limit the engine such that it cannot be deflected, then high elevation angles cannot be obtained. Nevertheless, in literature, angles below 90° are accepted as reasonable deflection angles (Ghobadi et al., 2020). When the thrust vector is elevated by 90° it creates a very large force in the normal direction. This increases the aerodynamic forces on the rocket and potentially poses a risk for the controllability and stability of the vehicle as well as the structural integrity. To cope with this problem, the upper limit for the thrust elevation is defined as 90°.

It is stressed that 90° is theoretically feasible, yet, in practice values such as 30°-40° are more realistic. A 90° of elevation angle provides a pure vertical thrust, which would not only limit the efficiency of the horizontal acceleration but could be unrealistic to attain due to certain hardware limitations. Although Daimler-Benz Aerospace (1998) has provided the detailed structure of FSSC-16, no hardware limitation is mentioned. For the sake of the research, it is assumed that a 90° deflection is possible.

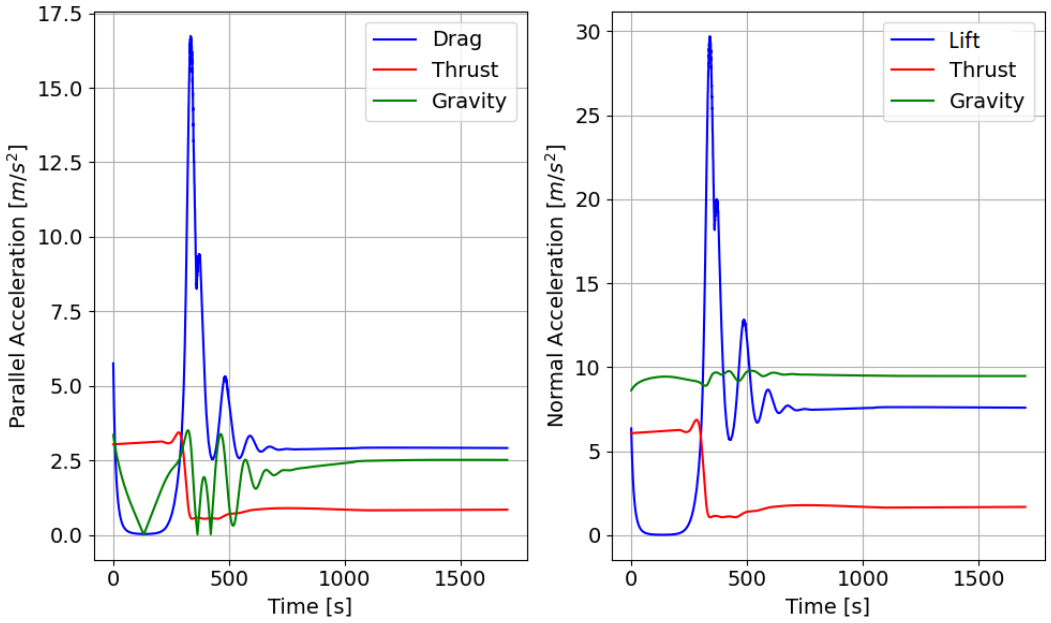

Figure 7.17: Parallel and normal acceleration history of the trajectory with adapted thrust parameters

7.4. Powered: Fractional Factorial Design with Taguchi Interactions

In this array, as depicted and explained in detail in Appendix A, seven factors are introduced with certain two-way interactions confounded. The factors are assigned to columns 1, 2, 4, 7, 8, 16, and 29. While the percentage contribution of these columns represents the main effects, the rest of the columns represent the interactions. Note that within the rest, columns 3, 5, and 6 are the columns that have confounded interactions. Knowing the exact distribution of the interactions, an analysis can be performed in a more structured manner. However, if interactions with high impact are represented in columns 3, 5, and 6, then there could be a confounding effect that has to be regarded. This can be assessed by swapping the column location of factors within a subset. Therefore, if factor A is assigned to column 1, in the next round factor A is assigned to column 16 while keeping the same factors but also changing their column location. If the original subset and the column-swapped subset yield similar amounts of percentage contributions, then it can be concluded that the subset is not suffering from any confounding effects. Note that, this is explained in more detail in the upcoming part of this section.

It is significant to note that, for each of the responses, which are fuel consumption, final heading angle, and final distance-to-go, a new set of subsets are chosen. The subset method is adapted to be able to capture the true relationship between the relevant factors and responses. Each response may have a different relationship with the factors, potentially with different functional forms. This indicates that for instance, while thrust magnitude has a linear relationship with fuel consumption, it could be non-linear for the final heading angle. Therefore, when all the responses are modelled with a single model, an oversimplification may need to be performed, which in turn may cause an inadequate explanation of the response variability.

Fuel Consumption

The first response to be analyzed is the fuel consumption. In an ideal environment, when the fuel flow is kept constant, the fuel consumption would have a linear relationship with respect to time. The engine that is being simulated in this study is non-throttable, therefore the fuel flow is constant across the trajectory. Although the above point indicates that it is expected to observe a linear relationship, the aerodynamic effects on the booster may introduce non-linearity. For instance, to overcome the drag and gravity force and pull up the nose of the booster, higher levels of energy is required at the last nodes. This energy can be provided by the thrusters increasing the fuel consumption. Nevertheless, with increasing thrust, not only more fuel would be consumed but also higher acceleration would be achieved. Consequently, velocity of the vehicle increases. As the velocity increases, the drag is increased exponentially, introducing a non-linear relationship between the two. Therefore, to assess

Table 7.1: Properties of selected fractional factorial subsets of the fuel consumption

	Parameters	Mean	STD	Variance
Subset-1	$T_1 - T_2 - T_3 - T_4 - T_5 - T_6 - T_7$	1.6964	0.4557	0.2076
Subset-1 Swapped Column	$T_3 - T_2 - T_4 - T_6 - T_7 - T_1 - T_5$	1.6968	0.4554	0.2074
Subset-2	$T_2 - T_3 - T_4 - T_5 - T_6 - T_7 - T_8$	1.7567	0.6625	0.4389
Subset-2 Swapped Column	$T_6 - T_4 - T_8 - T_2 - T_7 - T_5 - T_8$	1.7560	0.6617	0.4379
Subset-6	$\epsilon_1 - \epsilon_2 - \epsilon_3 - \epsilon_4 - \epsilon_5 - \epsilon_6 - \epsilon_7$	1.2039	0.0137	0.0002
Subset-7	$T_2 - T_3 - T_7 - T_8 - \epsilon_3 - \epsilon_7 - \epsilon_8$	1.7158	0.6415	0.4116
Subset-7 Swapped Column	$\epsilon_8 - T_2 - T_7 - \epsilon_3 - T_8 - T_3 - \epsilon_7$	1.7157	0.6418	0.4119
Subset-8	$T_2 - T_3 - T_5 - T_8 - \epsilon_2 - \epsilon_5 - \epsilon_8$	1.6924	0.5773	0.3333
Subset-8 Swapped Column	$T_5 - \epsilon_8 - \epsilon_2 - T_3 - \epsilon_5 - T_8 - T_2$	1.6926	0.5769	0.3329
Subset-9	$T_1 - T_5 - T_7 - T_8 - \psi_1 - \psi_5 - \psi_8$	1.6105	0.3330	0.1109
Subset-9 Swapped Column	$\psi_1 - T_7 - \psi_8 - T_1 - \psi_5 - T_5 - T_8$	1.6106	0.3331	0.1109

the correct relationship between the thrust parameters and the fuel consumption a design space exploration is conducted.

To have a comprehensive analysis, several different subset combinations are generated. The relevant subsets and the corresponding thrust parameters are presented in Table 7.1. Be aware that, the fuel consumption is normalized with respect to the flight time, so that a fair comparison can be carried out between different nodes without being concerned about the duration between two consecutive nodes. The methodology of the analysis is as followed. First, Subset-1 and Subset-2 are generated. These are the first subsets that are used to obtain a preliminary information about the response. Since they provide initial insights, they are universal among different responses. Afterwards, the thrust parameters of a subset is assigned to different columns. The subsets that are generated with this method are identified as Subset-n Swapped Column, in which n refers to an independent number chosen to identify the subset.

Afterwards, an ANOVA analysis is conducted to assess the percentage contribution of the thrust parameters and the interactions within a subset. The next subsets are generated using the thrust parameters that are either had the highest individual contribution or the highest interactions. In the meantime, the standard deviation, variance, and mean of the subsets are also assessed. The variance provides information on to what extent the data is distributed around the mean value. Therefore, a subset with a high variance indicates that the interactions of the individual thrust parameters, influence the response more than a subset with a lower variance. If a subset has a significantly low variance, even though it has high contributions such as 70% it will be negligible compared to others.

Considering the variance and mean at the same time, valuable insights can be obtained. A high variance and high mean would indicate that the factors within the subset have a wide range of effect on the response. This suggests that the interactions between these factors could be significant. Whereas, if the variance and the mean are low, it indicates that the subsets contribution to the response is low. Consequently, the effect of the factors are either insignificant, which can be checked by percentage contributions, or the interactions are stable.

The above point can be supported by considering the values in Table 7.1. Subset-6 is the subset with the smallest mean and variance. The low variance suggests that the thrust parameters in this set do not contribute to the variability of the response as much as the thrust parameters in other sets, such as Subset-2 which has the highest mean. The responses that are generated are all clustered around the low mean value. The results yield that the individual contribution of the thrust elevations are not sufficient to explain the variability of the fuel consumption.

The values of Subset-6 concludes that the interaction between elevation angles at different nodes is insignificant. However, it is worthwhile to mention that, by only looking at Subset-6 it is not possible to conclude whether all the thrust elevation interactions are insignificant. This can only be interpreted once the subset includes both the thrust elevation angle and another thrust parameter, such as the thrust magnitude. Hence, the Subset-7 and Subset-8 are generated. Looking at the mean value of

Table 7.2: Properties of selected fractional factorial subsets of the final distance-to-go

	Parameters	Mean	STD	Variance
Subset-1	$T_1 - T_2 - T_3 - T_4 - T_5 - T_6 - T_7$	5.6450	0.6955	0.4838
Subset-1 Swapped Column	$T_5 - T_3 - T_4 - T_7 - T_1 - T_2 - T_6$	5.6470	0.6977	0.4867
Subset-2	$T_2 - T_3 - T_4 - T_5 - T_6 - T_7 - T_8$	5.6578	0.8178	0.6687
Subset-2 Swapped Column	$T_4 - T_8 - T_6 - T_7 - T_3 - T_5 - T_2$	5.6610	0.8216	0.6750
Subset-4	$T_1 - T_2 - T_3 - T_4 - T_5 - T_6 - T_8$	5.5517	0.7459	0.5564
Subset-4 Swapped Column	$T_6 - T_2 - T_8 - T_4 - T_1 - T_5 - T_3$	5.5530	0.7430	0.5520
Subset-5	$\epsilon_1 - \epsilon_2 - \epsilon_3 - \epsilon_4 - \epsilon_5 - \epsilon_6 - \epsilon_7$	5.3710	0.1466	0.0215
Subset-6	$T_2 - T_3 - T_4 - T_7 - \epsilon_2 - \epsilon_3 - \epsilon_7$	5.5294	0.6612	0.4379
Subset-6 Swapped Column	$\epsilon_3 - T_4 - \epsilon_2 - T_3 - \epsilon_7 - T_2 - T_7$	5.5269	0.6480	0.4199
Subset-8	$T_2 - T_3 - T_7 - T_8 - \epsilon_2 - \epsilon_3 - \epsilon_7$	5.4691	0.7121	0.5071
Subset-8 Swapped Column	$T_3 - \epsilon_3 - T_2 - T_8 - T_7 - \epsilon_2 - \epsilon_7$	5.4671	0.7326	0.5366
Subset-11	$T_2 - T_3 - T_7 - T_8 - \psi_2 - \psi_3 - \psi_7$	5.8082	1.2474	1.5561
Subset-11 Swapped Column	$T_8 - \psi_7 - T_3 - \psi_2 - T_2 - \psi_3 - T_7$	5.7892	1.2986	1.6863

the Subset-7, it is noticed that the value is comparable to the mean of Subset-2. This suggests that, the central tendency and the dispersion of the two subsets are similar. Analyzing the data obtained from the two, it can be observed that when thrust elevation angles are coupled with thrust magnitudes, variability of the response is increased.

An important behavior is spotted once the mean and variance of the subsets and the corresponding swapped column subsets are analyzed. For each of the original and the swapped column subset, the mean and variance are almost identical. A difference can be observed in the fourth decimal place. When these values are identical, regardless of the column assignment, it is feasible to conclude that there is minimal interactions between the factors that are present in the subset.

Final Distance-to-go

The final distance-to-go is the target distance between the booster and the landing site. It is aimed to minimize the distance-to-go, ideally to 0.75°, to allow precise landing operations and the TAEM phase to begin successfully. However, the distance-to-go value is dependent on several parameters, few of these are the thrust parameters. The methodology followed for analysis of the relationship between the final distance-to-go and thrust parameters is identical to the methodology of fuel consumption. In the meantime, although the subset names are identical to the subset names of fuel consumption, the content of the subset is different, except for Subset-1 and Subset-2. Each time a new subset is analyzed same Subset-1 and Subset-2 are used as a first step for identifying the variability of the response. The content of the other subsets change depending on the parameters that are identified to be the most influential ones.

The results in Table 7.2 imply that Subset-11 is the most influential subset among all since it has the largest mean and variance. Subset-2, which contains only thrust magnitudes, is the second most influential subset. On the other hand, Subset-5 has the smallest mean and variance. This suggests that only changing the thrust elevation angles does not contribute to the final distance-to-go as much as only changing the thrust magnitudes, such as Subset-2. In the meantime, the values of Subset-6 show that when the thrust elevation angle is considered with thrust azimuth angles, it contributes to the variability of the response. It is stressed that the mean values in Table 7.2 are far from the nominal value which was around 2°. When certain factors are set to their maximum value and combined with other factors, which also have their maximum value, the booster performs undesired trajectories. Often various turn maneuvers are observed which drive the trajectory far from the desired final distance-to-go.

Keeping the above points in mind, when the percentage contributions are analyzed, it is obtained that T_1 is ineffective for the final distance-to-go. To begin with, between Subset-1 and Subset-2 there is a large increase in the variance. This discrepancy is observed once T_1 is removed and T_8 is added

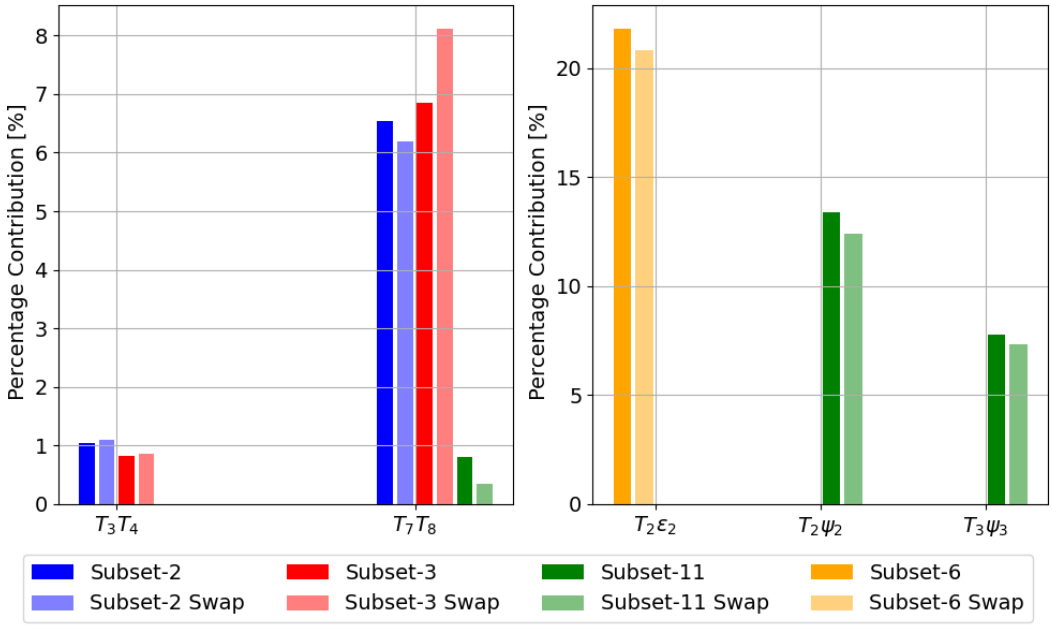

Figure 7.18: Percentage contribution of the thrust parameter interactions to the final distance-to-go across different subsets

to the subsets. When T_1 is again included in Subset-4 a decrease in the variance can be obtained compared to Subset-2. Meanwhile, in all the subsets T_1 had a percentage contribution below 1%.

From a physical perspective, it is reasonable that T_1 is less effective than the thrust magnitudes at other nodes. Note that, T_1 is right at the beginning of the ballistic phase. At this point, the booster's trajectory is dominated by the lift and gravitational force. To overcome the lift that is being generated and counteract the ballistic phase, the thrust force has to be sufficient enough to pull the nose of the booster. The fact that T_1 is ineffective indicates that even with the maximum values, the propulsion system cannot deliver the forces to overcome the aerodynamic and gravity forces at the very beginning of the ballistic phase. The thrust force applied at this point provides a forward acceleration to the vehicle, potentially assisting the ballistic maneuver. Later on, it is observed that T_2 and T_3 are significant parameters for the final distance-to-go response. Although node 2 and node 3 are also placed along the ballistic trajectory, they are at the points where the lift force is small due to raised altitude. Therefore, the generated thrust force can overcome the aerodynamic forces without any trouble, as it can also be observed from the first 250 seconds of the right graph in Figure 7.17. Finally from thrust magnitudes, it is identified that T_7 has a high percentage contribution to the distance-to-go. Since node 7 is one of the final nodes, right after the turn maneuver, it defines whether the leveled flight can be sustained by the booster.

Unlike the fuel consumption experiments, results of the original and swapped column subsets show a higher difference, around the first decimal place. Again considering Subset-11 and Subset-11 Swapped Column, a difference can be observed between the mean and variance values. This is the first indication of a possible interactions between the thrust magnitude and thrust azimuth angles. To identify these interactions further, the percentage contributions are assessed with ANOVA.

As is shown in Figure 7.18, T_7T_8 has a non-negligible contribution, since also Subset-2 and Subset-3 have relatively large variances. This phenomenon is physically reasonable, since if the thrust magnitude is too high at T_7 more fuel would be consumed. This would cause more decrease in the mass, before reaching T_8. Note that the leveled flight is identified as an unaccelerated flight, hence the equations of motion for a leveled flight are simplified to:

$$m\frac{dV}{dt} = -D + T\cos\epsilon_T = 0 \tag{7.4}$$

$$mV\frac{d\gamma}{dt} = L - mg + T\sin\epsilon_T = 0 \tag{7.5}$$

Thus, as the mass is reduced, to sustain a leveled flight the thrust magnitude also has to be reduced at T_8. Else, an increase in the altitude would be observed as the normal thrust force would be more than the normal gravitational force. Another incident that is observed in Figure 7.18 is the decrease in the percentage contribution of T_7T_8, as the thrust azimuth angles are introduced. Although the individual contribution of thrust azimuth angles are not significant, just like the elevation angles, they have a high contribution when they are coupled with the thrust magnitude. Potentially, the decrease in T_7T_8 when $T_2\psi_2$ and $T_3\psi_3$ are introduced could be linked to the fact that a strong thrust magnitude and azimuth couple could potentially induce an early turn maneuver. Due to the high altitudes at node 2 and node 3, sufficient thrust can be provided, as well as the bank angle. A turn maneuver can be induced. As a result, the contribution of the T_7T_8 would drop since the final range to be covered would be much smaller compared to previous cases.

Prior to the experiment, it was expected to observe strong interactions between the thrust magnitude and thrust elevation angles. Especially for the highest contributing nodes, such as node 2, 3, and 7. On the contrary, the analysis of Subset-6 till Subset-10 concludes that only the $T_2\epsilon_2$ interaction is high, as depicted in Figure 7.18. Looking at the equations of motion below:

$$m\frac{dV}{dt} = -D - mg\sin\gamma + T\cos\epsilon_T \tag{7.6}$$

$$mV\frac{d\gamma}{dt} = L - mg\cos\gamma\left[1 - \left(\frac{V}{V_c}\right)^2\right] + T\sin\epsilon_T \tag{7.7}$$

it can be observed that the thrust elevation contributes to the acceleration. However, only if the thrust magnitude is sufficiently high, the thrust elevation can assist with controlling the thrust vector and distributing the thrust magnitude in the desired axis. Since at node 2, the altitude is so high the aerodynamic forces are almost insignificant. Therefore, within the thrust magnitude range, the majority of the magnitudes yield a thrust force larger than the aerodynamic force. Meanwhile, although node 3 is also placed at a high altitude, it is a bit lower than node 2, therefore a decrease in the contribution of $T_3\epsilon_3$ can already be spotted as aerodynamic forces begin to rise again. Meanwhile, for the rest of the trajectory, even the highest thrust magnitude and thrust elevation couple are not the driving forces. Thus, they are not affecting the final distance-to-go as much as it was suspected previously. This phenomenon continues until the mass is sufficiently reduced such that the gravitational acceleration is smaller than the thrust acceleration. To cope with this and increase the effect of thrust elevation angle on the trajectory for controllability reasons, the maximum allowable thrust force of the engine has to be increased.

It is worthwhile to mention that during the analysis of factors, once it is suspected that one parameter is significantly more effective than the others, new subsets are generated by accounting for those parameters. Meanwhile, if it is identified that one parameter is less effective than others, such as T_1 for final distance-to-go, this parameter is grouped with both significantly effective and less effective parameters to confirm its effect.

Final Heading Angle

The final heading angle defines the direction in which the booster points at the final point of the trajectory. It is significant to keep the heading angle aligned with the target landing site as much as possible to also successfully meet with the TAEM conditions.

The analysis first began by comparing the values in Table 7.3. In contrast to the mean and standard deviation of the other two responses' subsets, the final heading angle subsets have a larger standard deviation than the mean. A large standard deviation indicates that the responses are not concentrated around the mean value. This variability in the response, combined with a small mean, suggests that outliers could be present in the data set. The outliers will introduce a disproportionate influence on the mean. Consider Subset-1, the corresponding standard deviation, and mean values suggest that certain $T_1 - T_2 - T_3 - T_4 - T_5 - T_6 - T_7$ combinations result in final heading angle values that are far from the bulk of responses, around the mean. Outliers are an indication of various things, one of these is the presence of strong interactions. To confirm this, the swapped column subsets and the individual contributions of the factors are analyzed in detail.

The results yield that the final heading angle is affected by the accumulative interactions between different thrust parameters by far more than other responses. To begin with, the analysis of Subset-1 and Subset-2 immediately showed a difference between the original subsets and the swapped column

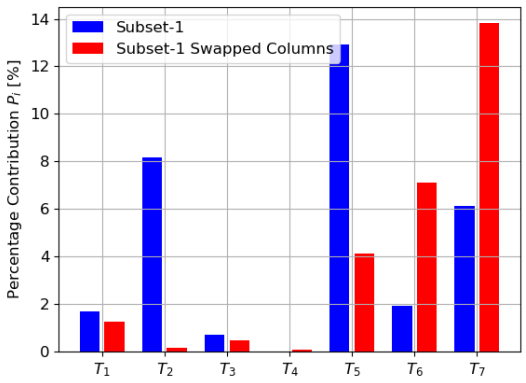

Figure 7.19: Percentage contribution of Subset-1 to final heading angle

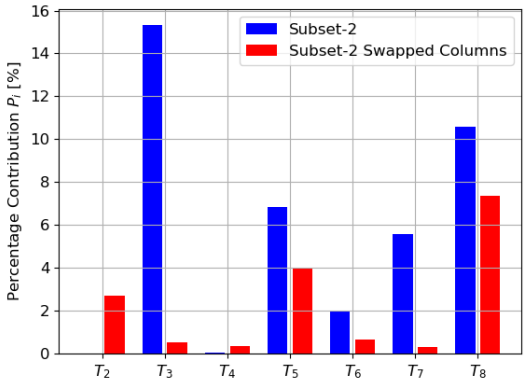

Figure 7.20: Percentage contribution of Subset-2 to final heading angle

Table 7.3: Properties of selected fractional factorial subsets of the final heading angle

	Parameters	Mean	STD	Variance
Subset-1	$T_1 - T_2 - T_3 - T_4 - T_5 - T_6 - T_7$	0.6991	1.7015	2.8952
Subset-1 Swapped Column	$T_5 - T_2 - T_6 - T_4 - T_7 - T_1 - T_3$	0.4603	1.7858	3.1891
Subset-2	$T_2 - T_3 - T_4 - T_5 - T_6 - T_7 - T_8$	-0.0674	1.5822	2.5035
Subset-2 Swapped Column	$T_5 - T_7 - T_4 - T_2 - T_3 - T_6 - T_8$	0.1356	1.5096	2.2789
Subset-8	$T_5 - T_6 - T_7 - T_8 - \psi_5 - \psi_6 - \psi_7$	0.1323	1.5257	2.3279
Subset-8 Swapped Column	$\psi_5 - \psi_7 - \psi_6 - T_7 - T_5 - T_8 - T_6$	-0.1766	1.6109	2.5948
Subset-9	$T_1 - T_3 - T_5 - T_7 - \psi_1 - \psi_3 - \psi_7$	0.5987	2.0471	4.1907
Subset-9 Swapped Column	$\psi_1 - T_1 - \psi_3 - \psi_7 - T_3 - T_7 - T_5$	0.7421	1.9921	3.9693

subsets. From Figure 7.19 and Figure 7.20, it can be observed that the percentage contributions are not consistent regardless of the order the factors are assigned. This indicates that there are large interactions within the model, potentially also affected by the confounding effects.

Different thrust parameters are combined to obtain a better understanding of the phenomena. However, the analysis of each subset concludes that there are high interactions between thrust parameters at different nodes. Especially the thrust azimuth angle and thrust magnitude contribute the most to the variation in the final heading angle. This complicates the analysis since a common trend cannot be spotted among the thrust parameters. Although a conclusive result cannot be obtained, it is suspected that the interactions between the thrust parameters in the mid-range nodes, right after Phase 1, are significant. That is due to two main reasons. First of all, after Phase 1, the turn maneuver is induced. Therefore, the heading angle is changed with banking. During this phase, the heading angle could be more sensitive to changes in the thrust azimuth, since certain values could interrupt the heading angle change that was induced by the turn maneuver. Secondly, as it was stated above, large differences can be observed between the percentage contribution of parameters at nodes 5, 6, 7, and 8. Meanwhile the variance across the original and swapped column subset shows a large variation in the variance as well, as is in Subset-8 in Table 7.3. These differences indicate that not only the individual effect of the factors are significant but also the interactions they have with other factors.

The complex interactions obtained on the heading angle could be due to the nature of the control method. In the fractional factorial design, the node control method is assigned without any regulations. This indicates that depending on the fractional factorial array, the corresponding parameters are assigned to either maximum or the minimum value without regarding the constraints or the objective of the optimization problem. This approach can be identified as a sequential control method, since at each node the thrust parameters are defined independent from other nodes or the overall system be-

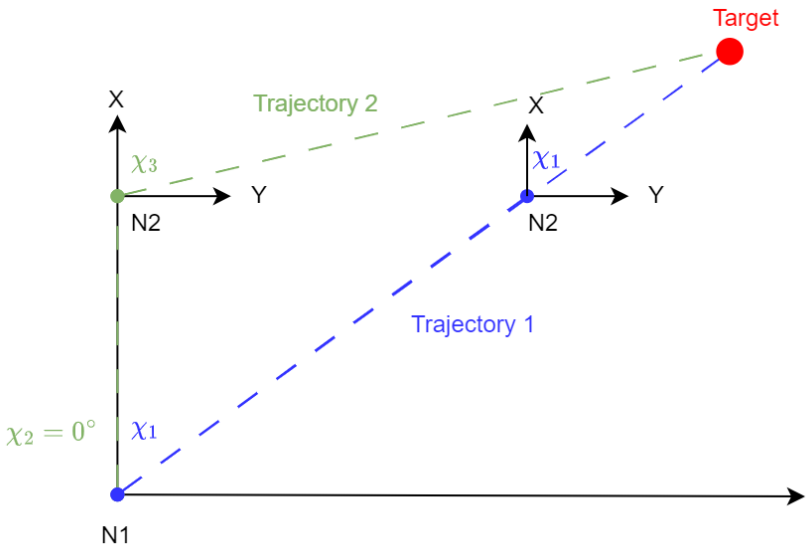

Figure 7.21: Example trajectories with two nodes and a target for explaining the heading angle change

havior. The independent control of the thrust parameters, could introduce unintended interactions in the overall response. There were certain interactions between nodes that are too far apart, such as the T_1T_6 couple that was observed in the original Subset-1 but not the Subset-1 Swapped Column. These interactions could be unintended and perhaps not as dominant on the response as it was observed. Therefore, other control approaches could introduce different interactions. A concurrent control or an optimization-based control, as it is simply adapted in thesis, would regard the overall system behavior and potentially eliminate few of the interactions that are identified here.

Although, one may expect to observe a weaker relationship as nodes are further apart due to the disturbances in the system, it is possible that the final heading angle suffers from long-range interactions. Especially, it is expected for the thrust azimuth angles to follow a long-range interactions, as these angles influence the booster's orientation. From a physical perspective, the effect of a wrong orientation in one node could propagate and it could take few nodes to correct for. An example is depicted in Figure 7.21 for a better explanation. It is seen that there are two separate trajectories, each have two nodes identified with N1 and N2 and a target point. N1 is same for both trajectories but each have a different initial heading angle. The first trajectory has a heading angle χ_1 which is aligned with the target point. Accordingly, the first trajectory suggests that when the heading angle is aligned with the target's heading angle from N1 onward, no large changes occur in N2 to change the heading angle, since at N2 the heading angle is still χ_1. On the other hand, the second trajectory have an initial heading angle $\chi_2 = 0°$. This suggests that if the heading angle at N1 is different, large changes have to be performed at N2 to align with the target point, since $\chi_2 \neq \chi_3$. Consequently, the changes in N1 influence the values in N2. It is suspected to see more complex interactions, as the data discussed above suggests, as the number of nodes are increased.

7.5. DSE Synthesis

Throughout this chapter, different design space exploration methods were utilized to analyze the design space. Two important outcomes are obtained. First, a general overview on which design space exploration is most appropriate for the problem at hand. Secondly, the final decision variable range is obtained, regarding the design space exploration results. These two outcomes are explained in more detail below.

DSE Overview

One-at-a-time simulation, full fractional factorial design, and fractional factorial design with Taguchi interactions are implemented. The findings from each method are as follows. The one-at-a-time simulation provided a preliminary insight into how each parameter affects the performance of the booster.

Table 7.4: Most and least effective nodes for each response

	Most effective	Least effective
Fuel consumption	Node 2 - Node 3 - Node 7 - Node 8	Node 1
Final distance-to-go	Node 2 - Node 7 - Node 8	Node 1 - Node 5
Final heading angle	Node 5 - Node 6 - Noed 7 - Node 8	Node 1 - Node 2

From this point on, it was possible to identify the need for a well-defined node control. When the thrust magnitude profile kept constant along the trajectory, either the fuel consumption was significantly high, for 100 kN it was around 50,000 kg of fuel, or the vehicle performed an ascending or a skipping flight due to the constant excessive thrust. It was established that by changing the magnitude of the thrust force, at different points along the trajectory, the fuel consumption as well as the applied thrust force can be more manageable. Furthermore, the same theory was tested with thrust azimuth angle as well. Implementing a single thrust azimuth angle along the entire trajectory yielded a wide range of final heading angles. When a secondary nodal point was provided, towards the end of the trajectory it was observed that the heading angle range can be controlled more effectively. Note that the final value of the heading angle was influenced by the commanded azimuth value at the new node.

In addition, a one-at-a-time simulation was also used to verify whether or not the simulation model has been set up correctly. Certain input parameters, in which the responses were already known, were fed to the simulation. Following this, the response of the booster was analyzed and compared to the expected behavior to compare and contrast. For instance, for the powered flyback booster, the engine setup was verified by testing the response of the booster to variable thrust magnitude values. After the verification, a fractional factorial design was implemented. The fractional factorial design is the first attempt to perform a structured design space exploration. It was expected to observe interactions between nodes since a thrust parameter in one node can influence the value of another parameter in the same or another node. Through this method, it is intended to confirm the presence of the interactions. Note that to identify the statistical significance of a factor or an interaction with the overall response, ANOVA is used.

The fractional factorial design was performed across different maximum thrust magnitude levels. The results showed that the percentage contribution of fuel consumption varied significantly across different thrust magnitude levels. However, in the presence of a well-representative, sufficient model, changing the maximum thrust magnitude should not vary the percentage contribution to the response, since the response should be adapted in the same manner. This suggests that due to complex and non-linear interactions, the changes in the response do not correlate with the changes in the thrust magnitude. Further investigation suggests that this was the case for all three of the responses, namely final fuel consumption, final distance-to-go, and final heading angle. This was observed by changing the sum of squares error across different maximum thrust magnitudes. Without any interactions, the main effect of the factors would be independent of one another. Therefore, changing the magnitude of one factor would not affect another factor, which keeps the overall contribution constant through different designs. As a final method, a fractional factorial design with Taguchi interactions was implemented. For each one of the responses, the individual contribution of the parameters and the interactions between different parameters were observed via 9-12 subsets. Depending on the variance of the subsets, the influence of the subset was determined. Since this experiment provided the final decision variable range, a detailed summary is provided separately in the upcoming section.

Overall, from the design space exploration it is concluded that each method served a different purpose. For complex studies, to have a comprehensive understanding of the design space it is suggested to use all the methods to build on top of one another.

FFD with Taguchi Interactions Overview

The fractional factorial design is a complex yet an insightful analysis. Nevertheless, since the results obtained from the analysis can be inconclusive and not trivial it is significant to have a preliminary idea about the parameters and a suspicion about their behavior. Without any a-priori information, the results would be much more complicated to interpret. Therefore, the method identified above scratched the surface of the relationship between different thrust parameters. Summary of the above analysis and the important nodes are identified in Table 7.4.

As a result, the decision variable range of certain parameters are re-adjusted to ease the optimization process. To begin with, since node 1 and node 2 are identified as the least effective parameter for the majority of the responses, the thrust magnitude for these nodes are restricted between 200-400 kN while the thrust elevation angles are restricted between 0°- 60°. Note that although these two nodes are identified as least effective, the thrust parameters are assigned to values other than zero. For instance, the $T_2\epsilon_2$ couple is identified significant for the final distance-to-go, if the T_2 is set to have zero or small thrust magnitudes, the $T_2\epsilon_2$ couple cannot influence the response any more. This could potentially restrict the optimization to a greater extend. Furthermore, it would be beneficial to consume fuel and reduce the mass of the vehicle at early stages. So that it would be ensured that the thrust magnitude provided at the last two nodes is sufficient to perform a leveled flight. To make sure that at the end of the trajectory the cruise conditions can be sustained, the last elevation angle is set between 50°-90°, while the last thrust magnitude is set to have high values, 200-400 kN, to overcome the gravitational force and lift the nose of the vehicle.

Finally, since the azimuth angles showed a great coupling with the final heading angle„ only the ψ_7 and ψ_8 are adjusted to have a maximum of 45° to avoid inducing a spiral at the end and deviate the final distance-to-go. Meanwhile, to avoid setting an inoperative range, the rest of the azimuth angles are kept at their full range. It is significant to note that setting up a wrong range has significant drawbacks on performance of the optimization problem. By setting a wrong limit for the decision variables, an infeasible solution space could be described. This indicates that the optimization algorithm has a limited exploration capabilities, potentially leading the search towards local optimum or sub-optimal solutions. Therefore, instead of jeopardizing the effectivity and efficiency of the optimization, only the ranges of the variables that clearly showed a relation in the fractional factorial design are adjusted.

8

Trajectory Optimization

The design space exploration provided a preliminary analysis of the design space as it allowed the vast space to be discovered in a well-structured manner. Building on the foundations laid during the design space exploration, in this chapter a trajectory optimization is performed to obtain the most suitable trajectory. By presenting the general optimization problem in Section 8.1 and the multi-objective problem in Section 8.2, it is aimed to provide a better understanding of the mathematical model. Later on, in Section 8.3 different optimization algorithms are presented, and the most suitable algorithm is selected. Finally, in Section 8.4, the optimum trajectories of both unpowered and powered flyback boosters are discussed.

8.1. General Optimization Problem

Utilizing optimization for trajectory planning has been a key tool in space engineering. The optimization process allows the identification of the desired trajectory while fulfilling various objectives and respecting certain operational limits. The trajectory optimization problem, both for ascent and descent is a nonlinear problem. Therefore, the problem is defined in a series of ordinary differential equations, as it was discussed in Chapter 4 thoroughly. The state vector is expressed as below:

$$\dot{\boldsymbol{x}} = \boldsymbol{f}(\boldsymbol{x}(t), \boldsymbol{u}(t)) \tag{8.1}$$

in which $x(t)$ has the state variables, such as position and velocity, and $\boldsymbol{u}(t)$ has the control variables. The state vector is subjected to path constraints and boundary constraints, as it is identified in Section 5.2.2. These constraints are often implemented in the form of inequality constraints, as mathematically expressed as below:

$$\boldsymbol{g}(\boldsymbol{x}(t), \boldsymbol{u}(t)) > 0 \tag{8.2}$$

$$\boldsymbol{g_f}(\boldsymbol{x}(t_f), \boldsymbol{u}(t_f)) > 0 \tag{8.3}$$

Note that Equation 8.2 represents a path constraint while Equation 8.3 represents a boundary constraint for the terminal point. Often inequality constraints are preferred over equality constraints. Instead of representing an exact physical relationship, the inequality constraints represent a range of feasible values for the solution. However, while using inequality constraints, it is significant to be aware of the drawbacks. Since an inequality constraint defines a boundary for the solution space, it is possible that multiple points satisfy the constraint. In that case, the solution to the optimization problem becomes non-unique since there would be multiple solutions. This poses a problem when there are strict regulatory constraints that require only one precise solution. However, in other cases, the non-uniqueness of the problem introduces an advantage as it shows that the solution can be robust and have flexibility. For trajectory optimization problems, a solution is accepted as long as it does not violate the constraints, therefore inequality constraints are feasible for the problem at hand.

Meanwhile, inequality constraints are less strict at imposing the constraint than the equality constraints. In such cases, the optimization becomes less sensitive to constraint violation, if a better objective function can be attained by violating the constraint with a neighboring value. This indicates that careful analysis of the results are required before a conclusion. There are certain constraints, such as the path constraints, that are structurally not possible for the vehicle to violate. Nevertheless, if a small gap is provided between the absolute maximum value of the constraint and the maximum value imposed in the simulation, than this does not pose a problem. In other cases, observing to what extent violation in a constraint improve the objective values, will provide additional insight on the trajectory. Also note that, often a non-linear inequality constraint is not trivial to solve. This could require more sophisticated optimization algorithms, potentially increasing the computational load.

Meanwhile an objective function of the problem is mathematically defined as below (Yokoyama and Suzuki, 2005):

$$\boldsymbol{J} = \phi(\boldsymbol{x}(t_0), \boldsymbol{x}(t_f)) \tag{8.4}$$

In the optimization problem at hand, the decision variables, also identified as the design variables, are the control parameters. For the unpowered flyback booster, these are the aerodynamic angles, and for the powered flyback booster, these are the thrust parameters. The decision variables are input to the state vector and then to the differential equations to describe the dynamics of the booster. Depending on the values obtained from the optimizer, the differential equations are solved and a trajectory, hence a value for the objective function, is obtained. The proposed solution is later on judged after an evaluation of the value and constraints individually.

8.2. Multi-objective Optimization

Complex problems need to satisfy multiple objectives to achieve the optimal solution. In such cases, the problem is defined as a multi-objective optimization. Although it is not difficult to combine different objectives in a single objective function, in such a method the results are driven by how the objective function is formulated. A multi-objective optimization can be performed to give freedom to the optimization algorithm to explore different trade-offs between the objectives. Mathematically, a multi-objective optimization is formulated as below (Qiao et al., 2019):

$$\text{min } \boldsymbol{F}(\boldsymbol{x}) = \big(f_1(\boldsymbol{x}), f_2(\boldsymbol{x}), ...f_m(\boldsymbol{x})\big)^T \text{ subjected to } x \in \Omega \tag{8.5}$$

The solution contains a set of points that are visualized in the objective space as a Pareto front. The individual solutions in the Pareto front represent the solutions that yield from optimal trade-offs between given objectives (Limleamthong and Guillén-Gosálbez, 2018). Therefore, each individual within the Pareto front represents a non-dominated solution. This indicates that multiple objectives cannot be improved simultaneously, without at least degrading one of the objectives.

Once a Pareto front is obtained, a local refinement method is implemented. The local refinement method is utilized to search the neighborhood of the current solution to ensure that the optimization algorithm truly converges. The neighborhood solutions are searched by adjusting the decision variables of the current solution. Therefore, a Monte Carlo analysis is performed around the optimum solution, with a range of $\pm$10%. Throughout this iterative process, a new solution may be identified that improves the objective function while obeying the constraints. As a result of this process, a more refined and appropriate solution is obtained compared to the initial solution of the optimization algorithm. However, if no improvement can be spotted in the solution, then it would conclude that the algorithm indeed converged.

8.3. Optimization Algorithms

When it comes down to choosing an optimization algorithm, there is no directly correct or a trivial choice. Different optimization algorithms have their strengths and weaknesses. Therefore, it is often recommended to base the optimization algorithm choice on the characteristics of the problem and specific requirements, such as robustness, convergence speed, and computational effort. However, the literature provides an insight on the commonly used and preferred optimization algorithms for the re-entry trajectory optimization problems (Shirazi et al., 2018). These are Non-dominated Sorting Genetic

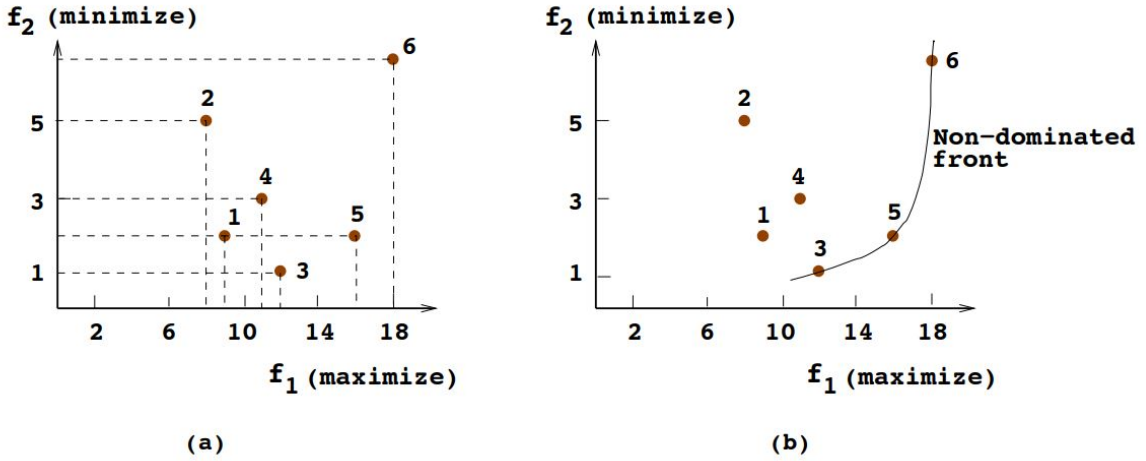

Figure 8.1: Example set of points (left) and the non-dominated front (right) (Deb, 2001)

Algorithm II (NSGA-II), Multi-Objective Evolutionary Algorithm Based on Decomposition (MOEA/D), and Particle Swarm Optimization (PSO). In this section, first the optimization algorithms are explained. By doing so, it is aimed to understand the convergence speed and the diversity of the solutions better. Then a comparison analysis is carried out between the NSGA-II and MOEA/D optimizer.

8.3.1. NSGA-II

The NSGA-II algorithm utilizes the fundamental logic behind the genetic algorithms. Genetic adaptors, such as selection, mutation, and crossover, are used to introduce diversity to the population. PyGMO uses simulated binary crossover (SBX). As a result, each gene from the partner is inserted with the desired crossover probability. Previously, multi-objective evolutionary algorithms (EAs) have been identified as poor optimizers due to their three main challenges: their intensive computational demand for large population sizes, lack of elitism, and the need for specifying the sharing parameter to preserve the diversity (Deb et al., 2002). NSGA-II is one of the first algorithms that was developed to cope with these three challenges of the early evolutionary algorithms. The algorithm has three main features: the elites of the population are carried to the next generations, crowding distance is utilized, and the non-dominated solutions are emphasized. Deb (2001) defines the domination such as: A solution x_1 is more dominant than a solution x_2, if the solution x_1 is equal or better than x_2 in all objectives and x_1 is strictly better than x_2 in at least one objective. The statement is visualized in Figure 8.1 in which the points that are not dominated by the other points create a front called a non-dominated front in the objective space. The above concept eases the definition of the Pareto-optimal solutions in the multi-objective space (Deb, 2001).

Among all the other metaheuristic approaches, evolutionary algorithms are suitable for a wide range of spacecraft trajectory problems. Therefore, often Genetic Algorithms (GA) such as NSGA-II are preferred in various studies. In multi-objective optimization, the algorithm provides a wide range of trade-offs between different mission objectives. This could be beneficial as a vehicle can have more than one optimum trajectory. For instance, currently, the trajectory of the vehicle is observed under three phases. However, if a set of decision vectors can be obtained such that the turn maneuver is initiated at the first phase, then another unique trajectory could be obtained. The working principle behind the algorithm is briefly discussed below (Deb et al., 2002, Bilgen, 2017):

1. The NSGA-II algorithm starts by initializing a random population with n individuals. Each individual is a specific decision vector that represents a solution.
2. Each individual's fitness function $f(x)$ is evaluated.
3. For each population, the first solution x_n is temporarily stored in P, later on every next solution x_{n+1} are added to the set P to compare with the solutions that are already in the set P. As a result:

Algorithm 1 Non-Dominated Sorting

if $x_n < x_{n+1}$ **then**
  remove x_{n+1} from set P
else if $x_{n+1} < x_n$ **then**
  remove x_n from set P
else
  Keep both
end if

After this code is iterated for all the individual solutions, the remaining points in the set P will define the first Pareto front. To find the next non-dominated set of individuals and identify the next Pareto front, the above process is repeated by discarding the solutions in set P.

4. While making sure that the solution is converging to a Pareto front, to keep the diversity, the crowding-distance is applied. The crowding-distance is calculated by sorting the population in an ascending order for each objective function. For l individuals in front I, the crowding-distance is then calculated by:

Algorithm 2 Crowding-Distance Assignment

for each i **do**
  $I[i]_{distance=0}$
end for
for each objective m **do**
  sorting in the ascending order
  if $i = 1$ **or** $i = l$ **then**
    $I[1]_{distance} = I[l]_{distance} = \infty$
  else
    for $l > i > 1$ **do**
      $I[i]_{distance} = I[i]_{distance} + \sum_{m=0}^{M}(I[I+1] \cdot m - I[I-1] \cdot m)$
    end for
  end if
end for

Note that $I[i] \cdot m$ defines the m^{th} objective value of the i^{th} individual of the front I.

5. Therefore, if both non-dominated ranking i_{rank} and local crowding-distance $i_{distance}$ are included, the fundamental rule followed by the algorithm to rank the individuals can be expressed as:

Algorithm 3 Crowding-Distance Comparison

if $i_{rank} < j_{rank}$ **or** $i_{rank} = j_{rank}$ **and** $i_{distance} > j_{distance}$ **then**
  $i <_n j$
end if

Note that the $<_n$ is the crowded-comparison operator that guides the selection process to a diverse, spread-out Pareto front.

6. To begin creating the offspring solutions a set of genetic operations are initiated. First one of these are the binary tournament selection.
7. Then the SBX with a crossover probability of cr is applied. Note that as cr is a probability variant, it is between 0 and 1. The SBX is further discussed by Deb and Kumar (1995).
8. Finally the offspring solutions are mutated with a mutation probability of m, which is between 0 and 1.
9. The fitness function $f(x)$ is evaluated for each of the offspring solution.
10. An intermediate population is then created by combining the offspring and parent solutions.

11. The procedure from step 3 to 6 is repeated for the intermediate population. When the intermediate solution is sorted according to non-domination, it is ensured that the elitism is applied.
12. If a convergence criteria or maximum number of generations are not reached yet the algorithm will continue to create offspring solutions. Therefore, the algorithm re-iterates from step 5 to step 11.

8.3.2. MOEA/D

The MOEA/D optimization in PyGMO is developed by Zhang and Li (2007). The MOEA/D optimizer operates by decomposing the multi-objective optimization problem into sub-problems and optimizing simultaneously. To achieve that, the multi-objective optimization problem is defined as a scalar optimization problem, in which the objective is an aggregation of all the objective functions (f_is). The aggregation function can be constructed in various methods. The Tchebycheff approach is the one implemented in PyGMO and is explained further here. According to the Tchebycheff approach, the scalar optimization problem is defined as (Zhang and Li, 2007, Bilgen, 2017):

$$\min\left[g\left(\boldsymbol{f}(\boldsymbol{x})|\boldsymbol{\lambda},\boldsymbol{z}\right)\right] = \min\left[\max_{i=1,..,m}\left(\lambda_i|f_i(\boldsymbol{x})-z_i\right)\right] \tag{8.6}$$

Note that m is the number of objective functions f_i, $\boldsymbol{\lambda}$ is the weight vector, $\boldsymbol{x}$ is the parameter vector, and $\boldsymbol{z}$ is the reference point vector. The individual components within the reference vector is defined as:

$$z_i = \min\{f_i(x)|x \in \Omega\} \tag{8.7}$$

in which i is up until the number of objectives m. Reference vector stores the best values z_i found for the objective $f_i(\boldsymbol{x})$. For each Pareto optimal point a weight vector $\boldsymbol{\lambda}$ exists such that the Pareto optimal point is the optimal solution of the scalar optimization problem expressed in Equation 8.6. How well the Pareto front is approximated is dependent on the number of weight vectors n and the weight vectors itself.

Each sub-problem is then optimized by using the information from the neighboring sub-problems. This allows MOEA/D to be less computationally intensive than NSGA-II, at least for the multi-objective 0-1 knapsack problems. The 0-1 knapsack problems, as mentioned by Zhang and Li (2007), are used in computer science to assess the performance of an optimization algorithm. However, the performance value obtained by this problem is just an indication. Since each optimization problem has unique properties and alternating levels of complexity, it is not guaranteed that the same performance is applicable to other optimization problems. Although the Zhang and Li (2007) states that the MOEA/D algorithm performed better than the NSGA-II algorithm, this is evaluated for the trajectory problem at hand in Section 8.3.3. The working principle behind the MOEA/D algorithm is explained as below (Zhang and Li, 2007):

Part 1: Initialization

1. Initiate the external population to store the non-dominated solutions during the search.
2. Create n number of evenly spread weight vectors, $\boldsymbol{\lambda_1}, ..., \boldsymbol{\lambda_n}$.
3. Calculate all the Euclidean distance between any two weight vectors for all the pairs. For each sub-problem create a vector $\boldsymbol{B}(i) = [i_1, ..., i_T]$ such that $\lambda^{i_1}, ..., \lambda^{i_T}$ are the T closest weight vectors to λ^i.
4. Randomly initialize a population that contains n parameter vectors.
5. Initialize the reference vector $\boldsymbol{z}$.

Part 2: Update

1. Select two random indices (k, l) from $B(i)$ and then generate a new solution y from x^k and x^l by utilizing the genetic operators.
2. Apply an improvement on y to produce y', in PyGMO a polynomial mutation is applied.

3. For each objective if $z_j < f_j(y')$ then set $z_j = f_j(y')$
4. Update the neighboring solutions.
5. Update the external population by removing the all the vector dominated by $F(y')$ from the external population. Or if no vectors in the external population are dominated then add $F(y')$ to the external population.
6. If a convergence criteria or maximum number of generations are reached than the algorithm stops. Else, the algorithm re-iterates the Part 2 until a stop criteria is reached.

The diversity in the MOEA/D is maintained through a diverse set of sub-problems. Therefore, during the decomposition if the weight vectors are chosen correctly, the optimal solutions to the sub-problems are evenly distributed. While preserving the diversity, it is also significant to regard the mating restriction. Therefore, the value of T, which defines the size of the neighborhood, should be chosen carefully. When two random indices are selected in the first step of the Part 2, a small T value would lead to similar two solutions, such that $x^k = x^l$. This restricts the algorithm by allowing it to discover a limited portion of the search space. Meanwhile, a too large value could be a less representative of the problem at hand and increase the computational load (Zhang and Li, 2007).

8.3.3. Optimizer Comparison

The choice of optimization algorithm is not trivial and is highly dependent on the problem at hand. Although the literature may provide preliminary insights into the performance of an optimizer, it is essential to perform a detailed analysis. The comparison is performed between the NSGA-II and MOEA/D algorithms. The reason why the PSO optimizer is left out is due to its less competitive performance. As it is stated by Shirazi et al. (2018), the probabilistic nature of the algorithm and the fact that the convergence criteria are ill-defined is evaluated as a poor performance criterion. Meanwhile, the evolutionary search strategy of NSGA-II and MOEAD algorithms alongside the incorporated constraint handling method introduces a large advantage. The optimizers are compared based on certain criteria. These are explained below.

- **Initial population:** It is important that the optimizer fairly explores the design space, thus it is preferred to have a widespread population. The initial population generated by the algorithm is an indication of how diverse the design space is.
- **Objective space and Pareto front:** Analysis of the objective space is a visualization of the multi-objective problem. It provides information on different solutions and trade-offs between different objectives. If the solutions are obtained successfully, a Pareto front can be observed in the objective space. The two objective spaces can be compared to assess the performance of the trade-off that is being performed by both optimizers.
- **Hypervolume:** The hypervolume indicator is a performance metric that is used to assess the quality of the results. As stated by Guerreiro et al. (2020), it is a widely used quality indicator for evolutionary multi-objective optimizers, such as NSGA-II and MOEA/D. The results are assessed by evaluating each point's proximity to the Pareto front (Guerreiro et al., 2020). Note that the hypervolume indicator does not provide an absolute measure of how good the result is. Instead, it provides a relative comparison between the two optimizers. Thus, a higher hypervolume indicates that the generated solutions are diverse and well-distributed in the objective space.
- **Convergence speed:** Due to the high dimensionality of the trajectory, the optimization problem at hand has a complex structure. This already poses a risk to the convergence of the solution and computational resources. Nevertheless, it is significant to note that the convergence speed is assessed together with the solution quality. It is possible that at the expense of fast convergence and optimizer gets stuck at the local optimum. Therefore, the assessment is carried out to identify an efficient optimizer that has near-optimal solutions.
- **Constraint handling:** Although there are multiple solutions for the optimization problem, a few of them may be violating some of the constraints. There are certain constraints, such as the final distance-to-go, that cannot be violated. The NSGA-II handles the constraints by assigning a penalty to the solution, which in return affects the fitness evaluation. Meanwhile, the MOEAD incorporates the constraints into the decomposition-based framework. This guides the search for solutions without constraint violation. Through comparison of the two, it is aimed to identify Which constraint handling method is more appropriate and effective for the problem at hand.

Table 8.1: Run time of NSGA-II and MOEA/D with various number of individuals and evolutions with several different seeds

	Number of Individuals	Number of Evolutions	Run Time [hrs]
NSGA-II (seed 42)	24	24	3.2
MOEAD (seed 42)	24	24	2.7
NSGA-II (seed 195)	24	24	2.9
MOEAD (seed 195)	24	24	3.1
NSGA-II (seed 42)	32	42	5.9
MOEAD (seed 42)	32	42	6.1
NSGA-II (seed 252)	60	24	4.5
MOEAD (seed 252)	60	24	3.9
NSGA-II (seed 42)	32	64	7.6

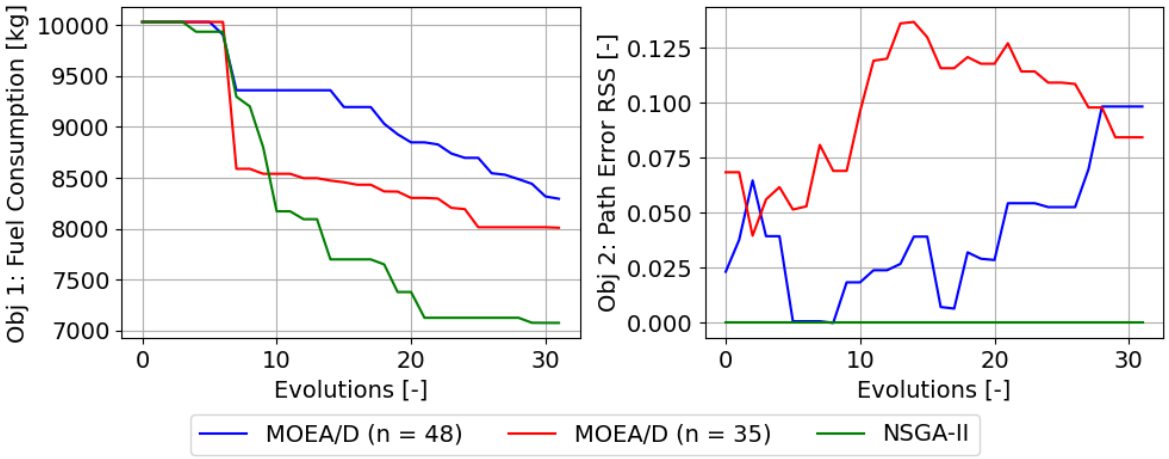

Figure 8.2: Development of the best individual over each evolution with seed 42

Before comparing the two optimization results, it is significant to regard the number of individuals and evolutions. Note that the convergence speed is directly dependent on the number of individuals in a population and how many times the population is evolved. Although a small population may converge faster, it may converge towards a local optimum. A large population size may be beneficial to explore a wide range of search space to converge towards a global optimum. Meanwhile, a large population size would dictate more individuals to evaluate, which could be computationally intensive. Ishibuchi et al. (2009) demonstrated that the computational time of NSGA-II is severely dependent on the number of individuals. Meanwhile, although MOEA/D's computational time may very depending on the number of individuals, after a certain point this increasing trend is slowed down. That is primarily due to the fact how each optimizer evaluates the fitness values. Nevertheless, to comprehend the computational effort required to solve the trajectory problem, a few test simulations are performed. In Table 8.1 the run time of various individual and evolution pairs is presented [1].

It is worthwhile to mention that the values in the table are just an indication. Since the problem is not linear, it is not possible to know how does the duration required to simulate the trajectory changes with each new evolution. In fact, it is expected to see a larger run time towards the final evolutions, since the optimization will be converging towards an optimum and previously early terminated trajectories are discarded. Since a comprehensive design space exploration is performed, the design space is already guided towards feasible solutions. Thus, an excessively large number of individuals are not required. It is decided to choose an optimization with 52 individuals and 32 evolutions. It is utmost importance to regard that the values in Table 8.1 are not used to compare the two optimization algorithms. That is mainly due to the reason that the few of the above batches either did not converge or they clearly converged to a local optimum, since the final distance-to-go is significantly far from 0.75°.

The discussion of the most suitable optimization algorithm begins by analyzing the development of

[1] Processor: Intel(R) Core(TM) i7-8750H CPU @ 2.20GHz 2.21 GHz, RAM: 15.8 GB

the best individuals over each evolution. In Figure 8.2 it can be seen that NSGA-II performs better than MOEA/D in the fuel consumption, Objective 1. On the other hand, for the path error RSS, an irregular pattern can be spotted. The NSGA-II algorithm immediately converges for Objective 2 while MOEA/D suffers from convergence and a non-regular behavior is observed over evolutions. The elitism is conserved in the MOEA/D by keeping the best solution and including that solution in the next population. As it was discussed in Section 8.3.2, elitism is conserved by defining neighboring sub-problems and performing genetic applications, such as mutation and crossover, on these sub-problems. Consequently, this helps the algorithm to keep the best solution while still exploring the solution space. However, even with elitism applied, it is still possible to observe a non-decreasing trend in the objective function, which is the case for the path error RSS, Objective 2. The MOEA/D algorithm aims to find a Pareto optimal solution. While a Pareto front is obtained, a trade-off between the two objectives is performed. This indicates that no solution can be improved for one objective without deteriorating the other objective (Zhang and Li, 2007). This is a regular phenomenon and it is often observed when there are conflicting objectives, such that optimizing Objective 2 further hurts Objective 1.

He et al. (2020) identify that often the normalization of the objective space causes negative results when combined with the MOEA/D optimization. As a result, the solutions are deteriorated. However, since the objective space is not normalized, it is ruled out as a reason behind the unexpected trend of Objective 2. Furthermore, the performance of the MOEA/D algorithm is heavily dependent on the weight vectors. If the weight vectors are poorly chosen, the algorithm may focus on optimizing one objective more than the other. However, to avoid this phenomenon, the grid method is implemented to generate the weights, such that the weights are uniformly distributed in the solution space. Thus, it is also identified that the observed phenomenon are not due to the selected weight distribution method. Later on, as can be seen in Figure 8.2 two different sizes are chosen for the neighborhood n, to evaluate whether or not the selected size of the weight vector's neighborhood has a large influence on the results. Although a decrease in the values can be observed when n is changed from 35 to 48, the hectic trend stayed identical. Meanwhile, increasing the n affected the convergence and performance of Objective 1. While solving the problem, a higher n value explores a larger design space, thus with the current computational power, it cannot converge to an optimum.

The reason behind the hectic trend of the Objective 2 may be due to the distinct exploration strategies implemented by each optimization algorithm. The behavior of the objective space with various evolutions is depicted in Figure 8.3 and Figure 8.4. As the NSGA-II algorithm utilizes non-dominated sorting, it can be observed that the solution space is pushed further into the optimum space, which is the minimum for both objectives. From Figure 8.4 it can be directly observed that from the first population, the NSGA-II algorithm can find solutions that have zero path error RSS. Those solutions are accepted as feasible by individuals and carried to the next generations. Meanwhile, MOEAD decomposes the multi-objective solution into a set of single-objective sub-problems. During this approach, no trajectory with zero path error RSS can be identified, perhaps due to the conflicting nature of the objectives. Thus, it is possible that decomposing the multi-objective function into a set of single-objective sub-problems is not effective for the problem at hand. As an alternative, to cope with this issue, the multi-objective flyback trajectory problem could be re-defined with 3 objectives. The first one is the fuel consumption, the second one is the path error RSS and the third one is the final distance-to-go.

It is not possible to assess the convergence performance by only regarding the best individuals for each objective over various evolutions. Therefore, to have a coherent understanding of the performance, the objective space is visualized in Figure 8.5. Note that the M in the legend is used to indicate the MOEA/D algorithm. The number that follows the letter M with a hyphen is the size of the weight's neighborhood. The letter E at the end identifies the evolution index. Finally, N-II is used to indicate the NSGA-II algorithm. Comparing the 32$^{\text{nd}}$ evolutions, it can be seen that the objective space of NSGA-II is much closer to the optimal space than both MOEA/D solutions. Not only the fuel consumption but also in terms of the path error RSS the NSGA-II algorithm dominates the MOEA/D.

It was previously identified that the diversity of the initial population is an important performance metric. Although the 1$^{\text{st}}$ evolution of each optimizer in Figure 8.5 suggests that a large design space is covered, this is evaluated with a hypervolume indicator. The PyGMO library already has a build-in hypervolume function, which calculates the hypervolume indicator between the Pareto front and a reference point. Guerreiro et al. (2020) defines the hypervolume indicator such as: Given a point set $S \subset \mathbb{R}^d$, in which d is the number of dimensions, and a reference point $r \subset \mathbb{R}^d$ the hypervolume indicator of S is the measure of the region that is weakly dominated by S and bounded by r. In Figure 8.6 the gray

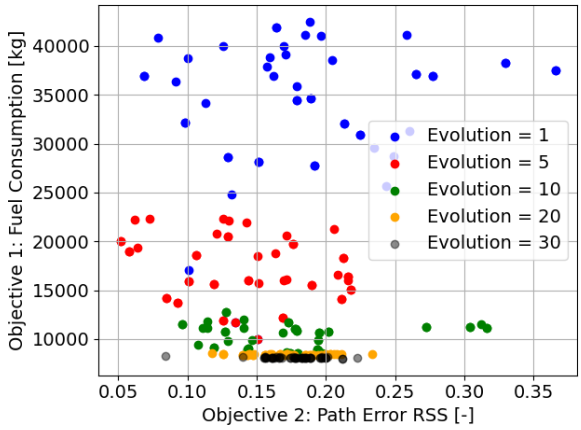

Figure 8.3: Development of the MOEA/D (n=35) population over various evolutions

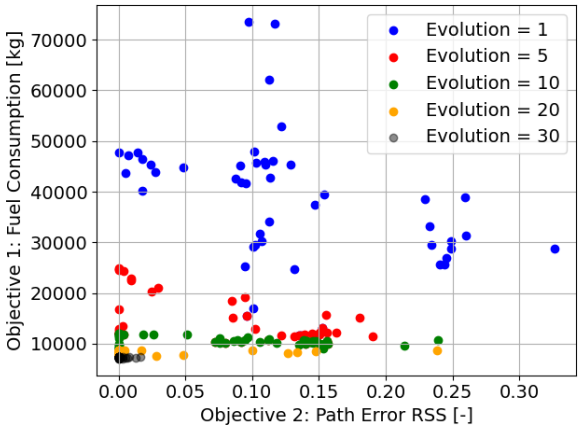

Figure 8.4: Development of the NSGA-II population over various evolutions

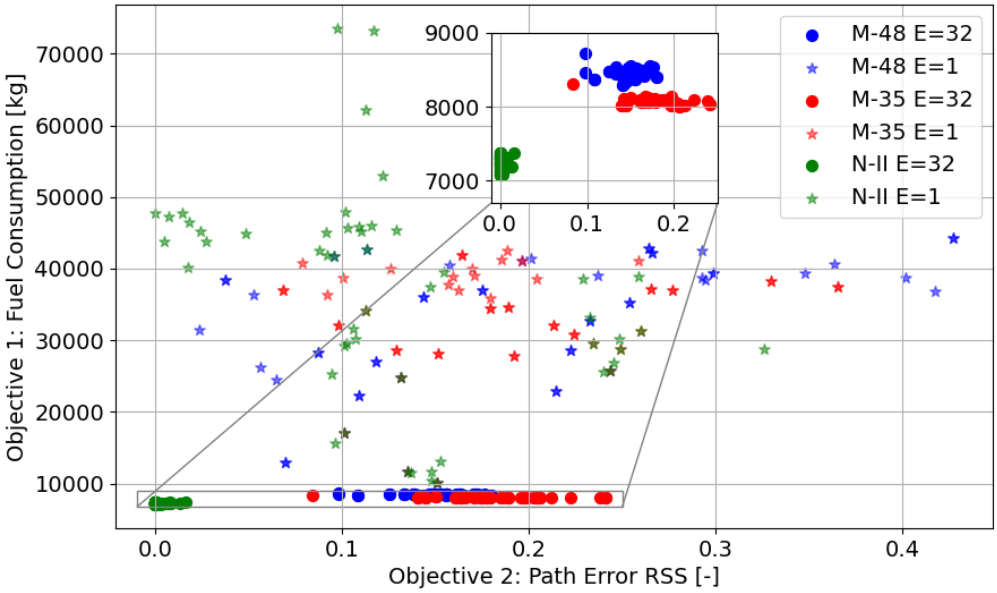

Figure 8.5: Development of the best individual over each evolution with seed 42

enclosed area is the hypervolume indicator of a two-dimensional design space with four points in set S and a reference point r. Accordingly, the volume of the space between the Pareto front individual and the reference point is identified as a hypervolume. The total hypervolume is calculated by summing up the hypervolumes of individual solutions.

While using the hypervolume function in PyGMO, the reference point r is provided by the user. However, there is an important assumption while selecting the reference point. It is assumed that a reference point is numerically larger or equal in one objective and strictly larger in at least one objective. In this study, a reference point is obtained by selecting a reference point that is at the outer boundary of both solution spaces. To do so, the two optimization's initial populations are combined and the maximum value of the Objective 1 and Objective 2 is taken to obtain the reference point. Looking at the outer boundary of the 1st evolution of NSGA-II and MOEA/D with n=35 in Figure 8.5, the reference point is selected as (73528.31, 0.37).

The larger the difference between the hypervolume indicator of the first and the last population, the better the performance of the optimization is. The larger final hypervolume indicator suggests that the

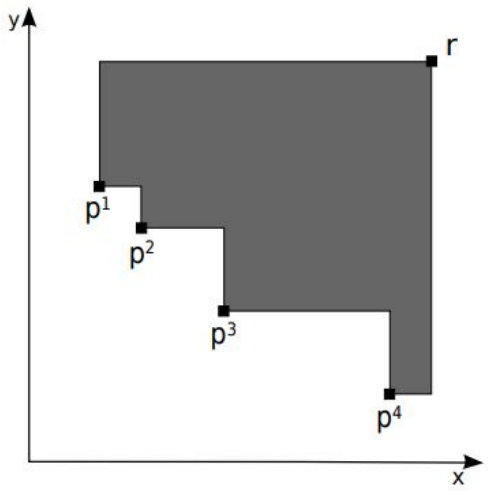

Figure 8.6: Example hypervolume indicator in a two-dimensional space (Guerreiro et al., 2020)

Table 8.2: Hypervolume indicator of the initial and final populations for different seeds

	Initial Population	Final Population	Reference Point
MOEA/D (seed 42)	18030	18702	(73528.31, 0.37)
NSGA-II (seed 42)	20305	24587	
MOEA/D (seed 252)	31921	32295	(70159.44, 0.60)
NSGA-II (seed 252)	29621	37445	

solution space moved further away from the reference point, towards a more optimal solution space. Thus, the hypervolume indicator is mainly used to assess the convergence performance. Nevertheless, it is also used to assess the diversity of the initial population. When the hypervolume indicator of the initial populations for different optimizers is compared, the larger number gives a more diverse initial population. The hypervolume indicator for each optimizer, with various seeds, is presented in Table 8.2. The values suggest that NSGA-II performed better in terms of the diversity of the initial population since the hypervolume indicator is larger compared to the MOEA/D algorithm. Meanwhile, as the difference between the hypervolume indicator of the initial and final population is comparably larger for the NSGA-II algorithm, it can score better than MOEA/D in terms of convergence to the optimum. Since a larger difference indicates that the design space moved further away from the initial population with each evolution.

Considering all the above points, a comprehensive decision can be taken. The computational power is taken as a significant limiting factor. It has been identified that MOEA/D had a limited performance with the available computational power. Not only it showed a hectic behavior for Objective 2, but also Objective 1 did not perform better than NSGA-II. One drawback of the NSGA-II, as it was mentioned by Ishibuchi et al. (2009), is the increased computational time, which is around 13 hours. Meanwhile, MOEA/D with n=35 had a computational time of 8-9 hours and MOEA/D with n=48 had a run time of 14. Since the larger neighbor size MOEA/D only slightly performed better in Objective 2 and did not improve Objective 1, it is discarded at the expense of increased run time, it is not chosen as a good optimizer. The hypervolume indicator also confirmed that NSGA-II has a better population diversity than the MOEA/D algorithm. Therefore, within the computational limit, the NSGA-II outperformed the MOEA/D algorithm and was chosen as the optimizer to be used in the research.

8.4. Optimization Results

The results that are obtained from the optimization process are discussed in this section. An extended analysis is performed to provide a more coherent understanding of the optimal solutions. The section is divided into two subsections, one for each vehicle. In each subsection a structured manner is followed. First, the objective space is discussed while identifying a few of the best individuals. Af-

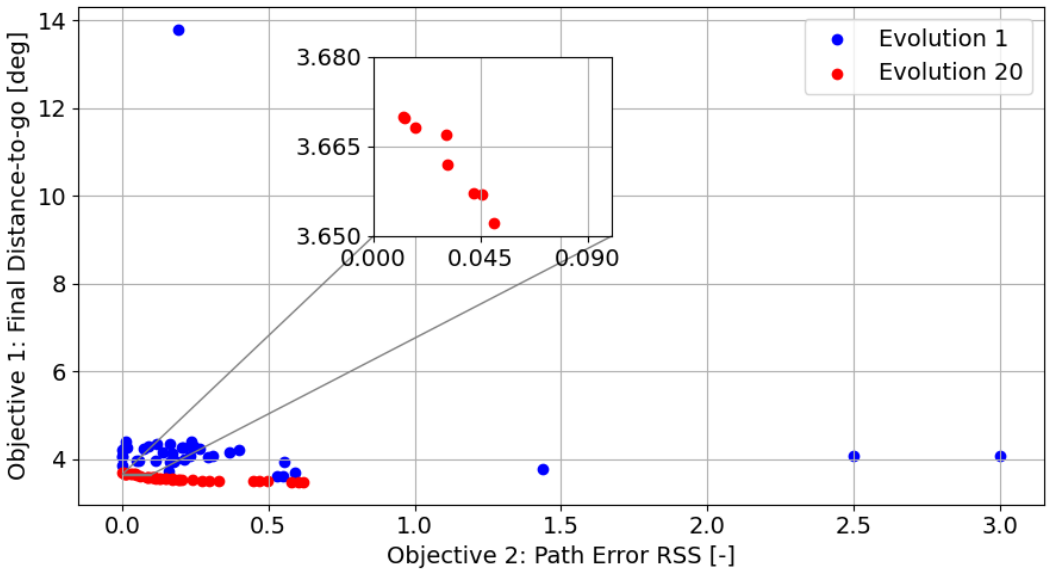

Figure 8.7: Objective space for the unpowered vehicle optimization

terward, the objective values alongside the trajectory histories are carefully analyzed to discuss the possible limitations of the trajectories. This information is used to perform a trade-off between the best individuals to choose the most optimum solution. In the end, a local refinement is performed to assess the validity of the optimal solution.

8.4.1. Unpowered Booster

After a familiarity is gained with the behavior of the aerodynamic angles and their effect on the trajectory, an optimization is performed. Previously it was identified that it is not feasible to initiate the turn maneuver for an unpowered vehicle during Phase 1. This is solely due to the nature of the ballistic flight. Since the vehicle gains altitude during this maneuver, the lift drops significantly. This results any aerodynamic steering command to be ineffective. Therefore, as long as the vehicle is unpowered, the ballistic flight has to be performed.

This causes the optimization to be performed in an decoupled manner. Therefore, the remaining two phases, Phase 2 and Phase 3, are optimized independent from one another. It is significant to note that the decoupled optimization approach have two major limitations. First of all, it poses a risk for the continuity of the trajectory, since the trajectory is now divided into two. Secondly, combination of the results that are obtained for each phase does not necessarily define the global optimum.

The resulting objective space is visualized in Figure 8.7. As it can be seen the distance-to-go values for the first evolution have a wide spread and are far from the optimal value. There are a few parameters, that had the objective value around 14°, note that these are the parameters that had a severe penalty due to the discrepancy they had between the final heading angle and the desired final heading angle. Therefore, they were the trajectories that failed to perform the turn maneuver successfully. Throughout the optimization process, when the fitness is evaluated, the individuals with the wrong final heading angle are killed off. In the final evolution, all the trajectories are terminated as they reach the desired final heading angle.

In real life, the RSS of the path error is a hard constraint due to the structural limitations of the booster. Thus, it is not possible to surpass the maximum allowable values. However, since the FESTIP study was not fully complete, for different phase studies, various limits were defined for the path constraints. Since it is not decided upon which value is the hard constraint, a contingency is regarded. This indicates that any individual that has the value 0-0.1 is regarded as the best individual for Objective 2. Looking back at the zoomed-in image in Figure 8.7, it can be seen that few individuals satisfy Objective 2. However, the final distance-to-go value obtained by these individuals, or any other individual within the last evolution, is far from the optimal value of 0.75°. Although Objective 1 is more flexible than Objective 2, the literature suggests that the expected values are within the range of 1.0°-0.75° (Mooij, 1997).

Table 8.3: The objective values for the best individuals

	Best Objective 1	Best Objective 2	Units
Final Distance-to-go	3.4859	3.6843	deg
Path Error RSS	0.6025	0	-

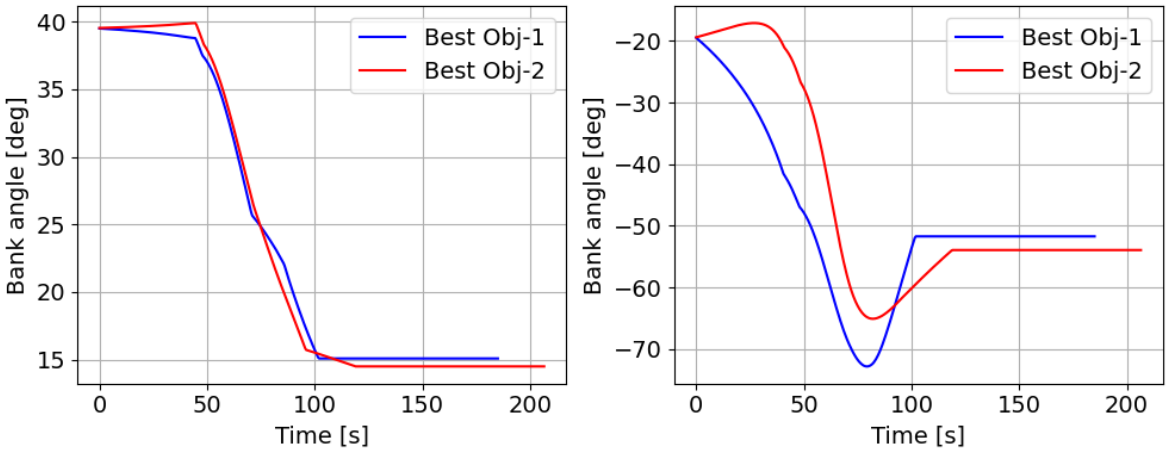

Figure 8.8: Comparison of the control histories of the two best individuals

Further analysis is performed on the control and trajectory history of the best individual, which is also the best objective 2, and the best objective 1 individual. It is aimed to obtain a more coherent understanding of the trajectory by comparing the two. These individuals and their corresponding objective values are represented in Table 8.3.

The control histories for both individuals are depicted in Figure 8.8. The angle of attack history for both individuals is comparable. When the values of the angle of attack are further investigated. It is identified that in the first 50 seconds, the vehicle flies with a 40° angle, which corresponds to the maximum angle of attack hence the maximum lift force. Meanwhile, as the vehicle dives deep into the atmosphere, the angle of attack value has shifted from the maximum lift to deliver the angle of attack that provides the maximum lift-to-drag ratio. Note that after 100 seconds on-wards the turn maneuver is initiated. At this point, maximizing the lift-to-drag ratio provides a greater lift, which is essential to sustain the centripetal force during the turn maneuver, while minimizing the resistive force, which is the drag. It is significant to note that, as these values of the angle of attack provide higher aerodynamic performance, they also cover a larger range while minimizing energy consumption. Meanwhile, a larger difference can be observed between the two bank angle histories. The latitude and longitude history presented in Figure 8.9 illustrates the effect of different bank angle histories. An early initiation of the turn maneuver alongside a smaller turn radius yields a smaller distance-to-go value at the expense of violating the g-load constraint.

As it is observed from the best individuals in Table 8.3, value of the first objective for each individual are significantly close to one another. Since distance-to-go value is not significantly improved by the smaller turn radius, it is not reasonable to risk the path constraints. Therefore, the best objective 2 case is identified as the best individual for this optimization.

Local Refinement

A local refinement process is followed after the optimization. Local refinement is a post-optimization process that is used to fine-tune and validate the solution. The methodology is as follows. Once the decision vector of the best individual is extracted, the values of each factor are altered between $\pm 10\%$ of the original value. Therefore, by introducing a small disturbance, the vicinity of the best individual is explored to identify whether more optimum solutions can be obtained. If the answer is no, it is confirmed that the result obtained is reliable and the optimization algorithm is not stuck at a local optimum. Since the first objective of the best individual is far from the optimal value, it was initially suspected that the optimization algorithm is stuck in a local optimum. The results obtained from the local optimum are

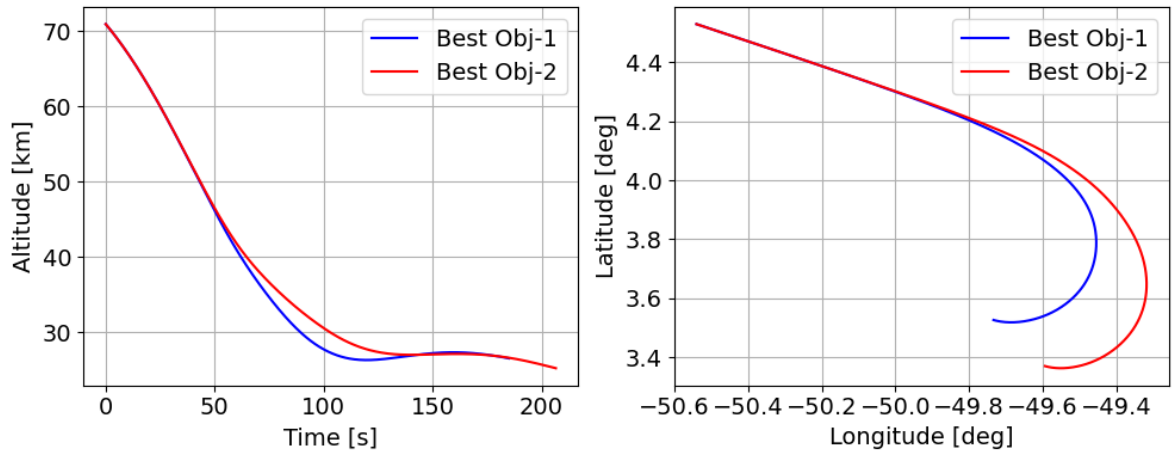

Figure 8.9: Comparison of the trajectory histories of the two best individuals

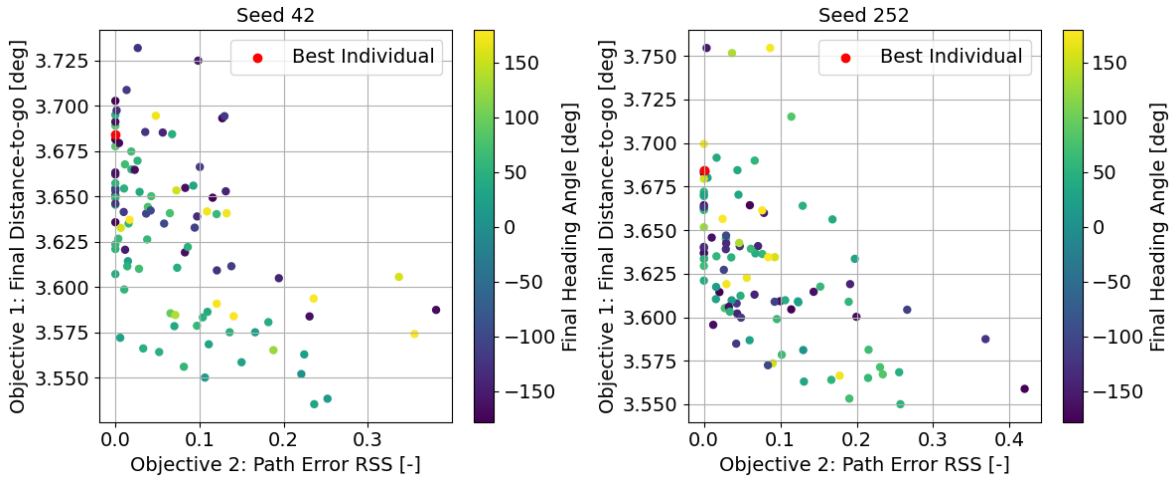

Figure 8.10: Objective space for the unpowered vehicle optimization

depicted in Figure 8.10. At a first glance, it seems like there are many other individuals that have 0 path error RSS and have a smaller distance-to-go than the best individual that was obtained from the optimization. However, once the final heading angle of these trajectories are regarded, it is analyzed that none of the trajectories fulfill the final heading angle constraint. Therefore, they have a significantly high penalized Objective 1, which raises the final distance-to-go value to 10°-14° again. As it was identified previously, the final heading angle is a critical constraint. It defines whether or not the vehicle is actually pointing towards the landing site and not meeting this constraint could potentially jeopardize the rest of the mission, such as precise landing. Therefore, the results of the local refinement refute the initial suspicion.

Note that since the Monte Carlo analysis is a random process, the reliability of the analysis is dependent on the number of iterations. Therefore, a sample size of 100 iterations is performed with 3 different seeds, which are 42, 195, and 252. Nevertheless, in all three cases, it is confirmed that the obtained result is the global optimum. Note that to avoid data clustering; only a few results are presented in here. To access the complete set of local refinement results one may refer to Appendix B.

Although it is validated that the best individual is indeed the global optimum, the large value of the individual for the final distance-to-go poses a challenge for Phase 3. It is suspected that a vehicle with only aerodynamic capabilities can not perform a glide back for a distance-to-go of 3.67°, which roughly corresponds to 390-410 km. Originally, the exact distance covered by 1 degree of latitude or longitude is dependent on the precise location since the Earth is not a perfect sphere. Nevertheless, since a spheroid Earth model is implemented in this study, the distance covered by 1 degree can be obtained

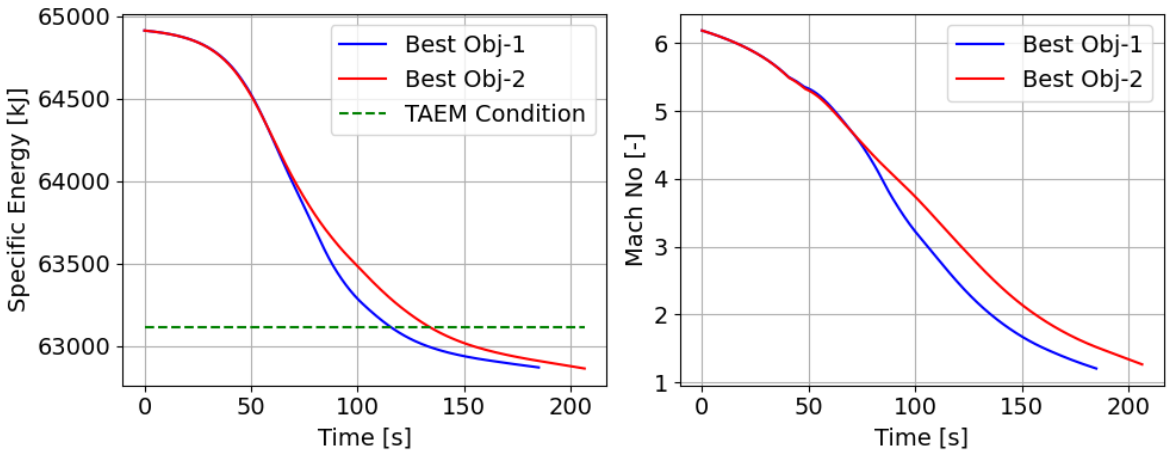

Figure 8.11: Comparison of the energy histories of the two best individuals

by using the simple arc length equation below:

$$\theta r = d \tag{8.8}$$

in which θ is 1 degree in radians and r is the radius of Earth, which is 6378 km. As a result, the distance d is calculated to be equal to 111 km.

To validate the above point, an energy state comparison is performed. For the re-entry vehicles, such as the Space Shuttle and HORUS, the TAEM phase starts at an altitude of 25-30 km, around Mach 2.5-3 (Moore, 1991). As the preliminary analysis of the trajectory yields, for the unpowered flyback booster at an altitude of 25 km the corresponding Mach value is changing between 1.2-1.5. The Mach number history for each individual is visually represented in Figure 8.11. Therefore, as the flyback booster separates at lower Mach numbers from the launcher, the flight trajectory of the booster is different from the flight trajectory of the Space Shuttle. Thus, the Mach number profiles for the two vehicle are not matching for the same altitudes. Nevertheless, for smaller vehicles Naftel and Powell (1993) state that the TAEM phase begins around Mach 0.8-1.1 at an altitude of 7-10 km. Although these values would depend on the mission characteristics, since Naftel and Powell (1993) also analyzed the glide back capabilities of a booster stage, the energy state comparison is predicated on the reported values. The specific energy, also identified as the energy height, is calculated using the equation below (Mooij, 2016):

$$E_h = 0.5V^2 + gh \tag{8.9}$$

in which V is the velocity of the vehicle, h is the altitude of the vehicle from center of the Earth, and g is the gravitational acceleration. It is stressed that the above representation of the energy is for a flat Earth. As was discussed in Chapter 4, the Coriolis acceleration and the centripetal acceleration are discarded during the analysis of this study, since the both terms would be dominated by the gravitational and aerodynamic acceleration and would become insignificant. Yet, another consequence of the flat Earth model is that g is a constant. Compared to the radius of Earth, Phase 3 of the flight is conducted in a relatively thin layer of the atmosphere. Thus, taking g as a constant is a feasible first order approximation.

The resulting energy states that are illustrated in Figure 8.11 suggest that the energy required for the TAEM condition is much more than the current energy of both individuals, at the end of their trajectories. This indicates that both individuals lack sufficient energy to successfully perform Phase 3 and meet the TAEM condition. At this point, the need for a propulsion system is emphasized so that the distance of 360 kilometers may be covered. With the capability of a powered flight, the booster may reduce its final distance-to-go more efficiently than an unpowered flight. The capabilities of the powered flyback booster are further studied in Section 8.4.2.

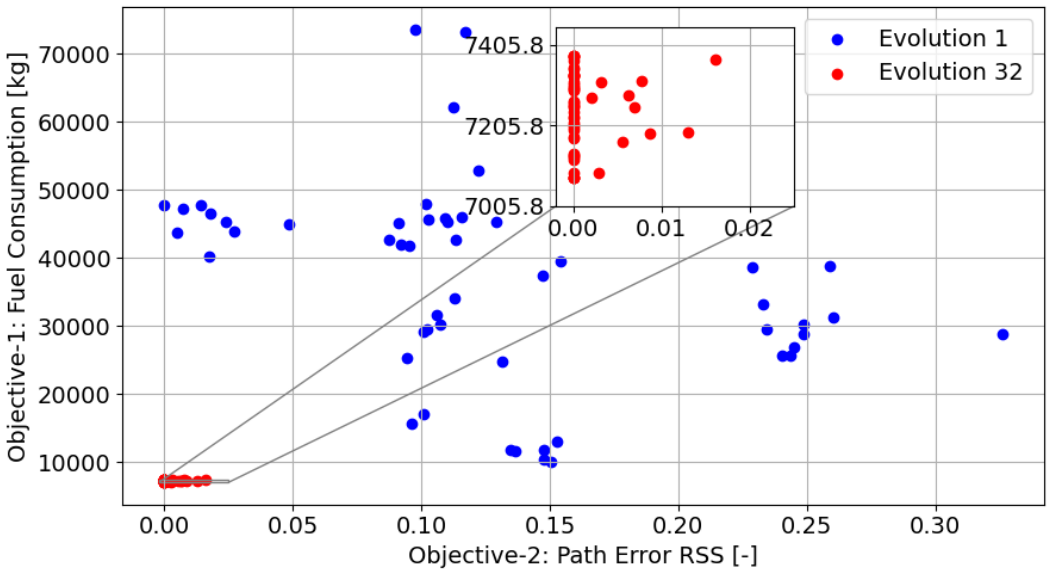

Figure 8.12: Objective space for the powered vehicle optimization with seed 42

8.4.2. Powered Booster

As it has been identified previously, the mission design continues with finding the optimal trajectory for the powered flyback booster. To have a more efficient process of finding the optimal solution, the decision variable range was adapted through a design space exploration. The resulting objective space is visualized in Figure 8.12.

The discussion of the results begins by analyzing the first population, which is identified as Evolution 1 in Figure 8.12. In the first population, the individuals are diversely spread in the objective space. There are significantly high values for fuel consumption as well as high values for the path error RSS. Further analysis of the initial population's fuel consumption values suggests that the large values are due to the penalty functions, as visualized in Figure 8.13. The unpenalized fuel consumption for the first individual is within 10,000 - 20,000 kg of fuel. As the final distance-to-go and final heading angle are added as a penalty function, the value of the first objective increases. Note that, the final heading angle penalty is relaxed for the powered vehicle. The values between $-70° < \chi < -50°$ are accepted as feasible values. This was due to the fact that while $-70°$ of a heading angle took the vehicle to a target point in which a TAEM phase can be conducted with a final HAC maneuver, values around $-60°$ to $-50°$ allowed the trajectory to meet with the main leg of the trajectory, forming a latitude and longitude profile that resemblances an airfoil or a teardrop.

Once the heading angle penalty constraint is relaxed, it is identified that the majority of the penalty is introduced by the final distance-to-go constraint. Considering the individuals in Figure 8.14 it can be seen that many of the trajectories are overshooting the target point before reaching a termination condition. This causes the vehicle to have large final distance-to-go values. Furthermore, due to the relatively long trajectories, the unpenalized fuel consumption values are also raised. Hence, the nominal value of unpenalized fuel consumption at Evolution 1 is around 10,000 - 20,000 kg, which is relatively when it is considered that the booster mass is only 57,000 kg.

Examination of Objective 2 yields that a wide range of path error RSS is covered in Evolution 1. In fact, from the first population, the optimizer could identify a few trajectories that did not violate any path constraints, hence having a 0 path error. Objective 2 is further inspected to obtain which path constraint is violated the most. Looking back at Section 5.2.2, the path constraints are imposed on the maximum heat flux, maximum g-load, and trim condition.

The heat flux constraint is often violated by re-entry vehicles. As the vehicle has a steep re-entry with high speeds, the compression and shock waves are increased in the atmosphere. Consequently, the vehicle experiences increased temperatures from the atmosphere, also known as aerodynamic heating, which leads to higher heat flux. Since the flyback booster does encounter these circumstances during its atmospheric flight, it was expected to observe no violation in the heat flux constraint.

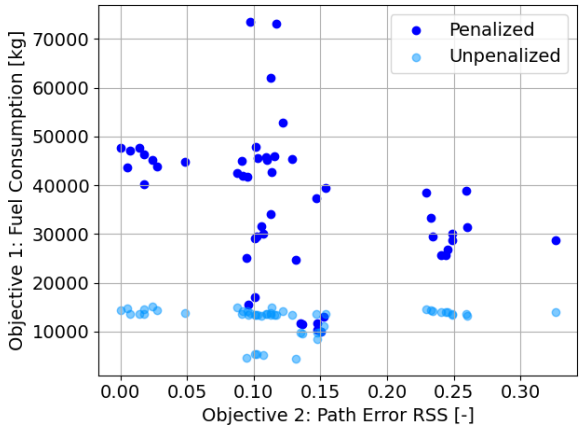

Figure 8.13: Comparison of the penalized and unpenalized objective space for Evolution 1

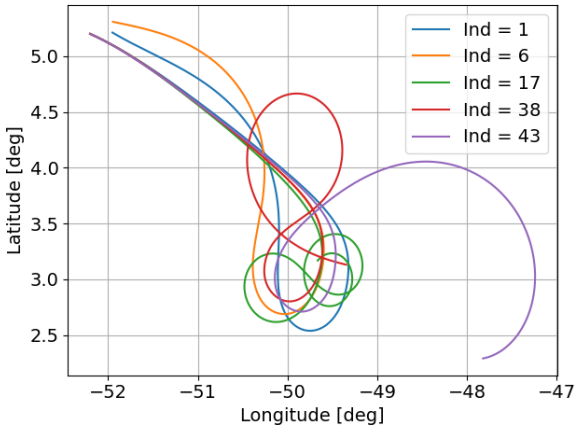

Figure 8.14: Latitude and longitude graph of random individuals from Evolution 1

In the meantime, it was expected to observe violations in g-load and trim conditions for certain trajectories. However, when the values are analyzed, it is identified that the individuals in Evolution 1 only violate the g-load constraint. Therefore, every trajectory in the first population is trimmable. The powered vehicle has a fixed angle of attack profile, which could dictate that the trim condition is fixed. Although the angle of attack and Mach number are the two main parameters that influence the trimmability of a vehicle, as the thrust elevation angle changes it was expected to observe a change in the trim condition, perhaps even identify untrimmable trajectories. A further discussion on this topic is carried out Section 9.3. Therefore, in Evolution 1 the only path constraint that is consistently violated is the g-load constraint.

Moving from the initial population to the final population, a significant drop in both objectives is identified. Meanwhile, a peculiar trend is spotted in the final population. Looking at Figure 8.12, it is not possible to observe a clear, well-defined Pareto front. Ciftcioglu and Bittermann (2009) state that the formation of the Pareto front is often dependent on the way the multi-objective optimization problem is defined. This situation occurs when there are conflicting objectives and the optimizer obtains a solution that represents the best compromise between these two objectives. Thus, achieving a certain level of optimum in one objective may cause another objective to have a fixed value, which is Objective 2, in this case. The conflicting nature of the objectives could be due to the constraint penalty introduced in Objective 1. As a result, the final solution space may not have a well-defined Pareto front but converges for one objective directly, while finding an optimum for the other one in the bounded space. Although the absence of a well-defined Pareto front does not necessarily indicate that the solution is bad, it could suggest that perhaps defining the multi-objective optimization problem differently could yield more optimal results.

The trend that is observed in Figure 8.12 is also identified as clustering. Clustering indicates that the solutions obtained by the algorithm are concentrated in a certain area of the design space. Originally, the NSGA-II algorithm avoids clustering by implementing the crowding distance. As it was explained in Section 8.3.1, the crowding distance measures the density of the Pareto front. A high crowding distance value indicates that the solution space has a more evenly spread Pareto front. Thus by introducing more diversity, clustering is avoided. However, although crowding distance is present, clustering can still be observed for the problem at hand. This indicates that certain characteristics of the optimizer challenge the algorithm and diversity cannot be maintained effectively with each evolution. The first reason is the complexity of the multi-objective problem, as identified above. The second reason is the premature convergence to a local Pareto front.

It is possible to avoid this phenomenon by increasing the population size, improving the initial guess, and implementing hybrid approaches, such as combining the NSGA-II algorithm with another algorithm, as was researched by Bilgen (2017). Note that the method adapted in this research is improving the initial guess through local refinement, which is implemented and explained at the end of this section.

Nevertheless, the significant individuals in the objective space can be identified for further inspection. Precisely, three individuals are chosen for further evaluation. The first individual has the best Objective

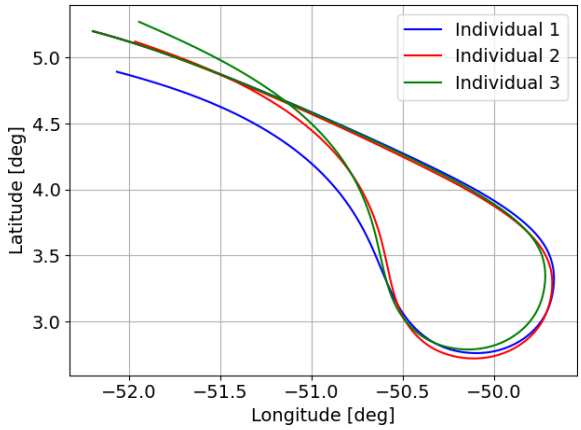

Figure 8.15: Latitude and longitude graph of chosen individuals from Evolution 32

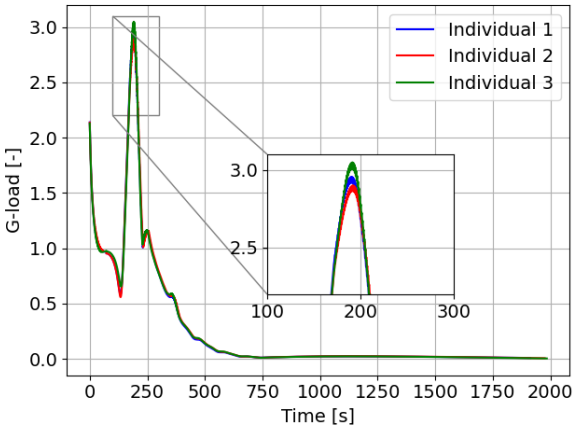

Figure 8.16: G-load vs. time of chosen individuals from Evolution 32

Table 8.4: Best individuals from Evolution 32 for seed 42

	Individual 1	**Individual 2**	**Individual 3**	**Units**
Fuel Consumption	7075.79	7380.12	7368.91	kg
Path Error RSS	0.0	0.0	0.016	-

1 and Objective 2, the second individual has the best Objective 2 but the worst Objective 1, and the final individual has the worst Objective 2 and a very high Objective 1. The objective values of each individual are presented in Table 8.4.

Looking at the latitude and longitude history of each individual in Figure 8.15, it is seen that the reason behind varying Objective 1 values is the fact that the termination condition for Individual 2 and Individual 3 is reached later than Individual 1. Consequently, more flight time caused the booster to consume more fuel. Individual 1 reaches the final distance-to-go without changing the final heading angle that is obtained from the turn maneuver. Thus -70.4° of a heading angle is sustained till the final termination condition of 0.75° is reached. Note that the other two termination conditions, which are the lower altitude and velocity, are not reached. This indicates that the vehicle was able to sustain a leveled flight until the desired final distance-to-go is reached. Meanwhile, Individual 2 carries to change its heading angle to -55.2° to meet with the main leg of the trajectory, which is the main difference of this trajectory from Individual 1. This extra maneuver is potentially causing the vehicle to burn more fuel. Meanwhile, Individual 3 overshoots the main leg and proceeds further until the final distance-to-go of 0.75° is reached. Both from Individual 1 and Individual 3, it can be identified that the booster meets with the TAEM conditions and even have sufficient offset to perform a HAC maneuver. Nevertheless, although all three trajectories almost seem identical, the longer two trajectories, Individual 2 and Individual 3 cause the vehicle to consume more fuel. This could indicate that perhaps the heading angle constraint should not have been relaxed, as higher heading angle values cause the vehicle to consume more fuel. Nevertheless, Individual 2 and Individual 3 could increase the fuel consumption in this fly back trajectory at the expense of reducing the fuel consumption in the TAEM phase. To make a conclusive decision about that further research is required.

When the path constraints of these three individuals are analyzed, it is observed that the only constraint that is consistently violated is the g-load. In Section 5.2.2 it was identified that the maximum allowable g-load is 3g. All three individuals come close to this constraint around 170-210 seconds, as it is depicted in Figure 8.16. In the final population, only Individual 3 has violated this constraint slightly. To observe the g-load of the vehicle the components that contribute to the total acceleration are regarded. These are the aerodynamic acceleration, gravitational acceleration, and thrust acceleration. The point in which the g-load rises to the vicinity of 3g, is the point after the peak altitude of Phase 1, as the booster dives to the deeper parts of the atmosphere. Due to the nature of this maneuver, the aerodynamic acceleration is rising at this point. The aerodynamic acceleration is dependent on the value of the lift and drag. Since the angle of attack profile of the powered vehicle is fixed, across different

Table 8.5: Best individuals from Evolution 0

	Individual 4	Individual 5	Units
Fuel Consumption	47,757.43	28,722.24	kg
Path Error RSS	0.0	0.326	-

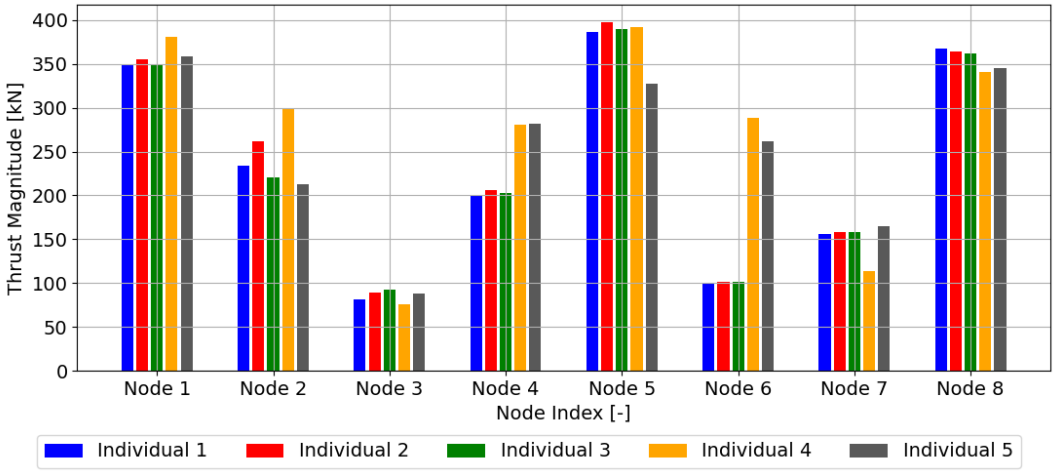

Figure 8.17: Thrust magnitudes for the selected individuals from Evolution 32 and Evolution 0

trajectories the lift and drag profiles are almost fixed as well. However, since the thrust force affects the trajectory there could be changes in other components of the lift and drag, such as the velocity and the density. Therefore, although the general behavior of the aerodynamic acceleration across different trajectories are fixed, the values may differ slightly.

Nevertheless, the main reason why the total acceleration is rising above 3g is due to the combination of the additional thrust acceleration and aerodynamic acceleration. However, since the vehicle has a direct control over the thrust force, the value of the thrust force is adapted through optimization to obtain a non-violated trajectory. In fact, the evolution of the thrust magnitude to comply with the g-load constraint can be examined better when the first population and the last population is observed simultaneously. Thus, two new individuals are identified. Individual 4 and Individual 5 are the best objective 2 and best objective 1 individuals, respectively, of Evolution 0. The values for these individuals are presented in Table 8.5. Looking at Figure 8.17 at certain nodes significant differences can be identified. Especially regarding the Node 5, which is the node that approximately corresponds to the 170-210 seconds. Meanwhile, the thrust profile of the last population is much more consistent, which is Individual 1, 2, and 3 in Figure 8.17.

One important point to highlight is that, from Figure 8.18, it can be observed that there are 7 operable nodes instead of 8 nodes. That is due to the fact that the vehicle is performing a pull-up maneuver from the 7^{th} node onward. This causes the vehicle to sustain the final altitude of 24 km. Consequently, the final node altitude of 10 km is not reached. As the booster pulls-up the nose at the 7^{th} node, it consumes less energy than pulling up the nose at 8^{th}. Since the 8^{th} node is at 10 km altitude, to pull the nose up at this point, the booster would have to overcome the additional increased atmospheric forces. It is also utmost importance to note that having the 8^{th} node defined is still important. Since there is an interpolation between the nodes, the values of the final node influence the trajectory. Without the 8^{th} node, the final value would stay constant for the rest of the trajectory. Meanwhile now, due to the interpolation, the value is not constant. This can be observed from the thrust magnitude graph in Figure 8.18. If it is desired to obtain an optimum trajectory only with 7 nodes then a new optimization has to be performed. This indicates that depending on the number of nodes, the solution space varies.

Upon considering all the discussions above, it is concluded that Individual 1 is the most optimum solution. At this point, the optimization is performed using the booster mass of 57,000 kg. This was the wet vehicle mass set by the Daimler-Benz Aerospace (1998). However, during their calculations and trajectory simulation, FESTIP only used fuel for Phase 3. Meanwhile, Phase 1 and Phase 2 are only

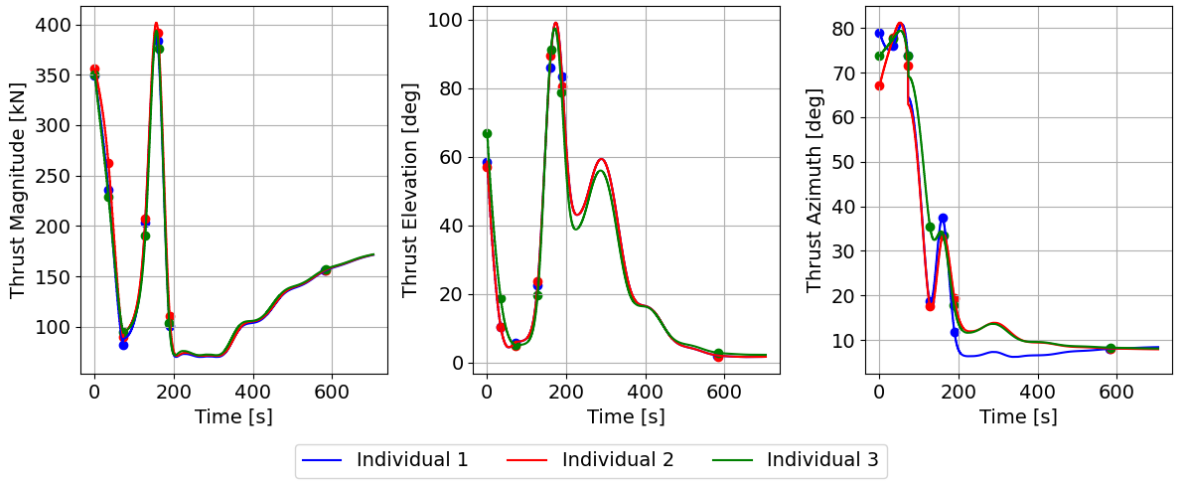

Figure 8.18: Thrust parameter history for the selected individuals of Evolution 32

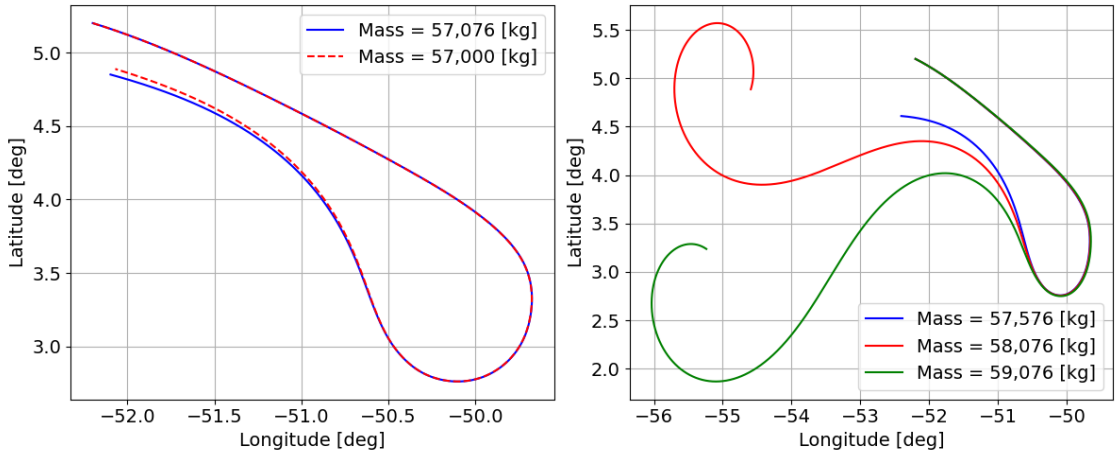

Figure 8.19: Optimum trajectory with different booster masses

performed by aerodynamic means. Thus, it could be that the initial fuel set by FESTIP is insufficient such that the vehicle may require more. As it is mentioned in Section 2.2.1, the mass properties of FSSC-16 suggest that FESTIP has calculated to have a fuel consumption of 7,000 kg, in which 5,000 kg is for the fly back and 2,000 kg is the reserved fuel. The optimum solution yields that the required fuel mass is 7,075.79 kg. The difference between the two calculations is around 76 kg, which corresponds to 1.082% of a difference. Not only this difference is significantly small, such that it is within the allowable limit for an error in mission design, which is around 10%-20% depending on the design phase, but also it does not significantly affect the trajectory (Hayhurst et al., 2016, SRE-PA and D-TEC staff, 2012).

When the optimum thrust parameters are used to simulate the trajectory with the new mass of 57,076 kg, it is observed that the booster can still follow the optimum trajectory, as it is visualized in Figure 8.19. This yields that when the reserved fuel is used and a bit more fuel is added, the booster can follow the optimal trajectory. Although no direct explanation is provided, perhaps FESTIP has calculated the 2,000 kg of reserved fuel accounting for the fact that the entire trajectory may be powered.

Finally, it is also investigated whether it is possible to add 2,000 kg of reserved fuel to this new mass of 57,076 kg and still follow the optimum trajectory. The results are shown in the right graph in Figure 8.19. When a reserved fuel of 2,000 kg or 1,000 kg is added the booster deviates from its optimum trajectory. This suggests that the trajectory is sensitive to booster mass and can tolerate around 1% of a change since 500 kg of fuel did not deviate the trajectory significantly. When the mass of the booster is increased, the required thrust to reach the desired conditions is also increased. Especially at the end of the trajectory, when the booster has to perform a pull-up maneuver by overcoming the

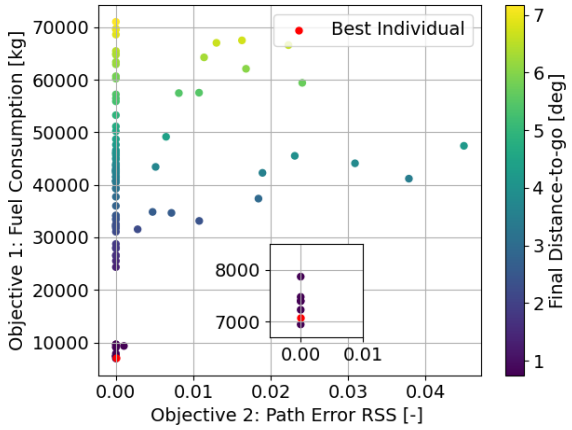

Figure 8.20: Powered optimization local refinement with seed 42

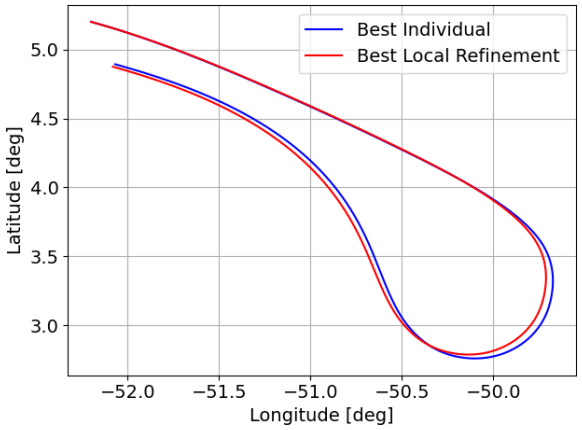

Figure 8.21: Latitude and longitude history of the best optimization and local refinement individuals

gravitational force. As the required thrust is increased, the propulsion system expels more fuel.

Local Refinement

To verify that the obtained solution is indeed the optimal, a local refinement process is followed. Local refinement is used to fine-tune the solution by exploring the objective space at the vicinity of the optimal solution. The process that is followed is identical to the one in Section 8.4.1. As it can be observed in Figure 8.20, out of 100 individuals, there is a single individual that performed better than the solution obtained by the optimization algorithm. The latitude and longitude history comparison of both individuals are presented in Figure 8.21. It is observed that the main difference is the radius of the turn maneuver, which could save that 130 kg of fuel for the best individual of the local refinement process.

The results suggest that a second round of optimization has to be performed to obtain a more optimal solution. It is possible to perform this optimization with two different methods. First a local optimizer can be implemented using the best individual, Individual 1, to discover the design space around. A second method is using the current global optimizer. However, if the optimization is re-initiated using an initial point that is close to a local minimum, which could be Individual 1 in this case, the algorithm converges towards the same region. When the optimization is initiated with a good initial guess, NSGA-II starts to search from a point that is already the optimal region in the design space. The diversity in the NSGA-II algorithm is preserved through non-dominated sorting and crowding distance. Nevertheless, when the initial guess is a non-dominated solution, which is Individual 1, the NSGA-II algorithm cannot escape to other design spaces.

Accordingly, a slight improvement in the optimal solution can be obtained due to crossover, mutation, and randomness of the algorithm. yet, it is expected to observe that the new optimal solution is significantly close to Individual 1. To cope with this problem, the optimization process has to be adapted to ensure that a different design space is discovered. This is achieved by using a different initial guess. This is achieved by adding the best individual of the local refinement to the initial population as an initial guess. When the NSGA-II algorithm encounters an initial guess that is superior to the previously converged solution, the search is guided towards this new region of the design space. Due to the non-dominated nature of the algorithm. Consequently, the offspring that follows this initial guess also have an improved objective value. Finally note that, the decision variable range is adapted, such that the range is $\pm$10% of the best individual of the local refinement. By doing so, the design space obtained by the local refinement is discovered further.

The results of the second optimization is presented in Figure 8.22. Note that the best individual of this optimization is identified as Individual 6, and the best individual of the previous optimization is Individual 1. Looking at Figure 8.23, it is seen that the largest difference in the thrust parameters is present in the thrust magnitudes. T_3, T_5, and T_8 has changed significantly between Individual 1 and Individual 6. In fact, the values of T_5 and T_8 exceeds the maximum allowable thrust limit of 400 kN. Note that the decision variable range was intentionally changed to explore this new design space, thus

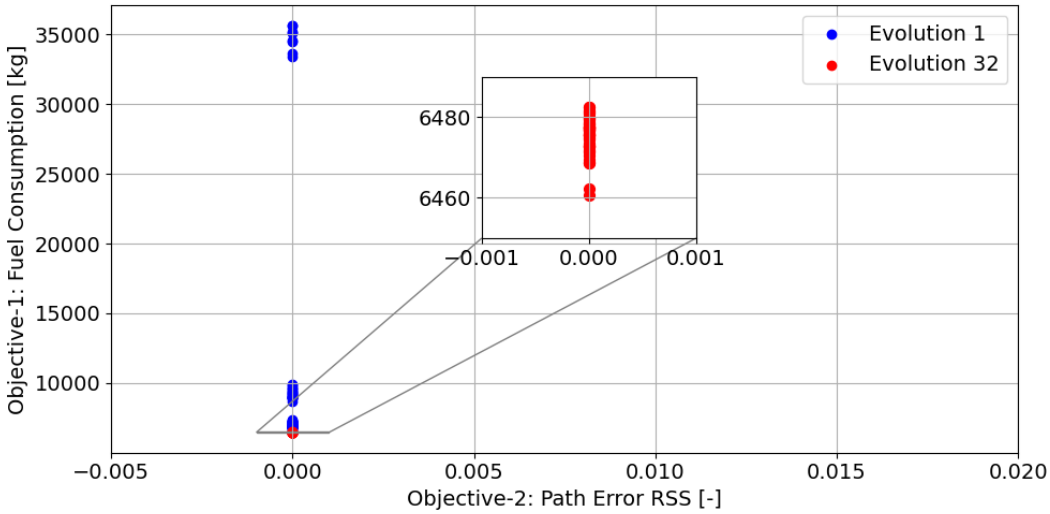

Figure 8.22: Objective space of the optimization with an adapted initial guess

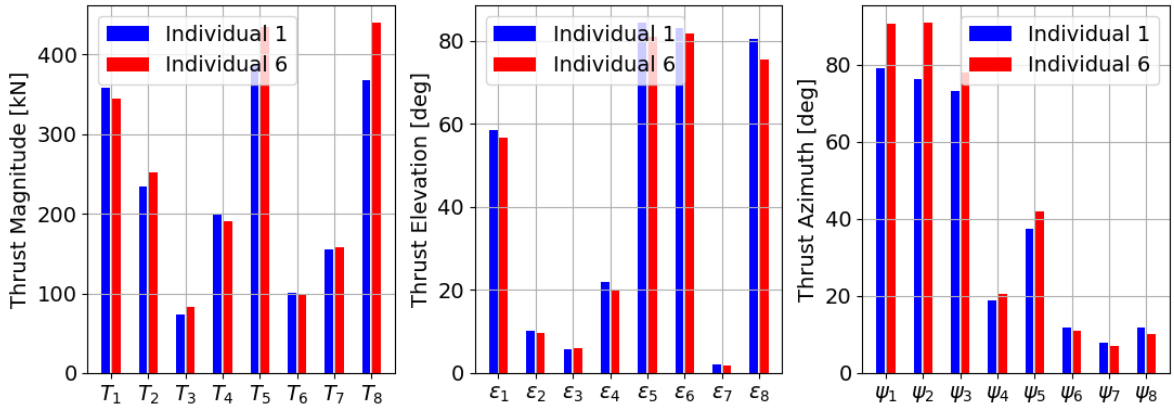

Figure 8.23: Comparison of the profiles of Individual 1 and Individual 6

it was expected to observe surpassing values. The thrust elevation profile is more or less in the same ballpark, whereas, the value of the thrust azimuth angle showed major differences for node 1 and node 2, hence ψ_1 and ψ_2.

A significant aspect that can be observed is that from the first evolution the parameters T_3, T_5, T_8, ψ_1 and ψ_2 changed to the values that are shown in Figure 8.23. Meanwhile this individual has a fuel consumption of 6,740 kg. The remaining parameters are changing minimally around these design points to adapt and obtain the least fuel consumption. In Section 7.4, it is discussed that the interactions between nodes are the driving factor for all three responses. To observe that the importance of the interactions, T_3, T_5, and T_8 values are changed to the ones of Individual 1. The resulting fuel consumption is around 8,623 kg, with a fuel rate of 4.78 kg/s. The fuel efficiency has dropped significantly. However, when each parameter is changed one by one, while the other two are fixed to their values in Individual 6, the resulting thrust values are still around 6,700 kg. The results suggest that the interaction between these three nodes are a driving factor for the fuel consumption.

The thrust elevation has a major influence on the trajectory, since it contributes to the final distance-to-go by defining the pull-up maneuver. However, the thrust elevation angle also has a large influence on the path error RSS, especially the trimmability of the vehicle. A comprehensive investigation on the trim and thrust elevation relationship is performed in Section 9.3. The algorithm guides the design space towards individuals that are not worse than the initial guess, which also have a zero Objective 2. As a result, Objective 2 value is consistently zero. Consequently, a clear conventional Pareto front cannot be observed.

Finally, in terms of fuel consumption Individual 6 is more efficient than Individual 1. Both individuals have the same fuel rate, which is 3.70 kg/s. Since Individual 6 reaches the desired point in a shorter duration, it also consumes less fuel compared to Individual 1. Note that, the FESTIP study did not have a definitive engine selection for FSSC-16, as they had a pool of three different engines. Thus, it would be recommended to select an engine that has only 10% more, thus 440 kN, than the current maximum allowable thrust. This would allow the vehicle to save an additional mass of 615.0 kg. Nevertheless, as the current engine does not have the increased thrust capability, Individual 1 is selected as the most optimum trajectory, once again.

9

Trajectory Reflection

The previous chapter concluded that the powered vehicle performed better at reaching to the vicinity of the desired final distance-to-go. In this chapter, it is aimed to perform a further investigation on the optimum trajectory. It is essential to gain a deeper understanding of the trajectory to identify the parameters that are most influential on the trajectory. Consequently, this provides valuable insights on the performance and feasibility of the trajectory. Information obtained from this analysis can later on be utilized to contribute to advanced development of reusable launch vehicles and flyback boosters.

9.1. Decision Variables Range Analysis

In Chapter 7 an extensive design space exploration process was followed to understand to what extend the chosen design variables affect the trajectory. It was identified that certain parameters influence the trajectory more than the others. As a result, new ranges were identified for the decision variables and implemented during the optimization process. Various literature state that by removing the unwanted design points or areas, the optimization process can be driven to desired solution spaces (Kang et al., 2011). However, since the performance of optimization is highly problem dependent, it is possible that the trajectory problem at hand is not sensitive to decision variable ranges. To evaluate the situation, a sensitivity analysis is conducted by comparing the solutions of the optimization when different ranges are used for the dependent variables. Three different set of ranges are used which are identified in Table 9.1.

Note that the adapted range decision variable is the one that is used in the optimization of the powered vehicle, as thoroughly explained in Section 8.4.2. Meanwhile, semi-adapted is the decision variables in which values of the $T_3 - T_7 - \psi_7 - \psi_8$ are changed. The T_3 and T_7 are adapted to have higher upper limit of 400 kN, while $\psi_7 - \psi_8$ adapted to have a higher lower limit of 30°. The importance of T_3 and T_7 is identified in Section 7.4. Especially low values of T_3 identified to be significant as that is the point where the vehicle begins to gain some lift. Thus excessive thrust could cause vehicle to skip. Furthermore, the lower limit of the ψ_7 and ψ_8 are adjusted to be 30°, because it was observed that in Adapted range optimization these final values are consistently around 15° - 25°. It is noteworthy to highlight that the value of the elevation angle at the final nodes are not changed. During the design space exploration, it was clearly identified that ϵ_7 and ϵ_8 significantly influence the flight-path angle, which consequently effects the final distance-to-go. Finally, the full range of the decision variables, as it was identified at the end of the Section 7.3, are used.

As it can be seen in Figure 9.1, all three optimizers converge to a solution. However, the con-

Table 9.1: Change in the optimal decision variables

Type	Changed Variables
Adapted range	None
Semi-adapted range	$T_3 - T_7 - \psi_7 - \psi_8$
Full-range	All

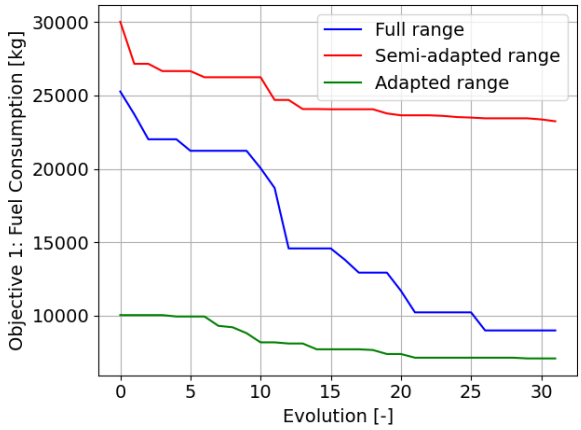

Figure 9.1: Best individual for Objective 1 at each evolution with seed 42

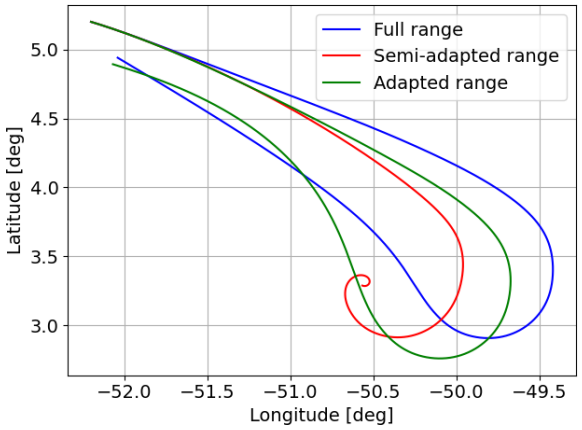

Figure 9.2: Latitude and longitude of the best individual at the final evolution with seed 42

Table 9.2: Change in the azimuth angle of the last two nodes across different ranged optimizations

	Full Range	Semi-adapted Range	Adapted Range	Units
ψ_7	18.0	57.51	8.0	deg
ψ_8	24.19	79.98	11.66	deg

vergence speed of the solutions is affected by the decision variable range. Comparing the initial and the final value of Objective 1, it is observed that the full range has the largest change in the value of Objective 1. Meanwhile both semi-adapted optimization and adapted optimization show convergence characteristics around 20th evolution. However, it is significant to note that fast convergence does not necessarily indicate that the converged value is the optimal solution or a feasible solution at all.

In Figure 9.2 the latitude and longitude histories for the best Objective 1 individual of all three trajectories are depicted. While the full range and adapted range optimizations could reach the vicinity of the desired final distance-to-go, the semi-adapted range optimization failed to do so. Instead, the vehicle gets stuck in the turn maneuver. Consequently, a spiral motion is observed. Since the range of the thrust azimuth angle at the last two nodes is adapted, the optimizer obtained values around the higher end of the range, rather than the lower end. The corresponding thrust azimuth angles are reported in Table 9.2. When the high azimuth angle is combined with a high thrust magnitude at the last node, which is around 400 kN for all three individuals, the booster has an excessive side force. As the side force increased, the booster could not get out of the turn maneuver and got stuck in a spiral motion. Therefore, partly changing the decision variable, without properly accounting for the decision variable range causes the algorithm to converge towards a local optimum, which is significantly less feasible than other local optimums.

It is significant to note that both the adapted range and full range converge towards relatively close values. Since the full range optimization shows a large decreasing trend over various evolution indices, it is possible that within a few more evolutions, the objective may drop further. In that case, a trade-off has to be performed. It is always a possibility to use the full decision variable range, especially when a design space exploration is not or cannot be performed. However, this may result in a higher computational time and a slower convergence speed. Meanwhile, the largest difference between the full range and adapted range optimization is in the thrust azimuth profile. Although the range of the thrust azimuth in the first node is not adapted, it can be seen that for a full range optimization, the optimizer found a much lower value. For the adapted range optimization $\psi_1 = 79°$ and for the full range optimization $\psi_1 = 29.14°$. The result suggests that, technically the booster is also possible to obtain a trajectory that can reach the final distance-to-go with a lower azimuth angle at the first node. However, this is in return for larger fuel consumption, since as it can be observed from Figure 9.2, the turn maneuver is initiated a lot later in the trajectory. Note that for the complete list of the decision variables for each individual refer to Table B.2,Table B.3, and Table B.4.

This indicates that the value of the decision variable range is a driving factor for the optimization

process since it guides the optimization toward a more feasible solution space. Although all three simulations have the same number of individuals and evolutions, the adapted range and semi-adapted optimizations converged before full range optimization. Not only the full range optimization converged in many later evolutions but also had a longer computational time. This was due to the fact that initially there was a much larger design space to explore. The fact that the optimizer's convergence is dependent on the decision variable range indicates that it is crucial to bind the decision variables' range.

9.2. Bank Angle and Lateral Stability Analysis

As it was discussed in Section 7.3, the flight dynamics at the end of the trajectory is a complicated matter. Later on in Section 7.4 it was confirmed that the last two nodes are the most prominent nodes that define the behavior of the trajectory. If the thrust vector control is insufficient at these nodes, the vehicle cannot sustain a leveled flight. The desired final distance-to-go of 0.75° cannot be reached. However, at this point, controlling only the thrust vector could pose some problems. As the booster performs a leveled flight at the end of the trajectory, the flight dynamics are similar to the one of an aircraft. Due to the aerodynamic effects and maneuvers, a strong coupling between the yaw and roll moment can be addressed. To avoid this phenomenon often the control system performs an active control on the bank angle and the heading angle.

In such cases, the control coupling can introduce untrimmability and instability in the system (Day, 1997). Note that due to the lack of an aerodynamic database below Mach 1.2, the trimmability cannot be assessed toward the end of the trajectory. However, instability can potentially be observed, through the eigenmotion of the vehicle. Whether the eigenvalue is real or complex, indicates whether the motion of the vehicle is unstable or aperiodic (Mulder et al., 2013). However, it is also possible to observe the potential instabilities of the system without the eigenmotion, through the analysis of the trajectory history. In Section 7.2, it was discussed that to control the heading angle, a bank angle control was introduced. To assess the influence of the couplings in the trajectory, the bank angle profile is disturbed. It is decided to choose the unpowered vehicle's bank angle profile to assess the sensitivity of the booster to the control coupling. Since it is known that the booster can fly with this angle history, the disturbances in the system can be evaluated in a more structured manner.

Therefore, once the bank angle history of the unpowered vehicle is fed to the system, the optimum trajectory is evaluated again. The corresponding results are depicted in Figure 9.3. From the latitude-longitude graph on the left, a disturbance can be observed directly. At the end of the trajectory, there is a spiral motion, which is an aperiodic eigenmotion that has the bank angle as its main driving parameter. The spiral motion primarily contains a rotation about the yaw-axis with some roll that is often induced due to an uncoordinated flight. Excessive or insufficient control inputs such as rudder ailerons, or thrust azimuth, in this case. In Figure 9.3 the left graph visualizes the constant heading angle change. It can be seen that the vehicle encounters this maneuver right at the end of the turn maneuver, after the first large heading change. Potentially, the reason is that the thrust azimuth at this instant in time induces a large side force, causing the vehicle to be stuck in the turn, inducing a spiral motion. This is also identified as a thrust-induced yaw motion.

Therefore, although the longitudinal stability of the vehicle is briefly assessed in this study, it is also significant to identify the lateral stability and controllability. Without a proper later control system, a disturbance in the bank angle profile might severely influence the optimum trajectory. Note that, Mooij (1997) has also addressed the symmetric and asymmetric coupling for the HORUS vehicle. Meanwhile, Viavattene (2018) addressed these instabilities and potential couplings for the FSSC-1.

9.3. Thrust Elevation and Trimmability Analysis

As it has been identified previously the vehicle model is set up such that there is an active trim logic. Depending on the current angle of attack α and the Mach number M, the vehicle can correct its pitch moment both for the powered and unpowered vehicle. For the unpowered vehicle, the trim is solely dependent on the aerodynamic properties and the control surfaces. However, when there is an active propulsion system, like in the powered flyback booster, the trim is also dependent on the thrust force. When there is a thrust elevation angle, the force is distributed along the longitudinal axis of the vehicle. The T_{Z_B} then contributes to the pitch moment, the rotation around the y_B axis. In certain cases, the additional force could affect the trimmability of the vehicle. As it was first introduced in Section 4.4.3, the pitch moment induced by the thrust force is expressed in the body reference frame as below:

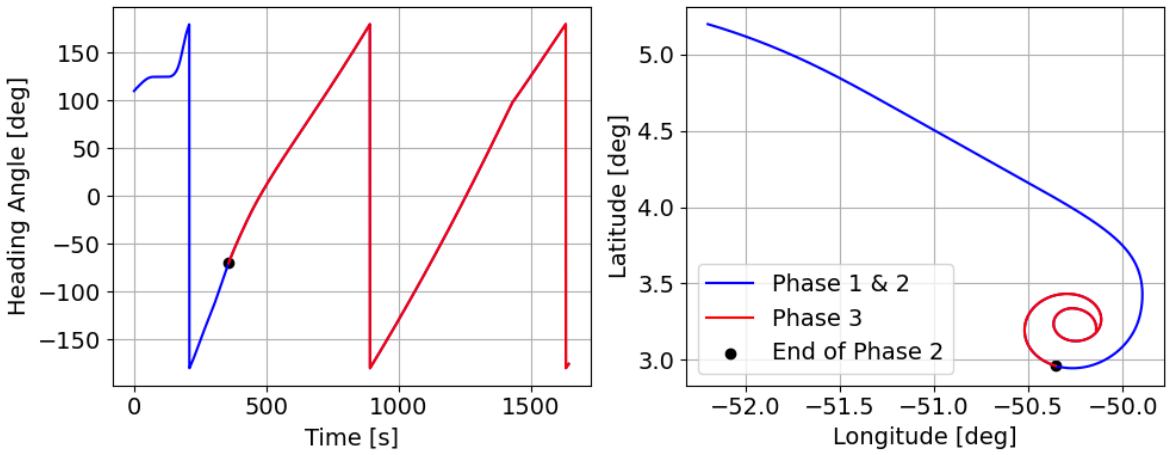

Figure 9.3: Visualization of the spiral motion due to the changed bank angle profile

$$M_{T,Y} = T_{Z_B} r_{X_B} \tag{9.1}$$

in which r_X is the distance between the CoT to CoM and M_{T_Y} is the moment around the Y_B axis due to the thrust force, thus the index T. Note that for FSSC-16 since the CoT coincides with the CoM in the Z_B axis, the forward thrust force T_{X_B} does not contribute to the pitch moment. This additional moment could affect the trimmability of the vehicle. To observe whether the thrust force effect the trimmability of the vehicle, the optimum trajectory is compared to a trajectory in which the thrust elevation is zero for the entire flight. The graphs in Figure 9.4 indicate that the vehicle is trimmable for both thrust elevation profiles. At the beginning of the trajectory, a bit of a difference in the deflection behavior of the body flap can be spotted. Between 0-200 seconds a difference in the deflection angles of the body flap can be spotted between the optimum thrust profile and $\epsilon_T = 0^\circ$ thrust profile. This difference is solely dependent on the force T_{Z_B}. Since this time incidence approximately corresponds to the ballistic flight, the aerodynamic forces are ineffective. Therefore, the pitch moment is driven by the thrust force in the Z_B axis, which is calculated using the thrust magnitude T and sinus of the thrust elevation angle ϵ_T. This indicates that the T_{Z_B} is high when the thrust elevation angle is far from zero. Consequently, the thrust force contributes to the pitch moment more and deflects the body flap more to correct for the pitch moment. Therefore, the body flap under zero thrust elevation profile followed a much constant and lower deflection angle profile. The zoomed-in graph is depicted in Figure 9.5. Afterward, during Phase 2, which roughly corresponds to 200-500 seconds, both the aerodynamic and thrust forces are contributing to the pitch moment. As the two forces are combined the uncorrected pitch moment became more negative, consequently the body flap is deflected negatively to induce counteracting positive pitch coefficient. Note that as the thrust force is located aft of the center of mass, it induces a negative pitch moment and pulls the nose of the vehicle down.

At this point, it is worthwhile to mention that, although changes in the thrust elevation angle affect the entire trajectory, the most dominant influence is observed in Phase 3. This was identified through the design space exploration and it confirms that the thrust elevation angle is highly coupled with the trajectory. However, Phase 3 is under below Mach 1.2. As was highlighted in Section 2.2.4, at this point the aerodynamic database misses the relevant information to assess the pitch moment. Therefore, the control surfaces are left at the final deflection point and kept constant for the rest of the flight.

The results suggest that the change in the thrust elevation angle has a very minor influence on the trim of the vehicle in Phase 1 and Phase 2. However, to observe whether or the trim and thrust force sustain this weak relationship, the change in the moment coefficient in Phase 3 is observed. Considering the trim graphs in Figure 9.4 again, although the C_m for the optimum thrust elevation profile is a bit higher, no considerable change in the C_m can be observed from 600 seconds onward. Thus, for the entire flight profile, a change in the thrust elevation angle has a minor influence on the deflection angles. Therefore, the thrust elevation angle does not severely affect the trimmability of the vehicle.

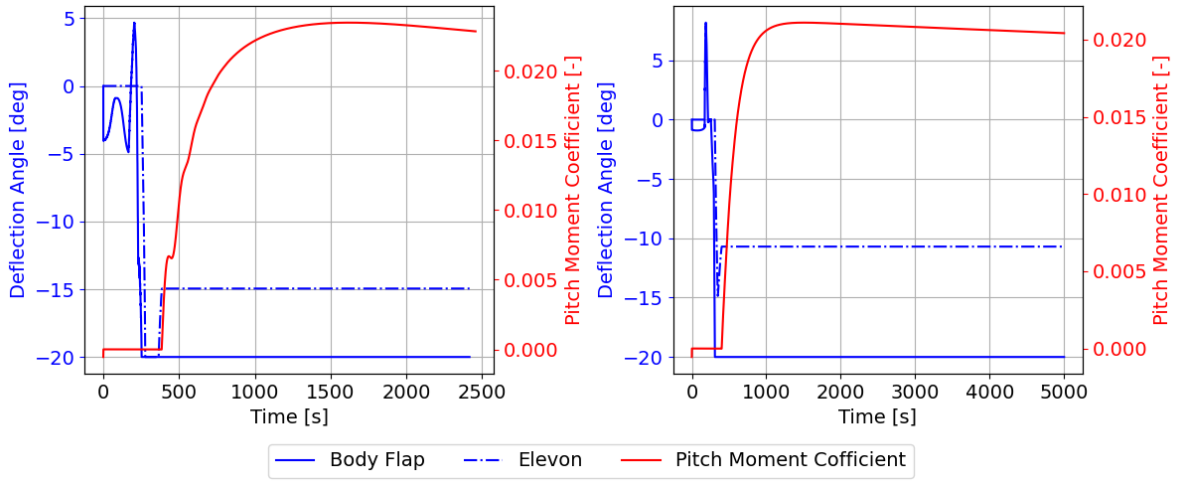

Figure 9.4: Optimum trust elevation profile (left) and $\epsilon_T = 0°$ profile (right)

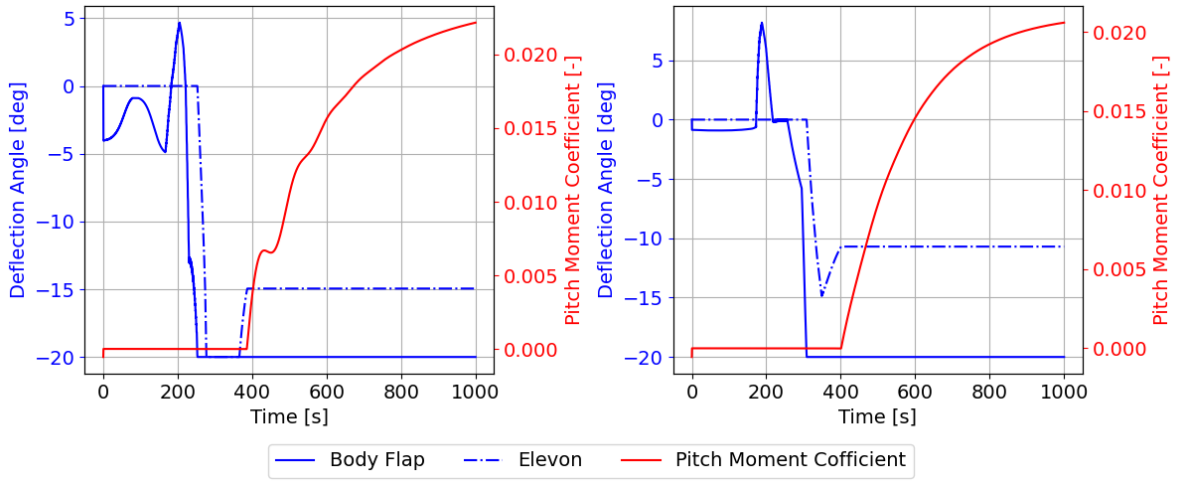

Figure 9.5: Zoomed in figure for the optimum trust elevation profile (left) and $\epsilon_T = 0°$ profile (right)

It is of utmost importance to regard that this weak relationship between the thrust and trim is dependent on the vehicle design. Changing the distance of the CoT from CoM or the magnitude of the thrust force could increase the pitch moment contribution of the thrust force. As a result, a more correlated relationship can be spotted between the trim and thrust as the aerodynamic surfaces would have to be deflected more to compensate for the increased thrust contribution. If there were to be a real decoupling between the trim and thrust, for any thrust condition, the deflection of the control surfaces must have been identical. This decoupling nature of the thrust and trim is highly advantageous for the control system of the booster. The longitudinal stability of the booster is solely dependent on the angle of attack α, Mach number M, and control surface deflections δ. The control system only has to optimize for these variables to sustain stability and discard the thrust elevation angle. Since there are fewer variables to take into account, the control system design can be more efficient. Feinreich et al. (1977) simulated a decoupled longitudinal flight for a short takeoff and landing (STOL) aircraft. As a result, it has been identified that such vehicles have better-handling qualities, which is a desirable behavior for a precise approach and landing.

10

Conclusions and Recommendations

The main research question of this thesis study was formulated as below:

RQ: *How can a mission design process be optimized for unpowered and powered flyback boosters to effectively compare the two configurations?*

To answer the above research question in a structured manner, the main research question was divided into six sub-questions:

- **SQ-1:** What are the characteristics of a flyback booster trajectory?
- **SQ-2:** What is the most suitable design space exploration technique for the fly back trajectory optimization problem?
- **SQ-3:** How sensitive is the flyback booster trajectory to aerodynamic and thrust parameter commands?
- **SQ-4:** How do the flight dynamics of the vehicle affect the development of the optimum trajectory?
- **SQ-5:** How does the optimum trajectory of a powered flyback booster differ from a trajectory of an unpowered flyback booster?
- **SQ-6:** How does the result of the design space exploration affect the optimization process?
- **SQ-7:** How does the optimum trajectory of the powered flyback booster perform under varying operational conditions?

This chapter will first discuss the conclusions derived from this study by answering the above questions in Section 10.1. Then in section 10.2, recommendations for further improvement will be presented.

10.1. Conclusions

As reusable launch vehicles became a more promising area in the aerospace industry, the concept of flyback booster has emerged. Throughout the years, preliminary analyses have been performed on different operational configurations, powered and unpowered. The trajectory differences between the powered and unpowered flyback booster significantly affect the overall mission. Therefore, a need to analyze the trajectories and perform a detailed mission design has evolved.

Understanding the characteristics of a trajectory is the key to identifying the relevant objectives and constraints of a mission. To investigate the design space exploration correctly, the first questions is answered accordingly, for the sake of convenience the questions are repeated:

SQ-1: What are the characteristics of a flyback booster trajectory?

It was found that the the identification of the trajectory is problem-specific since it is dependent on the initial conditions. Due to the current initial conditions, the booster first encounters a ballistic flight in Phase 1. The ballistic flight causes the booster to increase its range, as the booster flies further away from the launch site. Due to high altitudes at this instant, the booster does not have effective

aerodynamic control. Upon completion of Phase 1, the turn maneuver is initiated in Phase 2. This is the maneuver performed to change the heading angle of the booster to direct it toward the landing site in Kourou. Depending on the termination point of Phase 2, Phase 3 can be defined. This is the phase in which the vehicle performs a straight flight to the landing site. The definition of Phase 3 is highly dependent on the final conditions of Phase 2. For instance, if Phase 2 ends at high altitudes, the booster can perform Phase 3 in a descending manner. However, due to the TAEM conditions of flyback boosters, it is not advised to have a final altitude lower than 10 km. Therefore, if the booster is at the vicinity of 10 km at the end of Phase 2, then Phase 3 would be performed in a straight leveled flight until the final distance-to-go is reached.

The second sub-question is answered accordingly:

SQ-2: What is the most suitable design space exploration technique for the fly back trajectory optimization problem?

The strengths of different design space exploration were touched upon by implementing a one-at-a-time simulation, full fractional factorial design, and fractional factorial design with Taguchi interactions. The findings of the one-at-a-time simulation demonstrated the importance of the node control strategy. When the thrust magnitude profile kept constant along the trajectory, either the fuel consumption was significantly high, for 100 kN it was around 50,000 kg of fuel, or the vehicle performed an ascending or skipping flight due to the constant excessive thrust. It was established that by changing the magnitude of the thrust force, at different points along the trajectory, the fuel consumption as well as the applied thrust force can be more manageable. The main focus of the one-at-a-time simulation was to identify the preliminary relationship between the decision variables and the trajectory to verify the basic relationships.

The second experiment, the fractional factorial design, was the first attempt to perform a structured design space exploration. However, having 24 decision variables introduced a high dimensionality, which complicated the post-processing of the fractional factorial design. As deliberate confounding was introduced with the use of orthogonal arrays, it became impossible to identify which factor contributed to which interaction. The findings confirmed the presence of complex interactions as the percentage contribution of fuel consumption varied significantly across different thrust magnitude levels. In the presence of a well-representative, sufficient model, changing the maximum thrust magnitude should not vary the percentage contribution to the response, since the response should be adapted in the same manner. This suggests that due to complex and non-linear interactions, the changes in the response do not correlate with the changes in the thrust magnitude. Investigating the error sum of squares suggests that this was the case for all three of the responses, namely final fuel consumption, final distance-to-go, and final heading angle.

The third, and final, method was a fractional factorial design with Taguchi interactions with an L_{32} design matrix with Resolution IV. Upon selecting the design space matrix, for each response, a different set of subsets are generated to observe the contribution of interactions to the response with minimal confounding with the main factors' contribution. In the end, the final decision variable range is obtained through this method. The overall design space exploration process concluded that although the Taguchi interactions of the fractional factorial design provide the most direct information on the factors and interactions, the process of using different design space explorations is important to identify the limits of the design space. One-at-a-tine simulation and the full fractional factorial design adapted the decision variable range by a small amount which created the design space that is explored thoroughly in the fractional factorial design with Taguchi interactions.

The analysis of the design space provided important insights into the flight dynamics of the flyback booster, which in return answers the third and fourth sub-question:

SQ-3: How sensitive is the flyback booster trajectory to aerodynamic and thrust parameter commands?

SQ-4: How do the flight dynamics of the vehicle affect the development of the optimum trajectory?

The fractional factorial design with Taguchi interactions identified the nodes that have the highest influence on the response. For fuel consumption these are nodes 2,3,7 and 8; for final distance-to-go, these are nodes 2,7 and 8, and for final heading angle, these are nodes 5,6,7 and 8. For fuel

consumption, it was identified that the thrust magnitudes have a direct influence on fuel consumption. Meanwhile, the thrust elevation and thrust azimuth angles have an indirect influence, since these can affect the duration of the flight. It was identified that among thrust magnitudes, T_2, T_3, T_7, and T_8 have the most influence on fuel consumption. During Phase 1, the vehicle is performing an ascent due to the nature of a ballistic trajectory. T_2 and T_3 are in the first part of the trajectory. During this part, due to a lack of aerodynamic control the ballistic flight causes the vehicle to fly further away from the target, which also increased the flight time. By adopting the thrust magnitude at this point, the duration of the ballistic flight was adjusted. This had a significant effect on the overall fuel consumption. If T_7 and T_8 are not effectively controlled, the vehicle does not have enough force to sustain the leveled flight. Therefore, the trajectory may be terminated early due to another termination condition, such as altitude or velocity. This would directly influence fuel consumption. Note that thrust angles also influence the flight time, hence the fuel consumption. The duration difference introduced by angles is around tens of seconds. Meanwhile, the thrust magnitude introduces thousands of seconds of a difference since it extends Phase 3 by flying to the target point.

The results of the final heading angle showed that the interaction between various thrust parameters was the strongest for this response compared to the other two responses. Since the heading angle at the last instant may suffer from accumulated interactions along the trajectory, it was significantly difficult to identify a coherent behavior. However, a strong relationship could be observed for the mid-point nodes, which are nodes 5,6,7, and 8. These nodes roughly correspond to the turn maneuver and after the turn maneuver. These are the two important instants for the final heading angle since during the turn the initial heading angle is adjusted and after the turn, the nodes are responsible for sustaining the desired final heading angle.

The fifth sub-question is answered upon obtaining the final decision variable range through the fractional factorial design with Taguchi interactions:

SQ-5: How does the optimum trajectory of a powered flyback booster differ from a trajectory of an unpowered flyback booster?

The optimization process began with an optimizer comparison. Using different performance metrics it was found that NSGA-II was a more suitable optimizer, regarding the problem at hand and the computational imitations. The optimum trajectory of the unpowered vehicle was different from what was expected. The result yields that the aerodynamic capabilities are not sufficient to optimize the trajectory past a final distance-to-go below 3°. On the other hand, the powered flyback booster successfully reached the TAEM phase with a final distance-to-go of 0.75°. In the meantime, the booster only consumed 7075.79 kg of fuel and fulfilled all the path constraints. The fuel consumption value is promising since it is only 76 kg more than what FESTIP calculated in the design study of FSSC-16. The local refinement results of the powered vehicle concluded that although it is possible to obtain lower fuel consumption, to achieve that the thrusting capability of the vehicle has to be increased by at least 10%.

The two final sub-questions are closely related. Therefore, both are answered accordingly:

SQ-6: How does the result of the design space exploration affect the optimization process?
SQ-7: How does the optimum trajectory of the powered flyback booster perform under varying operational conditions?

Further analysis of the optimum trajectory was conducted to identify the parameters that affect the optimum design. Through a small optimization that used different decision variable ranges, it was confirmed that the adapted range optimization had the best performance, in terms of the resulting efficiency and computational speed, an analysis was conducted on the stability characteristics of the vehicle. First, the bank angle profile was investigated further. It was identified that proper bank angle control is essential to sustain the final heading angle within the desired limits. To test this statement, the bank angle profile of the unpowered flyback booster was fed to the powered flyback booster. It was established that a lack of bank angle control introduces instabilities in the trajectory, such as a spiral motion. Through a trimmability analysis, it was observed that the booster is trimmable regardless of the thrust elevation. Although the thrust elevation angle affects the moment distribution, the influence of the thrust elevation angle on the C_m was significantly minimal. This behavior was most likely due

to the distance between CoM and CoT. It was expected to observe an increase in the thrust moment with an increasing distance. Consequently, the control surfaces would be deflected more to balance the thrust moment. In case the thrust moment is so large that the saturated control surfaces can still not balance the additional moment, the thrust elevation angle would have been highly coupled with the trimmability.

The above discussion provides the mission specific conclusions, yet, by adopting the above points, the main research question is answered in a more general spectrum:

How can a mission design process be optimized for unpowered and powered flyback boosters to effectively compare the two configurations?

The present research provided a basis for the future advancement of reusable launcher technologies. The comparison of the optimum trajectories yields that the powered flyback booster has more operational flexibility than an unpowered flyback booster. Only with unpowered capabilities, the trajectory cannot be optimized enough to reach the desired final distance-to-go. To compare the two configurations efficiently, the mission design process is optimized by using an evolving design space exploration process. The utilized methods ranged from simple approaches, one-at-a-time, to complex approaches such as Taguchi design. The complex methods suggest that it is possible to encounter unaccounted interactions between decision variables that were unexpected prior to the experiments. This research demonstrates the importance of a complete design space exploration to identify the overall relationships between different decision variables and responses. For future studies on trajectory design, it is concluded that a comprehensive design space exploration is essential for an optimum mission design, which has a reduced computational load and is guided toward a feasible solution space.

10.2. Recommendations

Throughout the research, analyses of some concepts were above the scope of this thesis. Certain assumptions or first-level approximations were made to deal with these concepts. However, it is possible to extend the research by providing more complex models. This would allow the system to be approximated with higher accuracy. Therefore, the performance and capability analysis of the vehicle will also be more accurate. In the upcoming section, the concepts that require further improvement and a method for improving these concepts are discussed.

Recommendation-1: Aerodynamic database

The aerodynamic data that is used for the FSSC-16 was adapted from the HORUS aerodynamic database and the graphs that were reported by the FESTIP study. However, in both of these sources, the aerodynamics of the vehicle is only provided up until the transonic Mach numbers. Since the aerodynamic design is not the main focus of this thesis, it was previously assumed that if the complete aerodynamic database is provided, the vehicle can be trimmable while flying through the transonic Mach numbers.

Therefore, to have unbiased results and make sure that the vehicle is fully controllable, it is significant to have a complete aerodynamic database with a trimmable vehicle. The number of available analytical methods for obtaining the transonic aerodynamics of a vehicle is limited. Therefore, it is often preferred to use wind tunnel testing for obtaining these values. However, it is significant to note that wind tunnel testing for transonic flow is not trivial. There are certain issues associated with the topic. The reflected shock waves from the walls are one of these issues. To mitigate this the testing facility should be equipped with adequate resources, such as porous walls instead of slotted walls, to distort the flow (Vos and Farokhi, 2015). Therefore, with a correct vehicle model and sufficient resources, such as testing facilities, it is possible to obtain the complete database.

Finally, note that a simple approach would have been to use the data provided for the PHOENIX vehicle and scale it to adapt the FSSC-16. Since the two vehicles provide a very comparable behavior in supersonic Mach numbers, it is assumed that PHOENIX can provide adequate information, to a first approximation so that the trimming capabilities of the vehicle can be assessed. However, to do so, the database should be provided both for the main body and the control surfaces. Since the control surface data is not publicly available, the method can be complicated and further deviate the accuracy.

Recommendation-2: Fractional factorial design subset method

During this study, to have conclusive results about the percentage contribution of the interactions and the individual variables, the subset method is implemented. It has been identified that the subset method allowed interactions to be observed with less confounding effects. However, the reason behind this method is that the decision variable array is so large that the whole array cannot be assessed once without requiring immense computational effort. It has been identified that an L_{32} array with resolution IV can observe the effect of 7 variables at once with minimal confounding. Hence, the subsets are generated. Although conclusive results can be obtained, such a method requires various runs and visual inspection.

Instead of adapting the subset method, the fractional factorial design can be performed on all the decision variables in one go. Since the decision variable list contains 24 variables, a large enough array with resolution IV has to be implemented. This can require excessive computational and implementation effort since there are no off-the-shelf simulations or libraries that implement the Taguchi interaction arrays. Especially arrays that are larger than L_{32} are difficult to construct. However, if the computational power is available and the tables are implemented correctly, such a simulation would provide the percentage contribution of the complete interactions and the complete individual variables. In return, this would reduce the post-processing effort of the subset method.

Recommendation-3: Decision Variables

During this thesis, a comprehensive trajectory analysis is conducted. It was concluded that a powered vehicle performs better than an unpowered vehicle. However, it would be interesting to observe the powered and unpowered capabilities of the booster combined. Thus, the decision vector should have the aerodynamic angles and the thrust parameters. Although this would introduce higher dimensionality to the trajectory problem, it presents a more accurate trajectory. In such a trajectory it would be possible to observe how aerodynamic parameters interact with the thrust parameters. Perhaps the design decisions made for the thrust parameters could be altered once the aerodynamic angles are actively controlled, which could potentially reduce the fuel consumption. For instance, when the bank angle is actively controlled, it will have significant effects on the heading angle change and distance-to-go. To attain an integrated understanding of the booster capabilities, it is recommended to observe the powered and unpowered capabilities together.

Recommendation-4: Computational Capabilities

The analysis performed in Section 8.3.3 is restricted by the computational capabilities that are available. Nevertheless, it is would be interesting to observe whether MOEA/D performs better in the long run than the NSGA-II algorithm. To do so, it is required to have more evolutions with sufficient number of individuals. Thus, it would be recommended to repeat the optimization process using larger batches, such as more individuals and more evolutions. This can be achieved by utilizing a supercomputer, such as the DelftBlue, which has a significantly larger memory than personal laptops. Such a study would validate that the obtained solution is not limited by the number of evolutions and individuals, and it is indeed the global optimum.

Recommendation-5: Flyability of Optimal Trajectory

Flyability refers to the ability of the spacecraft to follow the optimal trajectory. It is recommended to perform a study to analyze the flyability of the optimal trajectory. During the optimization process, the path and control constraints were implemented to move the design space toward more realistic trajectories. However, there are unaccounted factors that should be assessed to identify whether or not the vehicle can perform the flight in reality. Two main examples of these factors are a hardware assessment and a stability and controllability analysis.

As was mentioned in Section 7.3, the thrust elevation angle had an upper limit of 90°. Consequently, the optimum trajectory had nodes that have thrust elevation angles that are close to 90°. Theoretically, 90° is a feasible value, yet, for real-life applications it is unrealistically high due to hardware limitations. Often engines are designed to operate efficiently in a specific deflection range. Surpassing this range could provide integration challenges with the vehicle's structure. Although FSSC-16 had a comprehensive structural design, no study was performed to assess the compatibility of the hardware components. Therefore, a detailed analysis should be performed to ensure that the optimal deflection values can be performed by the vehicle.

Furthermore, it would be interesting to observe how the stability and controllability of the booster is maintained across the whole trajectory. A flyable flyback booster would be equipped with a control system. To ensure that the control system can follow the optimal trajectory, the flyback booster's eigenmotion should be assessed. This would provide valuable insights into the potential risk associated with the stability of the vehicle. Accordingly, unfeasible trajectories that cannot maintain the desired flight-path angle can be avoided.

Recommendation-6: Results and Local Optimization

The global optimizer found a solution to the flyback problem. The solution was further assessed by a local refinement. For the unpowered vehicle, no better solution was obtained. For the powered vehicle, the local refinement found a better solution. This value was then used to initialize a second round of optimization to guide the design space toward a different design region. At this point, instead of using a global optimizer or performing a local refinement at all, a local optimizer could be utilized. A local optimization finds the best solution nearby the provided starting point. It is more efficient than a global optimizer for solution refinement. Whereas, compared to a local refinement, a local optimizer has a better search capability. It would be interesting to observe how the final solution improves when local optimization is performed, instead of a local refinement and the second global optimization.

References

Amar, S., & Gowtham Manikanta, R. T. (2012). Air Breathing Rocket Engines and Sustainable Launch Systems. *Applied Mathematics and Materials*, *232*, 310–315. https://doi.org/10.4028/www.scientific.net/amm.232.310

Bauer, W., Rickmers, P., Kallenbach, A., Stappert, S., Wartemann, V., Hans-Joachim Merrem, C., Schwarz, R., Sagliano, M., Grundmann, J. T., Flock, A., Thiele, T., Kiehn, D., Bierig, A., Windelberg, J., Ksenik, E., Bruns, T., Ruhe, T., & Elsäßer, H. (2020). Dlr reusability flight experiment refex. *Acta Astronautica*, *168*, 57–68. https://doi.org/https://doi.org/10.1016/j.actaastro.2019.11.034

Bayer, M. (n.d.). Description of the festip vthl-tsto system concept studies [Unpublished study report]. https://forum.nasaspaceflight.com/index.php?action=dlattach;topic=30547.0;attach=536078

Bilgen, J. S. (2017). *Global Ascent Trajectory Optimization of a Space Plane* (Master's thesis). Delft University of Technology. the Netherlands.

Bislip-Morales, C. B. (2020). *Hypersonic Point-to-Point Travel for the Common Man* (Master's thesis). Delft University of Technology. the Netherlands.

Borst, C. (2012). *Module 2: Gyroscopes from AE4302 Avionics and Operations* [Lecture Slides].

Caporicci, M. (2000). *The future of european launchers: The esa perspective*. European Space Agency.

Chen, J. (2021). *Spacecraft state propagation and orbit determination using jet transport* (Doctoral dissertation). Universitat Polit'ecnica de Catalunya. Barcelona.

Ciftcioglu, O., & Bittermann, M. (2009). Adaptive formation of pareto front in evolutionary multi-objective optimization. In W. dos Santos (Ed.), *Evolutionary computation* (pp. 417–444). In-teh.

Daimler-Benz Aerospace. (1998). *FESTIP System Concept Description*.

Day, R. E. (1997). *Coupling dynamics in aircraft: A historical perspective*. California, National Aeronautics and Space Administration.

Deb, K. (2001). *Multi-objective optimization using evolutionary algorithms*. John Wiley Sons, Inc.

Deb, K., & Kumar, A. (1995). Real-coded genetic algorithms with simulated binary crossover: Studies on multimodal and multiobjective problems. *Complex Syst.*, *9*.

Deb, K., Pratap, A., Agarwal, S., & Meyarivan, T. (2002). A fast and elitist multiobjective genetic algorithm: Nsga-ii. *IEEE Transactions on Evolutionary Computation*, *6*(2), 182–197.

Dijkstra, M., Mooij, E., & Sudmeijer, K. (2013). Trajectory optimization to support the study of hypersonic aerothermodynamic phenomena. *AIAA Atmospheric Flight Mechanics (AFM) Conference, 2013*, [AIAA 2013–4501]. https://arc.aiaa.org/doi/10.2514/6.2013-4501

Dirkx, D., Lainey, V., Gurvits, L., & Visser, P. (2016). Dynamical modelling of the galilean moons for the juice mission. *Planetary and Space Science*, *134*, 82–95. https://doi.org/https://doi.org/10.1016/j.pss.2016.10.011

Dirkx, D., Mooij, E., & Root, B. (2019). Propagation and estimation of the dynamical behaviour of gravitationally interacting rigid bodies. *Astrophysics and Space Science*, *364*(2), 37. https://doi.org/10.1007/s10509-019-3521-4

Dujarric, C. (1999). *Possible future european launchers– a process of convergence*. Paris, European Space Agency.

Feinreich, B., Seckel, E., & Ellis, D. R. (1977). *In-flight simulation study of decoupled longitudinal controls for the approach and landing of a stol aircraft*. USA, National Aeronautics and Space Administration.

Fowlkes, W. Y., & Creveling, C. M. (1995). *Engineering methods for robust product design using taguchi methods in technology and product development*. Addison-Wesley Publishing Company.

Ghobadi, M., Shafaee, M., & Nadoushan, M. J. (2020). Reliability approach to optimal thruster configuration design for spacecraft attitude control subsystem. *Journal of Aerospace Technology and Management*, *12*(2), 1–22.

Guerreiro, A. P., Fonseca, C. M., & Paquete, L. (2020). The hypervolume indicator. *ACM Computing Surveys (CSUR)*, *54*, 1–42.

Hanson, J. (2000). Advanced guidance and control project for reusable launch vehicles. *AIAA Guidance, Navigation, and Control Conference and Exhibit, 2000*, [AIAA 2000–3957]. https://doi.org/10.2514/6.2000-3957

Hayhurst, M., Bitten, R., Judnick, D., Hallgrimson, I., & Youngs, M. (2016). *Historical Mass, Power, Schedule Cost Growth for NASA Instruments Spacecraft* [Symposium Presentation].

He, L., Shang, K., & Ishibuchi, H. (2020). Simultaneous use of two normalization methods in decomposition-based multi-objective evolutionary algorithms. *Applied Soft Computing*, *92*, 106316. https://doi.org/https://doi.org/10.1016/j.asoc.2020.106316

Historic American Engineering Record & National Aeronautics And Space Administration. (1968). Space transportation system, lyndon b. johnson space center, 2101 nasa parkway, houston, harris county, tx [Retrieved from the Library of Congress]. https://www.loc.gov/item/tx1106/

Holmes, W. (2012). *Lecture Notes on AERO2705 Frames of Reference, Orbits and Ellipses* [Lecture Notes].

Ishibuchi, H., Sakane, Y., Tsukamoto, N., & Nojima, Y. (2009). Evolutionary many-objective optimization by nsga-ii and moea/d with large populations. *2009 IEEE International Conference on Systems, Man and Cybernetics*, 1758–1763. https://doi.org/10.1109/ICSMC.2009.5346628

Jordan-Culler, T. (2016). *Basics of Reentry Vehicle Flight Dynamics* [Presentation].

Kang, E., Jackson, E., & Schulte, W. (2011). An approach for effective design space exploration. In R. Calinescu & E. Jackson (Eds.), *Foundations of computer software. modeling, development, and verification of adaptive systems* (pp. 33–54). Springer Berlin Heidelberg.

Kenwright, B. (2012). A beginners guide to dual-quaternions: What they are, how they work, and how to use them for 3d character hierarchies. *WSCG 2012*.

Koelle, D. (2002). Development costs of reusable launch vehicles. *Acta Astronautica*, *31*(1-9), 23–21. https://doi.org/10.1016/S0094-5765(02)00090-5

Kumar, K., de Pater, I., & Showalter, M. (2015). Mab's Orbital Motion Explained. *Icarus*, *254*, 102–121. https://doi.org/https://doi.org/10.1016/j.icarus.2015.03.002

Limleamthong, P., & Guillén-Gosálbez, G. (2018). Combined Use of Bilevel Programming and Multi-objective Optimization for Rigorous Analysis of Pareto Fronts in Sustainability Studies: Application to the Redesign of the UK Electricity Mix. *28th European Symposium on Computer Aided Process Engineering, 2019*, 1099–1104. https://doi.org/10.1016/B978-0-444-64235-6.50192-3

McRuer, D. (1991). Design and modeling issues for integrated airframe/propulsion control of hypersonic flight vehicles. *1991 American Control Conference*, 729–734. https://doi.org/10.23919/ACC.1991.4791471

Mooij, E. (1994). *The Motion of a Vehicle in a Planetary Atmosphere* (LR-768). Delft University of Technology.

Mooij, E. (1998). *Aerospace-plane flight dynamics: Analysis of guidance and control concepts* (Doctoral dissertation). Delft University of Technology. the Netherlands.

Mooij, E. (2016). *AE4870B - Re-entry Systems* [Lecture Notes]. Delft University of Technology.

Mooij, E. (1995). *The Horus-2B Reference Vehicle* [Memorandum]. Delft, Delft University of Technology.

Mooij, E. (1997). *Linear quadratic regulator design for an unpowered, winged re-entry vehicle* (Vol. 03: Astrodynamics and satellite systems). Delft University Press.

Mooij, E. (2017). Re-entry guidance for path-constraint tracking. *AIAA Guidance, Navigation, and Control Conference, 2017*, [AIAA 2017–1265]. https://doi.org/10.2514/6.2017-1265

Mooij, E., & Dirkx, D. (2022). *AE4-866 - Propagation and Optimisation in Astrodynamics* [Lecture Notes].

Moore, T. E. (1991). *Space shuttle entry terminal area energy management*. USA, National Aeronautics and Space Administration.

Mulder, J., van Staveren, W., van der Vaart, J., de Weerdt, E., de Visser, C., in 't Veld, A., & Mooij, E. (2013). *Lecture Notes AE3202: Flight Dynamics* [Lecture Notes]. Delft University of Technology.

Naftel, J. C., & Powell, R. W. (1993). *Analysis of the Staging Maneuver and Booster Glideback Guidance for a Two-Stage, Winged, Fully, Reusable Launch Vehicle*. Virginia, National Aeronautics and Space Administration.

NASA. (2007). *Nasa systems engineering handbook* (1st ed.). National Aeronautics and Space Administration.

Peterson, W., Ankney, W., Bell, J., Berning, M., Bryant, L., Bufkin, A., Cain, L., Caram, J., B.Cockrell, D. Curry, T. D., Gomez, R., Hong, A., Jih, D., Labbe, S., M. Le, M. L., Lunney, B., Masciareili, J., Musler, J., Nuss, R., … Thornburg, R. (1994). *Liquid Flyback Booster Pre-Phase A Study Assessment Vol.2*. USA, National Aeronautics and Space Administration.

Qiao, J., Zhou, H., Yang, C., & Yang, S. (2019). A decomposition-based multiobjective evolutionary algorithm with angle-based adaptive penalty. *Applied Soft Computing*, *74*, 190–205.

Rana, L. (2017). *Space access systems design: Synthesis methodology development for conceptual design of future space access systems* (Doctoral dissertation). The University of Texas at Arlington. Arlington, Texas.

Schlotterer, M. (2008). Navigation system for reusable launch vehicle. *31st Annual AAS Guidance and Control Conference, 2008*, [AAS 08–076].

Schwarz, R., Kiehn, D., Trigo, G. F., Razgus, B., Wenzel, A., Seelbinder, D., Sommer, J., Theil, S., Markgraf, M., Dumke, M., Reigenborn, M., Körner, M. B., Solari, M., Braun, B., & Pfau, D. (2019). Overview of flight guidance, navigation, and control for the dlr reusability flight experiment (refex). *8TH European Conference for Aeronautics and Space Sciences (EUCASS)*.

Shirazi, A., Ceberio, J., & Lozano, J. A. (2018). Spacecraft trajectory optimization: A review of models, objectives, approaches and solutions. *Progress in Aerospace Sciences*, *102*, 76–98. https://doi.org/https://doi.org/10.1016/j.paerosci.2018.07.007

Sippel, M., Manfletti, C., & Burkhardt, H. (2006). Long-term/strategic scenario for reusable booster stages. *Acta Astronautica*, *58*(4), 209–221. https://doi.org/10.1016/j.actaastro.2005.09.012

SRE-PA and D-TEC staff. (2012). *Margin philosophy for science assessment studies* [Document].

Stappert, S., Rickmers, P., Bauer, W., & Sippel, M. (2019). Mission Analysis and Preliminary Re-entry Trajectory Design of the DLR Reusability Flight Experiment ReFEx. *8th European Conference for Aeronautics and Space Sciences, 2019*, [EUCASS 2019–436]. https://www.eucass.eu/doi/EUCASS2019-0436.pdf

Stengel, R. (2019). *Aircraft Flight Dynamics: Aerodynamic Moments* [Lecture Notes].

Sushnigdha, G., & Joshi, A. (2018). Trajectory design of re-entry vehicles using combined pigeon inspired optimization and orthogonal collocation method [5th IFAC Conference on Advances in Control and Optimization of Dynamical Systems ACODS 2018]. *IFAC-PapersOnLine*, *51*(1), 656–662. https://doi.org/https://doi.org/10.1016/j.ifacol.2018.05.110

Tapley, B., Ries, J., Bettadpur, S., Chambers, D., Cheng, M., Condi, F., Gunter, B., Kang, Z., Nagel, P., Pastor, R., Pekker, T., Poole, S., & Wang, F. (2005). Ggm02 an improved earth gravity field model from grace. *Journal of Geodesy*, *79*(8), 467–478. https://link.springer.com/article/10.1007/s00190-005-0480-z

Tetlow, M. R., Schöttle, U. M., & Schneider, G. M. (2001). Comparison of glideback and flyback boosters. *Journal of Spacecraft and Rockets*, *38*(5), 752–758. https://arc.aiaa.org/doi/10.2514/2.3742

Tetlow, M. R. (2003). *Commerical launch vehicle design and predictive guidance development* (Doctoral dissertation). The University of Adelaide. Australia.

Tramonti, L., & Brusch, R. G. (1972). Optimized space shuttle trajectory simulation. *NASA. Langley Res. Center Space Shuttle Aerothermodyn. Tech. Conf., vol. 4*.

Tudat Space. (2022). *About tudat*. Retrieved April 24, 2023, from https://docs.tudat.space/en/v0.3.1/_src_about/about.html

Vallado, D. A., & McClain, W. D. (2007). *Fundamentals of Astrodynamics and Applications* (2nd ed.). Kluwer Academic Publishers.

Vaughan, W. W. (2010). Guide to reference and standard atmosphere models. https://doi.org/https://doi.org/10.2514/4.867842.001

Viavattene, G. (2018). *Flying Qualities and Controllability of Hypersonic Spaceplanes* (Master's thesis). Delft University of Technology. the Netherlands.

Vos, R., & Farokhi, S. (2015). *Introduction to transonic aerodynamics* (Vol. Fluid mechanics and its applications). Springer Science+Business Media. https://doi.org/10.1007/978-94-017-9747-4

Wan, C., Pei, C., Dai, R., Jing, G., & Rea, J. R. (2021). Six-dimensional atmosphere entry guidance based on dual quaternion. https://doi.org/10.2514/6.2021-0507

Weiland, C. (2014). *Aerodynamic data of space vehicles* (1st ed.). Springer.

Wertz, J. R. (2000). Economic model of reusable vs. expandable launch vehicles. *IAF Congress: Economics and Commercialization of Space Activities*.

Wilken, J., Stappert, S., & Sippel, M. (2021). Parametric cost estimation in the preliminary design phase of reusable launch vehicles. *2nd ESA Space Cost Engineering Conference*.

Yokoyama, N., & Suzuki, S. (2005). Modified genetic algorithm for constrained trajectory optimization. *Journal of Guidance, Control, and Dynamics*, *28*(2), 139–144.

Zhang, Q., & Li, H. (2007). Moea/d: A multiobjective evolutionary algorithm based on decomposition. *IEEE Transactions on Evolutionary Computation*, *11*(6), 712–731. https://doi.org/10.1109/TEVC.2007.892759

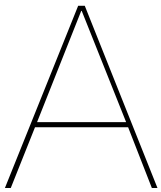

Fractional Factorial Design Array and Taguchi Design

Table 16.8 L32 (2^{7-2}) Resolution IV

Run	1 A	2 B	3	4 C	5	6	7 D	8 E	9	10	11	12	13	14	15	16 F
1	1	1	1	1	1	1	1	1	1	1	1	1	1	1	1	1
2	1	1	1	1	1	1	1	1	1	1	1	1	1	1	1	2
3	1	1	1	1	1	1	1	2	2	2	2	2	2	2	2	1
4	1	1	1	1	1	1	1	2	2	2	2	2	2	2	2	2
5	1	1	1	2	2	2	2	1	1	1	1	2	2	2	2	1
6	1	1	1	2	2	2	2	1	1	1	1	2	2	2	2	2
7	1	1	1	2	2	2	2	2	2	2	2	1	1	1	1	1
8	1	1	1	2	2	2	2	2	2	2	2	1	1	1	1	2
9	1	2	2	1	1	2	2	1	1	2	2	1	1	2	2	1
10	1	2	2	1	1	2	2	1	1	2	2	1	1	2	2	2
11	1	2	2	1	1	2	2	2	2	1	1	2	2	1	1	1
12	1	2	2	1	1	2	2	2	2	1	1	2	2	1	1	2
13	1	2	2	2	2	1	1	1	1	2	2	2	2	1	1	1
14	1	2	2	2	2	1	1	1	1	2	2	2	2	1	1	2
15	1	2	2	2	2	1	1	2	2	1	1	1	1	2	2	1
16	1	2	2	2	2	1	1	2	2	1	1	1	1	2	2	2
17	2	1	2	1	2	1	2	1	2	1	2	1	2	1	2	1
18	2	1	2	1	2	1	2	1	2	1	2	1	2	1	2	2
19	2	1	2	1	2	1	2	2	1	2	1	2	1	2	1	1
20	2	1	2	1	2	1	2	2	1	2	1	2	1	2	1	1
21	2	1	2	2	1	2	1	1	2	1	2	2	1	2	1	1
22	2	1	2	2	1	2	1	1	2	1	2	2	1	2	1	2
23	2	1	2	2	1	2	1	2	1	2	1	1	2	1	2	1
24	2	1	2	2	1	2	1	2	1	2	1	1	2	1	2	2
25	2	2	1	1	2	2	1	1	2	2	1	1	2	2	1	1
26	2	2	1	1	2	2	1	1	2	2	1	1	2	2	1	2
27	2	2	1	1	2	2	1	2	1	1	2	2	1	1	2	1
28	2	2	1	1	2	2	1	2	1	1	2	2	1	1	2	2
29	2	2	1	2	1	1	2	1	2	2	1	2	1	1	2	1
30	2	2	1	2	1	1	2	1	2	2	1	2	1	1	2	2
31	2	2	1	2	1	1	2	2	1	1	2	1	2	2	1	1
32	2	2	1	2	1	1	2	2	1	1	2	1	2	2	1	2
			1×2 4×7		1×4 2×7	1×7 2×4			1×8	2×8		4×8	16×29		7×8	

Run	17	18	19	20	21	22	23	24	25	26	27	28	29 G	30	31
1	1	1	1	1	1	1	1	1	1	1	1	1	1	1	1
2	2	2	2	2	2	2	2	2	2	2	2	2	2	2	2
3	1	1	1	1	1	1	1	2	2	2	2	2	2	2	2
4	2	2	2	2	2	2	2	1	1	1	1	1	1	1	1
5	1	1	1	2	2	2	2	1	1	1	1	2	2	2	2
6	2	2	2	1	1	1	1	2	2	2	2	1	1	1	1
7	1	1	1	2	2	2	2	2	2	2	2	1	1	1	1
8	2	2	2	1	1	1	1	1	1	1	1	2	2	2	2
9	1	2	2	1	1	2	2	1	1	2	2	1	1	2	2
10	2	1	1	2	2	1	1	2	2	1	1	2	2	1	1
11	1	2	2	1	1	2	2	2	2	1	1	2	2	1	1
12	2	1	1	2	2	1	1	1	1	2	2	1	1	2	2
13	1	2	2	2	2	1	1	1	1	2	2	2	2	1	1
14	2	1	1	1	1	2	2	2	2	1	1	1	1	2	2
15	1	2	2	2	2	1	1	2	2	1	1	1	1	2	2
16	2	1	1	1	1	2	2	1	1	2	2	2	2	1	1
17	2	1	2	1	2	1	2	1	2	1	2	1	2	1	2
18	1	2	1	2	1	2	1	2	1	2	1	2	1	2	1
19	2	1	2	1	2	1	2	2	1	2	1	2	1	2	1
20	1	2	1	2	1	2	1	1	2	1	2	1	2	1	2
21	2	1	2	2	1	2	1	1	2	1	2	2	1	2	1
22	1	2	1	1	2	1	2	2	1	2	1	1	2	1	2
23	2	1	2	2	1	2	1	2	1	2	1	1	2	1	2
24	1	2	1	1	2	1	2	1	2	1	2	2	1	2	1
25	2	2	1	1	2	2	1	1	2	2	1	1	2	2	1
26	1	1	2	2	1	1	2	2	1	1	2	2	1	1	2
27	2	2	1	1	2	2	1	2	1	1	2	2	1	1	2
28	1	1	2	2	1	1	2	1	2	2	1	1	2	2	1
29	2	2	1	2	1	1	2	1	2	2	1	2	1	1	2
30	1	1	2	1	2	2	1	2	1	1	2	1	2	2	1
31	2	2	1	2	1	1	2	2	1	1	2	1	2	2	1
32	1	1	2	1	2	2	1	1	2	2	1	2	1	1	2
	1×16	2×16		4×16	8×29		7×16	8×16	4×29	7×29		1×29			2×29

Figure A.1: L32 array with resolution IV showing the main effect and interactions for corresponding columns (Fowlkes and Creveling, 1995)

B

Optimization Results

As a part of the optimization process, the initial population is estimated with a random initializer. To ensure that the algorithm is not biased towards the chosen initial seed, which is 42, the optimization and certain other simulations that use the randomizer, such as the local refinement process, are run with two more seeds, which are 195 and 252. By running optimization with multiple seeds, it is aimed to assess whether the algorithm consistently converges to the same solution space. Consistently converging optimization will verify that the algorithm is indeed in the feasible solution space and is not severely influenced by the initial conditions. Thus, in this appendix, the different seeds are presented for each process that has a random initializer, such as optimization, local refinement, and a part of the sensitivity analysis.

B.1. Unpowered Optimization and Local Refinement

The unpowered optimization yielded unexpected results. To ensure that the obtained values are indeed the optimum solution, a local refinement was performed. Below in Figure B.1 the penalized objective space is observed. These figures are provided to have a better overview of the final penalty that is introduced due to a wrong heading angle alignment at the end of the optimization. Meanwhile, in Figure B.2, the same graph is provided for another seed.

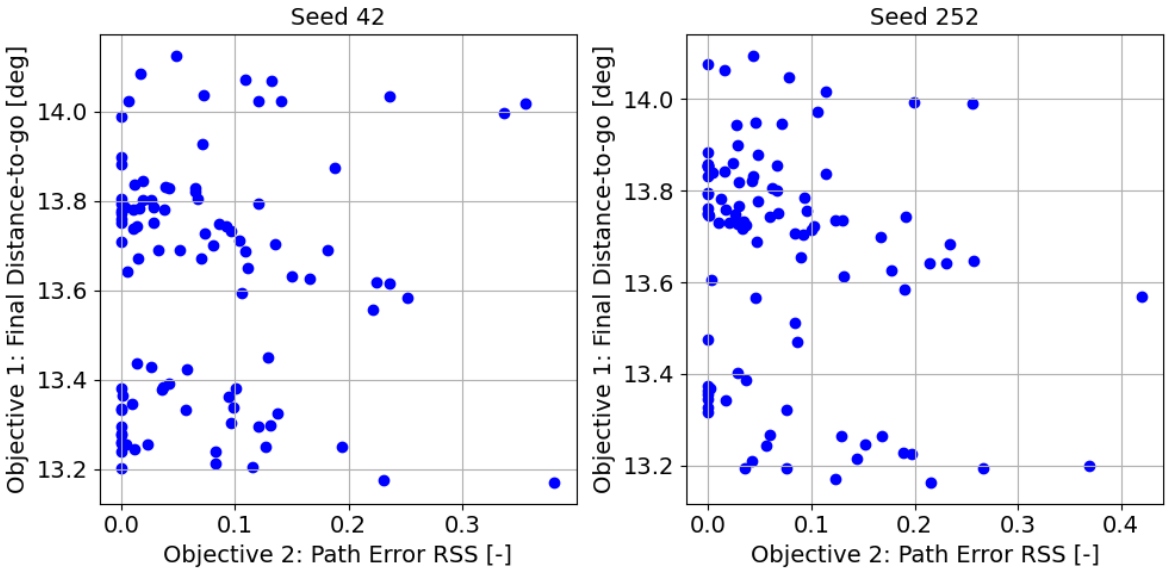

Figure B.1: Penalized objective space for the unpowered vehicle optimization

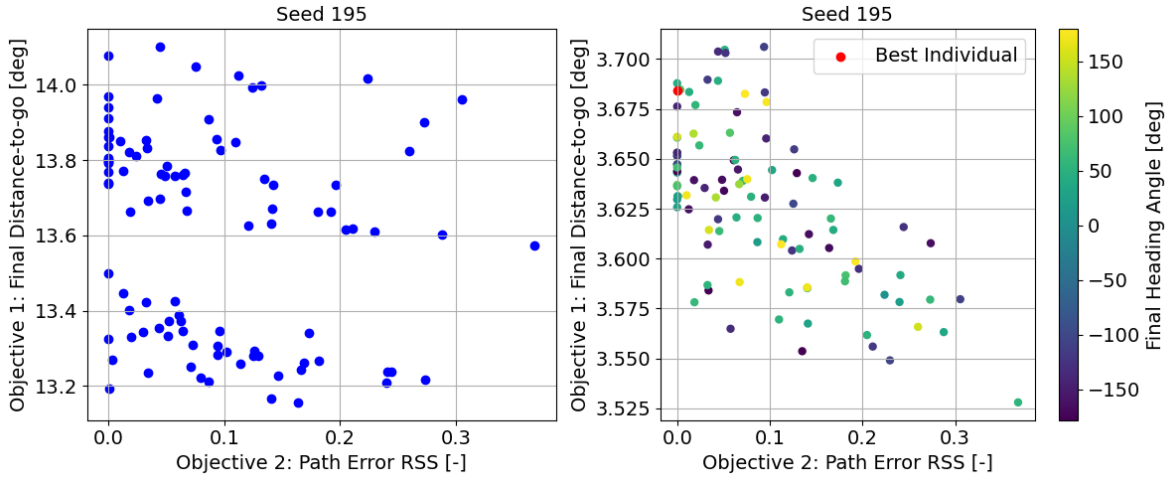

Figure B.2: Penalized and unpenalized objective space for the unpowered vehicle optimization with seed 195

B.2. Powered Optimization and Local Refinement

To ensure that the values obtained in Section 8.4.2 are not biased, the optimization is run with different seeds. In Figure B.3, the objective space for the powered booster with seed 252 is visualized. It can be seen that the initial population has a different spreading trend than the one in Section 8.4.2, which had a seed of 42. In the first population seed 42 could obtain individuals that relatively have low Objective 1, around 10,000-20,000 kg. Meanwhile, seed 52 could not obtain individuals with low Objective 1. Also Objective 2 spread of seed 252 is larger than seed 42 in the initial population. In terms of Objective 2, both seeds successfully bring the population to the same range of 0.01-0.02. On the other hand, the best Objective 1 value has a difference around 700 kg. The Individual 1, Individual 2, and Individual 3 for the seed 252 is reported in Table B.1.

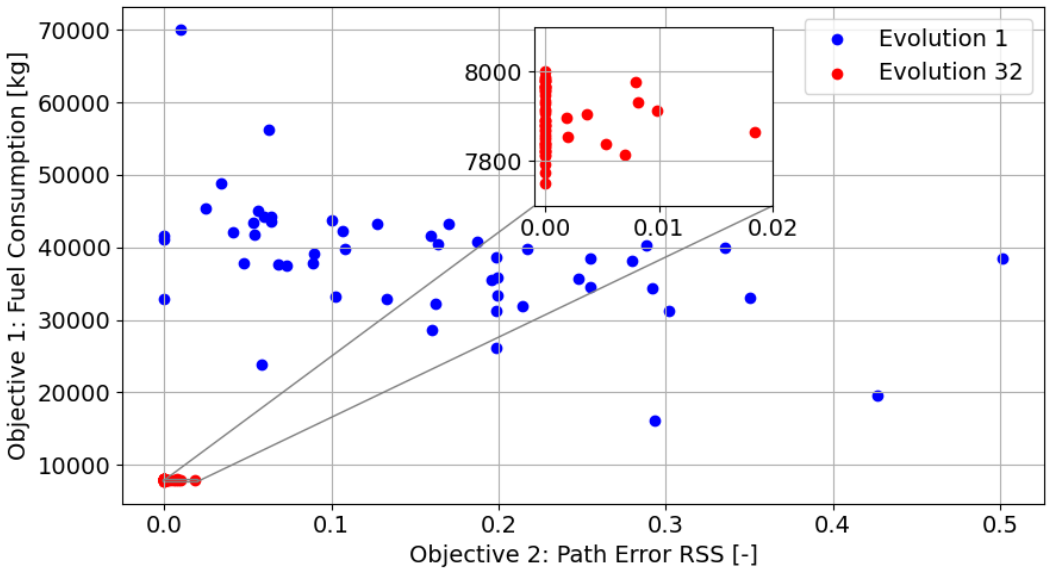

Figure B.3: Objective space for the powered booster optimization with seed 252

Since out of 100 individuals only one individual showed an improvement, to rule out the possibility of a bias. The local refinement process is also run with a seed 195 and seed 252. The results are presented in Figure B.4 and Figure B.5. Furthermore, in seed 252, it can be clearly identified that there are two individuals that performed better than the current optimal solution. This supports the necessity of a second optimization, as performed in the Section 8.4.2.

Table B.1: Best individuals from Evolution 32 for seed 252

	Individual 1	Individual 2	Individual 3	Units
Fuel Consumption	7775.66	7999.98	7865.92	kg
Path Error RSS	0.0	0.0	0.018	-

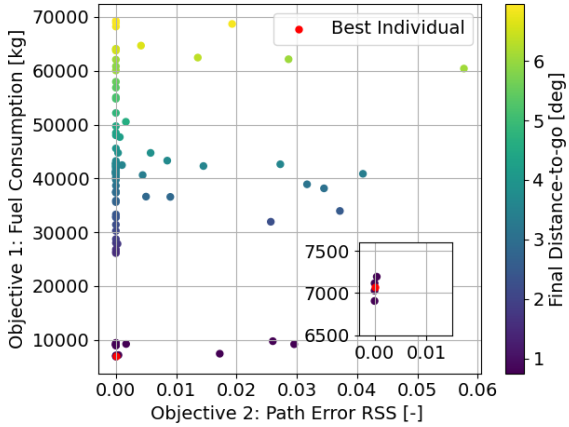

Figure B.4: Powered optimization local refinement with seed 195

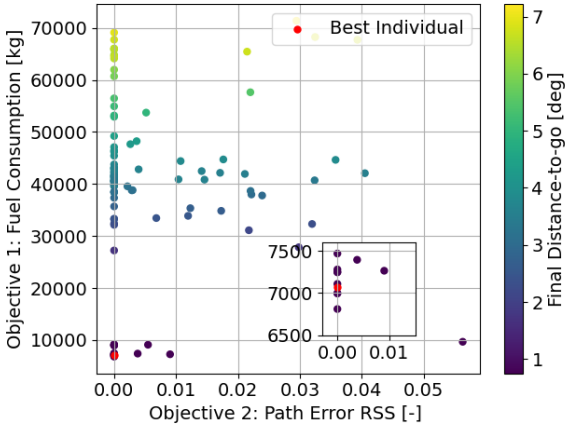

Figure B.5: Powered optimization local refinement with seed 252

B.3. Trajectory Reflection Results

The full set of decision variables for the best individuals in the decision variable analysis conducted in Section 9.1. The values below show that with different decision variable ranges, certain thrust parameters still had a final value that is at the vicinity of the optimal value. Often the semi-adapted range values showed the greatest variability from the optimal value.

Table B.2: Thrust magnitudes for different decision variable ranges

	Full Range	Semi-adapted Range	Adapted Range	Units
T_1	304.15	336.95	349.21	kN
T_2	10.30	236.05	234.17	kN
T_3	32.83	238.33	81.22	kN
T_4	390.89	259.87	200.53	kN
T_5	341.08	231.34	386.54	kN
T_6	127.26	133.79	100.06	kN
T_7	113.09	100.1	155.78	kN
T_8	383.06	395.17	367.95	kN

Table B.3: Thrust elevation angles for different decision variable ranges

	Full Range	Semi-adapted Range	Adapted Range	Units
ϵ_1	83.29	63.39	58.56	deg
ϵ_2	81.85	12.05	10.07	deg
ϵ_3	36.00	5.76	5.81	deg
ϵ_4	64.64	2.82	22.00	deg
ϵ_5	78.83	88.47	84.40	deg
ϵ_6	65.04	83.11	83.06	deg
ϵ_7	3.00	1.99	1.98	deg
ϵ_8	78.27	63.34	80.47	deg

Table B.4: Thrust azimuth angles for different decision variable ranges

	Full Range	Semi-adapted Range	Adapted Range	Units
ψ_1	28.15	68.90	79.00	deg
ψ_2	71.79	79.68	76.20	deg
ψ_3	74.07	79.72	73.25	deg
ψ_4	29.91	79.75	18.74	deg
ψ_5	18.93	5.03	37.31	deg
ψ_6	29.58	31.87	11.69	deg
ψ_7	18.00	57.51	7.99	deg
ψ_8	24.20	79.98	11.67	deg